

Electrochemical Sensors

A thesis submitted for the degree of

Doctor of Philosophy

in Physical and Theoretical Chemistry

Yuqi Chen

St John's College

Trinity Term 2023

Abstract

This thesis focuses on the development of electrochemical sensors, in which three main perspectives are explored. First, bespoke pH sensors for near-neutral conditions are developed for both freshwater and seawater. Inspired by the importance and challenge of detection in seawater, bromide and chloride quantifications are subsequently studied. In addition to the optimisation of the working electrode, the potential of using a reference electrode based on a redox couple with soluble solution redox species in electrochemical equilibrium with a solid is analysed referring to the specific case of the Ag/AgBr/Br^- reference electrode.

Chapter 1 serves as an introduction, providing essential background knowledge about fundamental electrochemistry and the electrochemical techniques employed throughout this thesis. Then, **Chapter 2** offers a generic account of the chemicals, reagents and instrumentation employed with specific details being given in subsequent individual chapters.

Chapters 3 - 4 report the study of amperometric pH sensing using an iridium electrode for application under near-neutral conditions. In **Chapter 3**, the electrochemical behaviour of iridium under neutral conditions is first studied, providing insight information about the redox mechanism forming pH-sensitive iridium hydrous oxide, and the consequent in-situ electrochemical fabrication conditions required. Then, by using the square wave voltammetry, the pH sensing character of electrochemically generated material is revealed, and the methodology validated in freshwater. Building on the findings from the previous chapter, **Chapter 4** presents a bespoke calibration-free pH sensor that utilises an in-situ modified iridium electrode for applications in seawater. The sensor is designed to be calibration-free by measuring the "super-Nernstian" response of Ir(III/IV) relative to the less sensitive upd H oxidation signal, with the pH reported on the total hydrogen ion scale. The optimized sensor can lead to a super-Nernstian response of high sensitivity in air-saturated seawater.

Chapters 5 and 6 focus on the chloride and bromide detection in seawater, of which the main challenges are the similar chemical properties between the two ions as halides and the presence of chloride at levels hundreds of times more concentrated than bromide, not to mention the complex matrix of the seawater. Analysis of bromide is first presented in **Chapter 5**. Noting the interference by chloride when present at high concentrations, traditional silver electrodes commonly used for amperometric halide measurements are seen to be not suitable. Instead, a bespoke reagent-free electrochemical bromide sensor is developed based on voltammetric oxidation at a macro-Pt electrode. By employing square wave voltammetry combined with the standard addition method, the proposed sensor is successfully validated in both artificial seawater and authentic natural seawater. In **Chapter 6**, three types of electrodes (Au, glassy carbon, and Pt) are further studied for the analysis of chloride and/or bromide in seawater. After studying their electrochemical behaviours in artificial seawater, we develop optimal voltammetric procedures for the detection using proper electrodes. Our findings indicate that the Au electrode is unsuitable for Cl^- and/or Br^- sensing due to its dissolution and passivation in ASW, while the use of glassy carbon results in poorly defined chloride and bromide signals. In contrast, platinum is identified as a favourable candidate for chloride detection in artificial seawater using square wave voltammetry. Based on the comprehensive analysis presented in **Chapters 5 and 6**, we recommend platinum electrodes for both bromide and chloride analysis in seawater due to their robust performance and reliable results.

In **Chapter 7**, we conduct an investigation of the voltammetry of a redox couple with soluble solution redox species in electrochemical equilibrium with a solid using the specific example of $Ag/AgBr/Br^-$, using both experimental and computational approaches. Through the analysis of the voltammetric waveshape and the apparent transfer coefficient, we find that the process yields apparent transfer coefficients significantly exceeding unity, thus highlighting the advantage of employing a reference electrode with a 1:0 process.

Acknowledgements

I am deeply grateful to my supervisor, Prof. Richard G. Compton, for introducing me to the world of electrochemistry and for the immense support and guidance he has provided throughout my academic journey, starting from my time as a summer student, a Part II student, and now a DPhil student. Moreover, I am indebted to him for bringing me into the welcoming embrace of the RGC family, where I have had the pleasure of meeting and collaborating with the exceptional individuals whom I express my gratitude to below. His enthusiasm, persistence, and commitment to progress have been truly inspiring and will remain with me always.

I extend my heartfelt thanks to Dr. Xiuting Li for offering me a position in the lab at Shenzhen University during the pandemic, providing academic support, and being patient in solving my problems. Her support was invaluable during the time I couldn't be in Oxford with Richard. I am also thankful to Dr. Danlei Li and Dr. Christopher Batchelor-McAuley for their guidance at the beginning of my DPhil study.

I am indebted to all the members of the RGC group since 2018. Special thanks to Dr. Yuanyuan Lu for her constant companionship and unwavering support in both my studies and personal life. I am grateful to Dr. Minjun Yang, Dr. Haotian Chen, Dr. Yifei Zhang, Dr. Yanjun Guo, Dr. Huanxin Li, Dr. Joseph Elliott, Dr. Ruiyang Miao, Yuanmin Zhang, and all the past and present group members. Working with you has been a truly enjoyable experience.

My gratitude also extends to my family for their love and encouragement. I want to thank my best friends Melody Lu and Clover Ye for their constant companionship and understanding since my undergraduate days. I am deeply touched that these wonderful people have always been there for me, whether during times of happiness or challenges.

I am thankful to Oxford for making my 18th birthday wish come true and providing me with a platform to gain incredible experiences and foster my all-round abilities. As I always say, my goal is to become a better version of myself. And once again, we are RGC family!

Glossary

Roman Symbols

Symbol	Meaning	Unit
A	Electroactive layer area	m^2
A_e	Electrode area	m^2
$[A^z]$	Bulk concentration of species A^z	mol cm^{-3}
C_d	Capacitance of the double layer per unit area	F m^{-2}
C_j	Concentration of species j	mol cm^{-3}
D	Diffusion coefficient	cm^2 s^{-1}
D_j	Diffusion coefficient of species j	cm^2 s^{-1}
d	Diffusion layer thickness	cm
I	Electrical current	A
I_p	Peak current	A
J	Heterogeneous reaction flux	mol cm^{-2} s^{-1}
$J_j(x)$	Flux of species j	mol cm^{-2} s^{-1}
$J_{m,j}(x)$	Migratory flux	mol cm^{-2} s^{-1}
$[j]$	Concentration of species j	mol dm^{-3}
E	Applied potential at the electrode	V
E^0	Standard electrode potential	V
E_f^0	Formal potential	V

E_{mid}	Mid-point potential	V
$E_{1/2}$	Half-wave potential	V
ΔE_p	Pulse height in SWV	V
ΔE_s	Staircase height in SWV	V
ΔE_{pp}	Peak to peak separation	V
F	Faraday constant	C mol^{-1}
f	Square wave frequency	Hz
$\Delta G_c^{\dagger}$, $\Delta G_a^{\dagger}$	Standard Gibbs energy change	J mol^{-1}
k^0	Standard electrochemical rate constant	cm s^{-1}
k_c, k_a	Rate constant for cathodic/anodic reactions	cm s^{-1}
m_T	Mass transport coefficient	cm s^{-1}
M	Molar mass	g mol^{-1}
N_A	Avogadro constant	mol^{-1}
n	Number of electrons transferred	Unitless
P^0	Standard pressure	N m^{-2}
Q	Total electric charge	C
R	Universal gas constant	J K^{-1} mol^{-1}
R_s	Solution resistance	Ω
T	Absolute temperature	K
t_p	Single potential pulse in SWV	s

t_s	Single potential cycle in SWV	s
X_{DL}	Debye length	Å
z	Charge of the species	C
z_j	Ionic charge of species j	C

Greek Symbols

Symbol	Meaning	Unit
α, β	Transfer coefficient	Unitless
ρ	Density	g cm^{-3}
μ_j	Chemical potential of species j	J mol^{-1}
$\bar{\mu}_j$	Electrochemical potential	J mol^{-1}
ϕ	Electrical potential	V
γ_j	Activity coefficient of species j	Unitless
ε_0	Permittivity of free space	C^2 J^{-1} m^{-1}
υ	Scan rate	Vs^{-1}
$\upsilon(x)$	Local fluid velocity	cm s^{-1}
Λ	Matsuda-Ayabe parameter	Unitless
Γ	Surface coverage of reactant at the electrode surface	mol cm^{-2}

Contents

Abstract ..... **i**

Acknowledgements ..... **iii**

Glossary ..... **i**

Contents ..... **vii**

Chapter 1 Introduction to Electrochemistry **1**

1.1 Electrochemical Equilibrium 1

1.2 Electrode Kinetics 7

1.3 Mass Transport 12

1.3.1 Diffusion 12

1.3.2 Convection 15

1.3.3 Migration 16

1.4 Faradaic and non-Faradaic Processes 17

1.4.1 Faradaic Processes 17

1.4.2 Non-Faradaic Processes 17

1.5 Electrochemical Cells 20

1.6 Electrochemical Techniques 21

1.6.1 Cyclic Voltammetry 21

1.6.2 Square Wave Voltammetry 28

1.6.3 Chronoamperometry 29

References 31

Chapter 2 Experimental 33

2.1 Chemicals and Reagents.....33

2.2 Electrochemical Instrumentation.....34

2.2.1 Preparation of Macrodisc Electrodes 35

2.2.2 Preparation of Iridium Wires 35

2.2.3 Fabrication of Silver Macrodisc Electrodes.....36

Chapter 3 A Simplified Methodology: pH Sensing Using an In-situ Activated Ir Eelectrode under Neutral Conditions 37

3.1 Introduction 37

3.2 Experimental 42

3.3 Results and Discussion.....44

3.3.1 Cyclic Voltammetric Study of Ir Metal Electro-Oxidation 44

3.3.2 Optimisation of the Electrode Activation 48

3.3.3 pH dependency of the Iridium Hydrous Oxide Layer in Buffer Solutions.....51

3.3.4 Real Sample Analysis: pH Measurement in Natural Water.....53

3.4 Conclusions 54

Appendices.....56

References.....66

Chapter 4 A Calibration-Free pH Sensor Using an In-Situ Modified Iridium Electrode for Bespoke Application in Seawater 70

4.1 Introduction 70

4.2 Experimental 77

4.3 Results and Discussion 78

4.3.1 Cyclic Voltammetry of Iridium and Iridium Oxides 79

4.3.2 Optimisation of Potential Cycling Activation 81

4.3.3 pH Dependency of the Voltammetric Responses of the Iridium Hydrous Oxide Layers 83

4.4 Conclusions 89

Appendix 90

References 91

Chapter 5 A Bespoke Reagent-free Amperometric Bromide Sensor for Seawater 95

5.1 Introduction 95

5.2 Experimental 100

5.3 Results and Discussion 102

5.3.1 Bromide Detection Using a Silver Macro-electrode 102

5.3.2 Electrochemical Study of Br^- with a Pt Macro-electrode 106

5.3.3 Sensitivity Analysis by Standard Additions Using SWV 108

5.3.4 Real Sample Analysis in Natural Waters 110

5.4 Conclusions 112

Appendices 113

References 119

Chapter 6 Direct Electrochemical Analysis in Seawater: Chloride and Bromide Detection.....122

6.1 Introduction.....122

6.2 Experimental.....126

6.3 Results and Discussion.....127

6.3.1 Cyclic Voltammetric Study of a Gold Electrode in Artificial Seawater.....127

6.3.2 Cyclic Voltammetry at Glassy Carbon and Platinum Electrodes in ASW.....131

6.3.3 Analysis of Bromide at a Glassy Carbon Electrode.....134

6.3.4 Analysis of Chloride at the Platinum Electrode.....136

6.3.5 Real Sample Analysis.....138

6.4 Conclusions.....139

Appendices.....140

References.....150

Chapter 7 Reversible Cyclic Voltammetry and Non-unity Stoichiometry: The Ag/AgBr/Br^- Redox Couple.....153

7.1 Introduction.....153

7.2 Experimental.....156

7.3 Theory (work of Dr. Haotian Chen).....156

7.3.1 Simulation of Voltammetry.....156

7.3.2 Extraction of Electrode Surface Concentrations from Experimental Voltammetric Data.....159

7.4 Simulation Methods (work of Dr. Haotian Chen) 159

7.5 Simulation Results (work of Dr. Haotian Chen) 160

7.6 Results and Discussion 164

7.7 Conclusions 170

Appendices 171

References 182

Conclusions 183

Chapter 1

Introduction to Electrochemistry

As a branch of physical chemistry, electrochemistry is a study of the relationship between electricity and chemical reactions, while electroanalysis is its sub-branch focusing on the analysis of chemical substances. This chapter introduces some fundamentals of electrochemistry and basic electrochemical techniques. The theoretical topics cover electrochemical equilibrium, electrode kinetics and electrode processes. Then, electrochemical methods, namely cyclic voltammetry, square wave voltammetry and chronoamperometry, are presented. These concepts and techniques are required for understanding the experimental results and their interpretation in later chapters.

1.1 Electrochemical Equilibrium

Electrochemical reactions cause chemical change at the interface between an electrode (typically a metal) and a solution containing the redox species of interest. This can be described by Eqn. (1.1), showing a simple one-electron transfer electrochemical equilibrium of a redox couple A^Z and B^{Z-1},

$$\boldsymbol{A^{Z}(aq) + e^{-}(m) \underset{k_a}{\overset{k_c}{\rightleftharpoons}} B^{Z-1}(aq)} \tag{1.1}$$

where A^Z and B^{Z-1} are the oxidised and reduced forms of the redox couple in solution phase. In contrast to normal chemical equilibria, the electrochemical equilibrium (Eqn. (1.1)) involves the transfer of electrons at the interface. [1, 2] During this process, the rate at which A^Z gains an electron from the electrode matches the rate at which B^{Z-1} loses an electron to the electrode at the point of equilibrium. This can be explained referring to the energy levels of A^Z and B^{Z-1} and the energy of the electrons in the electrode.

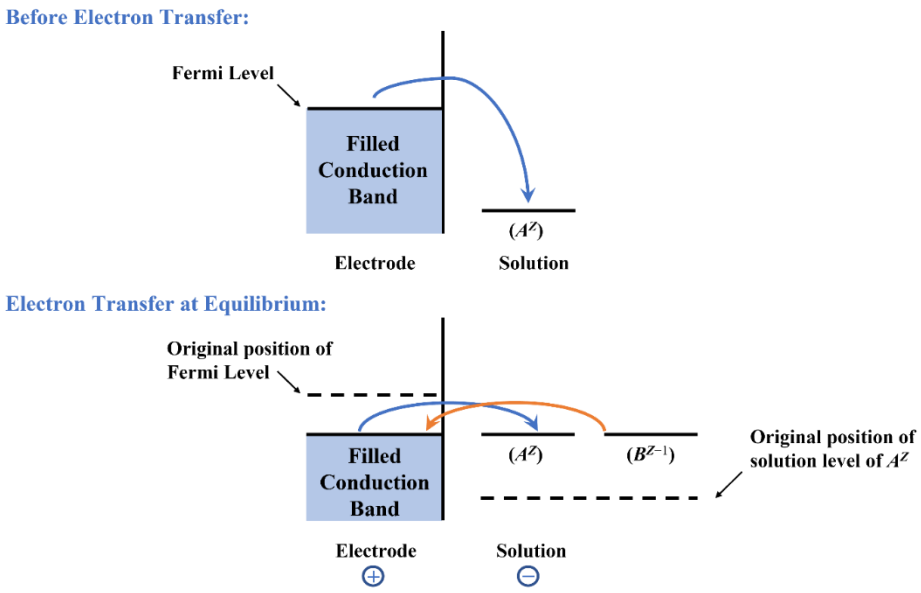

Figure.1.1 Schematic diagram of the energy levels change between the redox species in solution and the metallic electrode.

In the electronic structure of a metal, the Fermi level [3] is defined as an energy maximum of the conduction band continuously filled by delocalised electrons as shown in Figure.1.1. In contrast, the energy levels of A^Z and B^{Z-1} in the solution phase are discrete. From a thermodynamic perspective, we first analyse the situation 'before electron transfer', and consider the case in which the Fermi level of the electrode is higher than the lowest unoccupied molecular orbital of the species, A^Z, in the solution phase (Figure.1.1 (top)). To achieve an energetically favoured state, the electrons leave the Fermi level of the electrode and occupy the vacant orbital of A^Z, resulting in the formation of B^{Z-1}. As the electron transfer progresses, the development of positive charge at the electrode leads to a lower Fermi level of the electrode. At the same time, negative charge develops in the solution phase increasing the energy of the levels of the solution species. When the energy levels in the electrode and the solution match, the electron transfer takes place in both directions. This is illustrated in Figure.1.1 (lower), where B^{Z-1} is oxidised back to the original species A^Z. When the reaction rates of both directions become equal, a dynamic equilibrium is achieved, resulting in no net change in either the solution phase components or the electron energy level of the electrode. When equilibrium

is reached, there is charge separation at the interface between the electrode and the solution. This is the origin of the electrode potential at the electrode/solution interface. [1, 2]

The electrochemical equilibrium, as expressed in Eqn. (1.1), represents a balance between chemical and electrical energies of all entities involved, whereas the latter is not accounted for in normal chemical equilibria in which species are uncharged and/or in the same phase. This balance is described by two electrical potentials, ϕ_s (solution) and ϕ_m (electrode). To incorporate both chemical energies and electrical energies of a species (*j*), the electrochemical potential ($\bar{\mu}_j$) is introduced [2]:

$$\bar{\mu}_j = \mu_j + Z_j F \phi \tag{1.2}$$

where μ_j is the chemical potential (J mol^{-1}) of molecule *j*, Z_j is the charge of species *j*, F is the Faraday Constant (96485 C mol^{-1}), ϕ is the potential (V) of the solution phase (ϕ_s) or electrode phase (ϕ_m) in which species *j* is found. Notably, the second term, $Z_j F \phi$, represents the the electrical energy of species *j* with the same units as the chemical potential (Gibbs energy per mole). To study the electrochemical equilibrium as expressed in Eqn. (1.1) under conditions of constant temperature and pressure, the electrochemical potential can be expressed as:

$$\bar{\mu}_{A^z} + \bar{\mu}_{e^-} = \bar{\mu}_{B^{z-1}} \tag{1.3}$$

By substituting Eqn. (1.2) into Eqn. (1.3):

$$(\mu_{A^z} + zF\phi_S) + (\mu_{e^-} - F\phi_M) = \left(\mu_{B^{z-1}} + (z-1)F\phi_S\right) \tag{1.4}$$

Rearranging Eqn. (1.4) gives

$$F(\phi_S - \phi_M) = \mu_{B^{z-1}} - \mu_{A^z} - \mu_{e^-} \tag{1.5}$$

Note that:

$$\mu_j = \mu_j^0 + RT ln \frac{[j]}{[\ ]^0} \tag{1.6}$$

where μ_j^0 is the standard chemical potential, R is the universal gas constant (8.314 J K^{-1} mol^{-1}), T is the absolute temperature (K), $[j]$ is the concentration of species j (mol dm^{-3}) in solution and $[\ ]^0$ is the standard concentration (1 mol dm^{-3}), the latter assuming ideality. It follows that

$$\mu_{A^Z} = \mu^0_{A^Z} + RTln\frac{[A^Z]}{[\ ]^0} \tag{1.7}$$

$$\mu_{B^{Z-1}} = \mu^0_{B^{Z-1}} + RTln\frac{[B^{Z-1}]}{[\ ]^0} \tag{1.8}$$

Expanding the chemical potential terms in Eqn. (1.5) and rearranging gives:

$$\phi_M - \phi_S = \frac{\Delta\mu^0}{F} + \frac{RT}{F}\ln\left(\frac{[A^Z]}{[B^{Z-1}]}\right) \tag{1.9}$$

where

$$\Delta\mu^0 = \mu^0_{A^Z} + \mu_{e^-} - \mu^0_{B^{Z-1}} \tag{1.10}$$

Eqn. (1.9) is the Nernst equation [2, 4] which quantitatively shows the position of the electrochemical equilibrium of the A^Z/B^{Z-1} redox couple at a single electrode-solution interface, which depends on the concentrations of the two species at the equilibrium. Referring to Eqn. (1.6) with the standard concentration ($[\ ]^0$ = 1 mol dm^{-3}) being used, a standard pressure (P^0 = ~ 10^5 N m^{-2}) is applied for the gases if reactions involve. Meanwhile, the chemical potentials for pure solid or liquid approximate to their standard chemical potential so that no term of their concentration or pressure is involved.

As the Nernst equation, Eqn. (1.9), only applies to the ideal solutions, the activity (a_j) of species *j* is introduced for non-ideal solutions:

$$a_j = \gamma_j C_j \tag{1.11}$$

where the activity coefficient, γ_j, of species *j* considers the extent of the ion-ion and ion-solvent interactions in non-ideal solutions.

Accordingly, Eqn. (1.9) becomes:

$$\phi_M - \phi_S = \frac{\Delta\mu^0}{F} + \frac{RT}{F}\ln\left(\frac{\gamma_{A^Z}[A^Z]}{\gamma_{B^{Z-1}}[B^{Z-1}]}\right) \tag{1.12}$$

It is impossible to directly obtain (measure) an absolute value of ($\phi_M - \phi_S$) of a single electrode/solution interface in experiments. Alternatively, a voltmeter can be used to measure changes in the potential drop ($\phi_M - \phi_S$) by creating a second electrode/solution interface. Thus, if a second electrode, so called reference electrode [2], is introduced into the solution with a fixed

known potential, it is feasible to measure $(\phi_M - \phi_S)$ relative to the reference electrode as follows:

$$\boldsymbol{E = (\phi_M - \phi_S)_{working} - (\phi_M - \phi_S)_{reference}} \quad (1.13)$$

where E is the measured potential deference between the two electrodes.

In this case, the Nernst Equation becomes

$$\boldsymbol{E = E^0 + \frac{RT}{F} \ln \left(\frac{\gamma_{A^Z}[A^Z]}{\gamma_{B^{Z-1}}[B^{Z-1}]}\right)} \quad (1.14)$$

where E^0 is the standard electrode potential of the redox couple of A^Z and B^{Z-1}. Note that both electrode potentials (E) and E^0 are conventionally measured against the standard hydrogen electrode (SHE) as the reference electrode:

$$\boldsymbol{H^+(aq) + e^-(metal) \rightleftarrows \frac{1}{2} H_2(g)} \quad (1.15)$$

As the primary reference electrode, SHE is "standard" when the pressure of hydrogen gas is 1.101325×10^5 Nm^{-2}, and the proton concentration ($[H^+]$) is 1.18 mol dm^{-3} so that the protons behave as if they were in a 1 M solution at 298 K. [2] The International Union of Pure and Applied Chemistry (IUPAC) formally requires that potentials should be reported relative to this specific reference electrode. [5] However, the standard condition is hard to be maintained and the corresponding set-up is often impractical. Thus, other reference electrodes, e.g. a saturated calomel electrode (SCE) or a mercury-mercurous sulphate electrode (MSE), are commonly used in experiments with their fixed known potential relative to the SHE used for measuring the potential of the redox couples of interest. Then, by introducing the formal potential E_f^0 in terms of the standard potential and activity coefficient,

$$\boldsymbol{E_f^0 = E^0 + \frac{RT}{F} ln \left(\frac{\gamma_{A^z}}{\gamma_{B^{z-1}}}\right)} \quad (1.16)$$

It follows that:

$$\boldsymbol{E = E_f^0 + \frac{RT}{F} \ln \left(\frac{[A^Z]}{[B^{Z-1}]}\right)} \quad (1.17)$$

Formal potentials, E_f^0, provide the convenience of avoiding dealing with activities of redox

species during experiments.

For pH sensitive redox couples measured under standard conditions, unit activity of protons corresponds to a pH of 0. [2, 6] For a one-electron transfer reaction with m protons of the following stoichiometry,

$$A^{Z}_{(aq)} + \mathbf{m}H^{+} + e^{-}_{metal} \rightleftarrows B^{Z-1}_{(aq)} \tag{1.18}$$

the Nernst equation (1.14) becomes

$$E = E^{0} + \frac{RT}{F}\ln\left(\frac{\gamma_{A^{Z}}[A^{Z}] \times (\gamma_{H^{+}})^{m}[H^{+}]^{m}}{\gamma_{B^{Z-1}}[B^{Z-1}]}\right) \tag{1.19}$$

By introducing the formal potential (Eqn. (1.16)),

$$E = E^{0}_{f} + \frac{RT}{F}\ln\left(\frac{[A^{Z}]}{[B^{Z-1}]}\right) + m\frac{RT}{F}\ln(\gamma_{H^{+}})\,[H^{+}] \tag{1.20}$$

$$E = E^{0}_{f} + \frac{RT}{F}\ln\left(\frac{[A^{Z}]}{[B^{Z-1}]}\right) - 2.303m\frac{RT}{F}\mathrm{pH} \tag{1.21}$$

as

$$\mathrm{pH} = -\log_{10}(\gamma_{H^{+}}[H^{+}]) \tag{1.22}$$

$$\log_{10}N = \frac{\ln N}{\ln 10} = \frac{\ln N}{2.303} \tag{1.23}$$

and pH is defined by IUPAC in terms of the single ion activity of H^{+}. [7] If the pH of solution changes from '0' to '*x*' at 298 K, the formal potential will change by *x* times 0.059m V per pH unit (the so called *effective* formal potential). This pH-dependent Nernstian equation (Eqn. (1.21)) is applied in Chapter 3 and 4 in this thesis.

The Nernst equation (Eqn. (1.17) and (1.21)) demonstrate the relationship between potential and concentrations of the redox species. However, it is worthy to point out that it is limited to a dynamic equilibrium requiring fast electrode kinetics, which is not applicable for every electrochemical reaction. Thus, the kinetics of electrode processes will be considered and interpreted in the next section.

1.2 Electrode Kinetics

In the previous section, we introduced the concept of electrochemical equilibrium and the Nernst equation. Thermodynamics only provides insight of the equilibrium state but does not provide information regarding the crucial mechanisms involved in both approaching and maintaining equilibrium. Conversely, kinetics offers a quantitative understanding of the evolution of chemical changes, specifically the rate of the chemical reactions and the rate of electron transfers. Hence, in this section, we present a theoretical framework that allows for the interpretation of electrode kinetics.

Consider a simple electron-transfer reaction in aqueous solution

$$\boldsymbol{A^{Z}(aq) + e^{-}(m) \underset{k_a}{\overset{k_c}{\rightleftharpoons}} B^{Z-1}(aq)} \qquad (1.24)$$

happening at an electrode of area, A_e cm^2, where the heterogeneous rate constants k_c and k_a indicate the reduction ('cathodic') reaction of A^Z to B^{Z-1} and oxidation ('anodic') reaction of B^{Z-1} to A^Z respectively. The electron transfer process between the electrode and the reactant A^Z at the electrode-solution interface requires quantum mechanical tunnelling. This tunnelling phenomenon requires A^Z to be located within a distance of approximately 10 to 20 Å from the electrode, as within this proximity, the electron wavefunctions of A^Z and the electrode can overlap [8]. At a larger separation in distance, the rate of tunnelling is negligible. Therefore, the local concentration of the redox species in close proximity to the electrode surface is of interest rather than the concentration in the remote bulk solution. The generated electrical current (I, Ampere) is:

$$\boldsymbol{I = nFA_eJ} \qquad (1.25)$$

where n is the electron transfer number (being 1 for reaction (1.24)), F is the Faraday constant (96485 C mol^{-1}), A_e is the electrode area (cm^2) and J is the heterogeneous reaction flux at the electrode-solution interface (mol cm^{-2} s^{-1}):

$$\boldsymbol{J = k_c[A^Z]_0 - k_a[B^{Z-1}]_0} \quad (1.26)$$

where $[A^Z]_0$ and $[B^{Z-1}]_0$ indicate the concentrations of A^Z and B^{Z-1} at the electrode respectively, while k_c and k_a are the electrochemical rate constants with unit of cm s^{-1}.

Next, we introduce the Arrhenius Equation (Eqn. (1.27)), showing the exponential relationship between the rate constant of the chemical reactions and the reciprocal of the temperature:

$$\boldsymbol{k = A \times \exp\left(\frac{-\Delta G^{\dagger}}{RT}\right)} \quad (1.27)$$

where $\Delta G^{\dagger}$ is the standard Gibbs energy of activation. The exponential term represents the probability of surmounting the barrier between reactant and product, namely reaching the transition sate. A is the frequency factor for the reaction, R is the universal gas constant (8.314 J mol^{-1} K^{-1}) and T is the absolute temperature (K). [1, 9] The electrochemical rate constants, k_c or k_a, can be expressed as shown by Eqn. (1.28) and Eqn. (1.29):

$$\boldsymbol{k_c = A_c \exp\left(\frac{-\Delta G_c^{\dagger}}{RT}\right)} \quad (1.28)$$

$$\boldsymbol{k_a = A_a \exp\left(\frac{-\Delta G_a^{\dagger}}{RT}\right)} \quad (1.29)$$

where A_c and A_a relate to reduction and oxidation respectively; $\Delta G_c^{\dagger}$ and $\Delta G_a^{\dagger}$ are corresponding standard Gibbs energy difference (J mol^{-1}) between the transition state and either the reactants ($A^Z + e^-$) or products (B^{Z-1}) as follows:

$$\boldsymbol{\Delta G_c^{\dagger} = G_{\dagger}^0 - G_{reactants}^0} \quad (1.30)$$

$$\boldsymbol{\Delta G_a^{\dagger} = G_{\dagger}^0 - G_{products}^0} \quad (1.31)$$

where $G_{\dagger}^0$, $G_{reactants}^0$ and $G_{products}^0$ represents the standard molar Gibbs energy of the transition states, reactants and products. The energy profiles of the reaction (Eqn. (1.24)) are demonstrated in Figure.1.2.

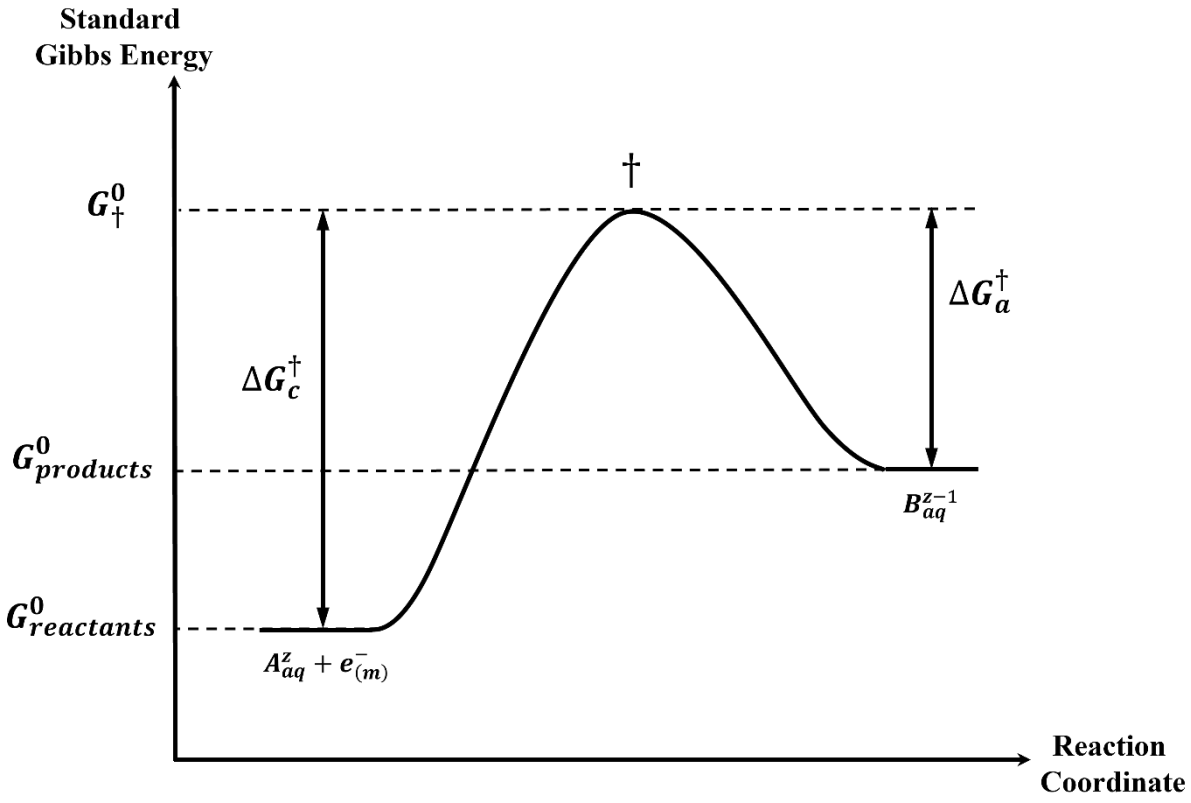

Figure.1.2 Standard Gibbs Energy profiles of an one-electron transfer reaction.

The Gibbs energies of activation can be expressed as:

$$\Delta G_c^\dagger = \Delta G_{0,c}^\dagger + \alpha F(E - E_f^0) \tag{1.32}$$

$$\Delta G_a^\dagger = \Delta G_{0,a}^\dagger - \beta F(E - E_f^0) \tag{1.33}$$

where α and β are the cathodic and anodic transfer coefficients, respectively, E is the applied potential and E_f^0 is the formal potential as introduced in Eqn. (1.16). For a one-electron transfer reaction, the coefficients vary from 0 to 1 with the following relationship:

$$\alpha + \beta = 1 \tag{1.34}$$

If α is near zero, the transition state will be reactant-like. Otherwise, the transition state will be product-like if α is close to unity. Notably when $\alpha \sim \beta \sim 0.5$, the transition state positions at the midpoint between reactants and products.

By substituting Eqn. (1.32) and (1.33) into Eqn. (1.28) and (1.29), the electrochemical rate constants (k_c and k_a) are expressed as:

$$\boldsymbol{k_c = A_c \exp\left(\frac{-\Delta G^{\dagger}_{0,c} - \alpha F(E - E^0_f)}{RT}\right)} \quad (1.35)$$

$$\boldsymbol{k_a = A_a \exp\left(\frac{-\Delta G^{\dagger}_{0,a} + \beta F(E - E^0_f)}{RT}\right)} \quad (1.36)$$

For a dynamic equilibrium, at which the concentrations of A^Z and B^{Z-1} at interface are equal, E equals to the formal potential and no net current flows:

$$\boldsymbol{J = k_c[A^z]_0 - k_a[B^{z-1}]_0 = 0} \quad (1.37)$$

Therefore, $k^0 = k^0_c = k^0_a = A_c \exp\left(\frac{-\Delta G^{\dagger}_{0,c}}{RT}\right) = A_a \exp\left(\frac{-\Delta G^{\dagger}_{0,a}}{RT}\right)$, while k^0 is the standard electrochemical rate constant with a unit of cm s^{-1} for a first order heterogeneous reaction. Following this, the general form of rate constants for all potentials can be present in terms of k^0:

$$\boldsymbol{k_c = k^0 exp\left[\frac{-\alpha F\left(E - E^0_f\right)}{RT}\right]} \quad (1.38)$$

$$\boldsymbol{k_a = k^0 exp\left[\frac{\beta F\left(E - E^0_f\right)}{RT}\right]} \quad (1.39)$$

Notably, assuming $\alpha \sim \beta \sim 0.5$, when the potential in the term of $\left(E - E^0_f\right)$ is changed by 1 Volt, the rate constants k_c and k_a are changed by factor of ca. 10^9. This evidences the significant sensitivity of the electrochemical rate constant, and hence the electrode kinetics, on the electrode potential.

Substituting Eqn. (1.38) and (1.39) into (1.26), then (1.25) gives:

$$\boldsymbol{I = FAk^0\left([A^z]_0 exp\left[\frac{-\alpha F\left(E - E^0_f\right)}{RT}\right] - [B^{z-1}]_0 exp\left[\frac{\beta F\left(E - E^0_f\right)}{RT}\right]\right)} \quad (1.40)$$

This important current-potential relation is known as the Butler-Volmer equation. [10-12] When $E \ll E^0_f$, the reduction process is significantly faster than the oxidation. Therefore, the oxidation term in Eqn. (1.40) is negligible,

$$\boldsymbol{I_{red} = FAk^0[A^z]_0 exp\,[\frac{-\alpha F\left(E - E_f^0\right)}{RT}]} \quad (1.41)$$

Similarly, when the oxidation process is much more dominant ($E \gg E_f^0$),

$$\boldsymbol{I_{ox} = FAk^0[B^{z-1}]_0 exp\,[\frac{\beta F\left(E - E_f^0\right)}{RT}]} \quad (1.42)$$

where I_{red} and I_{ox} are the reduction and oxidation currents respectively. Taking natural logarithms of both sides of Eqn. (1.41) and (1.42) with rearrangements, they become:

$$\boldsymbol{ln|I_{red}| = \frac{\alpha F}{RT} \times (-E) + c_1} \quad (1.43)$$

$$\boldsymbol{ln|I_{ox}| = \frac{\beta F}{RT} \times (+E) + c_2} \quad (1.44)$$

in which c_1 and c_2 are different constants. Plots of $ln|I_{red}|$ versus $(-E)$ or $ln|I_{ox}|$ versus $(+E)$ are called Tafel plots [13-15], where the slope of the calibration line can be converted to obtain the transfer coefficient α or β as shown in Fig.1.3. Note that to conduct Tafel analysis, it requires the concentrations of A^Z and B^{Z-1} at electrode surface being constant, which is not the case in reality due to the reactant depletion effects. Therefore, the mass transport will be discussed in the next section.

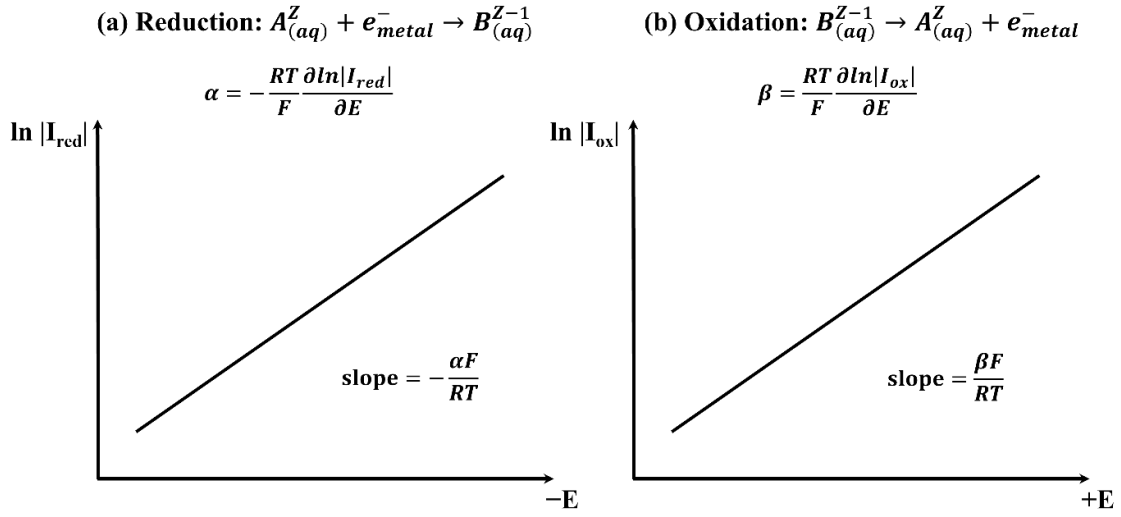

Figure.1.3 Tafel plots.

1.3 Mass Transport

In the previous section, we discussed the kinetics of electrode reactions at the electrode-solution interface, focusing only on the electron transfer rate of species at the electrode surface with an assumption of constant concentrations of reactants. However, it is important to acknowledge that in practical scenarios, the dynamics of electrochemical reactions involve the movement of reactants towards the electrode and products away from it, arising from the consumption of reactants and the formation of products. Hence, the comprehensive understanding of reaction kinetics encompasses not only the electron transfer rate but also the rate of mass transport. Mass transport occurs through various mechanisms notably diffusion, convection, and migration. The Nernst-Planck equation [16] shows the three types of mass transport along the x-axis (one-dimensional transport):

$$\boldsymbol{J_j(x)} \;=\; -\boldsymbol{D_j}\frac{\boldsymbol{\partial C_j(x)}}{\boldsymbol{\partial x}}\frac{\boldsymbol{\partial \phi(x)}}{\boldsymbol{\partial x}} + \boldsymbol{C_j v(x)} - \frac{\boldsymbol{Z_j F}}{\boldsymbol{RT}}\boldsymbol{D_j C_j} \qquad (1.45)$$

where $J(x)$ is the flux of species j (mol s^{-1} cm^{-2}) at distance x from the electrode surface and the three terms on the right side of the equation are diffusional flux, convection flux and migratory flux respectively. D_j is the diffusion coefficient (cm^2 s^{-1}), $\frac{\partial C(x)}{\partial x}$ and $\frac{\partial \phi(x)}{\partial x}$ are the concentration and potential gradients at distance x respectively, Z_j and C_j are the ionic charge (dimensionless) and concentration (mol cm^{-3}) of species j, respectively, and $v(x)$ is the local fluid velocity (cm s^{-1}).

In this section, we will investigate these three processes and assess their influence on the transport of electroactive species to an electrode surface.

1.3.1 Diffusion

Diffusion describes the spontaneous movement of species from high to low concentration and leading to the higher overall entropy. It is the most common phenomenon among the three modes of mass transport. During electrochemical studies, by applying an appropriate potential

to the electrode, the consumption of the reactant at the electrode surface (either through reduction or oxidation) leads to the depletion of the reactant's concentration. This establishes a concentration gradient between the electrode and the bulk solution, forming a distinct region known as the diffusion layer, as depicted in Figure.1.4. The so-called Nernst diffusion layer thickness (d) corresponds to the distance where the concentration extrapolated from the gradient near the electrode reaches the bulk value. The diffusional flux under the concentration gradient is quantified by Fick's 1st law [17] in one dimension, x:

$$\boldsymbol{J_{D,j} = -D_j \frac{\partial C_j(x)}{\partial x}} \qquad (1.46)$$

where $J_{D,j}$ is the diffusional flux (mol cm^{-2} s^{-1}) describing the number of moles of species passing through a unit area in a unit time. Note that diffusion coefficient (D_j) of the species (cm^2 s^{-1}) has a typical magnitude between 10^{-6} and 10^{-5} cm^2 s^{-1} in aqueous solution at 298 K and the negative sign represents the direction of the species movement from higher to lower concentration.

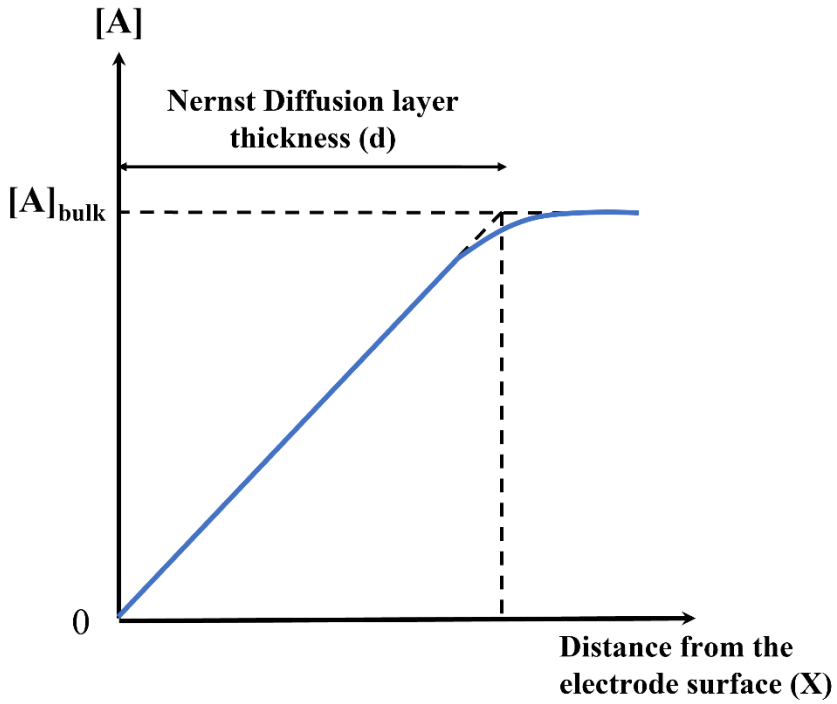

Figure.1.4 Definition of the Nernst diffusion layer.

Applying conservation of mass to Fick's 1st law gives Fick's 2nd law [18] which considers the variation of the concentration of the species with time, t, namely the rate of the concentration change, at point x:

$$\frac{\partial C(x)}{\partial t} = D_j \frac{\partial^2 C(x)}{\partial x^2} \tag{1.47}$$

Insight into the nature of the diffusion coefficient is given by Figure.1.5 that shows the movement of molecules in a 'box' with a width of $2\delta x$, in which at point x it is divided into two parts with an equal width of δx and a cross-sectional area of A. The molecules have equal probabilities for moving in either direction with a concentration of C_1 in the left part and C_2 in the right part. Therefore, assuming the molecules can travel a distance of δx within the average time δt, the number (moles) of molecules moving from left to right is $\frac{1}{2} C_1 A \delta x$, while the number from right to left is $\frac{1}{2} C_2 A \delta x$.

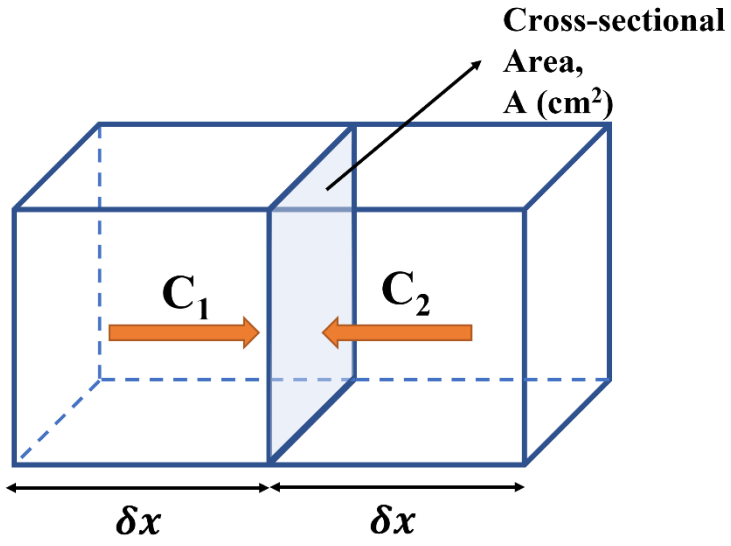

Figure.1.5 The molecular basis of Fick's 1st Law in one dimension.

Thus, the net rate of transfer through the cross-section positioned at *x* can be written as:

$$Rate_{net} = \frac{(C_1 - C_2) A \delta x}{2 \delta t} \tag{1.48}$$

As the diffusional flux ($J_{D,j}$) is expressed as:

$$J_{D,j} = \frac{(C_1 - C_2)\delta x}{2\delta t} \tag{1.49}$$

The concentration gradient $\frac{\partial C(x)}{\partial x}$ can be approximated to $-\frac{(C_1-C_2)}{\delta x}$, so that

$$J_{D,j} = -\frac{(\delta x)^2}{2\delta t}\frac{\partial C(x)}{\partial x} \tag{1.50}$$

By comparing Eqn. (1.50) to Fick's 1st law (Eqn. (1.46)), the diffusion coefficient (D_j) can be expressed as:

$$D_j = \frac{(\delta x)^2}{2\delta t} \tag{1.51}$$

Hence, the diffusion coefficient of a molecule reflects its mean square distance diffused in solution in a certain time, which can be converted to the famous Einstein-Smoluchowski equation [19-21]:

$$\sqrt{< x >^2} = \sqrt{2D_j t} \tag{1.52}$$

where $\sqrt{< x >^2}$ is the root mean square displacement in time, t. This is widely-used to estimate the thickness of the diffusion layer, *d* (cm). Furthermore, Eqn. (1.52) can be extended from one dimension to three dimensions as:

$$\sqrt{< x >^2 + < y >^2 + < z >^2} = \sqrt{6D_j t} \tag{1.53}$$

1.3.2 Convection

Convection is the movement of species resulting from a mechanical force in the solution, and has two types: natural convection and forced convection. [22, 23] Natural convection emerges due to density gradients caused by concentration or thermal gradients. In electrochemical systems, this can either be a result of the reactant consumption/product formation or imperfect temperature regulation of the electrolyte, which leads to the imprecision of experiments. For forced convection, this arises when an intentional motion is introduced, such as mechanical

stirring, pumping, electrode rotation, gas bubbling, and so on. The controlled operation, such as using rotating disks [24], is to facilitate quantitative studies with effective changes of the rates of mass transport. The flux due to convection ($J_{c,j}(x)$) is given by:

$$\boldsymbol{J_{c,j}(x) = C_j v(x)} \tag{1.54}$$

1.3.3 Migration

Migration is the movement of charged particles in the presence of a local electric field. For a charged species in the bulk region, the migratory flux, $J_{m,j}(x)$ **,** is:

$$\boldsymbol{J_{m,j}(x) = -\frac{Z_j F}{RT} D_j C_j \frac{\partial \phi(x)}{\partial x}} \tag{1.55}$$

During electrochemical analysis, a supporting electrolyte (typically non-electroactive at the potential of interest) at a higher concentration level than that of the electroactive substances under investigation is usually added to eliminate the effects of migration. To be more specific, most of the current is carried by the charged ions from the supporting electrolyte due to the much higher concentration instead of the minor species of interest. In addition, the use of a supporting electrolyte provides other benefits. One is that the differences of potential are be confined in a narrow region near the electrode. As emphasised in Section 1.2, the double layer must be constrained within 10-20 Å to ensure electron transfer by quantum mechanical tunnelling. Additionally, there is ohmic drop between the reference electrode and working electrode when current is flowing in an electrochemical cell, which can cause inaccuracy in potential measurements at the working electrode. This is minimised via the use of supporting electrolyte.

Diffusional transport is the main focus in this thesis, while the effects of convection and migration have been minimised in all the reported experiments.

1.4 Faradaic and non-Faradaic Processes

There are two types of current passing through a working electrode during an electrochemical experiment, related to Faradaic and non-Faradaic processes. [25]

1.4.1 Faradaic Processes

By applying a potential, the oxidation or reduction reaction of the electroactive species results in electron transfer at the electrode surface. This is described as Faradaic, which follows Faraday's law describing the amount of chemical reaction caused by the flow of current is proportional to the amount of electric charge passed [26, 27]:

$$\boldsymbol{Q = nFN} \qquad (1.56)$$

where Q is the total electric charge (C) transferred to or from the electrode, n is the number of electrons transferred in the electrode process ($A + ne^- \rightarrow B$), F is the Faraday constant (96485 C mol^{-1}) and N is the amount of formed product or consumed reactant (mol) of the species.

1.4.2 Non-Faradaic Processes

In electrochemical processes, both Faradaic and non-Faradaic processes coexist. Faradaic processes involve the transfer of electrons at the electrode/solution interface, while non-Faradaic processes involve the attraction or repulsion of ions or other species to or from the electrode, resulting in current flow without electron transfer across the electrode interface. Though our focus is primarily on investigating Faradaic processes, it is necessary to consider the influence of non-Faradaic processes to accurately analyse and separate the effects of interest.

The electrical double layer is the origin of non-Faradaic processes, a model of which is depicted in Figure.1.6. When the potential applied at the electrode surface is, for example, more positive than that of the solution, there will be more anions than cations adjacent to the positively charged electrode because of the electrostatic force. The converse applies to negative potentials. [28] The closest layer to the electrode is known as the compact or Stern layer,

consisting of solvent molecules and molecules or ions formed by desolvation due to the applied electrode potentials. The Inner Helmholtz Plane (IHP) corresponds to the electrical centres of the specifically adsorbed ions, while specific adsorption emphasises a significant chemical interaction between the ion and the surface. The Outer Helmholtz Plane (OHP) represents the region where solvated ions, not specifically adsorbed, interact with the charged electrode primarily through long-range electrostatic forces. The OHP is the boundary between the compact layer and the diffuse layer, while the latter extends into the bulk solution and contains non-specifically adsorbed solvated anions and cations. The presence of these layers plays a crucial role in maintaining electrical neutrality at the electrode-solution interface. The interface can be viewed as comprised of two layers of opposite charge thus resembling an electrical capacitor.

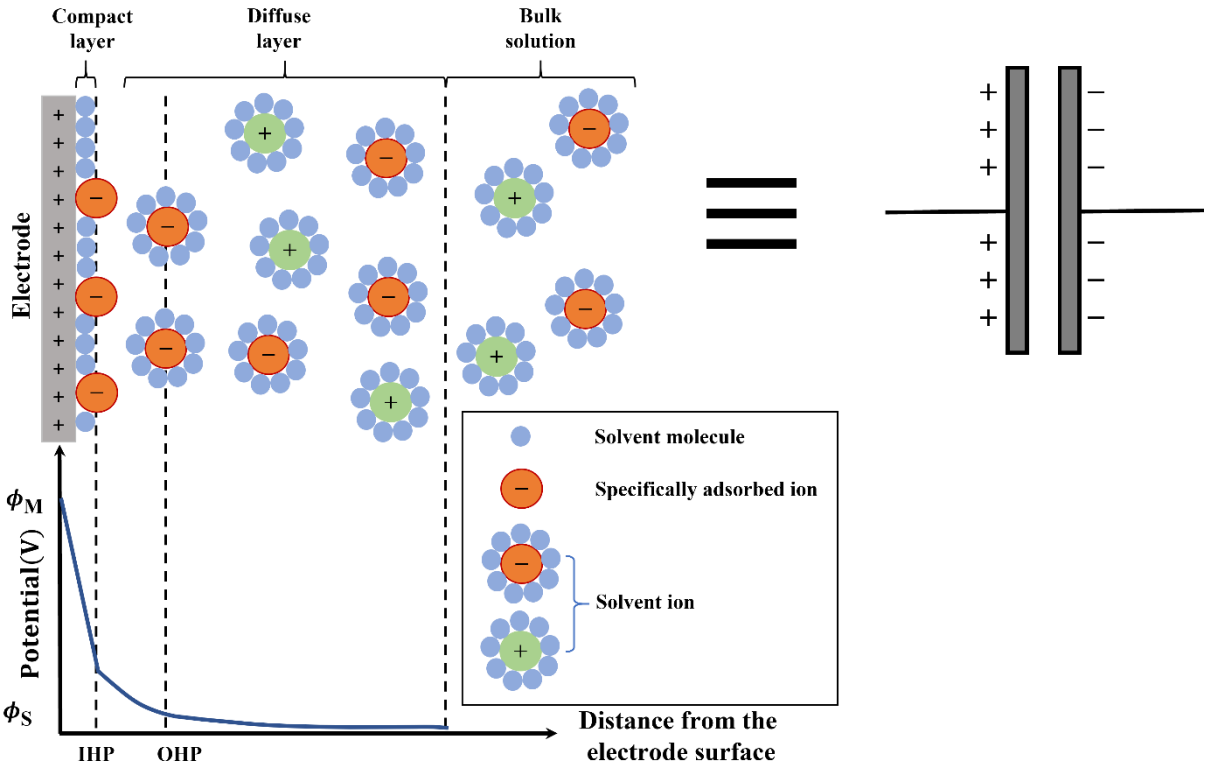

Figure.1.6 Left: schematic model of the double-layer region (top) and corresponding potential profile across the double layer (bottom); right: the analogue of a capacitor.

The thickness of the diffuse layer is described by the Debye length (χ_{DL}, Å) [29]:

$$\chi_{DL} = \frac{1}{ZF}\sqrt{\frac{\varepsilon_0 \varepsilon_r RT}{2C}} \tag{1.57}$$

where ε_0 is the permittivity of free space (8.854×10^{-12} C^2 J^{-1} m^{-1}) and ε_r is the dielectric constant. The Debye length is dependent of the concentration of supporting electrolyte, which decreases from 100 Å to 10 Å when the latter is increased from 1 mM to 0.1 M. As mentioned in previous sections, electrolytes with high ionic concentrations are usually added in most electrochemical experiments, notably voltammetry, to ensure the double layer is within the critical range (10-20 Å) for electron tunnelling. As a result, the electrostatic potential rapidly drops almost linearly as a function of distance from the electrode surface within the compact layer, then the decay is less rapid in the diffuse layer until reaching the electro-neutral bulk solution.

During electrochemical studies, current-potential curves obtained for different redox systems are significantly influenced by the electrical double layer, specifically the non-Faradaic current (often called the charging current or capacitive current, I_c). This arises due to the existence of the double-layer capacitance when the potential is applied [1]:

$$I_c = \frac{dQ}{dt} = C_d A \frac{dE}{dt} = C_d A \upsilon \tag{1.58}$$

where Q is the charge (C), t is the time (s), C_d is the capacitance of the double layer per unit area (F m^{-2}), E is the applied potential (V) across the electrode/solution interface, A is the electroactive layer area (m^2) and v is the scan rate (Vs^{-1}). In contrast to real capacitors, which have voltage-independent capacitances, the double-layer capacitance (C_d) in electrochemical systems often exhibits dependence on the applied potential. When an increasingly positive potential is applied at the electrode, the larger potential difference across the electrode/solution interface leads to a current flow resulting from the movement of ions within the solution phase and the electrode and/or the reorientation of dipole molecules of the solvent. Meanwhile,

referring to Eqn. (1.58), if there is a greater rate of potential change, namely a higher scan rate, the capacitive current shows a linear response to scan rate. In electrode reactions with low concentrations of electroactive species, the non-Faradaic current, arising from non-electron transfer processes, can be significantly greater than the Faradaic current associated with reduction or oxidation reactions. This may lead to challenges for electrochemical analysis, e.g. a non-ideal detection limit, but suitable voltammetric techniques, notably square wave voltammetry, can be used to decrease the effect.

1.5 Electrochemical Cells

Electrochemical studies are usually conducted in a typical set-up including a 'potentiostat' as the electrochemical control device and an electrochemical cell containing electrolyte. The electrochemical cell comprises a working electrode (WE), a reference electrode (RE) and a counter electrode (CE). [2] Three electrodes are immersed in the electrolyte solution and connected to the potentiostat as shown in Figure.1.7. The WE is the electrode under investigation and the reference electrode (RE) provides a predetermined and constant potential for potential difference measurements as discussed in Section 1.1. The additional counter electrode (CE) is required for the passage of the current and completing the circuit with the WE. Without the CE's presence, current passes through RE. This results in not only chemical changes within the RE, but also a potential drop ('IR_s' term in Eqn. (1.59)) between the WE and RE due to the electrical resistance (R_s) of the bulk solution. The former stops the RE from providing a constant reference potential, while the latter leads to an uncontrolled working electrode potential so that Eqn. (1.13) becomes (1.59).

$$\boldsymbol{E = (\phi_M - \phi_S)_{working} + IR_s - (\phi_M - \phi_S)_{reference}} \qquad (1.59)$$

Notably, when the WE is a microelectrode [30, 31], the current (I) passing through the circuit is so low (~ 10^{-9} A) that a two-electrode system containing a microelectrode and a RE can be used

for studies. This is because, first, the tiny current results in negligible chemical species change inside the RE so that the potential of the reference electrode stays constant. Secondly, the IR_s term in Eqn. (1.59) is also insignificant in this case. Therefore, in either a two or three-electrode system with a proper set-up, the applied potential *E* and its changes can alter the electrochemical driving force, $(\phi_M - \phi_S)_{\ working}$ directly. Quantitative electrochemical analysis based on the current-potential relationship becomes possible.

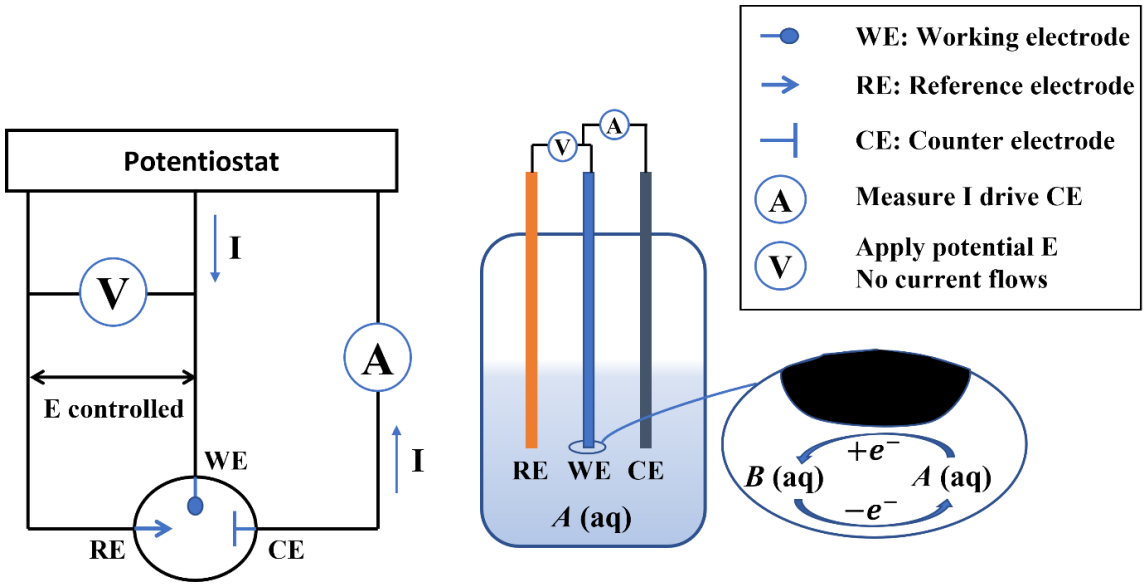

Figure.1.7 Schematic diagram of a three-electrode electrochemical cell.

1.6 Electrochemical Techniques

We next introduce four electrochemical techniques used in the later chapters: cyclic voltammetry, square wave voltammetry, and chronoamperometry.

1.6.1 Cyclic Voltammetry

Cyclic voltammetry (CV) [32] is a ubiquitously used electrochemical technique for studying the electrochemical characteristics of the analyte of interest at a chosen electrode. As shown in Figure.1.8, CV is performed with a linear sweep of the potential at a working electrode at a constant scan rate ($v = \frac{\partial E}{\partial t}$, Vs^{-1}). It usually starts from a potential (E_1) where no oxidation or

reduction of the analyte happens (no Faradaic currents) to a potential (E_2), at which point the oxidation or reduction process is fully driven. Then, the scan direction is reversed and usually returns to the initial value of the potential (E_1). Notably, the 'linear' sweep is actually generated digitally with various small potential steps ('staircase') in practice and the corresponding current is recorded continuously at each potential step [33]. The resultant voltammogram is plotted as a function of current I (y-axis) against potential E (x-axis). Linear sweep voltammetry (LSV) shares similarities with CV except that for the former only a forward potential sweep, from E_1 to E_2, is performed.

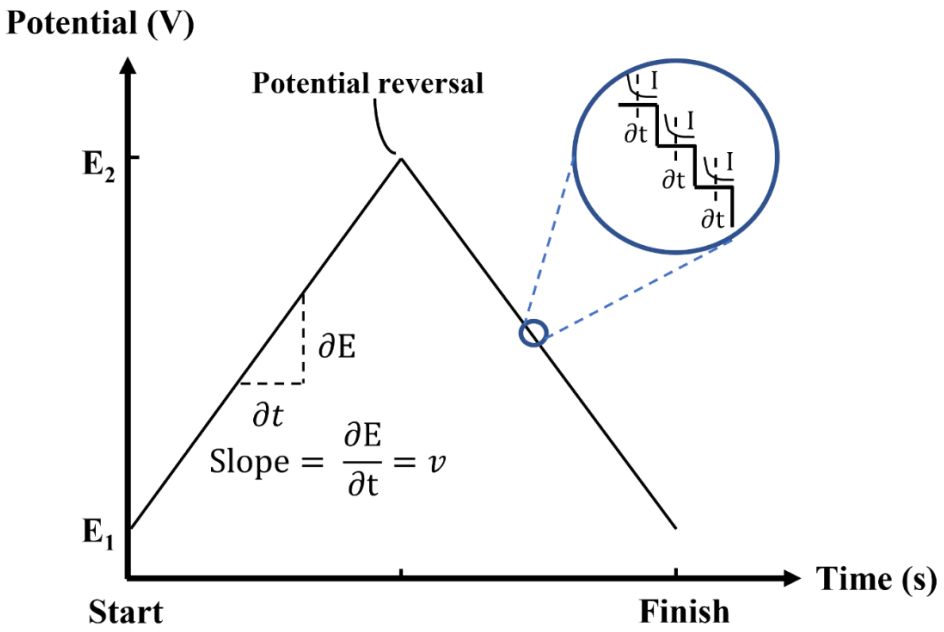

Figure.1.8 The potential-time of a cyclic voltammogram. The enlarged image shows the steps at each of which current is recorded at time t.

The voltammogram, which characterises the electrochemical response, is influenced by the rates of electron transfer and mass transport. The latter is dependent on the working electrode size, resulting in different diffusion patterns, in addition to the diffusion coefficient of the electroactive species. For the two types of working electrodes, macroelectrodes (usually with dimensions of millimetres or centimetres) and microelectrodes (dimensions on the scale of micrometres) [31], the corresponding diffusion patterns determined by the relative magnitude of

the electrode radius and diffusion layer thickness are illustrated in Figure.1.9 (a) and Figure.1.9 (b). For macroelectrodes, linear diffusion exhibits during electrolysis due to their much larger radius compared to the diffusion layer thickness ($r_e \gg d$). This results in a planar diffusion layer and a peak-shaped response in a cyclic voltammogram which will be discussed later. Conversely, microelectrodes experience convergent diffusion ('edge effects') due to their smaller radius to the diffusion layer thickness ($r_e \ll d$). This leads to an approximately hemispherical-shaped diffusion layer, enhanced mass transport rates, and a steady-state limiting current rather than a peak-shape current response being recorded. Meanwhile, due to the small dimensions of microelectrodes, the resulting tiny currents offer benefits of reduced capacitance, minimal ohmic drop (Section 1.5) and efficient mass transport, making them suitable for measuring faster electrode kinetics compared to macroelectrodes [34]. As shown in Figure.1.9 (c), microwire electrodes with one macro-dimension (length) and one micro-dimension (radius) show a combined mode, linear diffusion at the side and convergent diffusion at the end. They provide not only a larger surface area but also high mass transport rates conferred by micro-dimension. Most of the results presented in this thesis correspond to macroelectrode voltammetry.

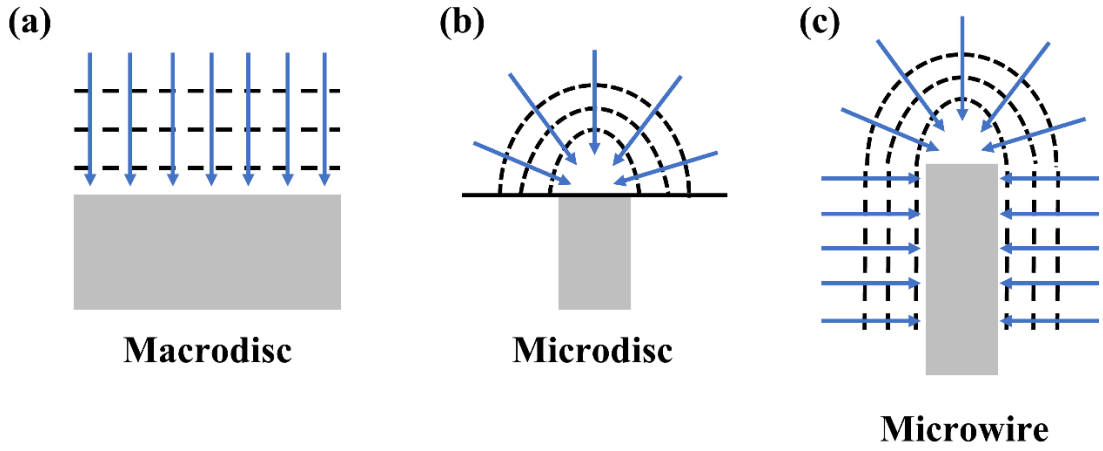

Figure.1.9 Diffusion at a macrodisc (a), microdisc (b) and microwire (c) electrodes. Arrows: diffusion of electroactive species. Dashed line : the diffusion layers.

The voltammograms obtained by macroelectrodes are divided into three types, namely reversible (green line), quasi-reversible (blue line) and irreversible (orange line) as shown in Figure.1.10. The different extent of reversibility is defined by comparing the standard electrochemical rate constant k^0 (Section 1.2) with the rate of mass transport, m_T (cm s^{-1}), where

$$\boldsymbol{m_T = \frac{D}{d}} \tag{1.60}$$

According to Eqn. (1.52), the diffusion layer thickness (d) is related to the time (*t*) required to scan the voltammetric feature which in turn can be related to the scan rate (v):

$$\boldsymbol{t \sim \frac{RT}{Fv}} \tag{1.61}$$

so that m_T can be estimated as

$$\boldsymbol{m_T \sim \sqrt{\frac{DFv}{RT}}} \tag{1.62}$$

Then, the Matsuda and Ayabe parameter, Λ, is introduced to define the limits of reversibility [35]:

$$\boldsymbol{\Lambda = \frac{k^0}{\sqrt{\frac{FDv}{RT}}}} \tag{1.63}$$

The following ranges are assigned to the three different classifications at macroelectrodes:

Reversible, $k^0 \gg m_T$

$$\boldsymbol{\Lambda \geq 15, k^0 \geq 0.3\sqrt{v}\ cm\ s^{-1}} \tag{1.64}$$

Quasi-reversible

$$\boldsymbol{15 > \Lambda > 10^{-3}, 0.3\sqrt{v} > \ k^0 > 2 \times 10^{-5}\sqrt{v}\ cm\ s^{-1}} \tag{1.65}$$

Irreversible, $k^0 \ll m_T$

$$\boldsymbol{\Lambda < 10^{-3}, k^0 \leq 2 \times 10^{-5}\sqrt{v}\ cm\ s^{-1}} \tag{1.66}$$

where *T*, *D* relate to 298 K and 1×10^{-5} cm^2 s^{-1} and α is assumed ~ 0.5.

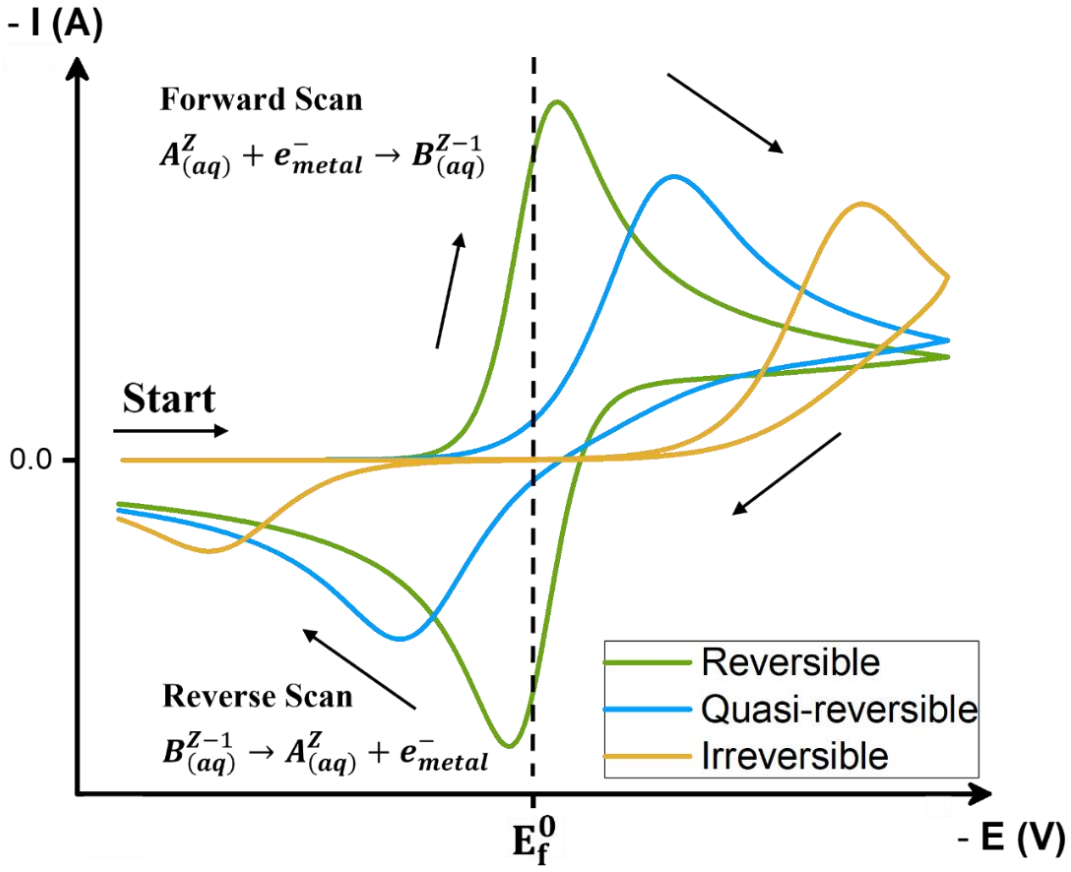

Figure.1.10 Voltammograms showing the electro-reduction of the electroactive diffusive species A^Z with different reversiblilties at macrodisc electrodes. Arrows show the starting point and scan direction. −I (A) plotted on y-axis: cathodic current above and anodic current below x-axis; −E (V) plotted on y-axis: left to right implies potential gets more negative.

Note that due to the square root dependence of the scan rate, all electrochemical processes can become electrochemically irreversible when the scan rate is fast enough in principle. Generally, the scan usually starts at a potential that is insufficient for the redox reaction to happen so no Faradaic current flows. Then, when the potential is swept cathodically, for an electrochemically reversible system (green curve in Figure.1.10), the electroactive species A^Z in the solution gets reduced with the cathodic current initiating at potentials close to the formal potential (E_f^0) of the A^Z/B^{Z-1} couple. In the case of a reversible couple the electrode kinetics are so 'fast' that the concentration of A^Z/B^{Z-1} at the electrode surface follows the Nernst Equation (Eqn. (1.14)). For the irreversible case (orange curve in Figure.1.10), as the electrode kinetics

near the formal potential are significantly slower than the rate of mass transport, the reduction peak of A^Z is only recorded when the electron transfer rate matches the diffusion rate when a high overpotential is applied according to the Butler-Volmer equation. As the potential further shifts negative, the current decreases due to inadequate diffusion of A^Z towards the electrode surface to replenish the consumed material. During the reverse scan, the accumulation of significant concentrations of B^{Z-1} near the electrode shifts the electrochemical balance to the reformation of A^Z from B^{Z-1}, during which a similar peak is recorded anodically, the peak shape again resulting from the relationship between electrode kinetics and the rate of mass transport as well as the finite amount of B^{Z-1} produced on the forward scan. Notably, the decreasing peak current from the reversible to the irreversible limits reflects the decreasing electron transfer kinetics (Eqn. (1.40)).

For more quantitative interpretations, three parameters can be used to distinguish the reversibility of a one-electron transfer reaction at macroelectrodes:

1) Peak-to-peak separation, ΔE_{pp}

Peak-to-peak separation, ΔE_{pp}, is defined as the difference between anodic and cathodic peak potentials. [2] As shown in Figure.1.10, the more irreversible the reaction is, the greater ΔE_{pp}. For a reversible system (green line in Figure.1.10), ΔE_{pp} is independent of scan rate and has a value of ca 57 mV at 298 K. In contrast, an irreversible reaction (orange line) with 'slow' electrode kinetics results in larger ΔE_{pp} dependent on scan rate. Quasi-irreversible systems (blue line) show an intermediate behaviour with the scan rate dependent ΔE_{pp}. [36]

2) Mid-point potential of the forward and back peak, E_{mid}

The mid-point potential is the average of the forward and backward potentials ($E_{mid} = \frac{E_{p,forward}+E_{p,backward}}{2}$), which can be related to the formal potential (E_f^0) in the reversible and irreversible limit.

Reversible:

$$\boldsymbol{E_{mid} = E_f^0 + \frac{RT}{2F} ln \left(\frac{D_{B^{z-1}}}{D_{A^z}}\right)} \quad (1.67)$$

Irreversible, assuming α = β = 0.5:

$$\boldsymbol{E_{mid} = E_f^0 + \frac{RT}{F} ln \left(\frac{D_{B^{z-1}}}{D_{A^z}}\right)} \quad (1.68)$$

Notably, when the diffusion coefficient of A and B are equal ($D_{A^z} = D_{B^{z-1}}$), $E_{mid} = E_f^0$.

3) Peak current, I_p

The peak current, I_p, of a simple one-electron transfer process free of homogeneous chemical complications at macroelectrodes can be described by the Randles-Sevcik equations [2, 37, 38]. For the reduction of A^Z as described above:

Reversible: $$\boldsymbol{I_p = 0.446 F A_e [A^z]_{bulk} \sqrt{\frac{F D_{A^z} v}{RT}}} \quad (1.69)$$

Irreversible: $$\boldsymbol{I_p = 0.496 \sqrt{\alpha} F A_e [A^z]_{bulk} \sqrt{\frac{F D_{A^z} v}{RT}}} \quad (1.70)$$

where A_e is the surface area of the electrode (cm^2), $[A^z]_{bulk}$ and D_{A^z} are the bulk concentration (mol cm^{-3}) and the diffusion coefficient (cm^2 s^{-1}) of species A^Z, v is the scan rate (Vs^{-1}), α is the transfer coefficient.

Discussed above is the scenario that both reactant and product are diffusive in solution phase. For surface-bound species, the voltammetric features differ. During a reversible process, both redox peaks occur at the formal potential of the redox couple with the peak tails end at zero current due to the finite adsorbed electroactive species. In the case of an irreversible process, two asymmetric peaks at either side of the formal potential are recorded. Meanwhile, the peak current of the surface-bound species is proportional to the scan rate rather than its square root as shown in Eqn. (1.69) and (1.70):

Reversible $$\boldsymbol{I_p = \frac{F^2}{4RT} v A_e \Gamma_A^0} \quad (1.71)$$

Irreversible $$\boldsymbol{I_p = \frac{\alpha F^2}{2.718RT} v A_e \Gamma_A^0} \quad (1.72)$$

where Γ_A^0 is the surface coverage of reactant at the electrode surface (mol cm^{-2}).

1.6.2 Square Wave Voltammetry

Square wave voltammetry (SWV) is a voltammetric technique that is commonly used to improve the sensitivity of voltammetry by reducing capacitive currents and so is often applied analytically. [39] The waveform of SWV is a symmetric square wave pulse modified by staircase potential ramp (Figure.1.11 (a)). The square wave is characterised by a square wave amplitude (pulse hight), ΔE_p, the staircase height (ΔE_s) and square wave frequency (*f*).

$$\boldsymbol{f = \frac{1}{t_s} = \frac{1}{2t_p}} \quad (1.73)$$

where t_s is the duration of single potential cycle and t_p is the duration of a single potential pulse ($t_p = \frac{1}{2} t_s$). The overall potential modulation is related to the scan rate (v) as follows [40]:

$$\boldsymbol{v = \frac{\Delta E_s}{2t_p} = f \Delta E_s} \quad (1.74)$$

During each square wave cycle, two current measurements (I_1 and I_2) are made at the end of both forward and backward potential pulse. As shown in Figure.1.11 (b), I_1 (blue line), I_2 (orange line) and their difference ($\Delta I = I_2 - I_1$, black line) are plotted against the staircase potential to create the square wave voltammogram. It is the subtraction of current that eliminates the non-Faradaic current, thereby increasing the sensitivity. Applications of SWV will be discussed in Chapters 3, 4 ,5, 6.

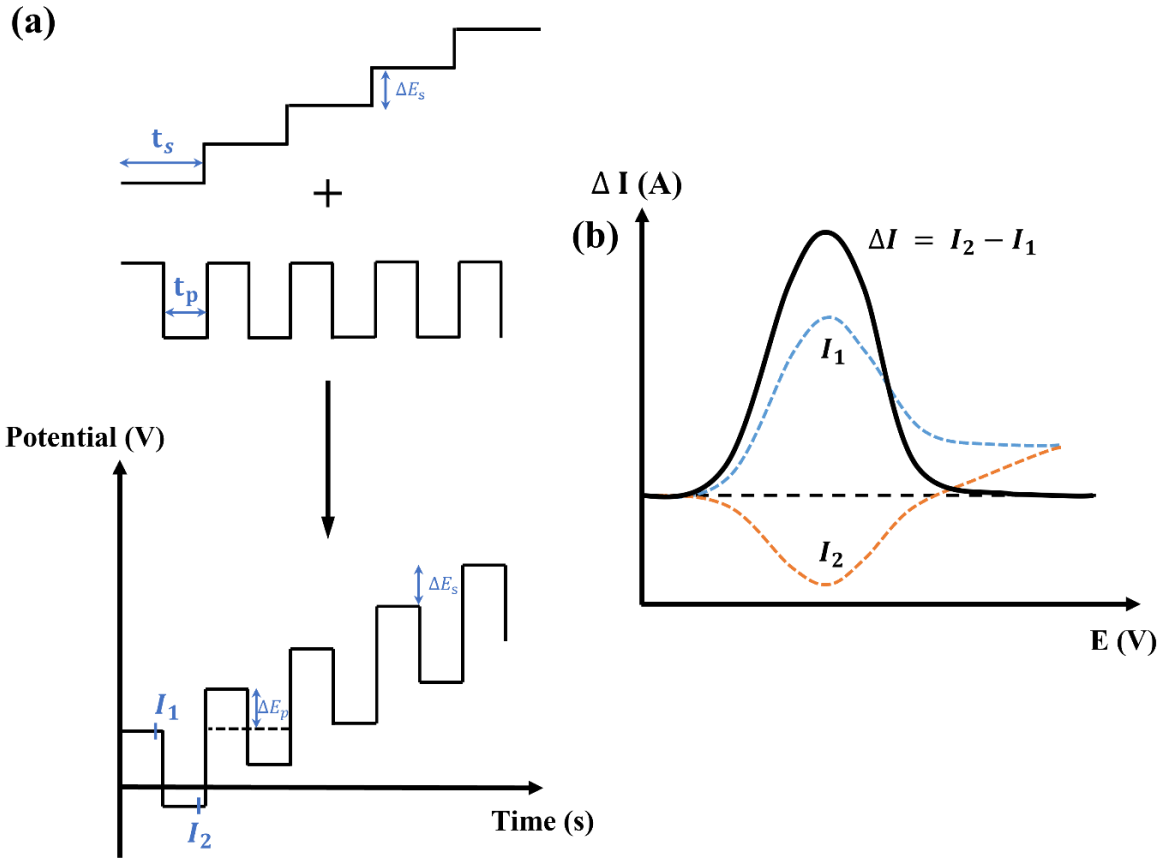

Figure.1.11 (a) The waveform of SWV; (b) voltammetric profiles obtained from a SWV scan.

1.6.3 Chronoamperometry

In chronoamperometry the potential of the working electrode is stepped from an initial potential E_1 where usually no Faradaic current flows to an over-potential E_2 at which the Faradaic process of interest is fully driven at the electrode interface. The resulting current versus time plot is shown in Figure.1.12 (a). For a macroelectrode with a linear-diffusion pattern, the Faradaic current near the electrode surface decays to zero as the reactant depletes in the vicinity of the electrode interface over time (Figure.1.12 (b)) [41]. The Cottrell equation[1] describes the relationship between current and time for the oxidation or reduction of a solution phase species:

$$\boldsymbol{I(t)} = \frac{\boldsymbol{nFA\sqrt{D}C^*}}{\boldsymbol{\sqrt{\pi t}}} \qquad (1.75)$$

where C^* is the bulk concentration of the species.

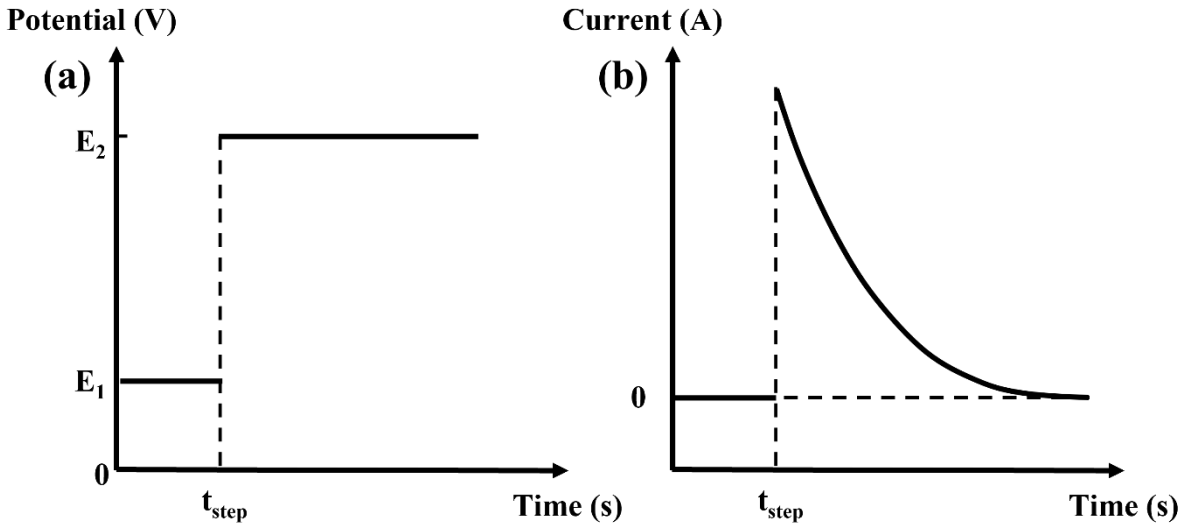

Figure.1.12 (a) The potential-time profile for a single step chronoamperometry. (b) The chroamperometic current as a function of time at a macroelectrode.

References

1. A. J. Bard, L. R. Faulkner and H. S. White, *Electrochemical Methods: Fundamentals and Applications*, John Wiley & Sons, 3rd Edition edn., 2022.
2. R. G. Compton and C. E. Banks, *Understanding Voltammetry*, World Scientific, 3rd edition, 2018.
3. H. Reiss, *The Journal of Physical Chemistry*, 1985, **89**, 3783-3791.
4. F. J. Vidal-Iglesias, J. Solla-Gullón, E. Herrero, A. Rodes and A. Aldaz, *Electrocatalysis*, 2013, **4**, 1-9.
5. A. D. McNaught and A. Wilkinson, *Compendium of Chemical Terminology*, Blackwell Science Oxford, 1997.
6. A. J. Bard, R. Parsons and J. Jordan, *Standard Potentials in Aqueous Solution*, Routledge, 2017.
7. R. P. Buck, S. Rondinini, A. Covington, F. Baucke, C. M. Brett, M. Camoes, M. Milton, T. Mussini, R. Naumann and K. Pratt, *Pure and Applied Chemistry*, 2002, **74**, 2169-2200.
8. T. Sakata and M. Azuma, *Bulletin of the Chemical Society of Japan*, 2013, **86**, 1158-1173.
9. K. J. Laidler, *Journal of Chemical Education*, 1984, **61**, 494.
10. J. Butler, *Transactions of the Faraday Society*, 1924, **19**, 734-739.
11. J. A. V. Butler, *Transactions of the Faraday Society*, 1924, **19**, 659-665.
12. J. A. V. Butler, *Transactions of the Faraday Society*, 1924, **19**, 729-733.
13. G. Burstein, *Corrosion Science*, 2005, **47**, 2858-2870.
14. D. Li, C. Lin, C. Batchelor-McAuley, L. Chen and R. G. Compton, *Journal of Electroanalytical Chemistry*, 2018, **826**, 117-124.
15. J. Tafel, *Zeitschrift für Physikalische Chemie*, 1905, **50**, 641-712.
16. E. Lee, in *Interface Science and Technology*, ed. E. Lee, Elsevier, 2019, vol. 26, pp. 3-45.
17. A. Fick, *Annalen der Physik*, 1855, **170**, 59-86.
18. A. Fick, *The London, Edinburgh, and Dublin Philosophical Magazine and Journal of Science*, 1855, **10**, 30-39.
19. M. Von Smoluchowski, *Annalen der Physik*, 1906, **326**, 756-780.
20. A. Einstein, *Annalen der Physik*, 1905, **17**, 208.
21. M. Islam, *Physica Scripta*, 2004, **70**, 120.
22. J. K. Novev and R. G. Compton, *Current Opinion in Electrochemistry*, 2018, **7**, 118-129.
23. J. Rubio-Garcia, A. Kucernak and A. Charleson, *Electrochemistry Communications*, 2018, **93**, 128-132.
24. C. Hagan and L. A. Coury, *Analytical Chemistry*, 1994, **66**, 399-405.
25. P. Biesheuvel, S. Porada and J. Dykstra, *arXiv preprint arXiv:1809.02930*, 2018.
26. M. Faraday, *Philosophical Transactions of the Royal Society of London*, 1834, 77-122.
27. F. C. Strong, *Journal of Chemical Education*, 1961, **38**, 98.
28. P. H. Rieger, *Electrochemistry*, Prentice Hall, United States, 1987.
29. E. J. Dickinson and R. G. Compton, *Journal of Electroanalytical Chemistry*, 2011, **661**, 198-212.
30. R. C. Engstrom, M. Weber, D. J. Wunder, R. Burgess and S. Winquist, *Analytical Chemistry*, 1986, **58**, 844-848.
31. R. J. Forster, *Chemical Society Reviews*, 1994, **23**, 289-297.
32. P. T. Kissinger and W. R. Heineman, *Journal of Chemical Education*, 1983, **60**, 702.

33. A. S. Barnes, I. Streeter and R. G. Compton, *Journal of Electroanalytical Chemistry*, 2008, **623**, 129-133.
34. O. Tutty, *Journal of Electroanalytical Chemistry*, 1994, **377**, 39-51.
35. H. Matsuda and Y. Ayabe, *Zeitschrift für Elektrochemie, Berichte der Bunsengesellschaft für Physikalische Chemie*, 1955, **59**, 494-503.
36. R. S. Nicholson and I. Shain, *Analytical Chemistry*, 1964, **36**, 706-723.
37. J. E. B. Randles, *Discussions of the Faraday Society*, 1947, **1**, 11-19.
38. A. Ševčík, *Collection of Czechoslovak Chemical Communications*, 1948, **13**, 349-377.
39. C. M. A. Brett and A. M. O. Brett, *Electrochemistry: Principles, Methods, and Applications*, Oxford University Press, Oxford, 1993.
40. J. G. Osteryoung and R. A. Osteryoung, *Analytical Chemistry*, 1985, **57**, 101-110.
41. W. Schwarz and I. Shain, *The Journal of Physical Chemistry*, 1965, **69**, 30-40.

Chapter 2

Experimental

This chapter describes generic experimental details notably the chemical reagents and electrochemical instrumentation used in the experiments reported in this thesis. Specific descriptions of each experiment can be found in the experimental section of each chapter (Chapters 3-7).

2.1 Chemicals and Reagents

All chemicals and reagents used in this thesis were of analytical grade and were used as received without any further purification as listed in Table 2.1. All solutions were prepared in ultra-pure water of a resistivity of 18.2 MΩ cm at 298K (Millipore, MA, USA).

Table 2.1 List of chemicals and reagents involved in this thesis

Chemical	Formula	Purity	Supplier
Sodium chloride	NaCl	99.5%	Sigma-Aldrich, UK
Potassium chloride	KCl	99.5%	Sigma-Aldrich, UK
Magnesium chloride hexahydrate	$MgCl_2 . 6H_2O$	99.0%	Sigma-Aldrich, UK
Calcium chloride dihydrate	$CaCl_2 . 2H_2O$	99.0%	Sigma-Aldrich, UK
Strontium chloride hexahydrate	$SrCl_2 . 6H_2O$	99.0%	Sigma-Aldrich, UK
Sodium Sulfate	Na_2SO_4	99.0%	Sigma-Aldrich, UK
Sodium bicarbonate	$NaHCO_3$	99.7%	Acros Organics, UK
Potassium bromide	KBr	99.0%	Sigma-Aldrich, UK
Sodium fluoride	NaF	99.0%	Sigma-Aldrich, UK / Macklin Biochemical Co., Ltd., China
Boric acid	H_3BO_3	99.5%	Sigma-Aldrich, UK

Potassium nitrate	KNO_3	≥99.0%	Sigma-Aldrich, UK
Sodium nitrate	$NaNO_4$	≥99.5%	Merck KGaA, Germany
2-Aminopyridine	$C_5H_6N_2$	99.0%	Sigma-Aldrich, UK
Tris(hydroxymethyl) Aminomethane	$C_4H_{11}NO_3$	99.0%	Alfa Aesar, USA
2-Amino-2-methyl-1,3-propanediol	$C_4H_{11}NO_2$	≥99.0%	Alfa Aesar, USA
Magnesium chloride	$MgCl_2$	98.0%	Sigma-Aldrich, UK
Calcium chloride	$CaCl_2$	97.0%	Sigma-Aldrich, UK
Hydrochloric acid	HCl	~37%	Fisher Scientific UK limited, UK
Hydrochloric acid	HCl	~37%	Guangzhou Chemical Reagent Factory, China
Potassium hydroxide	KOH	95.0%	Macklin Biochemical Co., Ltd., China
Citric acid	$C_6H_8O_6$	99.0%	Macklin Biochemical Co., Ltd., China
Sodium citrate	$Na_3C_6H_5O_7$	99.5%	Macklin Biochemical Co., Ltd., China
Monopotassium phosphate	KH_2PO_4	99.5%	Macklin Biochemical Co., Ltd., China
Dipotassium phosphate	K_2HPO_4	98.0%	Macklin Biochemical Co., Ltd., China
Sodium carbonate	Na_2CO_3	99.5%	Macklin Biochemical Co., Ltd., China

2.2 Electrochemical Instrumentation

The electrochemical measurements reported in Chapter 3 were conducted using a CHI760E Electrochemical Workstation (CH Instruments, Inc., Shanghai, China), whereas those in Chapters 4-7 employed a μAutolab II potentiostat made by Metrohm-Autolab BV (Utrecht, Netherlands). The experiments were performed using a standard three-electrode set-up (see Chapter 1) at a constant temperature of 25.0 ± 0.2 °C in a Faraday cage. The details of specific working electrodes, reference electrodes and counter electrodes are shown in Table 2.2 and will be discussed with reference to each experiment reported in the subsequent chapters.

Table 2.2 List of the electrodes used in this thesis

Type of Electrodes	Electrode	Parameters	Supplier
Working electrode	GCE	Diameter: 3.00 ± 0.01 mm	BASi, USA
	Au macrodisc	Diameter: 1.60 ± 0.01 mm	BASi, USA
	Pt macrodisc	Diameter: 1.66 ± 0.01 mm	BASi, USA
	Ag macrodisc	Diameter: 2.52 mm	Homemade (see Section 2.2.3)
	Iridium wire	Diameter: 0.10/0.125 mm	GoodFellow, UK
Reference electrode	SCE	+ 0.244 V vs. SHE	BASi, USA
	MSE in sat. K_2SO_4	+ 0.64 V vs. SHE	BASi, USA/CH Instruments, Inc., China
Counter electrode	Graphite rod	N/A	
	Platinum wire		

(GCE: glassy carbon electrode; SCE: saturated calomel electrode; MSE: mercury-mercurous sulfate electrode; SHE: standard hydrogen electrode)

2.2.1 Preparation of Macrodisc Electrodes

Before each use, the working electrodes were sequentially polished with 1.0, 0.3, and 0.05 μm alumina lapping compounds (Bucher, Germany) on soft lapping pads (Kemet Ltd., UK). The electrodes were then rinsed using ultra-pure water and dried with nitrogen (99.998%, BOC Gases plc, UK).

2.2.2 Preparation of Iridium Wires

An Ir electrode was pretreated by heating the metal by a Bunsen burner or a flame gun using gas liquefied petroleum gas (butane ≥ 95 %, Pan'an city Gas Co., Ltd., China) for 10 s to remove surface contamination and impurities.

2.2.3 Fabrication of Silver Macrodisc Electrodes

The homemade Ag macrodisc electrode was made of a silver rod fitted into a glass tube in a vacuum and glued using epoxy (H77 3OZ Kit, Epoxy Technology Inc, USA). The structure is shown in Figure.2.1.

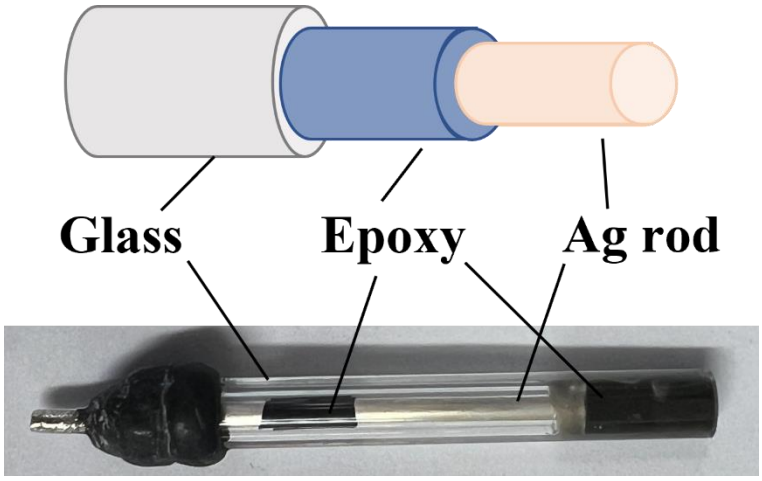

Figure.2.1 Schematic structure of the Ag macrodisc electrode.

Chapter 3

A Simplified Methodology: pH Sensing Using an In-situ Activated Ir Eelectrode under Neutral Conditions

Chapters 3 - 4 report the study of amperometric pH sensing using an iridium electrode for application under near neutral conditions, notably in freshwater (**Chapter 3**) and seawater (**Chapter 4**). In **Chapter 3**, the in-situ electrochemical fabrication of an iridium hydrous oxide film is optimised and shown to be achievable under neutral conditions rather than the acidic conditions hitherto employed. The formation of a pH sensitive Ir(III/IV) hydrous oxide film is confirmed via XPS. The amperometric pH sensing properties of this electrochemically generated material were investigated using square wave voltammetry. In the pH range 2-13, the iridium hydrous oxide redox signal has a pH dependency of 86.1 ± 1.1 mV per pH unit for midpoint. Finally, the newly developed pH sensor was used to measure the pH of a natural water sample with excellent results as compared to a conventional glass pH probe.

The work of **Chapter 3** has been published in the journal *Journal of Solid State Electrochemistry* [1]. It was carried out under the supervision of Prof. Richard G. Compton and in collaboration with Prof. Xiuting Li (Shenzhen University), Dr. Christopher Batchelor-McAuley (now Professor at Trinity College, Dublin) and Dr. Danlei Li (now Professor in Xi'an Jiaotong-Liverpool University) who helped with the interpretation of the experimental results.

3.1 Introduction

The determination of pH quantifies how acidic or basic an aqueous solution is. It is probably the most commonly made measurement by a chemical sensor. Real world examples of the importance of pH measurements abound. For example, the human body can be viewed as a large buffer solution with the blood pH being maintained within the near neutral range. Abnormally high blood pH (alkalosis), or abnormally low blood pH (acidosis) is used as an

indicator of numerous health issues including Bartter (BS) and Gitelman (GS) syndromes and hyperlactatemia. [2-4] Alternatively in environmental applications, pH is directly linked to the solubility of heavy metals; the lower pH the more toxic the water possibly is as the metals tend to be more soluble. [5] In food chemistry, pH data reveals the fractionation, solubility and functional properties of essential nutrients. [6]

IUPAC [7] defines pH as a function of the activity of the hydrogen ion in a solution,

$$\boldsymbol{pH = -\log a_{H^+} = -\log\left(\frac{m_{H^+}\gamma_{H^+}}{m^{\theta}}\right)} \qquad (3.1)$$

where a_{H^+} is the single ion activity (measured on the molality scale in mol kg^{-1}), γ_{H^+} is the activity coefficient of the hydrogen ion (H^+) at a molality of m_{H^+}, and m^{θ} is the standard molality (1 mol kg^{-1}). [8] Note that IUPAC chose to define the pH in terms of the single ion quantities despite it often being asserted that these are impossible to measure other than approximately, [9, 10] although some ingenious work arounds have been proposed. [11, 12] Rockwood has proposed an approach based on classical equilibrium thermodynamics and provides a clear historical summary of the debate [13].

To date, various methods, electrochemical and non-electrochemical, have been applied to measure pH values, as summarised by Vonau *et al*. [14] The glass pH meter is ubiquitously used in the laboratory and employs direct potentiometric measurements. It is a rapid and convenient method for determining the activity of the hydrogen ion in a solution. However, there are errors affecting its use, most notably the alkaline/acid errors at too high or too low pH, dehydration of the electrode, and a reliance on the accuracy of standard buffers. [15] Moreover, there is an essential need for regular, frequent and careful calibration, which must be referenced to a certified buffer solution. Note that the pH value and uncertainty of the reference buffer solution should also be determined using a calibrated measurement. Thus, a traceability chain can be established relating a measured pH to the pH of a primary buffer solution, the basis and the historical development of which is described by Spitzer. [16] Alternatives to the glass electrode

for potentiometric sensing have been suggested, for example by Inzelt. [17, 18] More generally, the use of potentiometric measurements however make precise and sensitive measurements challenging since the logarithmic relation between potential and activity results in a change of signal of a mere ca 60 mV per decade of concentration at 298K. Apart from a glass electrode, electrode materials like carbon can be functionalised for pH sensing by various surface modifications, e.g. film formation and physical adsorption. [19] Electrodes can also be chemically modified with organic compounds or polymers, such as quinhydrone [20-24] and polypyrrole [25]. These provide an amperometric response which can be sensitive and selective to H^+ ions. [20, 25-28] One advantage of using amperometrically measured peak potentials is the scope for the doubling of sensitivity to 120 mV/decade through the use of two simultaneously immobilised pH sensitive redox couples. [29, 30] A further merit of amperometric measurements is the ability to make calibration-free pH measurements [31], which will be discussed in **Chapter 4** specifically in the context of seawater, whilst on the other hand they are restricted to media containing some electrolyte.

Outside of electrochemistry, the fibre optic pH sensor is a non-electrochemical sensor with low cost and the ability for continuous sensing, which is commonly used in physiological studies. [32-35] Optical pH sensors usually consist of a pH indicator immobilised on an organic carrier. The indicator changes its chemical structure after interacting with H^+ ions, which leads to a variation of its optical response as a function of pH. [36] However, because the response of the colour change is sigmoidal with pH, the accuracy is constrained and the useful detection range can be relatively narrow, often being 2-4 pH units only. [37] To be more specific, the optical pH sensors can be based on absorption[34], reflectance intensity [38], and fluorescence intensity [35, 39, 40]. The use of fluorescence is common due to its high sensitivity compared with reflectometric devices. [40] The short response time and scope for miniaturization are further advantages. Notably Optiz and Lubbers developed a fluorescence pH sensor that can measure

the ionic strength and hydrogen ion activities simultaneously and continuously using hydroxypyrenetrisulfonic acid (HPTS) and β-methylumbelliferone. [41] Other indicators include 5- (and 6-) carboxynaphthofluorescein [40], and 7-hydroxycoumarin-3-carboxylic acid (HCC) [39] for pH measurements near-neutral values.

Metal/metal oxides or metal oxides pH sensors are widely studied especially in potentiometric mode based on the Nernst equation [42]. The potential determining reactions of some transition metal oxides MO_x involves H^+ ions and the number of electrons transferred during the process and its specific mechanism decide the E – pH relationship. pH sensitive metal/metal oxide systems M/MOx have been investigated including examples where M is antimony (Eqns. 3.2-3.3) [43-49], palladium (Eqns. 3.4-3.5) [44, 45, 50, 51], ruthenium (Eqns. 3.6) [52-54] and tungsten (Eqns. 3.7-3.8) [55-57] and applied as pH sensors. The following are typical of the potential determining equilibria for diverse M/MO_x systems:

$$\mathbf{Sb_2O_3 + 6H^+ + 6e^- \leftrightarrow 2Sb + 3H_2O} \quad (3.2)$$

$$\mathbf{Sb_2O_4 + 8H^+ + 8e^- \leftrightarrow 2Sb + 4H_2O} \quad (3.3)$$

$$\mathbf{PdO + 2H^+ + 2e^- \leftrightarrow Pd + H_2O} \quad (3.4)$$

$$\mathbf{PdO_2 + 4H^+ + 4e^- \leftrightarrow Pd + 2H_2O} \quad (3.5)$$

$$\mathbf{RuO_2 + 4H^+ + 4e^- \leftrightarrow Ru + 2H_2O} \quad (3.6)$$

$$\mathbf{W_4O_{12} + 24H^+ + 24e^- \leftrightarrow 4W + 12H_2O} \quad (3.7)$$

$$\mathbf{WO_2 + 4H^+ + 4e^- \leftrightarrow W + 2H_2O}$$

$$\mathbf{W_2O_5 + 2H^+ + 2e^- \leftrightarrow 2WO_2 + H_2O} \quad (3.8)$$

Whilst metal/metal oxide systems are commonly used in classical potentiometric mode in combination with a reference electrode to generate a potential reflecting the pH [45, 58-61], it is also possible to employ them in amperometric mode in which a pH sensitive voltammetric signal is used, the peak potential of which is used to indicate the pH [62-64]. One attraction of this approach is that the measurement generates a current-voltage plot, the shape of which allows the

assessment of the 'quality' of the measurement and hence the reliability of the data. This is particularly important under conditions where electrode fouling may occur, as in blood or other in vivo analysis [27, 65, 66], where in contrast to potentiometric measurements which simply deliver a number, amperometry/voltammetry allows the peak shape to provide an indication of the extent of for example electrode fouling or flag up a mis-functioning electrode. [67] One system where both potentiometry [45, 58, 68-71] and amperometry [27, 65] has been used in this way is the iridium/iridium oxide system.

The Ir/IrO_x redox couple is one of the most popular candidates for pH sensors especially in aggressive environments such as high temperature and/or pressure [58, 68, 70, 72-75]. The couple is further noted for its electrocatalytic behaviour for the O_2 and Cl_2 evolution reactions [76-80] and the electrochromic properties of its redox reactions [68, 72-74]. There are diverse methods for Ir oxide generation. Electrodeposition is one of the methods and uses a solution of potassium hexachloroiridate(III) as a precursor. [65, 81, 82] The conditions and process required to form the final IrO_x are complex and hard to control, which lead to limited reproducibility. [83-86] Iridium oxides can also be prepared by sol-gel chemistry [87, 88], sputtering [60, 89] or thermal methods [70, 86]. However, a pre-treatment, e.g., hydroxylation, is required prior to the usage of electrodes fabricated by the latter two approaches. This is because the resultant dry oxide films or anhydrous films are less hydrous than iridium oxide prepared electrochemically in an aqueous solution. [65, 69, 90] Meanwhile, sputtering is expensive, whereas the pH response of the thermally synthesised Ir electrode is highly dependent on the fabrication conditions. [91]

It has been reported that the anodic iridium oxide film (AIROF) can be synthesised by cyclic voltammetry and the potential determining redox reaction happens within the iridium oxide film rather than on the Ir metal which simply serves as a conductive support. [79, 80, 92-94] Similar phenomena were also observed for Rh, Ru, Os and W [76, 95-98]. Based on this, in this chapter, we develop a novel in-situ AIROF fabrication methodology for pH sensing. Instead of

employing ex-situ potential cycling under acidic or basic conditions as previously explored [44, 68, 93, 94, 99, 100], neutral conditions were newly applied with the AIROF being generated *in-situ* so facilitating more remote and diverse pH measurements notably in medical and environmental applications. To further simplify the procedure, constant potential electrolysis (CPE) activation was applied and further optimised to mimic and replace CV activation, followed by square wave voltammetry (SWV) to obtain resultant the redox peaks used for pH measurement. The pH dependency of the redox peak position and scope of the method are studied in buffer solutions with different pH values. The methodology is applied to the pH measurement in authentic samples of pond water giving good agreement with pH values obtained independently by a classical commercial pH meter.

3.2 Experimental

Chemicals and Reagents

Solutions were prepared in ultra-pure water with a resistivity of 18.2 MΩ cm at 298K (KMD-SHZ, CD Haochun Inc., China). All chemicals were of analytical grade and were used as received without any further purification. Buffer solutions were prepared using chemicals purchased from Shanghai Macklin Biochemical Co., Ltd.: citric acid (99.0%)/sodium citrate (99.5%) for the pH range 2.99–4.81 (0.1 M), monopotassium phosphate (99.5%)/dipotassium phosphate (98.0%) for the pH range 5.99–8.00 (0.2 M) and sodium carbonate (99.5%)/sodium bicarbonate (99.8%) for the pH range 9.02-9.85 (0.1 M). To obtain pH = 1-2 solutions, hydrochloric acid (mass fraction = 36-38%, Guangzhou Chemical Reagent Factory, China) was diluted; for pH = 10.78-12.75, potassium hydroxide (95%, Shanghai Macklin Biochemical Co., Ltd.) was used. All solutions contained 100 mM KCl (99.0%, Sigma-Aldrich, China) as supporting electrolyte. The pH values of buffers were measured using a pH meter (SevenCompact. Mettler Toledo Instrument (Shanghai) Co., Ltd) calibrated using standard buffers of pH 4.01 ± 0.02, 7.00 ± 0.02, and 9.21 ± 0.02.

Electrochemical Apparatus

A high purity Ar flow was used to remove oxygen from all aqueous solutions prior to study. Electrochemical measurements were performed in a thermostatic (25 ± 1 °C) Faraday cage using a CHI760E Electrochemical Workstation (CH Instruments, Inc., Shanghai, China). A standard three electrode set up was used, consisting of a mercury/mercury sulphate/saturated K_2SO_4 solution reference electrode (MSE, + 0.64 V vs. NHE at 25 °C, CH Instruments, Inc., China), a platinum wire counter electrode, and an iridium electrode (0.1 mm in diameter, GoodFellow, UK) as the working electrode. An Ir electrode was pretreated by heating the metal using a flame gun using gas liquefied petroleum gas (butane ≥ 95 %, Pan'an city Gas Co., Ltd., China) for 10 s to remove surface contamination and impurities. Cyclic voltammetry was used to study the electrochemical behaviour of the Ir electrode, while square wave voltammetry was conducted to determine the pH dependency of *in-situ* modified Ir wire after constant potential electrolysis (CPE) activation.

XPS Study and Sample Preparation

The four pure Ir wires (0.125mm in diameter, Alfa Aesar (China) Chemicals Co., Ltd) were pre-flamed as discussed above. For three pre-flamed Ir wires, the potential cycling activation, starting at −0.6 V vs MSE then scanning anodically to 0.45 V vs MSE and then cathodically to −1.05 V vs MSE for 625 cycles was conducted in a degassed PBS solution (pH = 7.25). Then, the cyclic voltammetry was stopped at −1.05 V, −0.1 V or 0.3 V vs MSE respectively, followed by application of the end potential for 60 s. The three Ir samples with electrochemical activation and the one without were prepared ex-situ and sealed in separate vacuum tubes. The calibrated X-ray photoelectron spectroscopy (XPS, K-Alpha+) spectra are referenced to the C 1s peak at 284.6 eV and were carried out for surface elemental analysis.

Real Sample Analysis

Pond water from Wenshan Lake located in Shenzhen University, China (113.93 °E, 22.54 °N) was used for the real sample analysis. Prior to further analysis, natural water samples were filtered using filter paper (pore size: 1 μm) to remove solid impurities. The KCl was then added to the natural water to realise a concentration of 100 mM.

3.3 Results and Discussion

In the following sections, we first explore the oxidative voltammetry of iridium metal under conditions of near neutral pH to show the in-situ formation of iridium hydrous oxide features that are subsequently used as the basis for amperometric pH sensing. XPS is used to confirm the inferred redox chemistry. Next, the in-situ formation of iridium hydrous oxide under conditions of different fixed potentials is explored with the aim of permitting in-situ sensor generation from an iridium electrode. This process is then optimised for the formation of pH sensitive iridium hydrous oxides. The pH response was further explored using square wave voltammetry (SWV). Finally, the developed method was employed to determine the pH of a natural water sample.

3.3.1 Cyclic Voltammetric Study of Ir Metal Electro-Oxidation

The formation of iridium hydrous oxides on the surface of an iridium wire was investigated voltammetrically. It was recognised that for reproducible data prior to a measurement, the surface of the Ir wire should be completely free of oxide which is commonly found on such surfaces. For some electrode materials it is possible to remove such traces of oxide electrochemically but this is known to be unreliable for iridium, leaving a small amount of hydrous oxide on the surface. [93, 101, 102] For this reason, prior to voltammetry Ir surfaces were treated by pre-flaming in the present work to renew the surface of the metal electrode between each experiment. The effects of pre-flaming are shown in Section A4.1 where a clear memory

effect for an electrode without preflaming was observed, whereas the cyclic voltammograms are reproducible when using a preflamed electrode.

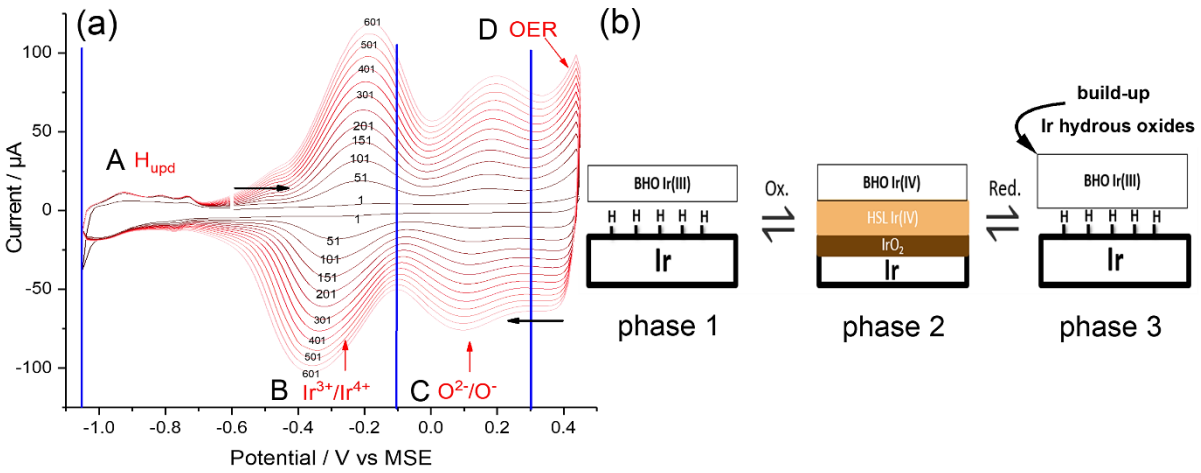

Figure.3.1 (a) Cyclic voltammograms in a degassed buffer solution with pH=7.25 showing the activation of an Ir wire at a scan rate of 0.5 V s^{-1} for multiple cycles. The start potential was −0.6 V vs MSE. The blue lines show the potentials used for constant potential oxide generation (see text); (b) schematic mechanism of Ir electrode activation. BHO = bulk hydrous oxide; HSL = hydrated surface layer. [93]

To explore the electrochemical behaviour of an Ir wire in neutral solution, the pre-flamed Ir electrode was immersed in a degassed 0.2 M phosphate buffer solution (PBS) with 0.1 M KCl (pH = 7.25). Cyclic voltammetry was conducted for 625 cycles starting at a potential of −0.6 V with scan reversal at a potential of 0.45 V to −1.05 V vs MSE where the potential again reversed as shown in Figure.3.1 (a). The figure shows four voltammetric features labelled A, B, C and D. Feature A is assigned to the underpotential adsorption of hydrogen (H_{upd}) [103, 104]

$$\mathbf{M(s) + H_3O^+ + e^- \rightleftharpoons M - H_{ad} + H_2O \rightleftharpoons \frac{1}{2}H_2 + M - H_2O_{ad}} \qquad (3.9)$$

In contrast to feature A, features B and C steadily increase with increasing scan number. This voltammetric response is markedly different from that observed for platinum. [105] Here feature B is attributed to the Ir (III/IV) redox transition with formation of hydrous oxides. This process has been reported to involve various possible redox reactions between the reduced and

oxidised forms of hydrous oxides where the exact stoichiometric composition of the hydrous film is reported as hard to determine. [65, 68, 106] The equilibria suggested by Olthuis *et al*. [68] and Burke *et al*. [106] are

$$\mathbf{Ir_2O(OH)_3O_3^{3-} + 3H^+ + 2e^- \rightleftharpoons 2Ir(OH)_2O^- + H_2O} \qquad (3.10)$$

$$\mathbf{[-Ir^{IV} - (OH)_x - Ir^{IV} -]_n + 3nH^+ + 2ne^- \rightleftharpoons [-Ir^{III} - (OH)_{x-3} \cdot 3H_2O - Ir^{III} -]_n} \qquad (3.11)$$

The equilibria in (3.10) and (3.11) suggest a super-Nernstian pH dependency of ca 89 mV per pH unit, reflecting the relative numbers of electrons and protons consumed in reaction (3.10) and (3.11). [58, 65, 107]

There are different reported interpretations of Feature C. Pickup *et al*. suggested that it corresponds to further oxidation of the Ir hydrous oxides, e.g. from Ir (IV) to Ir (VI). [93] However, later reports from Pfeifer *et al*. [79, 80, 92] proposed assigning it to the oxidation of the oxide anion O^{2-}, contained in the IrO_x matrix in form of adsorbed OH groups, to O^-

$$\mathbf{IrO_xO^{II-}H \rightleftharpoons IrO_xO^{I-} + H^+ + e^-} \qquad (3.12)$$

Feature D is related to the oxygen evolution reaction (OER):

$$\mathbf{2H_2O \rightarrow O_2 + 4H^+ + 4e^-} \qquad (3.13)$$

It has been suggested that the IrO_xO^{I-} formed during the redox reaction in Feature C is the catalyst for OER where Eqn. (3.14) explains its possible electrocatalytic behaviour [80]:

$$\mathbf{IrO_xO^{I-} + H_2O \rightarrow IrO_xO^{I-} - O^{I-} - H + H^+ + e^- \rightarrow IrO_x + O_2 + 2H^+ + 3e^-} \qquad (3.14)$$

Based on the literature it is possible to summarise the likely sequence of events underpinning the voltammetry shown in Figure.3.1 (a). Figure.3.1 (b) schematically shows the state of the surface of the iridium electrode at different stages of the voltammetry and seeks to explain the build-up of the features B and C from one potential cycle to the next. Initially during the first sweep of potential cycling, the pure Ir is oxidised to IrO_2 by potentials ranging from –

0.65 V to 0.15 V vs MSE and its surface immediately becomes hydrated when an anodic potential is applied. The resulting Ir (IV) hydrous oxide can subsequently only be reduced back to Ir (III) in contrast to IrO_2 that is thought to be capable of being reduced to pure Ir when the cyclic voltammetry is swept cathodically to −1.05 V vs MSE. [93] Phase 1 shows a pure Ir wire with bulk Ir(III) hydrous oxide (BHO Ir(III)) accumulated from previous scans on its surface. When an anodic potential is applied (between −0.65 V to 0.15 V vs MSE), the Ir metal is again partly oxidised to IrO_2 and the previously formed BHO Ir(III) is oxidised to form BHO Ir(IV). Note that the Ir (IV) hydrated surface layer (HSL Ir (IV)) shown at phase 2 differs from BHO Ir(IV) formed in previous cycles, which is newly formed and bonded to the inner IrO_2 layer. Then, by applying cathodic potentials lower to –1.05 V vs MSE, neither the BHO nor the HSL Ir (IV) can be reduced to oxidation states lower than Ir (III). As a result, a new layer of BHO Ir (III) from HSL Ir (IV) is added to the original Ir metal surface as shown in Phase 3. Consequently, as the number of potential cycling increases as shown in Figure.3.1, a progressive build-up of the Ir hydrous oxide layer was observed with scans due to the repeated redox process mentioned above. Referring to the cyclic voltammogram in Figure.3.1 (a), the thickness of accumulated Ir hydrous oxide after 625 cycles is estimated to be around 0.46 μm, assuming the H_{upd} represents a monolayer (Section A4.2).

To confirm the proposed interpretation and analyse the formed Ir hydrous oxide layer, three surfaces were electrochemically generated for XPS with a pure Ir wire surface cleaned by flaming for comparison. Figure.A3.3 shows the resulting (a) Ir 4f and (b) O 1s XPS spectra and Table A3.1 reports the details of the spectra, which are consistent with the proposed mechanism above and to be more specific, the formed thick layer is iridium (III/IV) hydrous oxide as a result of potential cycling. The presence of this even when the sample for spectroscopic evaluation is withdrawn at –1.05 V indicates the chemical irreversibility of the formation of this layer. (See detailed discussion in Section A3.3)

To conclude, an Ir wire can be activated under neutral rather than acid conditions forming an iridium (III/IV) hydrous oxide layer, which is pH sensitive. In the following we use this approach to develop a pH sensor based on the in-situ activation of an Ir electrode under neutral pH conditions.

3.3.2 Optimisation of the Electrode Activation

In this sub-section, the most effective potential range of potential cycling for the growth of Ir hydrous oxide is first studied based on the conclusions of the last section. Then, constant potential oxidation is optimised to mimic the cyclic voltammetry by applying various fixed potentials for defined periods of time to develop a method of in-situ generation of the pH sensitive Ir hydrous oxide.

Optimisation of the potential window for the growth of pH sensitive iridium hydrous oxide

As shown in Figure.3.2 (a), cyclic voltammetry of a pre-flamed Ir wire with different potential ranges were conducted in a degassed 0.2 M PBS solution with 0.1 M KCl (pH = 7.25) at 0.5 V s^{-1}. The CV starts at a potential of −0.6 V and first swept anodically to a fixed potential of 0.45 V and the swept to different cathodic limits varies from –1.05 V to –0.7 V vs MSE. The 10th cycle is displayed in Figure.3.2 (a) to find the optimised cathodic potential. Figure.3.2 (b) shows the 10th cyclic voltammograms with the cathodic potential being fixed at –1.05 V and the anodic potential was progressively increased to 0.5 V from 0.2 V vs MSE.

The resultant Ir (III/IV) redox couple in Figure.3.2 (a) becomes better defined with a high signal to background level at a reductive limit of −1.05 V, whilst in Figure.3.2 (b), the redox couple of the 10th cycle becomes better-defined when the positive potential limit is extended to 0.45V. Extending the limits beyond −1.05V or +0.45V showed no further improvement in the quality of the signal, which is consistent with literature. [93, 108] Pickup *et al*. also suggested that the hydrous oxide begins to dissolve when more positive potentials were applied. [93] From our measurement it is clear that the potentials between 0.2 and 0.45 V, has greater influence on the

formation of the Ir hydrous oxide, while extension of the cathodic limit increases the rate of growth only slightly. An explanation for this may be that the completion of redox transition between $O^{2-/-}$ contained in the IrO_x matrix in form of adsorbed OH groups (Feature C) is a prerequisite of hydrous oxide formation.

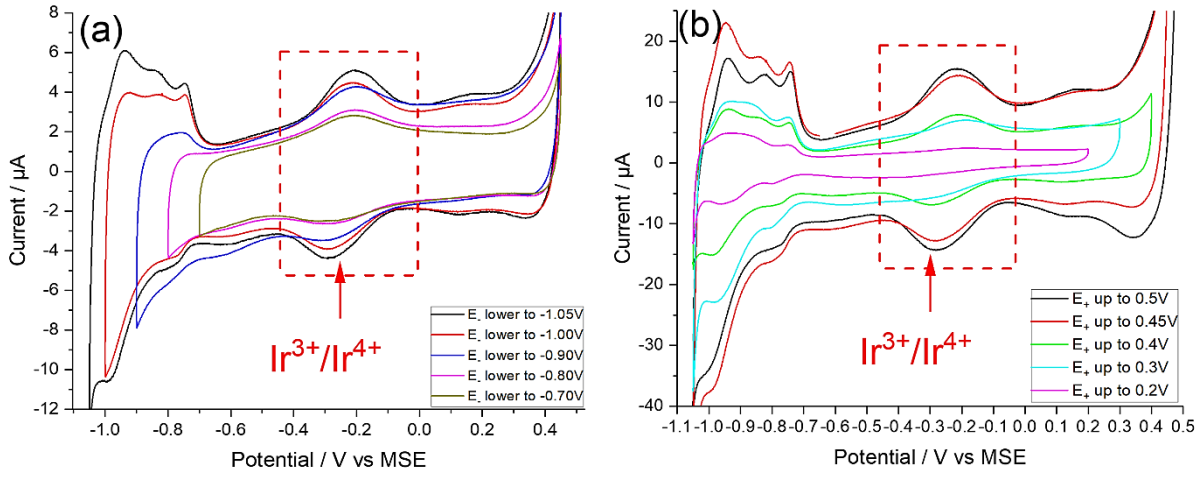

Figure.3.2 Cyclic voltammograms of the 10th cycle in degassed buffer solution with pH=7.25 starting at a potential of −0.6 V for activation of Ir wire with different (a)cathodic and (b)anodic potentials at a scan rate of 0.5 Vs^{-1}.

To summarise, for the growth of hydrous oxide, the potential range must embrace both the upper critical limit and the lower critical limit, to be more specific, anodically to 0.45 V and cathodically to –1.05 V vs MSE. One can also conclude that during cyclic voltammetry only around 20% of the experimental potential scan, whilst the electrode is at extreme potentials, actually induces the chemistry for the growth of hydrous oxide. This latter observation encourages seeking a simpler activation method using constant potential electrolysis as below.

Optimisation of constant potential electrolysis (CPE) for in-situ Ir hydrous oxide growth.

Different potential sequences were developed with timescales dictated by the observation that potential cycling between −1.05 V and 0.45 V for 10 cycles was effective to obtain a clear redox couple, suggesting that around 12 seconds might be needed at each potential limit to demonstrate a comparable effect as the potential cycling. Thus, three CPE methods were

analysed. Figure.3.3 (a-c) are the plots of potentials against time to demonstrate the three CPE activations to mimic and enhance the potential cycling activation established as above. For method 1 in Figure.3.3 (a), a potential of 0.45 V was applied for 12 s, followed by a potential of −1.05 V for 12s. Method 2 has the same total activation time at each limit potential but was divided into six repeats of potential so that 2 s was spent on each potential on every repeat (Figure.3.3 (b)). As shown in Figure.3.3 (c), method 3 is a CPE method with four repeats of potential switch (2 s for each potential segment) for a shorter overall duration (16 s rather than 24 s). Figure.3.3 (d) shows the three cyclic voltammograms resulting from the three activation methods and, as expected, display the presence of two redox couples ($Ir^{3+/4+}$ and $O^{2-/-}$) as characterised above with mid-potentials of ca. −0.26 V and 0.13 V vs MSE respectively. Comparison of the three voltammograms shows that Method 1 produces a much weaker signal than Methods 2 and 3 but that there is a negligible difference between the later.

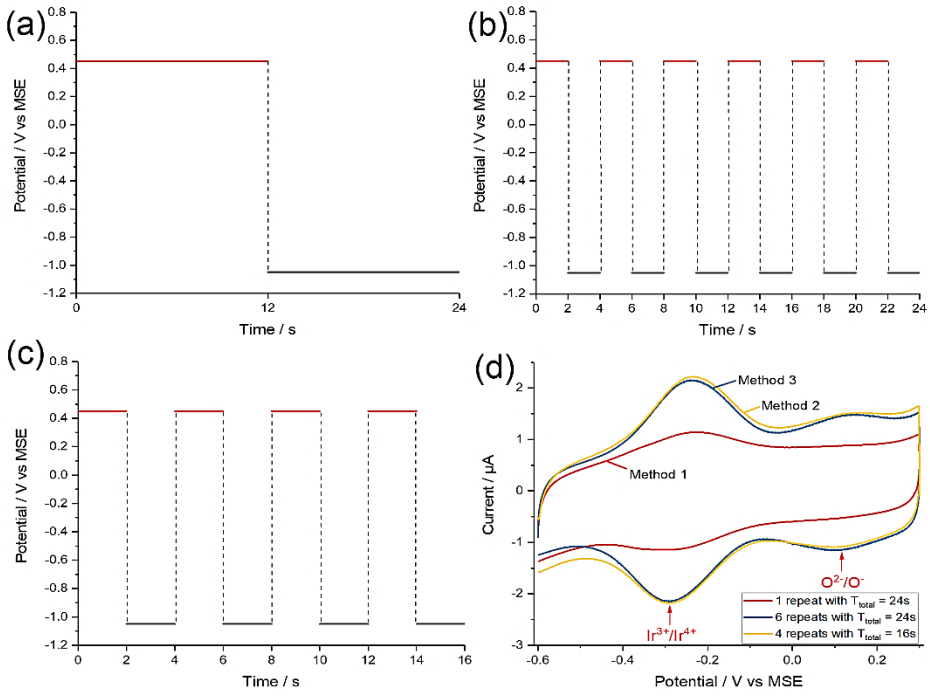

Figure.3.3 CA activation with switch of potentials at 0.45 V and −1.05 V vs MSE (a) for one time with 12 s at each potential, (b) for six times with 2 s at each potential and (c) for four times with 2 s at each potential; (d) resultant cyclic voltammograms of the 10th cycle after CA activation in degassed buffer solution with pH=7.25 at a scan rate of 0.1 V s^{-1}.

We conclude that CPE is effective for the growth of Ir hydrous oxide films. In particular, CPE with four repeats of potential switch between 0.45 V and −1.05 V vs MSE (Method 3) will be used as the in-situ Ir electrode fabrication method for further study as reported below.

3.3.3 pH dependency of the Iridium Hydrous Oxide Layer in Buffer Solutions

In this section, the pH dependency of the iridium hydrous oxide layer is investigated by square wave voltammetry (SWV) using an Ir wire activated by the CPE method established as above. The optimisation of SWV parameters, including frequency, step potential, and amplitude, in a degassed 0.2 M PBS solution with 0.1 M KCl (pH = 7.25) was implemented to obtain the best-defined square wave voltammograms for pH measurements (Section A4.4). The optimised SWV with frequency of 90 Hz, amplitude of 60 mV, and step potential of 1 mV were applied for pH measurements in buffer solutions with various pHs. Prior to the measurements, the pHs of buffers were measured with a pH meter, with an uncertainty of 0.01 (x-axis error-bar in Figure.3.4). SWVs were first scanned anodically to obtain a net oxidative peak (Figure.3.4 (a)) and then scans were immediately reversed to obtain a desired reduction peak (Figure.3.4 (b)). The expected Ir(III/IV) SWV peaks were observed in the potential range within ca 0.11 to −0.73 V for scans in both directions for pH = 2 – 13, while for pH = 2 – 5, a small peak was seen during the oxidation scan, with peak potentials being about 0.32 V more negative than that of the target oxidation peak. However, the pre-peak was deemed not to interfere with the measurements of the main peak to be used for the pH determination. For pH values lower than 2 (Section A4.5), three peaks were observed during oxidation scans, notably, at ca –0.12 V, 0.09 V and 0.31 V for pH = 1.15 and −0.11 V, 0.06 V and 0.22 V vs MSE for pH = 1.86 (Figure.A3.5 (a)). The reduction signals were broad for both pH values, and this was attributed to the overlap of 2 peaks (see Figure.A3.5 (b)). Given the voltammetric complexity seen at low pH it was decided to focus on the pH range from 2.0 to 13.0 for establishing a measurement protocol.

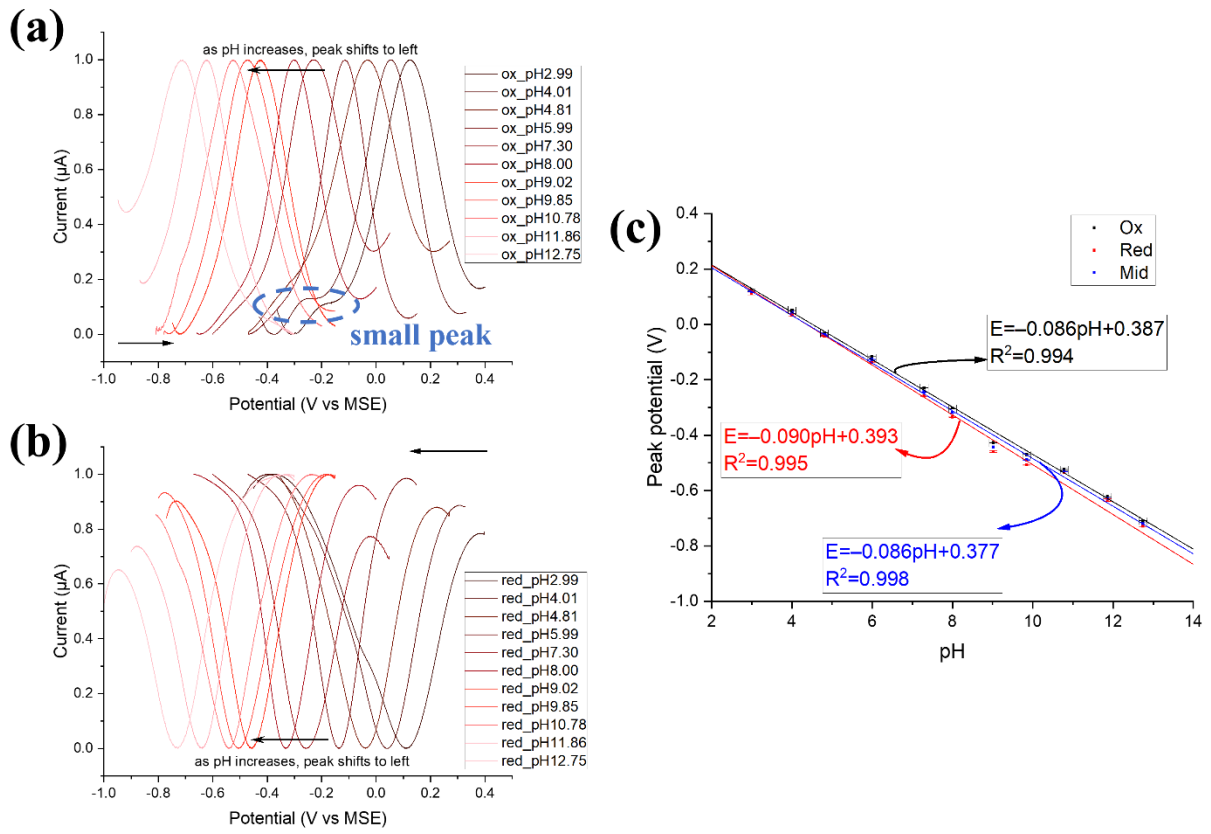

Figure.3.4 Normalised square wave voltammetry (frequency 90 Hz, step potential 1 mV, and amplitude 60 mV) response of an iridium hydrous oxide on iridium wire electrode with varying pH of different buffers ranging from 2.99 to 12.75 (a) oxidation and (b) reduction. (c) Plots of potentials against pH value reading from the pH meter (black dots: oxidation, red dots: reduction and blue dots: mid-point potential).

The analytically useful (for pH measurement) Ir(III/IV) redox couple obtained in solutions with pH = 2-13 showed a shift in the peak potentials towards more negative potentials as the pH increased for both oxidative and reductive scans. To analyse the data, the oxidation/reduction peak potentials and midpoint potential of the in-situ fabricated iridium hydrous oxide electrode were all recorded. Plots of potentials against pH as measured from pH meter are shown in Figure.A3.4 (c). The gradients of the slopes were 85.6 ± 2.3, 90.0 ± 2.1 and 86.1 ± 1.1 mV per pH unit for oxidation/reduction peak potentials and midpoint potential respectively. The pH dependency is above the ca 60 mV per pH unit response of a classical glass electrode but consistent with the equilibria proposed by Olthuis *et al*. [68] and Burke *et al*.

[106] being around 89 mV per pH unit as given in Eqns (3.10) and (3.11) above where three protons are transferred per two electrons. The higher response per pH unit is a clear merit of the iridium oxide approach to pH sensing.

3.3.4 Real Sample Analysis: pH Measurement in Natural Water

The pH dependency of the in-situ fabricated iridium hydrous oxide layer on an iridium wire in buffer solutions was obtained and investigated in the previous section using CPE activation method followed by SWV to improve signal-to-background ratio of the redox peak of interest. This electrode was subsequently employed for pH sensing of a natural water sample (Wenshan Lake located in Shenzhen University, China) to investigate the capability of the use under real world conditions.

First, an iridium wire was activated using CPE with 4 repeats of potentials which switched between 0.45 V and −1.05 V vs MSE in a 0.2 M PBS solution with 0.1 M KCl (pH = 6.91). Then, SWV with the step potential of 1 mV, amplitude of 60 mV and frequency of 90 Hz was conducted in the pond water containing 0.1 M KCl. The effect of 0.1 M KCl as supporting electrolytes in pond water on the pH measurement using an Ir wire is demonstrated in Section A4.6. The oxidation peaks were recorded using SWV which initially swept to positive potentials and the scans were then reversed to obtain reduction peaks (blue dashed lines in Figure.3.5 (a-b)). The redox peaks obtained in the natural water samples were overlaid with previous results (solid lines). Three repeat experiments were done for an improved accuracy of the measurements; the average Ir(III/IV) oxidation peak from SWV is at –0.195 ± 0.005 V and reduction peak is at –0.241 ± 0.007 V with a corresponding average mid-point potential of –0.218 ± 0.005 V vs MSE. The pH value of the pond water sample was then calculated to be 6.92 ± 0.08 by adapting the pH dependency obtained in buffer solutions (blue dots in Figure.3.5 (c)). The reliability and accuracy for pH sensing in pond water using such iridium electrode have been proved by comparing the calculated pH value (6.92 ± 0.08) and the value measured

with a commercial pH meter (6.91± 0.01). Thus, one can conclude that this in-situ fabricated Ir wire is an ideal pH sensor under near neutral conditions.

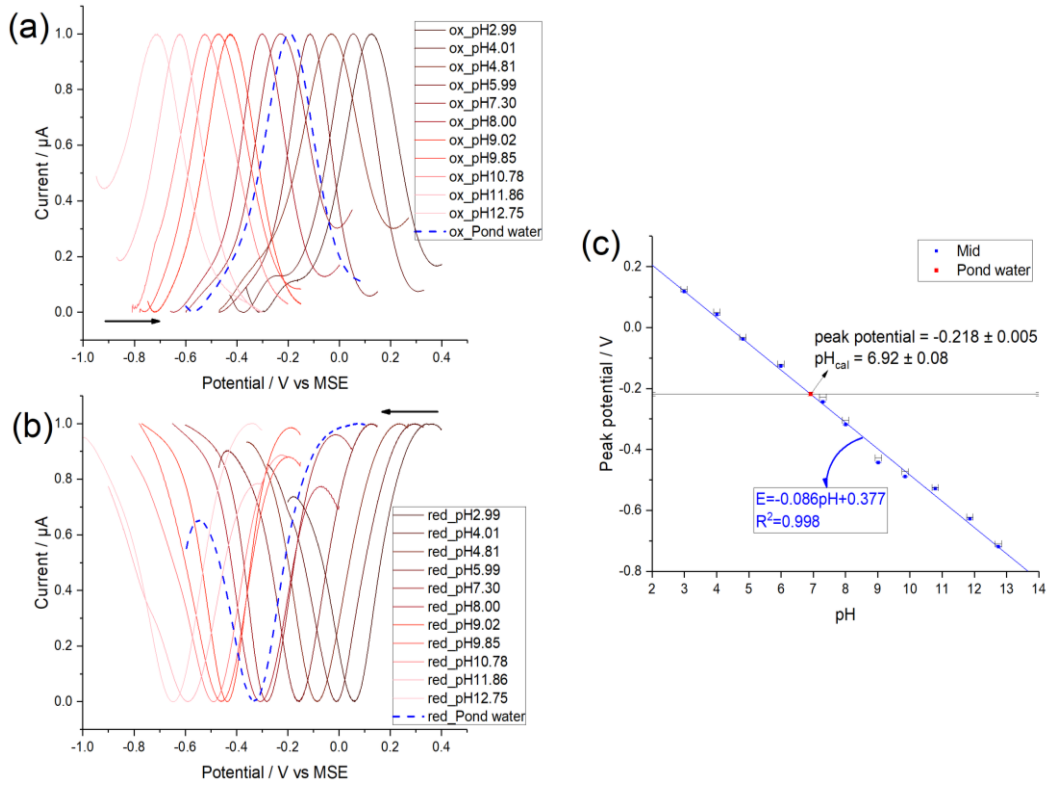

Figure.3.5 Overlaid square wave voltammetry (frequency 90 Hz, step potential 1 mV, and amplitude 60 mV) response of iridium hydrous oxide on an iridium wire in degassed pond water after CPE activation in PBS solution with the same pH = 6.91(a) oxidation and (b) reduction. (c) Overlaid average mid-point potential obtained in pond water with the plots of potentials against pH value reading from the pH meter from previous section (black dots: pond water and blue dots: mid-point potential obtained previously).

3.4 Conclusions

In this work, the fabrication and performance of an iridium oxide electrode was studied. First, the cyclic voltammetry combined with XPS study demonstrated that an Ir wire can be activated under neutral rather than acid or basic conditions and the pH sensitivity of the formed iridium hydrous oxide layer is controlled by the Ir (III/IV) couple at all potentials used for pH measurements. Cyclic voltammetry was used to identify the potentials required to form the pH

sensitive layers, allowing a significant simplification of the formation by using constant potential electrolysis (CPE) with four repeats of potential switch between 0.45 V and −1.05 V vs MSE rather than potential cycling. Then, the pH dependency of the electrode was studied in buffer solutions employing square wave voltammetry. The detection limit is pH = 2-13 and the gradients of the slopes being 85.6 ± 2.3, 90.0 ± 2.1 and 86.1 ± 1.1 mV per pH unit for oxidation/reduction peak potentials and midpoint potentials respectively. Finally, the measured pH of a natural water sample using the Ir electrode is 6.92 ± 0.08, while that obtained by a pH meter is 6.91 ± 0.01. The insignificant difference proves that this in-situ fabricated Ir wire is an ideal pH sensor for use under near neutral conditions and where in-situ generation is advantageous.

Appendices

Section A3.1: Cyclic Voltammetric Study about the Effect of Preflaming on an Ir Wire

This section presents the effect of pre-flaming on the electrochemical behaviour of an Ir wire electrode. Such effect was studied by comparing the corresponding cyclic voltammetry obtained using electrodes with pre-flaming (black and red lines in Figure.A3.1) and without preflaming (green line in Figure.A3.1). The voltammograms were recorded from a starting potential of −0.6 V. These were first swept anodically to 0.45 V vs MSE, then swept cathodically to −1.05 V vs MSE. Prior to the 1st (black line) and 2nd repeat (red line), the electrode was flamed prior to the next measurement. Between the 2nd and 3rd repeat (green line), the Ir electrode was washed by DI water and dried with Ar. Comparison of the voltammograms show the inference that flaming led to a fresh, clean surface and facilitated reproducible voltammetry.

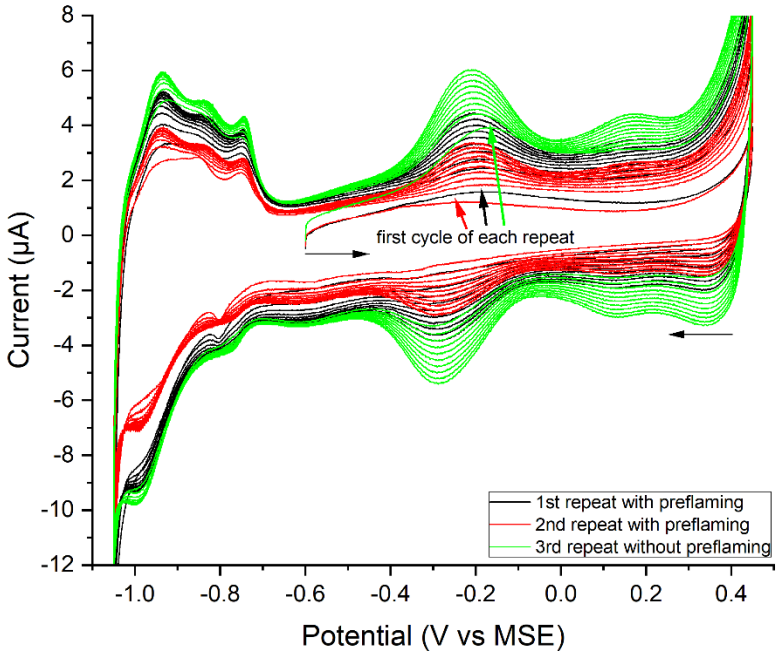

Figure.A3.1 Cyclic voltammograms (sequential 10 cycles) in a degassed buffer solution with pH=7.25 for activation of Ir wire at a scan rate of 0.5 Vs^{-1}. The start potential was −0.6 V vs MSE; 1st repeat with pre-flaming (black line), 2nd repeat with pre-flaming (red line) and 3rd repeat without pre-flaming (blue line).

Section A3.2: Estimation of the Thickness of the Accumulated Ir Hydrous Oxide Layer

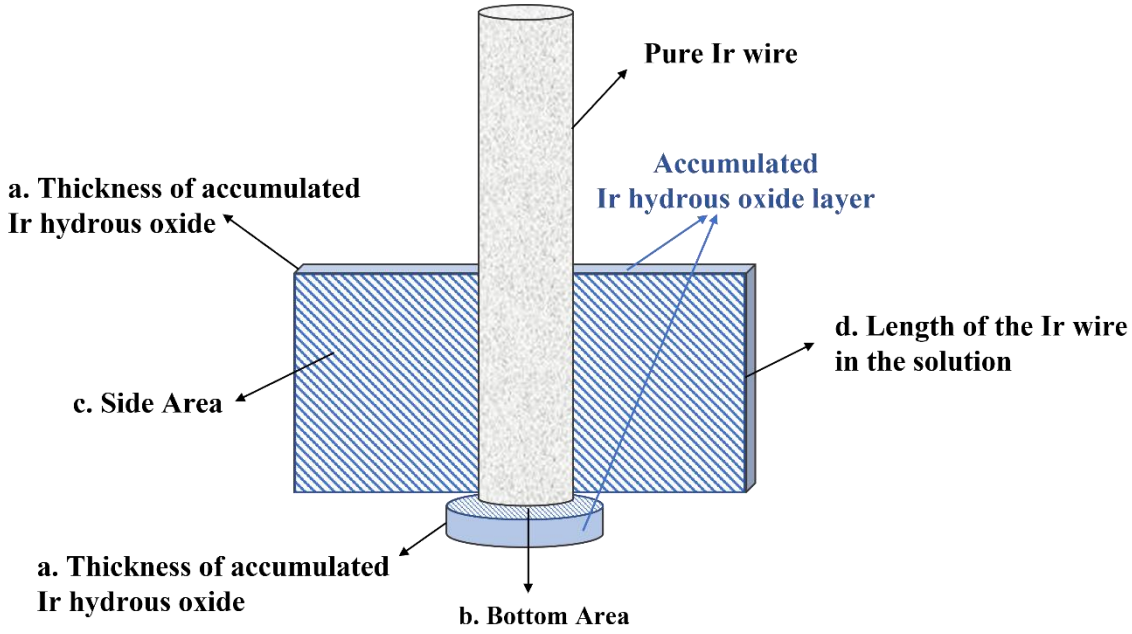

Figure.A3.2 A schematic model for accumulated Ir hydrous oxide (blue) on the surface of the Ir wire (grey part). (a) the thickness; (b) bottom area; (c) side area of accumulated Ir hydrous oxide; (d) the length of the pure Ir wire with the formation of Ir hydrous oxide by potential cycling in a neutral PBS solution.

This section summarises the calculation of estimated thickness of accumulated Ir hydrous oxide after 625 cycles. Referring to the cyclic voltammogram in Figure.3.1 (a) and the schematic model of the accumulated Ir hydrous around the Ir (Figure.A3.2), the thickness (a, Figure.A3.2) is estimated to be around 0.5 μm, assuming the H_{upd} signal corresponds to that of a monolayer. The calculation is shown as below.

The number of electrons transferred during redox reaction:

$$\text{No. of } e^{-}\text{transfered during redox reaction} = \frac{\dfrac{\text{integrated peak area}}{\text{scan rate}}}{\text{charge of 1 } e^{-}} = \frac{\dfrac{3.4 \times 10^{-5}\ \text{A V}}{0.5\ \text{V s}^{-1}}}{1.6 \times 10^{-19}}$$

$$= 4 \times 10^{14}$$

Hence, the moles of accumulated Ir hydrous oxide is calculated to be:

$$n_{\text{Ir hydrous oxide}} = n_{e^-} = \frac{\text{No. of } e^- \text{transfered}}{\text{Avogadro constant}} = \frac{4 \times 10^{14}}{6.02 \times 10^{23}} = 7 \times 10^{-10} \text{ mol}$$

Assuming Ir hydrous oxide has the same density (12 g cm^{-3}) and molar mass (223 g mol^{-1}) as IrO_2, the total volume of accumulated Ir hydrous oxide is:

$$\text{Volume}_{\text{Ir hydrous oxide}} = \frac{\text{mole} \times \text{molar mass}}{\text{density}} = \frac{7 \times 10^{-10} \text{ mol} \times 223 \text{ g mol}^{-1}}{12 \text{ g cm}^{-2}}$$

$$= 1.4 \times 10^{-8} \text{ cm}^3$$

Referring to H_{upd} signals, which represents a monolayer, the surface of accumulated Ir hydrous oxide can be estimated to be:

$$\text{Surface area on the Ir wire} = \frac{\text{No. of } e^- \text{transfered during Hupd}}{Q_{lit} \times \% \text{ of surface coverage}} = \frac{\frac{2 \times 10^{-6} \text{ A V}}{0.5 \text{ V s}^{-1}}}{218 \times 10^{-6} \text{ C} \times 0.65}$$

$$= 0.03 \text{ cm}^2$$

As shown in Figure.A3.2, the Ir hydrous oxide formed on the electrode is assumed to be a cuboid and a flat cylinder with the same thickness. Note that for the cuboid the difference between the perimeter of the inner and outer layer is negligible. Thus, the length of the Ir wire activated in the solution is calculated to be:

$$\text{Length of the Ir wire reacted} = \frac{\text{total surface area} - \text{bottom area}}{\pi \times \text{diameter}_{\text{Ir wire}}}$$

$$= \frac{0.03 \text{ cm}^2 - \pi \times \left(\frac{0.01 \text{ cm}}{2}\right)^2}{\pi \times 0.01 \text{ cm}} = 0.95 \text{ cm}$$

Finally, the thickness of Ir hydrous oxide is:

$$\text{Thickness of Ir hydrous oxide} = \frac{\text{Volume}}{\text{side area} + \text{bottom area}}$$

$$= \frac{1.4 \times 10^{-8} \text{ cm}^3}{\pi \times 0.01 \text{ cm} \times 0.95 \text{ cm} + \pi \times \left(\frac{0.01 \text{ cm}}{2}\right)^2} = 0.5 \, \mu m$$

Section A3.3: Ex-situ XPS Study of the Ir Hydrous Oxide Layer

This section reports the analysis of the Ir hydrous oxide layer using XPS. Three surfaces were electrochemically generated for XPS characterisation using the following procedures. First, cyclic voltammetry was started at a potential of −0.6 V, scanned anodically to 0.45 V and reversed back to −1.05 V vs MSE at 0.5 V s^{-1}. Then, after 625 cycles the voltammetry was stopped at one of three different potentials, −1.05 V, −0.1 V, or 0.3 V vs MSE respectively, indicated by blue lines in Figure.3.1 (a). After termination of the cycling the potential was maintained at the end potential for 60 s. A pure Ir wire surface cleaned by flaming was also studied by XPS for comparison.

Table A3.1 Summary of XPS results

Applied Potentials	Ir $4f_{7/2}$		Ir $4f_{5/2}$		O 1s	
	BE/eV	FWHM/eV	BE/Ev	FWHM/eV	BE/eV	FWHM/eV
Pure Ir	60.30	0.99	63.28	1.00	531.48	3.07
−1.05 V	61.47	1.45	64.37	1.54	531.16	2.74
−0.1 V	61.23	1.94	64.12	2.13	531.61	2.70
0.3 V	61.67	1.94	64.56	2.13	531.31	2.63

Figure.A3.3 shows the resulting (a) Ir 4f and (b) O 1s XPS spectra. For the pure Ir wire, narrow Ir $4f_{7/2}$ (FWHM = 0.99 eV) and Ir $4f_{5/2}$ (FWHM = 1.00 eV) signals were found at 60.30 and 63.28 eV binding energy (BE) respectively (black dashed line). The Ir peaks ($4f_{7/2}$ and Ir $4f_{5/2}$) of the other three samples have B.E.s higher than these of pure Ir wire and the values fall into the range corresponding to Ir (III) and (IV), being around 61.50 and 64.30 eV respectively (Table A3.1). [79] The broadening of peaks comparing to pure Ir's spectra also confirms that there are mixtures of Ir (III) and (IV) compounds with different compositions. [78-80, 92] Note that exposure to oxygen in the ex-situ conditions could contribute to the broadening of the Ir (III) and (IV) peaks.

Turning to the O 1s signals, the presence of such a peak on the Ir metal is due to the chemisorbed oxygen on the Ir surface, which cannot be removed by preflaming. [109] For the three samples, signals were seen with a BE of ca 531.5 ± 0.5 eV in all cases. Typical O 1s binding energies range according to chemical environment from, for transition metal oxides is at 530 ± 0.5 eV, for hydroxides is at 531.5 ± 0.5 eV and for water of hydration or adsorbed water is at 533 ± 1 eV. [101] The data in Figure.A3.3 (b) and Table A3.1 are again consistent with the formation of a thick layer of iridium hydrous oxide resulting from potential cycling. The presence of this even when the sample for spectroscopic evaluation was withdrawn at – 1.05 V indicates the chemical irreversibility of the formation of this layer.

In a conclusion, an Ir wire can be activated under neutral rather than acid conditions forming a pH sensitive iridium (III/IV) hydrous oxide layer, which is stable at all potentials during activation once it formed.

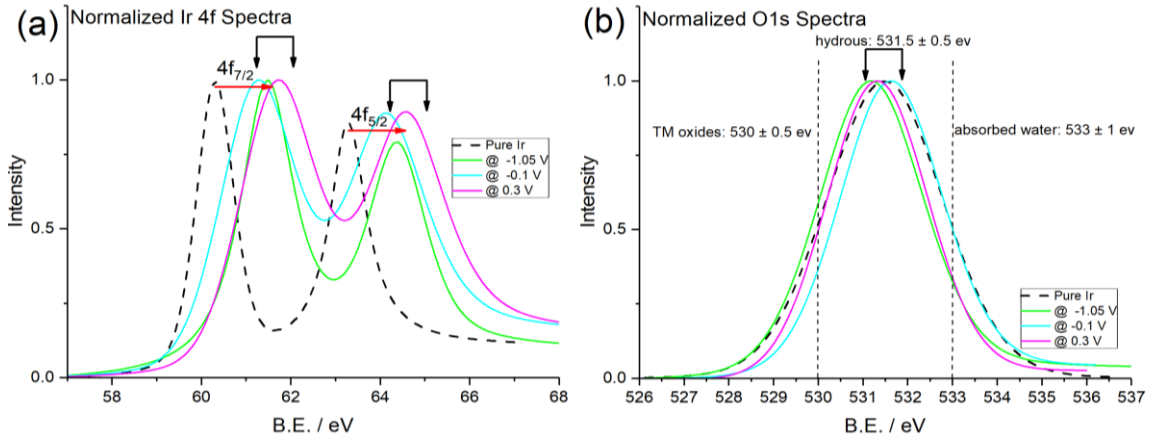

Figure.A3.3 Overlaid x-ray photoemission spectra after cyclic voltammetry stopped at various potentials vs MSE in degassed buffer solution with pH=7.25 s for activation of Ir wire at a scan rate of 0.5 Vs^{-1}: (a) Ir ($4f_{7/2}$ and $4f_{5/2}$) surface, (b) O 1s.

Section A3.4: Optimisation of SWV Parameters to Study the pH Dependency of Iridium Hydrous Oxide Layers in Buffer Solutions

This section reports the effect of three parameters (step potential, frequency and amplitude) on the SWV signal as tested in a PBS buffer solution (pH=7.25), referring to the corresponding current to background ratio of the Ir(III/IV) couple.

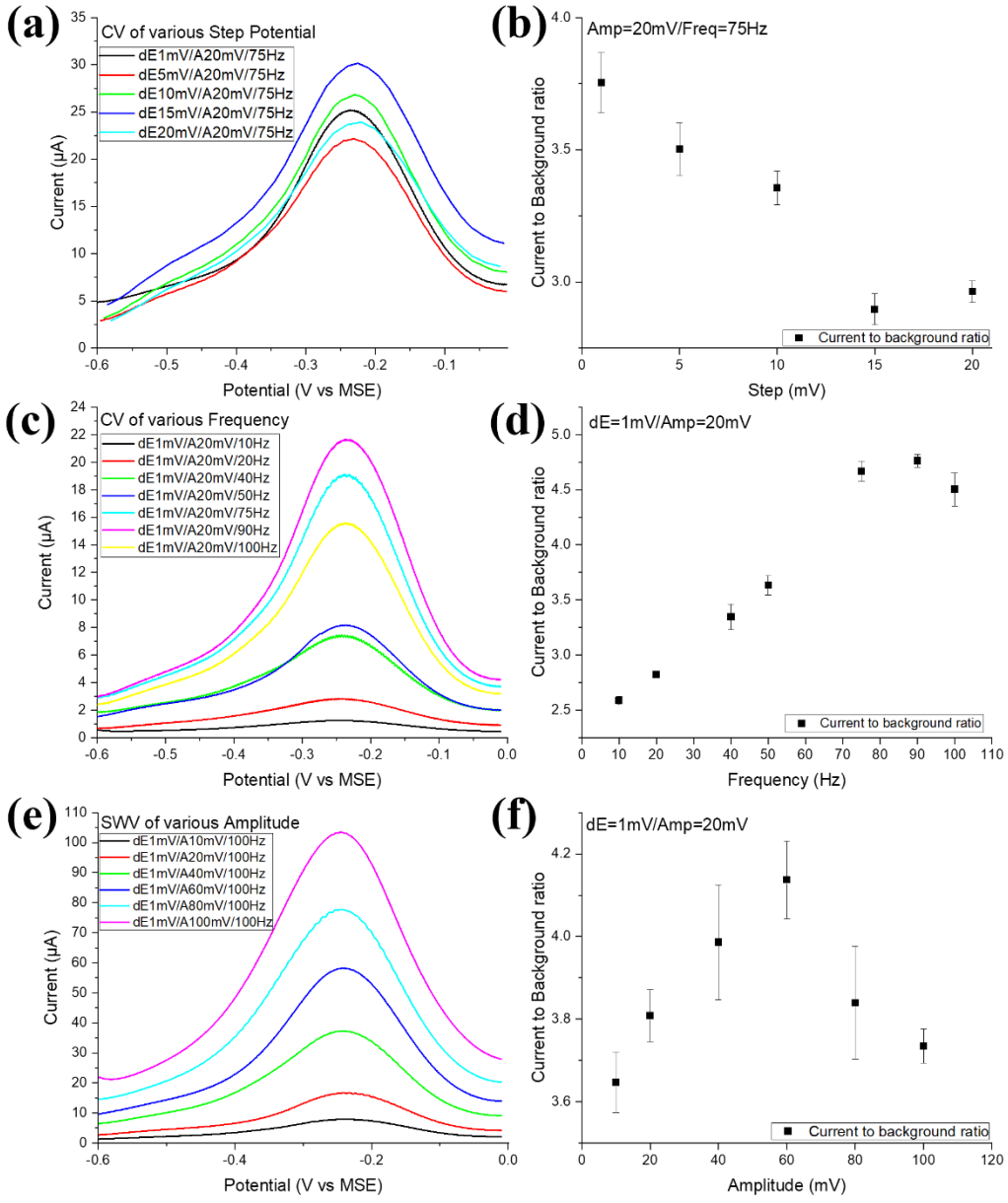

Figure.A3.4 Effect of the (a) step potential (c) frequency and (e)amplitude parameter on the SWV signal tested in a buffer solution (pH=7.25); corresponding current to peak potentials of the resultant oxidation peaks obtained by SWV with various parameters: (b), (d) and (f).

Figure.A3.4 (a) shows the SWV signals obtained with various step potentials from 1 to 20 mV along with a constant frequency of 75 Hz and constant amplitude of 20 mV. The corresponding plot of current to background ratio as a function of step potential is presented in Figure.A3.4 (b) showing that the smallest step potential (1 mV) gives the largest current to background ratio. Then, with the step potential being fixed at 1 mV, the effect of frequency was studied using SWV with a fixed amplitude parameter of 20 mV. The resulting voltammograms are shown in Figure.A3.4 (c). How the current to background ratio varies with a function of frequency is plotted in Figure.A3.4 (d), which demonstrates that the current to background ratio increases with frequency and reaches a maximum when the frequency is 90 Hz. To analyse the effect of third parameter, the amplitude, the SWV signals were recorded as shown in Figure.A3.4 (e) with fixed step potential of 1 mV and frequency of 90 Hz. The maximal current to background ratio was obtained for amplitude being 60 mV (Figure.A3.4 (f)). Thus, the following parameters, step potential = 1 mV, amplitude = 60 mV and frequency = 90 Hz, were selected for further measurements.

Section A3.5: pH Dependency of an Ir Hydrous Oxide Layer in Aqueous HCl (pH = 1.15 and 1.86)

This section reports that abnormal redox signals were observed when a fabricated Ir electrode was used in solutions with pH lower than 2. To study this, CPE method developed above was first conducted to activate an Ir electrode in HCl solutions with 0.1 M KCl (pH =1.15 and 1.87). Then, SWV signals with optimised parameters were recorded by an initial scan to positive potentials for an oxidative peak and then scans were reversed immediately to obtain a reduction peak. Three peaks were observed during oxidation scans, notably, at ca – 0.12 V, 0.09 V and 0.31 V for pH = 1.15 and −0.11 V, 0.06 V and 0.22 V vs MSE for pH = 1.86 (Figure.A3.5 (a)). The reduction signals were broad for both pH values, and this was attributed to the overlap of 2 peaks (see Figure.A3.5 (b)). Given the voltammetric complexity seen at low pH, it was concluded that the useful analytical pH range was from 2.0 to 13.0.

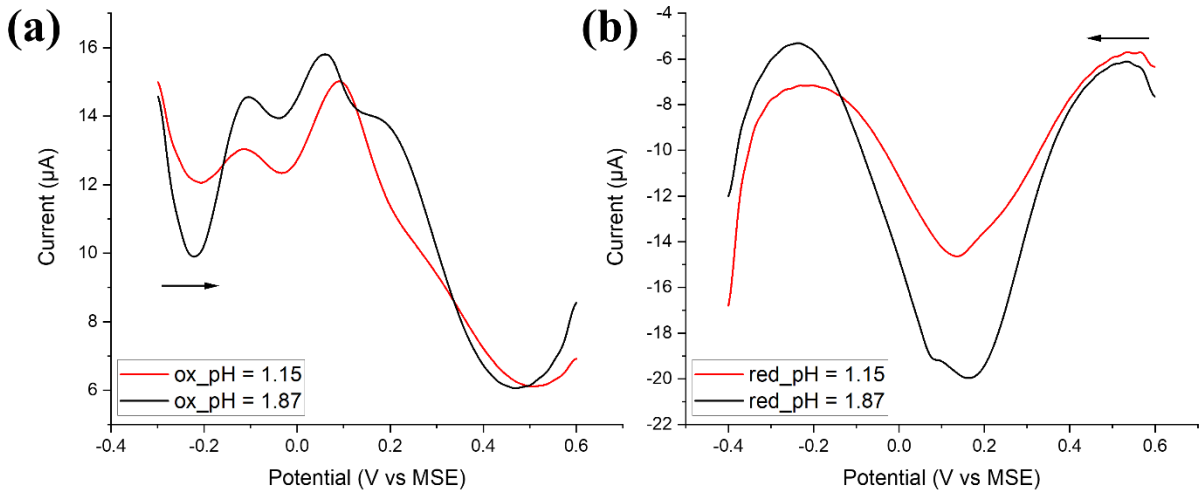

Figure.A3.5 Square wave voltammetry (frequency 90 Hz, step potential 1 mV, and amplitude 60 mV) response of iridium hydrous oxide on iridium wire electrode in HCl + 0.1 M KCl solutions with pH = 1.15 and 1.87 (a) oxidation and (b) reduction.

Section A3.6: The Effect of 0.1 M KCl in Pond Water on the pH Measurement Using a Fabricated Ir Wire.

This section presents the effect of adding 0.1 M KCl to pond water on the pH measurement using a fabricated Ir wire. Such effect was studied by comparing the 10th scan of cyclic voltammogram (Figure.A3.6 (a)) and the square wave voltammogram (Figure.A3.6 (b-c)) after CPE activation in pond water with (black line) and without KCl (red line) (pH=6.91). Each continuous scan using cyclic voltammetry was recorded from a starting potential of −0.6 V The scan was first swept anodically to 0.45 V vs MSE and then swept cathodically to −1.05 V vs MSE. SWVs were first scanned anodically from −0.6 V vs MSE for an oxidation reaction (Figure.A3.6 (b)) and then scans were immediately reversed for a reduction reaction (Figure.A3.6 (c)). No peak related to Ir (III/IV) transition was observed for either CV or SWV conducted in pond water without KCl addition, whereas clear redox peaks at ca. −0.2 V vs MSE were observed when 0.1 M KCl was added to pond water. The results demonstrate that the 0.1 M KCl added as supporting electrolytes to pond water is necessary for accurate pH measurement.

We suggest the added 0.1 M KCl supporting electrolyte ensures that the potential drop occurs within a distance within 10-20 Å of the working electrode surface, which is the distance for electron transfer between the electrode and the solution phase species by quantum mechanical tunnelling. The Debye length can be used to estimate how far the induced electric field of a charged electrode surface persists,

$$\kappa^{-1} = \frac{1}{\sqrt{8\pi\lambda_B N_A \times 10^3 \times I_{ion}}}$$

where λ_B is the Bjerrum length (m), N_A is the Avogadro constant and I_{ion} is ionic strength (M). Thus, adding KCl increases the ionic strength and leads to a decrease in Debye length, which screens the electrical field at the electrode and ensures that mass transport to and from the

electrode can be viewed as diffusion only. The undesirable migration causes complexities so that it is difficult to interpret the data even qualitatively at times. Therefore, the KCl addition is necessary for the accurate pH measurement of pond water as approached via amperometric methods.

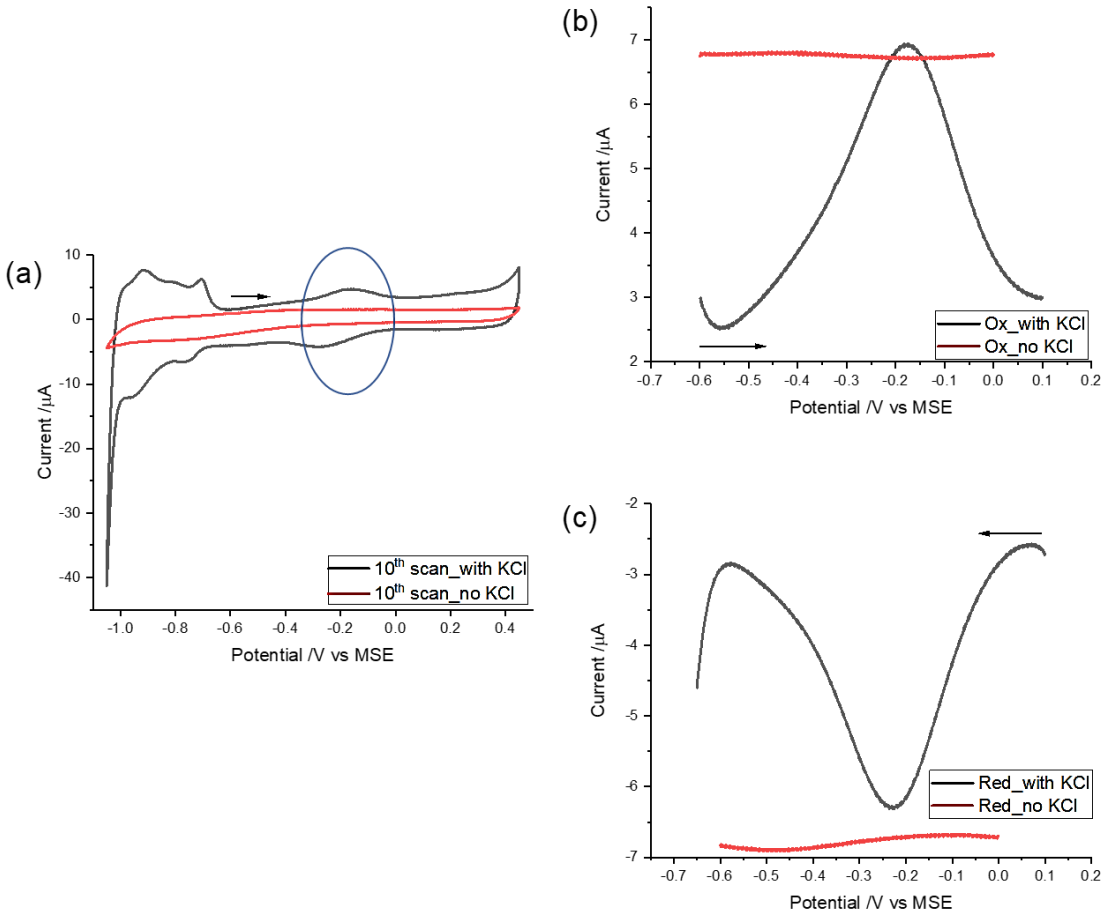

Figure.A3.6 (a) Overlaid cyclic voltammograms of the 10th cycle in degassed PBS solutions with (black line) and without (red line) 0.1 M KCl (pH=6.91) starting at a potential of −0.6 V at a scan rate of 0.5 Vs^{-1}. (b) Oxidation peaks (c)Reduction peaks obtained by square wave voltammetry (frequency 75 Hz, step potential 1 mV, and amplitude 60 mV) using an iridium wire after CPE activation in degassed PBS solutions with (black line) and without (red line) 0.1 M KCl (pH=6.91).

References

1. Y. Chen, X. Li, D. Li, C. Batchelor-McAuley and R. G. Compton, *Journal of Solid State Electrochemistry*, 2021, **25**, 2821-2833.
2. J. A. Kellum, *Critical Care*, 2000, **4**, 6.
3. J. H. Galla, *Journal of the American Society of Nephrology*, 2000, **11**, 369-375.
4. B. A. Mizock and J. Falk, *Critical Care Medicine*, 1992, **20**, 80-93.
5. J. P. Michaud, *A Citizien's Guide to Understanding and Monitoring Lakes and Streams*, Envirovision-Environmental Consulting Service, 1991.
6. D. M. Ragab, E. E. Babiker and A. H. Eltinay, *Food chemistry*, 2004, **84**, 207-212.
7. I. Mills, T. Cvitas and K. Homann, *Quantities, Units and Symbols in Physical Chemistry*, Blackwell Science Ltd, Oxford, 2nd edn., 1993.
8. R. P. Buck, S. Rondinini, A. Covington, F. Baucke, C. M. Brett, M. Camoes, M. Milton, T. Mussini, R. Naumann and K. Pratt, *Pure and Applied Chemistry*, 2002, **74**, 2169-2200.
9. F. Malatesta, *Journal of Solution Chemistry*, 2000, **29**, 771-779.
10. P. H. Rieger, *Electrochemistry*, Prentice Hall, United States, 1987.
11. M. Shibata, M. Kato, Y. Iwamoto, S. Nomura and T. Kakiuchi, *Journal of Electroanalytical Chemistry*, 2013, **705**, 81-85.
12. M. Shibata, H. Sakaida and T. Kakiuchi, *Analytical Chemistry*, 2011, **83**, 164-168.
13. A. L. Rockwood, *ChemPhysChem*, 2015, **16**, 1978-1991.
14. W. Vonau and U. Guth, *Journal of Solid State Electrochemistry*, 2006, **10**, 746-752.
15. D. A. Skoog, D. M. West, F. J. Holler and S. R. Crouch, *Fundamentals of Analytical Chemistry*, Cengage learning, 2013.
16. P. Spitzer and K. W. Pratt, *Journal of Solid State Electrochemistry*, 2011, **15**, 69-76.
17. K. Borsos and G. Inzelt, *Journal of Solid State Electrochemistry*, 2016, **20**, 1215-1222.
18. G. Inzelt and K. Borsos, *Studia Universitatis Babes-Bolyai, Chemia*, 2015, **60**, 23-30.
19. H. Kahlert, *Journal of Solid State Electrochemistry*, 2008, **12**, 1255-1266.
20. C. Aquino-Binag, P. J. Pigram, R. N. Lamb and P. W. Alexander, *Analytica Chimica Acta*, 1994, **291**, 65-73.
21. H. C. Leventis, I. Streeter, G. G. Wildgoose, N. S. Lawrence, L. Jiang, T. G. J. Jones and R. G. Compton, *Talanta*, 2004, **63**, 1039-1051.
22. G. G. Wildgoose, M. Pandurangappa, N. S. Lawrence, L. Jiang, T. G. J. Jones and R. G. Compton, *Talanta*, 2003, **60**, 887-893.
23. G. G. Wildgoose, H. C. Leventis, I. Streeter, N. S. Lawrence, S. J. Wilkins, L. Jiang, T. G. Jones and R. G. Compton, *ChemPhysChem*, 2004, **5**, 669-677.
24. F. Scholz, H. Düssel and B. Meyer, *Fresenius' Journal of Analytical Chemistry*, 1993, **347**, 458-459.
25. G. Hailin and L. Yucheng, *Sensors and Actuators B: Chemical*, 1994, **21**, 57-63.
26. O. LeBlanc, J. Brown Jr, J. Klebe, L. Niedrach, G. Slusarczuk and W. Stoddard Jr, *Journal of Applied Physiology*, 1976, **40**, 644-647.
27. K. Chaisiwamongkhol, C. Batchelor-Mcauley and R. G. Compton, *The Analyst*, 2017, **142**, 2828-2835.
28. M. A. Makos, D. M. Omiatek, A. G. Ewing and M. L. Heien, *Langmuir*, 2010, **26**, 10386-10391.
29. I. Streeter, H. C. Leventis, G. G. Wildgoose, M. Pandurangappa, N. S. Lawrence, L. Jiang, T. G. Jones and R. G. Compton, *Journal of Solid State Electrochemistry*, 2004, **8**, 718-721.

30. N. S. Lawrence, M. Pagels, S. F. Hackett, S. McCormack, A. Meredith, T. G. Jones, G. G. Wildgoose, R. G. Compton and L. Jiang, *Electroanalysis: An International Journal Devoted to Fundamental and Practical Aspects of Electroanalysis*, 2007, **19**, 424-428.
31. L. Xiong, C. Batchelor-McAuley and R. G. Compton, *Sensors and Actuators B: Chemical*, 2011, **159**, 251-255.
32. B. Gu, M.-J. Yin, A. P. Zhang, J.-W. Qian and S. He, *Opt. Express*, 2009, **17**, 22296-22302.
33. B. D. Gupta and S. Sharma, *Optics Communications*, 1998, **154**, 282-284.
34. J. I. Peterson, S. R. Goldstein, R. V. Fitzgerald and D. K. Buckhold, *Analytical Chemistry*, 1980, **52**, 864-869.
35. C. Munkholm, D. R. Walt, F. P. Milanovich and S. M. Klainer, *Analytical Chemistry*, 1986, **58**, 1427-1430.
36. J. Zhang and L. Zhou, *Sensors (Basel)*, 2018, **18**, 3195.
37. F. B. M. Suah, M. Ahmad and M. N. Taib, *Sensors and Actuators B: Chemical*, 2003, **90**, 182-188.
38. P. T. Sotomayor, I. M. Raimundo Jr, A. J. Zarbin, J. J. Rohwedder, G. O. Neto and O. L. Alves, *Sensors and Actuators B: Chemical*, 2001, **74**, 157-162.
39. H. Offenbacher, O. S. Wolfbeis and E. Fürlinger, *Sensors and Actuators*, 1986, **9**, 73-84.
40. O. S. Wolfbeis, N. V. Rodriguez and T. Werner, *Microchimica Acta*, 1992, **108**, 133-141.
41. N. Opitz and D. W. Lübbers, *Sensors and Actuators*, 1983, **4**, 473-479.
42. A.-S. Feiner and A. McEvoy, *Journal of Chemical Education*, 1994, **71**, 493.
43. W. Vonau, M. Decker, U. Enseleit and F. Gerlach, *Journal of Solid State Electrochemistry*, 2020, **24**, 3269-3277.
44. S. Głab, A. Hulanicki, G. Edwall and F. Ingman, *Critical Reviews in Analytical Chemistry*, 1989, **21**, 29-47.
45. E. Kinoshita, F. Ingman, G. Edwall, S. Thulin and S. Głąb, *Talanta*, 1986, **33**, 125-134.
46. G. Edwall, *Medical and Biological Engineering and Computing*, 1978, **16**, 661-669.
47. E. J. Roberts and F. Fenwick, *Journal of the American Chemical Society*, 1928, **50**, 2125-2147.
48. J. T. Stock, W. C. Purdy and L. M. Garcia, *Chemical Reviews*, 1958, **58**, 611-626.
49. C. R. Caflisch, L. R. Pucacco and N. W. Carter, *Kidney International*, 1978, **14**, 126-141.
50. E. Kinoshita, F. Ingman, G. Edwall and S. Glab, *Electrochimica Acta*, 1986, **31**, 29-38.
51. K. S. Kim, A. Gossmann and N. Winograd, *Analytical Chemistry*, 1974, **46**, 197-200.
52. B. Xu and W.-D. Zhang, *Electrochimica Acta*, 2010, **55**, 2859-2864.
53. A. Fog and R. P. Buck, *Sensors and Actuators*, 1984, **5**, 137-146.
54. C. Colombo, T. Kappes and P. C. Hauser, *Analytica Chimica Acta*, 2000, **412**, 69-75.
55. L. B. Kriksunov, D. D. Macdonald and P. J. Millett, *Journal of the Electrochemical Society*, 1994, **141**, 3002-3005.
56. L. T. Dimitrakopoulos, T. Dimitrakopoulos, P. W. Alexander, D. Logic and D. Brynn Hibbert, *Analytical Communications*, 1998, **35**, 395-398.
57. R. Cisternas, L. Ballesteros, M. L. Valenzuela, H. Kahlert and F. Scholz, *Journal of Electroanalytical Chemistry*, 2017, **801**, 315-318.
58. L. D. Burke, J. K. Mulcahy and D. P. Whelan, *Journal of Electroanalytical Chemistry and Interfacial Electrochemistry*, 1984, **163**, 117-128.
59. J. A. Mihell and J. K. Atkinson, *Sensors and Actuators B: Chemical*, 1998, **48**, 505-511.
60. K. G. Kreider, M. J. Tarlov and J. P. Cline, *Sensors and Actuators B: Chemical*, 1995, **28**, 167-172.

61. M. J. Avena, O. R. Cámara and C. P. De Pauli, *Colloids and Surfaces*, 1993, **69**, 217-228.
62. E. M. Guerra and M. Mulato, *Materials Sciences and Applications*, 2014, **05**, 459-466.
63. R. D. C. Campos, D. T. Cestarolli, M. Mulato and E. M. Guerra, *Materials Research*, 2015, **18**, 15-19.
64. M. Jamal, K. M. Razeeb, H. Shao, J. Islam, I. Akhter, H. Furukawa and A. Khosla, *Scientific Reports*, 2019, **9**, 4659.
65. K. Chaisiwamongkhol, C. Batchelor-Mcauley and R. G. Compton, *The Analyst*, 2019, **144**, 1386-1393.
66. D. O'Hare, K. H. Parker and C. P. Winlove, *Medical Engineering & Physics*, 2006, **28**, 982-988.
67. *UK Pat.*, WO/2020/217056, 2020.
68. W. Olthuis, M. A. M. Robben, P. Bergveld, M. Bos and W. E. Van Der Linden, *Sensors and Actuators B: Chemical*, 1990, **2**, 247-256.
69. M. J. Tarlov, S. Semancik and K. G. Kreider, *Sensors and Actuators B: Chemical*, 1990, **1**, 293-297.
70. S. Yao, M. Wang and M. Madou, *Journal of the Electrochemical Society*, 2001, **148**, H29.
71. S. Bause, M. Decker, F. Gerlach, J. Näther, F. Köster, P. Neubauer and W. Vonau, *Journal of Solid State Electrochemistry*, 2018, **22**, 51-60.
72. W. C. Dautremont-Smith, *Displays*, 1982, **3**, 67-80.
73. C. M. Lampert, *Solar Energy Materials*, 1984, **11**, 1-27.
74. W. C. Dautremont-Smith, G. Beni, L. M. Schiavone and J. L. Shay, *Applied Physics Letters*, 1979, **35**, 565-567.
75. I. Lauks, M. Yuen and T. Dietz, *Sensors and Actuators*, 1983, **4**, 375-379.
76. B. Conway and J. Mozota, *Electrochimica Acta*, 1983, **28**, 9-16.
77. J. Mozota and B. Conway, *Journal of the Electrochemical Society*, 1981, **128**, 2142–2149.
78. S. Siracusano, V. Baglio, S. A. Grigoriev, L. Merlo, V. N. Fateev and A. S. Aricò, *Journal of Power Sources*, 2017, **366**, 105-114.
79. V. Pfeifer, T. E. Jones, J. J. Velasco Velez, C. Massue, M. T. Greiner, R. Arrigo, D. Teschner, F. Girgsdies, M. Scherzer, J. Allan, M. Hashagen, G. Weinberg, S. Piccinin, M. Havecker, A. Knop-Gericke and R. Schlogl, *Physical Chemistry Chemical Physics*, 2016, **18**, 2292-2296.
80. V. Pfeifer, T. E. Jones, J. J. Velasco Velez, R. Arrigo, S. Piccinin, M. Havecker, A. Knop-Gericke and R. Schlogl, *Chemical Science*, 2017, **8**, 2143-2149.
81. J. E. Baur and T. W. Spaine, *Journal of Electroanalytical Chemistry*, 1998, **443**, 208-216.
82. A. Salimi, M. E. Hyde, C. E. Banks and R. G. Compton, *Analyst*, 2004, **129**, 9-14.
83. T. Katsube, I. R. Lauks, J. van der Spiegel and J. N. Zemel, *Japanese Journal of Applied Physics*, 1983, **22**, 469.
84. M. L. Hitchman and S. Ramanathan, *Analyst*, 1991, **116**, 1131-1133.
85. P. G. Pickup and V. I. Birss, *Journal of the Electrochemical Society*, 1988, **135**, 41.
86. T. Y. Kim and S. Yang, *Sensors and Actuators B: Chemical*, 2014, **196**, 31-38.
87. C. Nguyen, S. Rao, X. Yang, S. Dubey, J. Mays, H. Cao and J.-C. Chiao, *Sensors*, 2015, **15**, 4212-4228.
88. W.-D. Huang, H. Cao, S. Deb, M. Chiao and J. C. Chiao, *Sensors and Actuators A: Physical*, 2011, **169**, 1-11.
89. L. Kuo, Y. Chou, K. Chen, C. Lu and S. Chao, *Sensors and Actuators B: Chemical*, 2014, **193**, 687-691.

90. M. Wang, S. Yao and M. Madou, *Sensors and Actuators B: Chemical*, 2002, **81**, 313-315.
91. X. Chen, C. He, C. Du, X. Li and M. Wu, *Journal of University of Science and Technology Beijing*, 2011, **2**.
92. V. Pfeifer, T. E. Jones, J. J. Velasco Vélez, C. Massué, R. Arrigo, D. Teschner, F. Girgsdies, M. Scherzer, M. T. Greiner, J. Allan, M. Hashagen, G. Weinberg, S. Piccinin, M. Hävecker, A. Knop-Gericke and R. Schlögl, *Surface and Interface Analysis*, 2016, **48**, 261-273.
93. P. G. Pickup and V. I. Birss, *Journal of Electroanalytical Chemistry and Interfacial Electrochemistry*, 1987, **220**, 83-100.
94. L. D. Burke and D. P. Whelan, *Journal of Electroanalytical Chemistry and Interfacial Electrochemistry*, 1984, **162**, 121-141.
95. L. D. Burke and E. J. O'Sullivan, *Journal of Electroanalytical Chemistry and Interfacial Electrochemistry*, 1978, **93**, 11-18.
96. S. Hadzi-Jordanov, H. Angerstein-Kozlowska, M. Vukovic and B. Conway, *The Journal of Physical Chemistry*, 1977, **81**, 2271-2279.
97. F. Colom, J. H. Gonzalez and J. Peinado, *Journal of Electroanalytical Chemistry and Interfacial Electrochemistry*, 1978, **89**, 397-406.
98. L. Burke and D. Whelan, *Journal of Electroanalytical Chemistry and Interfacial Electrochemistry*, 1982, **135**, 55-65.
99. S. Gottesfeld and J. McIntyre, *Journal of the Electrochemical Society*, 1979, **126**, 742.
100. M. L. Hitchman and S. Ramanathan, *Analyst*, 1988, **113**, 35-39.
101. M. Peuckert, *Surface science*, 1984, **144**, 451-464.
102. J. L. Taylor, D. E. Ibbotson and W. H. Weinberg, *Surface Science*, 1979, **79**, 349-384.
103. N. Dubouis and A. Grimaud, *Chemical Science*, 2019, **10**, 9165-9181.
104. G. Jerkiewicz, *Electrocatalysis*, 2010, **1**, 179-199.
105. G. Jerkiewicz, G. Vatankhah, J. Lessard, M. P. Soriaga and Y.-S. Park, *Electrochimica Acta*, 2004, **49**, 1451-1459.
106. L. D. Burke, M. E. Lyons, E. J. M. O'Sullivan and D. P. Whelan, *Journal of Electroanalytical Chemistry and Interfacial Electrochemistry*, 1981, **122**, 403-407.
107. S. Carroll and R. P. Baldwin, *Analytical Chemistry*, 2010, **82**, 878-885.
108. H. Angerstein-Kozlowska, B. E. Conway and W. B. A. Sharp, *Journal of Electroanalytical Chemistry and Interfacial Electrochemistry*, 1973, **43**, 9-36.
109. P. Zhdan, G. Boreskov, A. Boronin, W. Egelhoff Jr and W. Weinberg, *Surface Science*, 1976, **61**, 25-36.

Chapter 4

A Calibration-Free pH Sensor Using an In-Situ Modified Iridium Electrode for Bespoke Application in Seawater

Building on the results presented in the previous chapter, in **Chapter 4**, a bespoke calibration-free pH sensor using an in-situ modified Ir electrode for applications in seawater is reported. The electrochemical behaviour of an iridium wire in air-saturated synthetic seawater was studied and the formation of pH-sensitive surface layers was observed that featured three pH-sensitive redox couples, Ir(III/IV), $IrO_xO^{I-}/IrO_xO^{II-}H$, and H_{upd}/H^+, where H_{upd} is adsorbed hydrogen deposited at underpotential conditions. The amperometric properties of the electrochemically activated Ir wire were investigated using linear sweep voltammetry first, followed, second, by square wave voltammetry with the formation conditions in seawater for the optimal pH sensitivity of the redox couples identified. The sensor was designed to be calibration-free by measuring the "super-Nernstian" response, in excess of ca 60 mV per pH unit, of Ir(III/IV) relative to the less sensitive upd H oxidation signal with the pH reported on the total hydrogen ion scale. The pH dependency of the optimised sensor was 70.1 ± 1.4 mV per pH unit at 25 °C, showing a super-Nernstian response of high sensitivity.

The work of **Chapter 4** has been published in the journal *Sensors* [1].

4.1 Introduction

As discussed in **Chapter 3**, pH measurements in chemistry are ubiquitous. As defined by IUPAC [2], pH is a function of the activity of the hydrogen ion in a solution:

$$\boldsymbol{pH = -\log a_{H^+} = -\log\left(\frac{m_{H^+}\gamma_{H^+}}{m^{\theta}}\right)} \qquad (4.1)$$

where a_{H^+} is the single ion activity (measured on the molality scale in mol kg^{-1}), γ_{H^+} is the activity coefficient of the hydrogen ion (H^+) at a molality of m_{H^+}, and m^{θ} is the standard

molality (1 mol kg^{-1}). Note that the pH is defined by IUPAC in terms of the single ion quantities and so IUPAC regard Eqn. (4.1) as a 'notional definition'. Historically, the development of primary pH standards utilised a 'primary method of measurement' that is based on the Harned cell, which comprises a hydrogen electrode and a silver/silver-chloride electrode in a cell containing hydrochloric acid electrolyte and without a liquid junction [3]. Debye–Hückel theory [4] is used for the required chloride ion activity coefficient estimation via the Bates–Guggenheim convention [5] with the latter restricted to ionic strengths of less than 0.1 mol kg^{-1}. This leads to uncertainties of at least 0.003 in pH. It is noteworthy that the seawater has a high ionic strength (I~0.7 mol kg^{-1}) [6] so that pH measurements in seawater are expected to require specific procedures.

Seawater comprises about 97.2 percent of the Earth's known water and covers approximately 71 percent of its surface. Seawater compositions vary with their biological content, as well as reflecting local coastal industry and geology [7]. pH is an important oceanographic parameter, which is essential for investigating the dynamic state of the chemical and biological processes. First, there is a close interplay between pH, chlorophyll-a (chl-a), and dissolved oxygen (DO) [8]. The pH value of seawater is normally 8.1 but can be higher for eutrophic waters [9] because of the emission of nitrogen- and phosphorous-containing species resulting from human activities [10]. While a high pH may inhibit the photosynthesis of algae [11, 12], chl-a is an important indicator for the presence of algae, notably for assessing eutrophication. pH variations can thus reflect direct changes in chl-a concentration [8]. Second, and of current vital importance, the pH of seawater is a significant reference for ocean acidification as a result of carbon emission and reflects its ecological effects [10, 13]. Carbon uptake via seawater is a major sink of CO_2, during which the formation of carbonic acid from atmospheric carbon dioxide lowers the pH of seawater (Eqn. (4.2)). For example, the pH of seawater is thought to have decreased from 8.2 before the Industrial Revolution in Western Europe to about 8.1 today [10].

$$CO_2 + H_2O \rightarrow H_2CO_3 \quad (4.2)$$

Meanwhile, carbonate in seawater is important for marine life to build shells and skeletons. Under conditions of severe acidification, shells and skeletons can dissolve (Eqn. (4.3)).

$$2H^+ + CaCO_3 \rightarrow Ca^{2+} + H_2O + CO_2 \quad (4.3)$$

Third, pH is also directly linked to the solubility of heavy metals. [14, 15] The lower the pH, the more toxic the water possibly is as the metals tend to be more soluble. Thus, significant attention needs to be paid to the pH variation of seawater in order to maintain the environmental ecological balance.

The concept and measurement of pH was initiated over a century ago [16] by Sorensen working in the Carlsberg Laboratory (Copenhagen, Denmark), leading ultimately to the IUPAC definition. The latter, however, is not recommended for seawater because of its high ionic strength. Instead, three scales were developed using proton concentration scales rather than the activity scale as defined by IUPAC [17-21]. Specifically, the three scales are the free hydrogen ion scale (Eqn. (4.4)), the total hydrogen ion scale (Eqn. (4.5)) and the seawater scale.

The free hydrogen ion scale [22-24] is defined by:

$$pH_F = -\log m_{H^+} \quad (4.4)$$

where the total amount of H^+ is calculated in terms of its concentration (molality) rather than activity. In contrast, the total hydrogen ion scale accounts better for the complex chemical environment of seawater in which SO_4^{2-} ions, if present, can react with H^+ to form the ion HSO_4^- [18, 25], so in terms of the addition of HCl, the resulting H^+ concentration is less since some protons form HSO_4^-. With this definition:

$$\boldsymbol{pH_T = -\log m_{H^+} - \log m_{HSO4^-} = -\log\left\{m_{H^+}[1 + \frac{m(SO_4^{2-})}{K(m_{HSO_4^-})}]\right\}} \qquad (4.5)$$

where $m_{SO_4^{2-}}$ is the stoichiometric concentration of sulphate and $K(HSO_4^-)$ is the dissociation constant for bisulphate ion [17, 20, 24, 26, 27].

The seawater scale recognises the possible presence of both sulphate and fluoride ions [26, 28], but this scale was suggested to be unhelpful by Dickson [29] in 1993, stating that fluoride should simply be treated as a minor acid base species [17]. Nevertheless, in reporting seawater measurement data, it is necessary to state which units and scales are used.

Millero et al. [17] proposed an experimental approach in which pH was studied in terms of the proton concentration with a unit of kg-H_2O^{-1}, while the buffers were prepared in seawater using Bis(2-amino-2-methyl-1,3-propaneldiol), Tris(2-amino-2-hydroxymethyl-1,3-propaneldiol), Morpholine, or 2-Aminopyridine referring to the recipes suggested by Bates and co-workers [22, 30-32]. Then, the corresponding potentials of the buffers with different pH were measured with a Harned cell approach and the resultant pH values were in good agreement with the total hydrogen ion scale. [29, 30] Bates's work provided a good insight for the results discussed below; Tris/HCl buffers prepared in synthetic seawater are applied for the experiments reported later in this paper.

In addition to optical fibre sensing applied for marine environment monitoring [33], spectrophotometry is commonly used to measure the pH of seawater [34, 35]. Spectrophotometry is based on different absorbance characteristics of the basic and acidic forms of sulfonephthalein indicators, L^{2-} and HL^- (from the secondary dissociation $HL^- \overset{K_2}{\leftrightarrow} H^+ + L^{2-}$), the relative amounts of which alter measurably within the range of pH values seen in normal seawater environments. The selection of the specific indicator used, commonly a sulfonephthalein derivative, [36] is decided by the specific pH range of candidate analyte. The log of the secondary dissociation constant (log K_2) of the sulfonephthalein indicator should be

comparable to the expected pH of the sample solution, i.e., ($\log K_2$ (indicator) − 1) < pH (sample) ≤ $\log K_2$ (indicator) [35, 37]. For example, bromocresol green ($K_2 \approx 10^{-4.4}$) [37, 38] is appropriate for acidified samples used in determinations of seawater alkalinity [39], while thymol blue ($K_1 \approx 10^{-8.6}$) [40] is most appropriate for surface waters, where generally 7.90 ≤ pH ≤ 8.40 [35, 41]. The relationship between the pH and the measured parameters is represented by Eqn. (4.6):

$$\boldsymbol{pH = pH_2 + \log[L^{2-}]/[HL^{-}] = pH_2 + \log\left(\frac{A_\lambda - A_{\lambda_{Min}}}{A_{\lambda_{Max}} - A_\lambda}\right)} \qquad (4.6)$$

where $pH_2 = -\log K_2$, K_2 is the HL^- dissociation constant; A_λ is the absorbance at wavelength λ and is related to pathlength (l), total indicator concentration (D_T) and molar absorbance (a_λ) through the well-known Beer-Lambert relationship $A_\lambda = a_\lambda * D_T * l$ [37, 40].

It is noteworthy that spectrophotometry can realise measurements to within ± 0.001 pH units while potentiometry has a precision no better than ± 0.02 pH units depending on multiple parameters [19, 42]. In terms of potentiometric techniques for pH sensing, a H^+ ion-selective glass electrode-based pH meter is common in the laboratory. However, it requires regular calibrations by standard buffers. More importantly, the use of low ionic strength buffers to calibrate a glass electrode for use in high ionic strength solutions, namely seawater, may cause errors [18, 20]. Beyond the glass pH meter, in the case of potentiometric titrations, an all-solid-state ion-selective electrode (ISE), with functionalised multiwalled carbon nanotubes being drop casted on a glassy carbon electrode, were developed by Cuartero et al. [43]. This ISE was applied in a 600 mM NaCl to mimic seawater environments. However, similarly to the glass pH meter, calibrations are recommended to be made every hour prior to and during the measurements to compensate for electrode drift and for changes in temperature. Finally, pH is calculated referring to the measured potential E using the calibrated linear relationship (Eqn. (4.7)):

$$E = E^0 + s \times \log[a_1(H^+)] \qquad (4.7)$$

where the slope s is equal to $2.303 \times \frac{RT}{zF}$ (R is the gas constant, T is the temperature, z is the charge of the ion, and F the Faraday constant) based on the Nernst equation [43].

Even when conducted with the greatest expertise and diligence, potentiometry simply reports a single number from which it is often difficult, if not impossible, to ascertain the quality or validity of the measurement (Figure.4.1). This consideration is especially important in complex matrixes such as seawater and blood where electrode fouling is often encountered. In response to this need, we have suggested the use of amperometry/voltammetry where the response in the form of a current-voltage plot allows for a measure of the quality of response to be judged [44-47]. The concept is shown schematically in Figure.4.1 from which it is apparent that the peak shape and width allow for a measure of measurement 'quality' and for deciding whether the electrode needs to be repositioned, cleaned, or replaced. For example, as shown by the right part of Figure.4.1, the black voltammogram obtained by amperometry is better-defined than the red one and the associated measurement is more reliable.

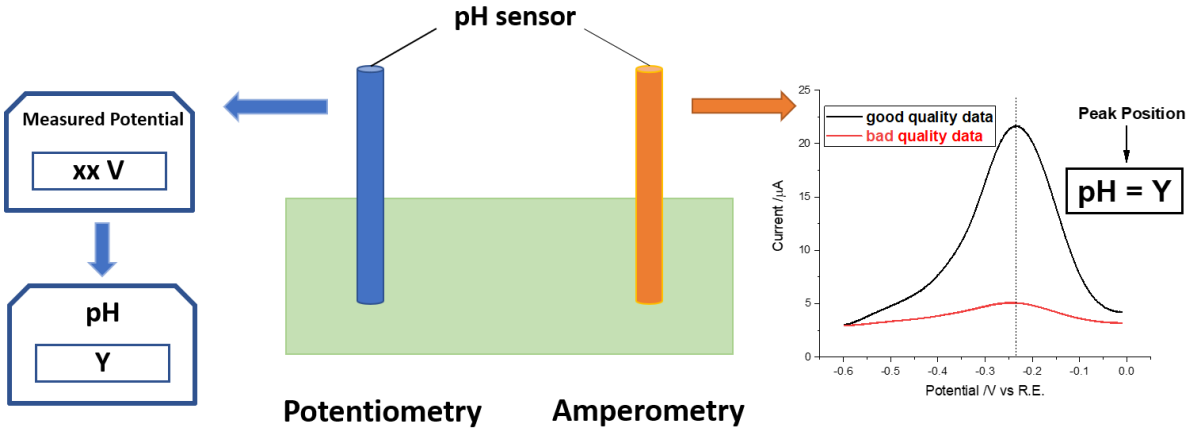

Figure.4.1 ***A schematic diagram to contrast potentiometric and amperometric measurements (see text).***

Whilst amperometric pH sensors have found wide application [48-54], there has been only limited application of amperometric pH measurements in seawater, although Sisodia et al. [55]

recently reported an electropolymerised 2-(methylthio)phenol modified glassy carbon based electrode as an voltammetric pH sensor in seawater that had a sub-Nernstian response in buffers (pH = 4–9.2) of 51 mV/pH unit.

In this chapter, we develop a metal oxide electrode for amperometric pH detection based on pH-sensitive anodic iridium oxide film (AIROF) synthesised by cyclic voltammetry in seawater on the surface of an iridium wire. Noteworthy, as discussed in the previous chapter, is that in contrast to the iridium oxide with a near-Nernstian response (ca. 60 mV per pH unit) prepared by other methods, e.g., sol-gel [56, 57] chemistry, sputtering [58, 59], and thermal methods [60, 61], AIROF formed on the bespoke electrode is able to respond with a super-Nernstian slope as reported [62-64]. The observed pH responses are summarised in Table A4.1. [89, 90] Secondly, the bespoke sensor is calibration-free. All the electrochemical reactions investigated in this project take place in a three-electrode system [65]. The basis of calibration-free amperometric pH measurement is the recording of two or more voltammetric peaks with different sensitivity to pH. Then the *difference* of the associated peak potentials, if measured in the same voltammogram at essentially the same time, is independent of any drift for example in the reference potential [48, 51, 66, 67]. In the case of the iridium wire-based sensors, the analytical pH responses arise from the pH dependency of the potential of the strongly pH sensitive $Ir^{3+/4+}$ redox couple measured relative to the much less pH-sensitive hydrogen underpotential re-oxidation. As the potentials of these redox reactions are collected during one measurement and only the *relative* potentials between them are used analytically, the stability and accuracy of the reference electrode are not important. Linear sweep voltammetry was investigated first, followed by square wave voltammetry to explore the relative sensitivity of the pH dependency to the two techniques. The super-Nernstian relationship coupled with the capability of assessing the measurement quality imply the validity and merit of the bespoke sensor.

4.2 Experimental

Chemicals and Reagents

Solutions were prepared using deionised water with a resistivity of 18.2 MΩ cm at 298 K (Millipore, Millipak Express 20, UK). All chemicals were of analytical grade and were used as received without any further purification. Three synthetic seawater samples with defined pH values were prepared for the calibration of a HACH LANGE Sension^{+} PH31 pH meter, one of 2-Amino pyridine, Tris(hydroxymethyl) Aminomethane, and 2-Amino-2-methyl-1,3-propanediol was dissolved in synthetic seawater separately with a molarity of 0.08 M, with the corresponding pH values of 'standard seawater buffers' being defined as 6.77, 8.07 and 8.81, respectively. These solutions have been shown to give good correlation with the total hydrogen ion scale as discussed above [17, 29]. The composition of synthetic seawater and corresponding buffers is presented in Table 2.1 following a literature recipe [29]. To study the pH dependency of the bespoke electrode, synthetic seawater samples were prepared with their pH values adjusted by adding a trace of HCl. Details of the chemicals and reagents were listed in Section 2.1.

Table 4.1 Chemical composition of synthetic seawater

	Constituent	Moles	Weight/g in 0.5 L	Final pH
Synthetic Seawater	NaCl	0.388	11.32	N/A
	KCl	0.011	0.39	
	$MgCl_2$	0.055	2.61	
	$CaCl_2$	0.011	0.6	
	Na_2SO_4	0.029	2.08	
	HCl	0.04	1.73 (mL in vol.)	
One of:	2-Aminopyrine	0.08	3.76	6.77
	Tris	0.08	4.84	8.07
	Bis	0.08	4.2	8.81

Electrochemical Apparatus

Electrochemical measurements were performed using a μAutolab II potentiostat (Metrohm-Autolab BV, The Netherlands). A standard three-electrode set-up was used, consisting of a saturated calomel reference electrode (SCE + 0.244 V vs SHE, BASi Inc., USA), a graphite rod counter electrode, and an iridium wire (0.1 mm in diameter, GoodFellow, UK) as the working electrode. The Ir electrode was pretreated by heating the metal using a Bunsen burner for 10 s to remove surface contamination and impurities. The electrochemical set up was thermostated at a constant value of 25.0 ± 0.2 °C. High purity N_2 flow (BOC Gases plc, U.K.) was used to remove oxygen from aqueous solutions as needed prior to the electrochemical measurements. Cyclic voltammetry (CV) was used to study the electrochemical behaviour of the Ir electrode and for the potential cycling activation. Linear sweep voltammetry (LSV) and square wave voltammetry (SWV) were conducted to determine the pH dependency of in situ modified Ir wire after a potential cycling activation.

4.3 Results and Discussion

In the following sections, we first analyse the voltammetry of an iridium wire in synthetic seawater under conditions of controlled pH. We demonstrate that it is possible to reproducibly form layers of iridium oxide in synthetic seawater and assign the various pH-sensitive redox couples, which are subsequently used as the basis for the amperometric calibration-free pH sensing without the need for any degassing to remove dissolved oxygen. Next, potential cycling is developed as a simple method of electrode activation directly within seawater and this is optimised in terms of the potential range used. Further optimisation of the pH sensor is made in respect of recording the various relevant redox couples pertinent to pH measurements and characterising the corresponding pH dependency of a calibration-free sensor. Linear sweep voltammetry was investigated first, followed by square wave voltammetry to improve sensitivity and precision.

4.3.1 Cyclic Voltammetry of Iridium and Iridium Oxides

Cyclic voltammetry was conducted to study the formation of iridium hydrous oxides on the surface of an iridium wire and other redox reactions that occur during potential cycling. It was discovered, as discussed in the previous chapter, that to ensure reproducible data, the surface of the Ir wire should be free of oxide prior to voltammetric measurements. Accordingly, as reported in previously [47], the Ir surface was treated by pre-flaming to renew the surface of the metal electrode between experiments. To explore the voltammetric behaviour of an Ir wire and the effect of degassing, the pre-flamed Ir electrode was first immersed in air-saturated synthetic seawater buffered by Tris(hydroxymethyl) Aminomethane/HCl to give a pH close to typical natural seawater (8.1 [10]), and then the same process was repeated in a degassed solution. Cyclic voltammetry was conducted for 100 cycles starting at a potential of −0.2 V vs SCE with scan reversal at a potential of 0.9 V with a subsequent sweep to −0.8 V vs SCE where the potential was again reversed as shown in Figure.4.2 (a). In Figure.4.2 (b), the 40th scan of cyclic voltammograms obtained in synthetic seawater with and without degassing are overlaid. In Figure.4.2 (a), this procedure leads to the steady build-up of a surface layer, the thickness of which increases with each potential cycle. This has been explained by the mechanism reported in the previous chapter and elsewhere [47]. These redox features display in conventional electrolytes [68-70] and are closely mirrored in the data obtained in seawater. In Figure.4.2 (b), comparison of the data with and without degassing shows no difference of peak shape or numbers of peaks between the two, with four clearly discernible voltammetric features labelled as A, B, C, and D. This implies that degassing has no effect on the voltammetry and represents an important step in respect of developing amperometric pH measurements for direct use in seawater without the need for removal of oxygen from dissolved air.

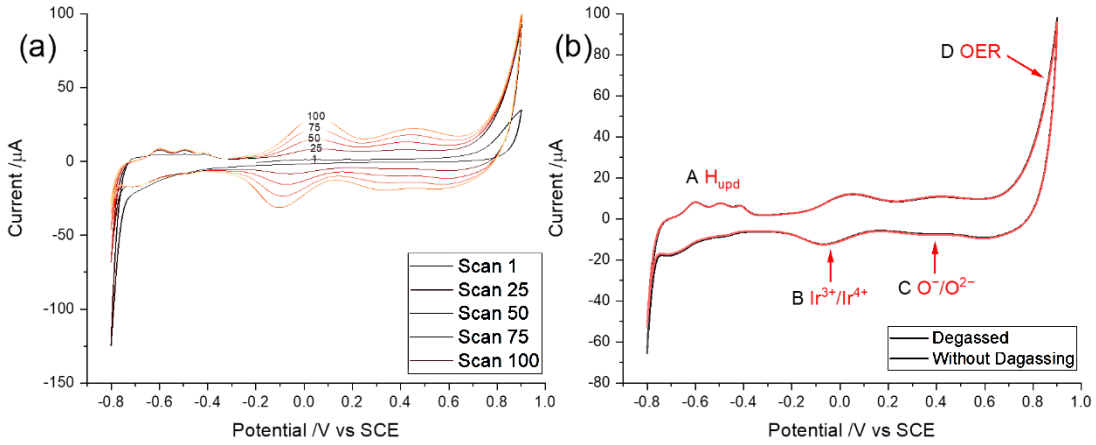

Figure.4.2 (a) Cyclic voltammograms showing the activation of an Ir wire at a scan rate of 0.5 V s^{-1} for multiple cycles. The start potential was −0.2 V vs SCE in air-saturated synthetic seawater with pH = 8.1. (b) Overlaid 40th cyclic voltammograms in synthetic seawater with pH = 8.1 using an Ir wire at a scan rate of 0.5 Vs^{-1}; degassed: black line, without degassing: red line.

Feature A was assigned to the re-oxidation of underpotential deposited (UPD) adsorbed hydrogen, H_{upd}, formed at very negative potentials (more negative than −0.32 V vs SCE). It is notable that it is a one proton–one electron transfer reaction with the reductive formation described by Eqn. (4.8) and the oxidative desorption by Eqn. (4.9) [71-74]:

$$M(s) + H_3O^+ + e^- \rightleftharpoons M - H_{ad} + H_2O \rightleftharpoons \frac{1}{2}H_2 + M - H_2O_{ad} \quad (4.8)$$

$$M - H_{ad} \rightleftharpoons H^+ + e^- + M \quad (4.9)$$

where M is an empty adsorption site on the surface.

Feature B was attributed to the Ir(III/IV) redox transition associated with the formation of hydrous oxides [47, 69, 70, 75], where the oxidation peak is at a potential of ca 0.08 V vs SCE and the reduction peak is at ca −0.04 V vs SCE. Note that this process involves various possible redox reactions and the exact stoichiometric composition of the hydrous film is reported as hard to determine [46, 64, 76]. The number of electrons and protons transferred during the redox process is with a ratio of 2:3 leading to a "super-Nernstian" pH dependency of ca 89 mV per pH unit [46, 77, 78], as implied in the reaction suggested by Olthuis *et al.* [64]:

$$\boldsymbol{Ir_2O(OH)_3O_3^{3-} + 3H^+ + 2e^- \rightleftharpoons 2Ir(OH)_2O^- + H_2O} \qquad (4.10)$$

where "super-Nernstian" means a response of greater than 60 mV per pH unit. The average transfer of 1.5 protons per electron are understood in terms of two iridium ions each gaining an electron and the associated oxide ions gaining three protons. Note that the redox reaction between $Ir_2O(OH)_3O_3^{3-}$ and $Ir(OH)_2O^-$ is denoted as Ir(III/IV) for simplification in this paper.

Feature C shows an oxidation peak at about 0.42 V with the corresponding reductive peak at 0.37 V vs SCE. Pickup *et al.* [79] and Kasian *et al.* [80] suggested that the redox couple in Feature C can be attributed to further oxidation of the Ir hydrous oxides, e.g., from Ir (IV) to Ir (V/VI), while Pfeifer *et al.* [69,70,75] assigned it to the oxidation of the oxide anion O^{2-}, contained in the IrO_x matrix in form of adsorbed OH groups, to O^-:

$$\boldsymbol{IrO_xO^{II-}H \rightleftharpoons IrO_xO^{I-} + H^+ + e^-} \qquad (4.11)$$

Feature D is related to the oxygen evolution reaction (OER) [69]:

$$\boldsymbol{2H_2O \rightarrow O_2 + 4H^+ + 4e^-} \qquad (4.12)$$

It is noteworthy that the four features are all pH sensitive but have different pH dependencies, which is significant for the development of a bespoke pH sensor for seawater in respect to facilitating calibration-free measurements below.

4.3.2 Optimisation of Potential Cycling Activation

The different redox processes encountered during potential cycling were identified and explained in the previous section. To obtain better resolved pH-sensitive redox couples and improve the sensitivity in respect of pH detection, the most effective potential range of potential cycling was studied in the following. To be specific, the effect of the cathodic limit potential was investigated first, followed by that of the anodic limit potential.

As shown in Figure.4.3 (a), cyclic voltammograms with different potential range using a pre-flamed Ir wire were measured at a scan rate of 0.5 V s^{-1} in an air-saturated Tris/HCl solution

prepared in synthetic seawater (pH = 8.14). Note that as the potential range shifts as pH changes, conducting the optimisation in synthetic seawater of a typical and average pH results in a potential range applicable to a wide range of seawaters, the pH of which can vary from 7.5 to 8.5 depending on the local conditions [42]. The cyclic voltammetry starts at a potential of −0.2 V and is first swept anodically to a fixed potential of 0.9 V, then swept to different cathodic limits varying from −0.8 V to −0.6 V vs SCE. To find the optimised cathodic potential, the 40th cycles of each voltammogram were displayed in Figure.4.3 (a). Figure.4.3 (b) shows the 40th scans of the CVs with the cathodic potential being fixed at −0.8 V, while the anodic potential was progressively increased to 0.7 V from 0.9 V vs SCE.

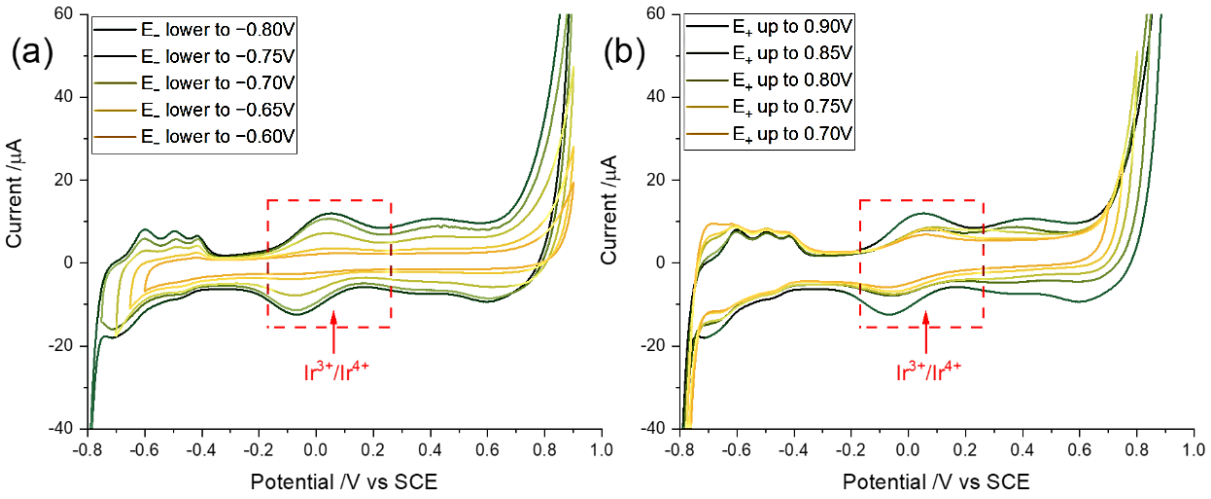

Figure.4.3 ***Cyclic voltammograms of the 40th cycle SCE in air-saturated synthetic seawater with pH = 8.14 starting at a potential of −0.2 V for activation of an Ir wire with different (a) cathodic and (b) anodic potentials at a scan rate of 0.5 Vs^{-1}.***

The signal to the background level of the most dominant Ir(III/IV) redox couple is assigned to be the reference for determining the effectiveness of the potential range as it is the best defined and most prominent. The effectiveness was judged on the basis that the higher the signal to background level, the better for pH detection. In Figure.4.3 (a), the redox couple of the 40th cycle becomes better defined with a reductive limit of −0.8 V whilst, in Figure.4.3 (b), the highest resolution is achieved with an anodic potential limit extended to 0.9 V. It is significant

that the anodic limit has a greater effect on Feature C compared to the cathodic limit. To be more specific, the trend for Feature C to disappear was more obvious as the anodic side was narrowed while the Feature B stayed relatively constant. Pfeifer et al. [69] reported that the IrO_xO^{I-} formed during the redox reaction in Feature C is the catalyst for OER (Eqn. (4.13))):

$$\boldsymbol{IrO_xO^{I-} + H_2O \rightarrow IrO_xO^{I-} - O^{I-} - H + H^+ + e^- \rightarrow IrO_x + O_2 + 2H^+ + 3e^-} \quad (4.13)$$

Thus, the redox feature of interest correlates with the onset of the ORR. Meanwhile, the trend of signal to background level improvement gets less significant when the potential limit is extended either more anodically or cathodically, consistent with literature reports [79, 81]. Noting that Pickup et al. [79] reported that the hydrous oxide begins to dissolve when more positive potentials were applied, so no further extension of the potential window was explored. Considering the data in Figure.4.3, we infer from potential sweeps within the ranges (A) −0.6 V to −0.8 V (H_{upd} region) and (B) 0.7 V to 0.9 V (OER region) that both are important for the growth of the Ir hydrous oxide. To be specific, anodic sweeps to 0.9 V and cathodic to −0.8 V vs SCE must be embraced by the potential window, so that the in-situ fabrication method of an Ir wire responds well to pH.

4.3.3 pH Dependency of the Voltammetric Responses of the Iridium Hydrous Oxide Layers

Following the activation of the Ir wire by potential cycling under the potential range optimised above, next the pH dependencies of the two redox signals within the iridium hydrous oxide layer ($Ir^{3+/4+}$, $IrO_xO^{I-}/IrO_xO^{II-}H$) and the H underpotential deposition are investigated for the pH range 7.5–8.5 in this section. Linear sweep voltammetry (LSV) was first applied, followed by square wave voltammetry (SWV) to explore the relative sensitivity of the pH dependency of the two techniques.

Linear Sweep Voltammetry

Prior to the measurements, the pH of buffers with values 7.50–8.50 were measured with a pH meter calibrated by 'standard seawater buffers', which were defined as discussed above, using the total hydrogen ion scale. LSVs were first scanned cathodically from 0.90 to −0.80 V vs SCE at a scan rate of 0.5 V s^{-1} obtaining reduction peaks for IrO_xO^{I-} and Ir^{4+} and for the formation of adsorbed (upd) hydrogen (Figure.4.4 (a)). Then, scans were immediately reversed to 0.90 V generating the corresponding oxidation peaks (Figure.4.4 (b)). All measurements were repeated more than three times. The pH-sensitive redox couples obtained in synthetic seawater in the range of pH from 7.50–8.50 had peak potentials which shifted towards more negative potentials as the pH increased for both oxidative and reductive scans. The reduction peak of Ir^{4+} shifted from ca 0.018 to −0.084 V when pH increased from 7.50 to 8.50, while H_{upd} signal moved from −0.66 to −0.72 V (Figure.4.4 (a)). For re-oxidation peaks, that of Ir (III) occurred at ca 0.097 V vs SCE for pH = 7.50, and then shifted to 0.011 V when pH = 8.50, while the signals of H desorption moved from −0.59 V to −0.61 V when pH increased from 7.50 to 8.50. The $IrO_xO^{I-}/IrO_xO^{II-}H$ LSV reduction peak obtained by CV was not apparent by LSV so that its pH dependency was not studied in this section. Thus, SWV was used to increase the signal sensitivity, which will be discussed in the next section.

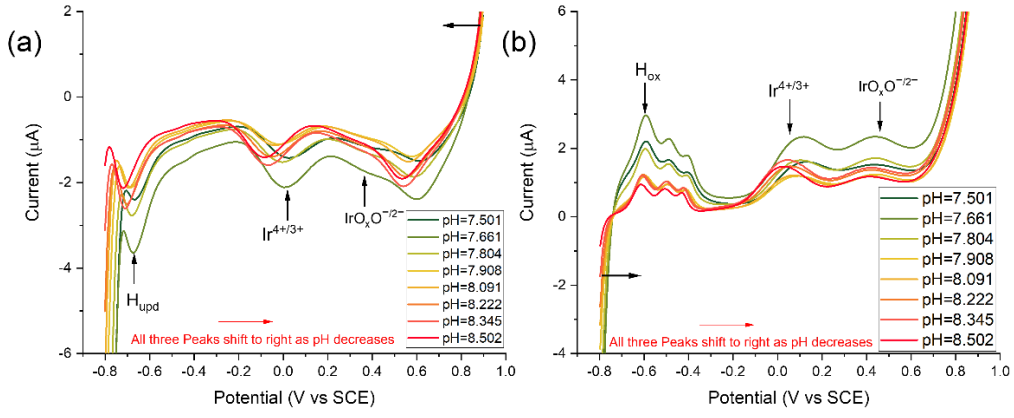

Figure.4.4 Linear sweep voltammograms with a scan rate of 0.5 Vs^{-1} using an activated iridium wire electrode with varying pH of different buffers ranging from 7.50 to 8.50 (a) reduction and (b) oxidation.

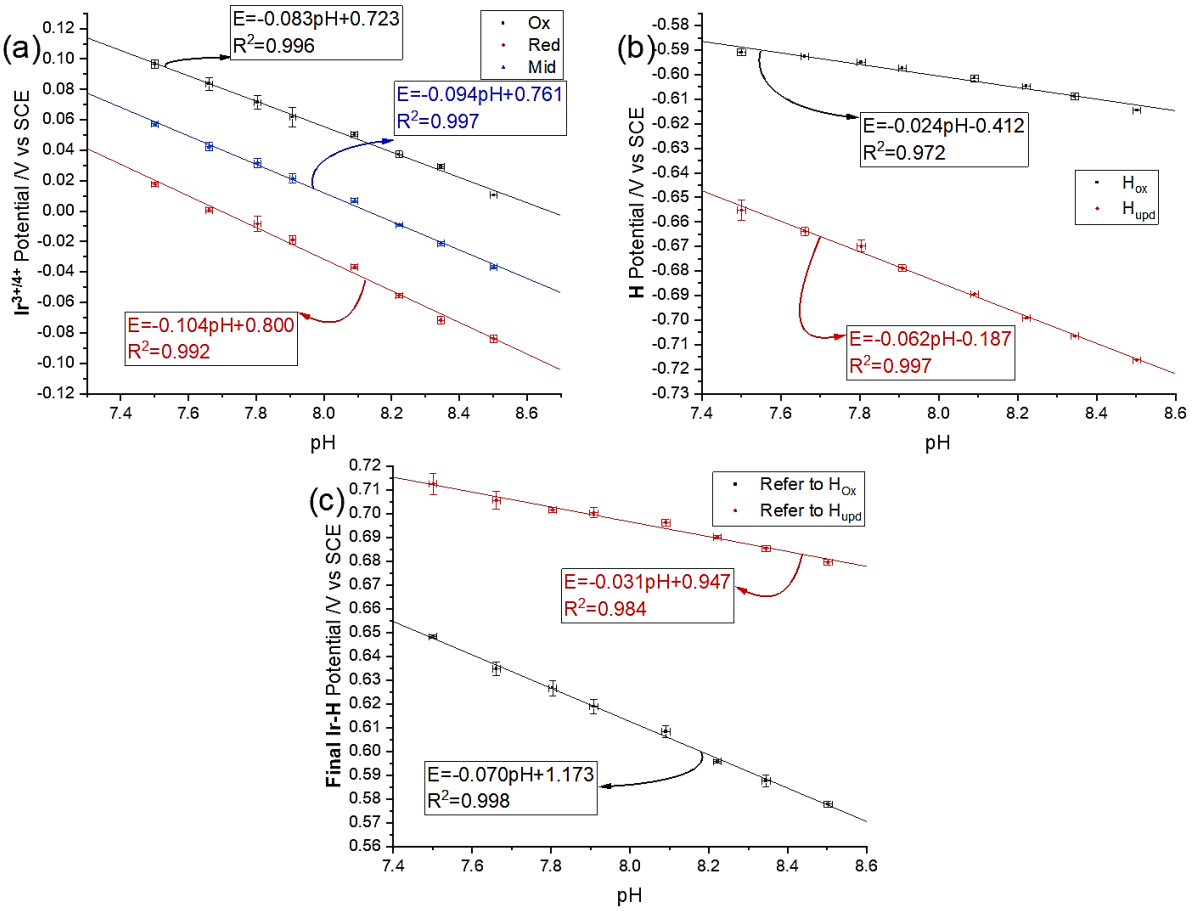

Figure.4.5 Plots of oxidation (black dots), reduction (red dots) peak, and midpoint (blue dots) potentials against pH value with the latter read from a pH meter (defined using total hydrogen ion scale) (a) $Ir^{III/IV}$ (b) $H_{upd/ox}$, and (c) $Ir^{III/IV}$ midpoints pH dependency referring to either H_{upd} or H_{ox}; x-axis error-bar is the uncertainty (0.01) of pH measured with a pH meter.

To analyse the data, the oxidation and reduction peak potentials of Ir(III/IV) (Figure.4.5 (a)) and H_{upd}/H_{ox} (Figure.4.5 (b)) were recorded with the corresponding midpoint potentials of Ir(III/IV) being calculated. Ir(III/IV) redox reaction showed a super-Nernstian relationship (93.7 ± 2.1 mV per pH unit), which is a clear merit of the iridium oxide approach to pH sensing. Meanwhile, the super-Nernstian pH dependency agrees with the equilibria proposed by Olthuis et al. [64] as indicated in Eqn. (4.10), namely three proton–two electron transfer reaction. In Figure.4.5 (b), the H_{upd} peak showed a near-Nernstian response (62.3 ± 1.5 mV per pH unit). As discussed in Section 4.3.1, the pH dependency is consistent with the expected one proton–

one electron transfer [73, 74]. The best-defined reoxidation peak (pointed by an arrow in Figure.4.4 (b)) was studied and resulted in less pH sensitivity (23.6 ± 1.6 mV per pH unit). To develop a calibration-free sensor, the super-Nernstian redox couple of Ir(III/IV) was reported relative to one or another of the less pH-sensitive H redox signals (Eqn. (4.14) or Eqn. (4.15)):

$$\boldsymbol{y_{potential} = mid_{Ir} - E(H_{ox})} \text{ (Figure.4.5c, black dots)} \quad (4.14)$$

$$\boldsymbol{y_{potential} = mid_{Ir} - E\left(H_{up}\right)} \text{ (Figure.4.5c, red dots)} \quad (4.15)$$

In this way, the reported response becomes independent of the reference electrode value and hence of any drift in the latter, for example, because of electrode fouling or variable liquid junction potentials. Figure.4.5 (c) shows the experimental data analysed according to both Eqn. (4.14) and Eqn. (4.15). The slope using H_{ox} as the reference signal was 70.1 ± 1.4 mV per pH unit, while it was 31.3 ± 1.6 mV per pH unit referring to H_{upd} peak potentials. One can conclude that referring to H_{ox} results in a higher pH sensitivity with a smaller uncertainty. In the next section, SWV was explored to identify any possible improvements in the analytical responses.

Square Wave Voltammetry

In this section, the signal-to-background ratio of the redox peaks of interest is explored using square wave voltammetry (SWV) following potential cycling activation of the iridium wire. The optimisation of the SWV parameters, including frequency, step potential, and amplitude, was implemented to obtain the best-defined square wave voltammograms for pH measurements as identified elsewhere [47]. The optimised SWV parameters, namely a frequency of 90 Hz, an amplitude of 60 mV, and a step potential of 1 mV, were applied for pH measurements in synthetic seawater for various pH values. First, an iridium wire was activated by potential cycling activation with a potential window between −0.80 V and 0.90 V vs SCE at a scan rate of 0.5 V s^{-1} for 40 cycles in synthetic seawater solutions (pH = 7.50-8.50). Then, SWVs with optimised parameters were conducted following in situ activation. All measurements were repeated three times. The reduction peaks were recorded first, which

initially swept to the negative potential, −0.80 V vs SCE, from 0.90 V (Figure.4.6 (a)), and the scans were then reversed to obtain oxidation peaks (Figure.4.6 (b)). The peak potentials of the resulting pH-sensitive redox couples shifted towards more negative potentials as the pH increased for both oxidative and reductive scans. Interestingly, whilst a peak attributable to the $IrO_xO^{I-}/IrO_xO^{II-}H$ redox couple was not apparent in the linear sweep voltammetry, it was apparent in the SWV because of the increased resolution. The redox couples occurred at similar potentials as observed in the CVs, with physically insignificant differences of the order of 10^{-3} V. To be more specific in terms of pH dependency, the reduction peak occurred at ca 0.42 V vs SCE in a pH = 7.50 seawater and shifted to ca 0.33 V when the pH was 8.50. Meanwhile, the reduction peak of Ir^{4+} shifted from ca 0.044 to −0.062 V, and the H_{upd} signal moved from −0.60 to −0.65 V when the pH increased from 7.50 to 8.50 (Figure.4.6 (a)). In the cases of the reoxidation peaks, that of $IrO_xO^{II-}H$ appeared at ca 0.44 V vs SCE for pH = 7.50 and shifted to 0.36 V when pH = 8.50, while the Ir(III) oxidation peaks were shifted from ca 0.058 to −0.027 V. The signals of H oxidation moved from −0.59 V to −0.63 V when pH increased from 7.50 to 8.50 (Figure.4.6 (b)). Note that capacitive effects can cause illusory peak-like features in addition to OER at high potentials by SWV, which do not appear on LSV.

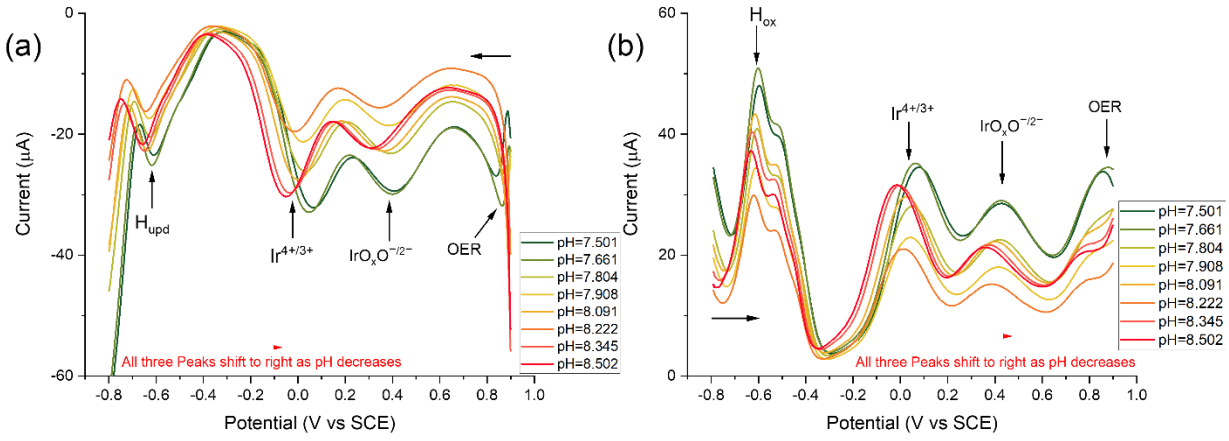

Figure.4.6 Square wave voltammograms (frequency 90 Hz, step potential 1 mV, and amplitude 60 mV) response using an activated iridium wire electrode in synthetic seawater with varying pHs ranging from 7.50 to 8.50 (a) reduction and (b) oxidation.

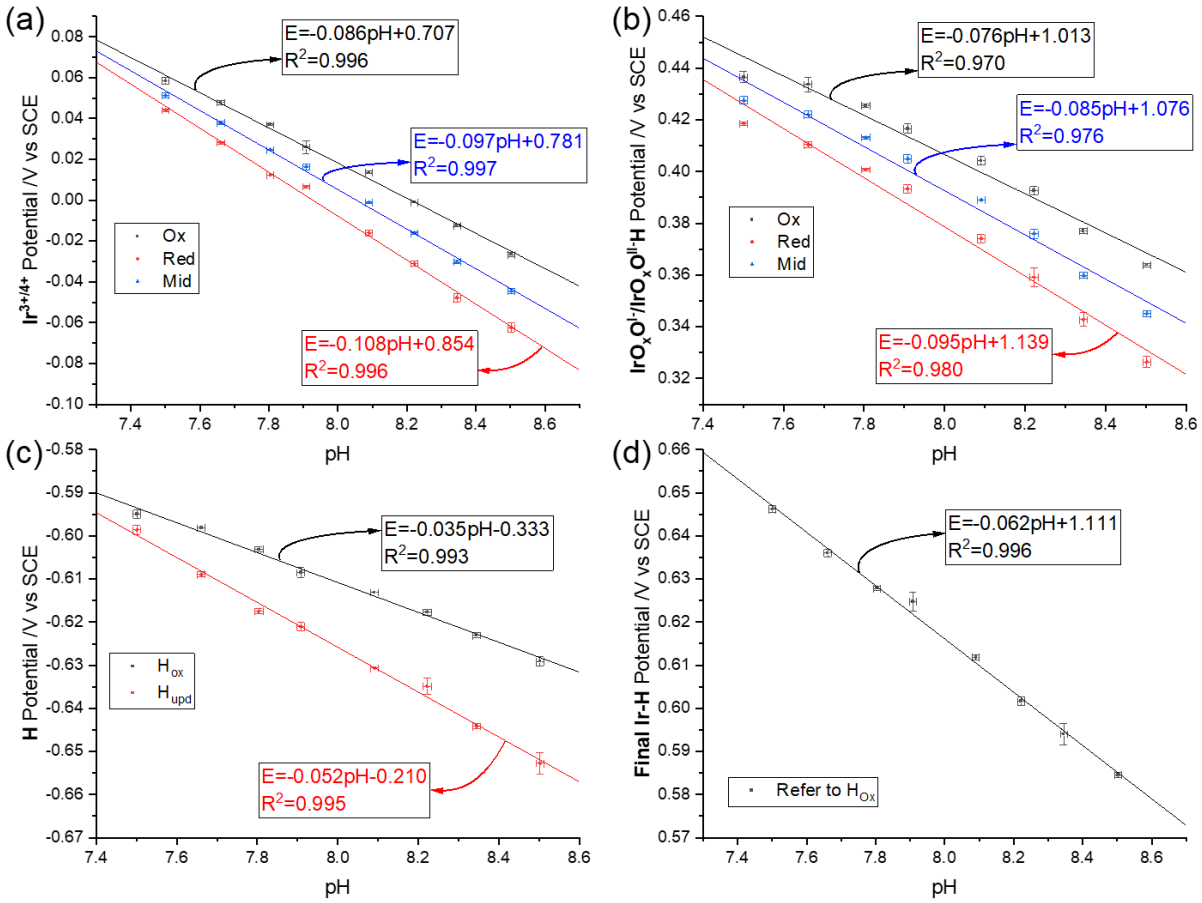

Figure.4.7 Plots of oxidation (black dots), reduction (red dots) peak, and midpoint (blue dots) potentials against pH with the latter read from a pH meter (with total hydrogen ion scale) (a) $Ir^{III/IV}$ (b) $IrO_xO^{I-}/IrO_xO^{II-}H$ (c) H_{upd}/H_{ox} and (d) $Ir^{III/IV}$ midpoints pH dependency referring to H_{ox}; x-axis error-bar: the uncertainty (0.01) of pH measured with a pH meter.

For data analysis, the oxidation and reduction peak potentials of Ir(III/IV) (Figure.4.7 (a)) and $IrO_xO^{I-}/IrO_xO^{II-}H$ (Figure.4.7 (b)) were recorded with the corresponding midpoint potentials being calculated. The pH dependencies of H_{upd} and H oxidation are shown in Figure.4.7 (c). Similar to the results obtained by LSV, Ir(III/IV) showed a super-Nernstian relationship, 96.9 ± 2.0 mV. It is noteworthy that $IrO_xO^{I-}/IrO_xO^{II-}H$ redox reactions also showed a super-Nernstian pH dependency (85.4 ± 5.4 mV per pH unit), which is in contrast to the one proton–one electron transfer mechanism (Nernstian) proposed by Pfizer (Eqn. (4.11)). However, because the formed iridium hydrous oxide is amorphous, it is difficult to deduce the

precise mechanism and stoichiometric composition [80, 82, 83]. For consistency and convenience, we refer to this redox couple as $IrO_xO^{I-}/IrO_xO^{II-}H$ in the following but note the uncertainty in assignment. The H_{upd} peak showed a close Nernstian relationship (52.0 ± 1.6 mV per pH unit), again consistent with a one proton–one electron transfer mechanism [73, 74], while the best-defined reoxidation peak (highlighted by the arrow in Figure.4.6) had a weaker pH sensitivity, being 34.7 ± 1.2 mV per pH unit. Eqn. (4.14) was again used to calculate the pH dependency to facilitate calibration-free sensing using SWV, being 61.8 ± 1.7 mV per pH unit referring to H_{ox}. It was concluded that SWV offered no benefit over LSV, with a small loss of sensitivity and a slightly higher uncertainty whilst requiring more complex and costly instrumentation.

4.4 Conclusions

We have made and validated a bespoke pH sensor for use in seawater based on an iridium wire electrode. The pH sensitive Ir oxide electrode is formed and activated using an in-situ fabrication method in synthetic seawater under neutral conditions by potential cycling. This method can facilitate in the specific case of seawater, by virtue of the in-situ method of formation, remote and more diverse pH measurements in contrast to formation via electrodeposition [46, 84, 85], sol-gel chemistry [56, 57], sputtering [58, 59], or thermal methods [60, 61], which often require complex conditions and processes; notably, a pre-treatment, hydroxylation [46, 86, 87], is required for the latter three methods. The work in this chapter has developed the general approach of chapter 3 in the context of seawater. The optimised potential cycling regime creates three pH-sensitive redox couples on the electrode surface, namely Ir(III/IV), H_{upd}/H_{ox}, and $IrO_xO^{I-}/IrO_xO^{II-}H$. The former two are used so as to realise a calibration-free measurement as coded in Eqn. (4.14). The combination of the measurements removes the effects of drift of the reference electrode since both couples are measured almost simultaneously relative to the same arbitrary reference electrode. The pH sensitive potential difference leads to a calibration-free pH sensor, responding to the total free hydrogen ion scale [17, 29] for use in seawater. The

developed sensor shows a super-Nernstian response of 70.1 ± 1.4 mV per pH unit at 25 °C, over the pH range of 7.50 to 8.50 corresponding to the usual range found in seawater [9, 42].

Appendix

Section A4.1: Performance of Iridium Oxide-based pH Electrodes Made by Different Methods

Table A4.1 Performance of iridium oxide-based pH electrodes made by different methods

Fabrication method	pH dependency	Authors/Year
Electrodeposition	101 mV per pH unit	Chaisiwamongkhol et al. [46]/2019
Electrodeposition	63-82 mV per pH unit	Baur et al. [84]/1998
Sol-gel	48-59 mV per pH unit	Nguyen et al. [56]/2015
Sol-gel	51 mV per pH unit	Huang et al. [57]/2011
Sputtering	59 mV per pH unit	Kuo et al. [58]/2013
Sputtering	54 mV per pH unit	Kreider et al. [59]/1995
Thermal	59 mV per pH unit	Ardizzone et al. [60]/1981
Thermal	59 mV per pH unit	Hitchman et al. [61]/1992
(AIROF)	71 mV per pH unit	Kinoshita, E. et al. [62]/1986
(AIROF)	75 mV per pH unit	Hitchman et al. [63]/1988
(AIROF)	62-74 mV per pH unit	Olthuis et al. [64]/1990

Iridium oxide is one of the most popular candidates for pH sensors, which can be generated by different methods [88, 89]. Electrodeposition is one of the methods and uses a solution of potassium hexachloroiridate(III) as a precursor. [46, 84] Iridium oxides can also be prepared by sol-gel [56, 57] chemistry, sputtering [58, 59] or thermal methods [60, 61]. Cyclic voltammetry is a method of the anodic iridium oxide film (AIROF) synthesis [62-64], which was applied in this chapter. Note that the redox mechanism and corresponding pH response of the synthesised Ir oxide electrode is highly dependent on the fabrication method as shown in Table A4.1.

References

1. Y. Chen and R. Compton, *Sensors*, 2022, **22**, 3286.
2. I. Mills, T. Cvitas and K. Homann, *Quantities, Units and Symbols in Physical Chemistry*, Blackwell Science Ltd, Oxford, 2nd edn., 1993.
3. R. P. Buck, S. Rondinini, A. Covington, F. Baucke, C. M. Brett, M. Camoes, M. Milton, T. Mussini, R. Naumann and K. Pratt, *Pure and Applied Chemistry*, 2002, **74**, 2169-2200.
4. E. Hückel and P. Debye, *Physikalische Zeitschrift*, 1923, **24**, 1.
5. R. G. Bates and A. K. Vijh, *Journal of The Electrochemical Society*, 1973, **120**, 263C.
6. Y. R. Hunter and J. S. Kuwabara, *Bulletin of Environmental Contamination and Toxicology*, 1994, **52**, 311-318.
7. Y. Guo and R. G. Compton, *Talanta*, 2021, **232**, 122502.
8. C. Zang, S. Huang, M. Wu, S. Du, M. Scholz, F. Gao, C. Lin, Y. Guo and Y. Dong, *Water, Air, & Soil Pollution*, 2011, **219**, 157-174.
9. M. Scholz, *Wetland Systems to Control Urban Runoff*, Elsevier: Amsterdam, The Netherlands, 2015.
10. U.S. Environmental Protection Agency, https://www.epa.gov/ocean-acidification/understanding-science-ocean-and-coastal-acidification, (accessed on 6 December 2021, 2021).
11. K. H. Bowmer and W. A. Muirhead, *Fertilizer Research*, 1987, **13**, 13-29.
12. L. Jin, Z. Wang, X. Zhu, Y. Zhang and L. Sheng, *Environmental Ecology*, Beijing: HigherEducation, Beijing, China, 1992.
13. I. Halevy and A. Bachan, *Science*, 2017, **355**, 1069-1071.
14. M. C. Chuan, G. Y. Shu and J. C. Liu, *Water, Air, and Soil Pollution*, 1996, **90**, 543-556.
15. A. C. M. Bourg and J. P. G. Loch, Springer Berlin Heidelberg, 1995, pp. 87-102.
16. S. Sörensen and S. Palitzsch, *Comptes Rendus Chimie*, 1910, **9**, 8.
17. F. J. Millero, J.-Z. Zhang, S. Fiol, S. Sotolongo, R. N. Roy, K. Lee and S. Mane, *Marine Chemistry*, 1993, **44**, 143-152.
18. A. Dickson, *Geochimica et Cosmochimica Acta*, 1984, **48**, 2299-2308.
19. C. H. Culberson, *Marine Electrochemistry*, 1981, 187-261.
20. F. J. Millero, *Limnology and Oceanography*, 1986, **31**, 839-847.
21. M. Whitfield, R. Butler and A. Covington, *Oceanologica Acta*, 1985, **8**, 423-432.
22. R. W. Ramette, C. H. Culberson and R. G. Bates, *Analytical Chemistry*, 1977, **49**, 867-870.
23. R. Bates and C. Culberson, *The Fate of Fossil Fuel CO_2 in the Oceans*, 1977, 45-61.
24. K. Khoo, R. W. Ramette, C. H. Culberson and R. G. Bates, *Analytical Chemistry*, 1977, **49**, 29-34.
25. I. Hansson, 1973.
26. A. Dickson and J. Riley, *Marine Chemistry*, 1979, **7**, 89-99.
27. A. G. Dickson, *Deep Sea Research Part A. Oceanographic Research Papers*, 1990, **37**, 755-766.
28. A. Dickson and F. J. Millero, *Deep Sea Research Part A. Oceanographic Research Papers*, 1987, **34**, 1733-1743.
29. A. G. Dickson, *Deep Sea Research Part I: Oceanographic Research Papers*, 1993, **40**, 107-118.
30. R. G. Bates and J. G. Calais, *Journal of Solution Chemistry*, 1981, **10**, 269-279.
31. R. G. Bates and W. P. Erickson, *Journal of Solution Chemistry*, 1986, **15**, 891-901.

32. J. B. Czerminski, A. G. Dickson and R. G. Bates, *Journal of Solution Chemistry*, 1982, **11**, 79-89.
33. R. Min, Z. Liu, L. Pereira, C. Yang, Q. Sui and C. Marques, *Optics & Laser Technology*, 2021, **140**, 107082.
34. R. H. Byrne and J. A. Breland, *Deep Sea Research Part A. Oceanographic Research Papers*, 1989, **36**, 803-810.
35. T. D. Clayton and R. H. Byrne, *Deep Sea Research Part I: Oceanographic Research Papers*, 1993, **40**, 2115-2129.
36. E. Hudson-Heck and R. H. Byrne, *Analytica Chimica Acta*, 2019, **1090**, 91-99.
37. R. Byrne, G. Robert-Baldo, S. Thompson and C. Chen, *Deep Sea Research Part A. Oceanographic Research Papers*, 1988, **35**, 1405-1410.
38. D. W. King and D. R. Kester, *Marine Chemistry*, 1989, **26**, 5-20.
39. J. Breland and R. Byrne, *Deep Sea Research*, 1993, **40**, 629-641.
40. R. H. Byrne, *Analytical Chemistry*, 1987, **59**, 1479-1481.
41. T. Takahashi, W. S. Broecker, A. E. Bainbridge and R. F. Weiss, *Carbonate chemistry of the Atlantic, Pacific and Indian Oceans: The results of the Geosecs expeditions, 1972-1978*, Lamont-Doherty Geological Observatory, Palisades, New York, 1980.
42. A. G. Dickson, *Marine Chemistry*, 1993, **44**, 131-142.
43. M. Cuartero, N. Pankratova, T. Cherubini, G. A. Crespo, F. Massa, F. Confalonieri and E. Bakker, *Environmental Science & Technology Letters*, 2017, **4**, 410-415.
44. *UK Pat.*, WO/2020/217056, 2020.
45. K. Chaisiwamongkhol, C. Batchelor-Mcauley and R. G. Compton, *Analyst*, 2017, **142**, 2828-2835.
46. K. Chaisiwamongkhol, C. Batchelor-Mcauley and R. G. Compton, *Analyst*, 2019, **144**, 1386-1393.
47. Y. Chen, X. Li, D. Li, C. Batchelor-McAuley and R. G. Compton, *Journal of Solid State Electrochemistry*, 2021, **25**, 2821-2833.
48. N. S. Lawrence, M. Pagels, S. F. Hackett, S. McCormack, A. Meredith, T. G. Jones, G. G. Wildgoose, R. G. Compton and L. Jiang, *Electroanalysis: An International Journal Devoted to Fundamental and Practical Aspects of Electroanalysis*, 2007, **19**, 424-428.
49. I. Streeter, H. C. Leventis, G. G. Wildgoose, M. Pandurangappa, N. S. Lawrence, L. Jiang, T. G. Jones and R. G. Compton, *Journal of Solid State Electrochemistry*, 2004, **8**, 718-721.
50. G. G. Wildgoose, M. Pandurangappa, N. S. Lawrence, L. Jiang, T. G. J. Jones and R. G. Compton, *Talanta*, 2003, **60**, 887-893.
51. H. C. Leventis, I. Streeter, G. G. Wildgoose, N. S. Lawrence, L. Jiang, T. G. J. Jones and R. G. Compton, *Talanta*, 2004, **63**, 1039-1051.
52. G. G. Wildgoose, H. C. Leventis, I. Streeter, N. S. Lawrence, S. J. Wilkins, L. Jiang, T. G. Jones and R. G. Compton, *ChemPhysChem*, 2004, **5**, 669-677.
53. J. Phair, L. Newton, C. McCormac, M. F. Cardosi, R. Leslie and J. Davis, *Analyst*, 2011, **136**, 4692.
54. C. Dai, C.-W. I. Chan, W. Barrow, A. Smith, P. Song, F. Potier, J. D. Wadhawan, A. C. Fisher and N. S. Lawrence, *Electrochimica Acta*, 2016, **190**, 879-886.
55. N. Sisodia, M. Miranda, K. L. McGuinness, J. D. Wadhawan and N. S. Lawrence, *Electroanalysis*, 2020.
56. C. Nguyen, S. Rao, X. Yang, S. Dubey, J. Mays, H. Cao and J.-C. Chiao, *Sensors*, 2015, **15**, 4212-4228.
57. W.-D. Huang, H. Cao, S. Deb, M. Chiao and J. C. Chiao, *Sensors and Actuators A: Physical*, 2011, **169**, 1-11.

58. L. Kuo, Y. Chou, K. Chen, C. Lu and S. Chao, *Sensors and Actuators B: Chemical*, 2014, **193**, 687-691.
59. K. G. Kreider, M. J. Tarlov and J. P. Cline, *Sensors and Actuators B: Chemical*, 1995, **28**, 167-172.
60. S. Ardizzone, A. Carugati and S. Trasatti, *Journal of Electroanalytical Chemistry and Interfacial Electrochemistry*, 1981, **126**, 287-292.
61. M. L. Hitchman and S. Ramanathan, *Talanta*, 1992, **39**, 137-144.
62. E. Kinoshita, F. Ingman, G. Edwall, S. Thulin and S. Głąb, *Talanta*, 1986, **33**, 125-134.
63. M. L. Hitchman and S. Ramanathan, *Analyst*, 1988, **113**, 35-39.
64. W. Olthuis, M. A. M. Robben, P. Bergveld, M. Bos and W. E. Van Der Linden, *Sensors and Actuators B: Chemical*, 1990, **2**, 247-256.
65. R. G. Compton and C. E. Banks, *Understanding Voltammetry*, World Scientific, 3rd edition, 2018.
66. L. Xiong, C. Batchelor-McAuley and R. G. Compton, *Sensors and Actuators B: Chemical*, 2011, **159**, 251-255.
67. *EP Pat.*, EP 1702208 B1, 2016.
68. P. G. Pickup and V. I. Birss, *Journal of the Electrochemical Society*, 1988, **135**, 41.
69. V. Pfeifer, T. E. Jones, J. J. Velasco Velez, R. Arrigo, S. Piccinin, M. Havecker, A. Knop-Gericke and R. Schlogl, *Chemical Science*, 2017, **8**, 2143-2149.
70. V. Pfeifer, T. E. Jones, J. J. Velasco Velez, C. Massue, M. T. Greiner, R. Arrigo, D. Teschner, F. Girgsdies, M. Scherzer, J. Allan, M. Hashagen, G. Weinberg, S. Piccinin, M. Havecker, A. Knop-Gericke and R. Schlogl, *Physical Chemistry Chemical Physics*, 2016, **18**, 2292-2296.
71. N. Dubouis and A. Grimaud, *Chemical Science*, 2019, **10**, 9165-9181.
72. G. Jerkiewicz, *Electrocatalysis*, 2010, **1**, 179-199.
73. X. Yang, J. Nash, N. Oliveira, Y. Yan and B. Xu, *Angewandte Chemie*, 2019, **131**, 17882-17887.
74. J. Zheng, W. Sheng, Z. Zhuang, B. Xu and Y. Yan, *Science Advances*, 2016, **2**, e1501602.
75. V. Pfeifer, T. E. Jones, J. J. Velasco Vélez, C. Massué, R. Arrigo, D. Teschner, F. Girgsdies, M. Scherzer, M. T. Greiner, J. Allan, M. Hashagen, G. Weinberg, S. Piccinin, M. Hävecker, A. Knop-Gericke and R. Schlögl, *Surface and Interface Analysis*, 2016, **48**, 261-273.
76. L. D. Burke, M. E. Lyons, E. J. M. O'Sullivan and D. P. Whelan, *Journal of Electroanalytical Chemistry and Interfacial Electrochemistry*, 1981, **122**, 403-407.
77. S. Carroll and R. P. Baldwin, *Analytical Chemistry*, 2010, **82**, 878-885.
78. L. D. Burke, J. K. Mulcahy and D. P. Whelan, *Journal of Electroanalytical Chemistry and Interfacial Electrochemistry*, 1984, **163**, 117-128.
79. P. G. Pickup and V. I. Birss, *Journal of Electroanalytical Chemistry and Interfacial Electrochemistry*, 1987, **220**, 83-100.
80. O. Kasian, J.-P. Grote, S. Geiger, S. Cherevko and K. J. J. Mayrhofer, *Angewandte Chemie International Edition*, 2018, **57**, 2488-2491.
81. H. Angerstein-Kozlowska, B. E. Conway and W. B. A. Sharp, *Journal of Electroanalytical Chemistry and Interfacial Electrochemistry*, 1973, **43**, 9-36.
82. R. M. Kluge, R. W. Haid and A. S. Bandarenka, *Journal of Catalysis*, 2021, **396**, 14-22.
83. H. G. Sanchez Casalongue, M. L. Ng, S. Kaya, D. Friebel, H. Ogasawara and A. Nilsson, *Angewandte Chemie*, 2014, **126**, 7297-7300.
84. J. E. Baur and T. W. Spaine, *Journal of Electroanalytical Chemistry*, 1998, **443**, 208-216.
85. A. Salimi, M. E. Hyde, C. E. Banks and R. G. Compton, *Analyst*, 2004, **129**, 9-14.

86. M. J. Tarlov, S. Semancik and K. G. Kreider, *Sensors and Actuators B: Chemical*, 1990, **1**, 293-297.
87. M. Wang, S. Yao and M. Madou, *Sensors and Actuators B: Chemical*, 2002, **81**, 313-315.
88. S. Głab, A. Hulanicki, G. Edwall and F. Ingman, *Critical Reviews in Analytical Chemistry*, 1989, **21**, 29-47.
89. S. Yao, M. Wang and M. Madou, *Journal of the Electrochemical Society*, 2001, **148**, H29.

Chapter 5

A Bespoke Reagent-free Amperometric Bromide Sensor for Seawater

In addition to pH, the topic of the previous chapter, measurement of the exact concentration of bromide in seawater, usually present at the ca milli-Molar level, is significant for evaluating geological, biological and environmental conditions. Although silver electrodes are commonly used for amperometric halide measurements, providing selectivity for the ions with similar concentrations, the bromide signal obtained in seawater is masked by that from chloride ions which are present at hundred millimolar levels. Thus, in **Chapter 5**, an alternative bespoke reagent-free electrochemical bromide sensor for seawater was developed with the benefits of low cost, simplicity and rapidity. This is based on the voltammetric oxidation of bromide at a Pt macro-electrode, which results in a well-defined signal that is clearly distinct from the chloride oxidation peak in seawater. The sensitive quantification was performed by square wave voltammetry combined with the standard addition method, and validated in both artificial seawater and authentic natural seawater. The measured bromide concentrations of three real samples show good agreement with independent results obtained by ion chromatography.

The work of **Chapter 5** has been published in the journal *Talanta* [1].

5.1 Introduction

71 percent of the earth's surface is covered by the ocean, while 96.5 percent of the known water on the earth consists of seawater. [2] Human activities are changing the ocean through eutrophication, pollution, warming, acidification, deoxygenation, and nutrient flux reduction amongst other concerns. [3, 4] As discussed in **Chapter 4**, the decrease in the pH of seawater from 8.2 to 8.1 is thought to have resulted from the Industrial Revolution, and arises from the increased formation of carbonic acid due to more carbon dioxide emissions (Eqn (5.1)). [5]

$$CO_2 + H_2O \rightarrow H_2CO_3 \quad (5.1)$$

Conversely, the physical and chemical parameters of seawater can be used to track its condition and monitor anthropogenically induced alterations, which is essential to assist regulating societal and industrial development. Usually, seawater contains only a trace of bromide being present at ca milli-Molar concentrations, but information about exact levels is important for evaluating-geological, biological and environmental conditions. For example, the levels of bromide ions in the surface and ground waters near the sea are greatly changed by and indicative of seawater intrusion. [6] Further, bromide can be converted to the reactive gas species, bromine (Br_2) and to hypobromous acid (HOBr), leading to surface ozone depletion via the chemistry (Figure.5.1). Note that the sequence of reactions $Br + O_3 \rightarrow BrO + O_2$ followed by $BrO + BrO \rightarrow 2Br + O_2$ indicates a catalytic loss mechanism for ozone. [7] Importantly, bromide is naturally present in fossil fuels, notably coal, so environmental trends due to fossil fuel activities are reflected in bromide concentration changes in surface seawater. [8] Furthermore, as a result of industrial wastewater discharge, bromide can combine with organic pollutants forming toxic compounds, e.g. bromoacetonitriles, bromoacetamides and bromonitromethanes. [8-10] Finally, we note that a high concentration of bromide itself can be toxic to humans. All these factors emphasise the importance of bromide detection in seawater. [11, 12]

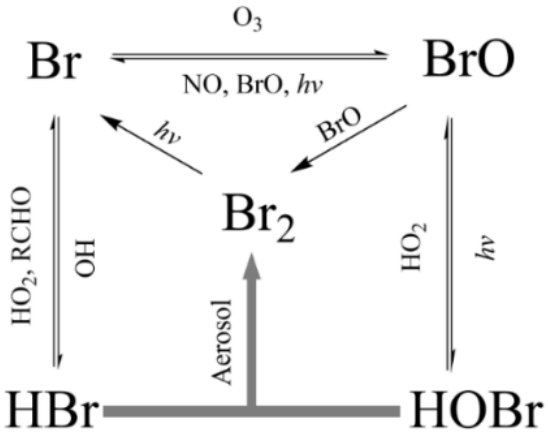

Figure.5.1 Schematic reaction diagram of bromide. Thin lines indicate gas-phase reactions. The thick lines show an aerosol reaction. [7]

Table 2.1 shows the composition of seawater [13] in which chloride is the most dominant anion. In contrast, bromide has a typical concentration of just 0.86 mM, which is much lower than that of chloride. Although the local concentrations of chloride and bromide depend on location and season [14, 15], the ratio between them in normal seawater mostly stays relatively constant (being around 300:1 w/w) [16, 17]. Indeed, the chloride ion concentration is sometimes used to give approximate estimates of bromide levels, despite that this risks errors where unusual levels of bromide exist. Nevertheless, to successfully measure the concentration of bromide, the potential interference by Cl^- present at hundred millimolar levels must be considered.

***Table 5.1 Concentrations of major ions in surface seawater* [13]**

Ion	Molar Concentration /mM
Na^+	4.81×10^{2}
Mg^{2+}	5.41×10^{1}
Ca^{2+}	1.05×10^{1}
K^+	1.05×10^{1}
Sr^{2+}	9.20×10^{-2}
Cl^-	5.59×10^{2}
SO_4^{2-}	2.89×10^{1}
HCO_3^-	1.89
CO_3^{2-}	1.89×10^{-1}
Br^-	8.63×10^{-1}
$B(OH)_4^-$	8.39×10^{-2}
$B(OH)_3$	3.42×10^{-1}
F^-	7.00×10^{-2}

Present bromide detection and quantification techniques include kinetic-spectrophotometric [6, 18-24], chromatography [25, 26], capillary electrophoresis [27-31] and electrochemistry [32-35]. Several studies on bromide detection using the kinetic-spectrophotometric method have been reported. [6, 18-24] In this approach a strong oxidising agent such as chloramine T is commonly used for the formation of OBr^- from bromide, followed by

a reaction with an indicator resulting in a colour change, e.g. converting phenol red to bromophenol blue. [18] However, the presence of other ions that can react with the oxidising agent is always a concern. For example, apart from hydroxylamine (NH_2OH) that can be found in ground, surface waters and coastal water albeit with lower concentrations [18, 36, 37], other halides, especially chloride in seawater, present significant interferences. [6, 22] Meanwhile, the sensitivity of some methods is temperature dependent [23, 24] or the dilution of samples is required [6].

In addition to kinetic-spectrophotometric method, chromatography [25, 26] combined with a suitable detector is one of the 'gold standards' for sample quantification. For example, ion chromatography is specifically recommended by CEN and ISO [38] for the analysis of drinking water. However, the method requires expensive instruments and time-consuming procedures, including repeated calibration and dilution of the analyte. [39] Capillary electrophoresis (CE) is often applied for bromide detection in medicine [27, 28] and analysis of human serum [29], while the application in seawater has been studied by Fukushi *et. al* [30] and Kocatürk *et. al* [31]. Even though CE is a good alternative to IC due to shorter sample preparation and analysis time, smaller reagent consumption and cheaper fused silica capillaries used instead of chromatographic columns [31], electrochemistry may nevertheless prove a better option, offering benefits of low cost, simplicity and rapidity with comparable selectivity.

Potentiometry is widely applied as an electrochemical technique for bromide detection. In particular, the use of a bromide ion-selective electrode (Br-ISE) has been reported in several studies. [32-35] However, if the electrode is developed from scratch, the fabrication procedure is often complex and a preconditioning step may also be required. Zahran *et al.* reported PVC-membrane cocktails consisting of different compositions that required optimisation. [33] Meanwhile, the whole process was found to be time-consuming, subject to inconsistent manual fabrication methods, with difficulty for manufacturing in small sizes as well as the electrodes having short lifetimes [40]. For example, a Br-ISE based on a silver bromide membrane needs to

be preconditioned by 48 hours of soaking in 0.01 M KBr solutions. [41] Moreover, though these bespoke electrodes reported by Zahran *et al.* and Rechnitz *et al.* are nominally bromide selective, the selectivity coefficient towards Cl^- is about 10^{-2}, [33, 41] which is not sufficient for seawater with the presence of chloride in hundreds of millimolar in comparison with the sub millimolar levels of bromide. Whilst there are many commercially available potentiometric sensors [42-44], they are subject to interference from other ions, notably and for example Cl^-, I^-, S^{2-}, CN^- and strong reducing agents. For example, the description of ECD S80 Bromide Sensors [44] emphasises that Cl^-, I^- and S^{2-} will form insoluble precipitates on the electrode surface diminishing the response. Moreover, commercial ISEs are also costly. More generally, the logarithmic relation between potential and bromide activity results in a change of signal of a mere ca 60 mV per decade of concentration at 298 K, which makes it challenging to deliver a precise and sensitive detection by potentiometry. Meanwhile, there is no guarantee of the quantification accuracy, especially in complex matrixes with the risk of interference or malfunction/fouling of electrodes. However, an amperometric measurement *via* voltammetry provides a possible alternative robust and inexpensive, reagent-free method for bromide detection. To be more specific, silver-based electrodes are commonly used for bromide, or general halide measurements, [45-47] based on the chemistry shown in Eqn. (5.2):

$$\boldsymbol{AgX(s) + e^- \rightleftharpoons Ag + X^-} \qquad (5.2)$$

where X = Cl^-, Br^- and I^-. Several literature reports [48, 49] have stated that Cl^-, Br^- and I^- with similar concentrations can be selectively detected by using silver electrodes, as the deposition peaks of each silver halide occur at different formal potentials (Eqns. (5.3)-(5.5)) [50]:

$$\boldsymbol{AgCl + e^- \rightleftharpoons Ag + Cl^-; E_{Ag/AgCl} = 0.2223\ V\ vs\ SHE} \qquad (5.3)$$

$$\boldsymbol{AgBr + e^- \rightleftharpoons Ag + Br^-; E_{Ag/AgBr} = 0.0711\ V\ vs\ SHE} \qquad (5.4)$$

$$\boldsymbol{AgI + e^- \rightleftharpoons Ag + I^-; E_{Ag/AgI} = -0.1522\ V\ vs\ SHE} \qquad (5.5)$$

However, in real samples, most importantly seawater with chloride concentration significantly higher than bromide, the bromide signal is masked by the much larger chloride signal as reported below. In order to replace the use of silver electrodes in the context of seawater, we explore other electrode materials notably a platinum electrode that can selectively quantify the bromide concentration despite the high concentration of chloride in seawater.

5.2 Experimental

Chemicals and Reagents

Table 5.2 Chemical composition of synthetic seawater [51]

Formula	Molar Concentration (mol dm^{-3})
NaCl	4.20×10^{-1}
KCl	9.39×10^{-3}
$MgCl_2 . 6H_2O$	5.46×10^{-2}
$CaCl_2 . 2H_2O$	1.05×10^{-2}
$SrCl_2 . 6H_2O$	6.38×10^{-5}
Na_2SO_4	2.88×10^{-2}
$NaHCO_3$	2.38×10^{-3}
KBr	8.40×10^{-4}
NaF	7.15×10^{-5}
H_3BO_3	4.85×10^{-5}

Solutions were prepared using deionised water with a resistivity of 18.2 MΩ cm at 298 K (Millipore, Millipak Express 20, U.K.). All chemicals were of analytical grade and were used as received without any further purification. Potassium nitrate (KNO_3, ≥99%) served as a supporting electrolyte was purchased from Sigma-Aldrich, UK. Following a literature recipe [51], artificial seawater (ASW) was prepared with the composition of which is presented in Table 5.2. Details of the chemicals and reagents were listed in Section 2.1.

Electrochemical Apparatus

Electrochemical measurements were performed using a μAutolab II potentiostat (Metrohm-Autolab BV, Netherlands). A standard three-electrode set-up was used in a Faraday

cage, being thermostated at a constant value of 25.0 ± 0.2 °C. A graphite rod always served as the counter electrode in all experiments. Either a mercury-mercurous sulfate electrode (MSE +0.64 V vs SHE, BASi, USA) and a silver macro-disc electrode (diameter of 2.52 ± 0.01 mm, geometric area of 0.05 cm^2, homemade) or a saturated calomel electrode (SCE +0.244 V vs SHE, BASi Inc., USA) and a platinum macro-electrode (diameter of 1.66 mm, geometric area of 0.02 cm^2, BASi, USA) were used as combinations of reference and working electrodes. This is because that a slight leakage of chloride from a SCE can lead to AgCl deposition at a silver electrode when a corresponding potential is applied. Both electrodes were polished using a sequence of 1.0, 0.3 and 0.05 μm alumina lapping compounds (Bucher, Germany) prior to use. High purity N_2 flow (BOC Gases plc, U.K.) was used to remove oxygen from aqueous solutions as needed prior to the electrochemical measurements. Cyclic voltammetry (CV) was used to study the electrochemical behaviour of both working electrodes in either artificial or natural seawater. Prior to each voltammetric measurement when using a Ag macro-disc electrode, an initial 1-minute electrochemical cleaning at –1.45 V vs MSE was conducted. [47] Square wave voltammetry (SWV) combined with standard additions was applied to determine the concentration of bromide using a Pt macro-disc electrode in either solution.

Sample collection and ion chromatography analysis

Three samples of natural seawater were studied. Two samples, sourced from the department of Earth Sciences, Oxford University, were collected from the L4 Station [52] in the English Channel (50° 15.00' N, 4° 13.02' W) at a depth of ca. 10m, with one being collected in September 2020 and the other in October 2021. Another sample was collected off the coast of Dartmouth, Great Britain (50°20'N 3°32'W), at a depth of about 1m in April 2022. 500mL of each sample was filter sterilised using 0.22 μm pore size Steritop filter units (Steritop Threaded Bottle Top Filter | SCGPS05RE (merckmillipore.com)) and was then kept refrigerated in the dark for the time leading up to these experiments. Ion chromatography measurements were

made using a Dionex (Thermo Scientific, Sunnyvale, CA, USA) ICS-5000+ SP instrument. Separations were carried out using a Dionex IonPac AS23-4um analytical column. The three samples of seawater were each diluted 200-fold with deionised water with a resistivity of 18.2 MΩ cm at 298 K prior to the analysis.

5.3 Results and Discussion

In the following sections, we first use cyclic voltammetry to study the electrochemical behaviour of a silver macro-disc electrode for bromide detection both in chloride-free solutions and in the presence of chloride at hundred millimolar levels corresponding to the concentration levels in natural seawater. We found that whilst an amperometric or voltammetric approach for bromide detection is viable for pure bromide solutions or in the presence of low levels of other halide ions, in the presence of high chloride concentrations the bromide oxidation signal is masked and the method fails. As an alternative voltammetric approach, the use of a platinum macro-disc electrode is explored and shown to be selective and sensitive enough for Br^- ion detection despite the presence of high levels of Cl^- in artificial seawater. Next, a sensitivity analysis is carried out in artificial seawater using the method of standard additions, while square wave voltammetry (SWV) with optimised parameters was applied to improve the sensitivity and precision. Finally, the bespoke method is applied for the quantitative analysis of bromide in three samples of natural seawater, the results of which are compared with that obtained by ion chromatography with good agreement being found.

5.3.1 Bromide Detection Using a Silver Macro-electrode

Bromide detection in the presence of the other halide ions, notably Cl^- and I^-, in an aqueous solution has been extensively studied using silver electrodes. For example, the selective determination of chloride and bromide ions in serum using cyclic voltammetry has been realised by Arai *et al*. who studied the behaviour of a silver macro-disc electrode in a PBS buffer with

similar concentrations of halides (5 mM for Cl^-, 2 mM Br^- and 2 mM I^-). [49] The measured CV indicated three clearly separated and well-defined redox peaks corresponding to the Ag/AgCl/Cl^-, Ag/AgBr/Br^- and Ag/AgI/I^- redox couples respectively. Meanwhile, silver nanowires [46] or nanoparticles [53] were also reported for successful selective halide measurements where voltammetric detections were conducted in solutions made of three halide ions with equal or similar concentrations, 5 mM in 0.1 M PBS for the former case and 80 μM for the latter. Hence, as a starting point for bromide detection in seawater, we explored the possible selectivity of silver electrodes towards bromide in the presence of high chloride concentrations.

Following a 1-minute electrochemical cleaning of a Ag macro-disc electrode at –1.45 V vs MSE, cyclic voltammetric experiments, in which the potential sweep started at −0.90 V vs MSE, swept towards −0.05 V before returning back to −0.90 V were conducted in a cell containing 0.1 M potassium nitrate and varying concentrations of potassium bromide (0.2, 0.4, 0.8, 1.2 and 1.6 mM). Each experiment was repeated three times. A control experiment was performed to analyse the behaviour of the silver electrode in the absence of bromide ions as shown by the black dashed line in Figure.5.2, showing no voltammetric signal in a blank scan. In contrast, one anodic peak ($Peak_1$) with its reduction peak ($Peak_{1'}$) were observed when the measurement was conducted in bromide solutions with different concentrations (all the lines in Figure.5.2 except the black dash line). The redox peaks shifted to a more negative positions as the bromide concentration increases. To be more specific, when the bromide concentration increased form 0.2 mM to 1.6 mM, the potential of $Peak_1$ moved from –0.27 V to –0.33 V vs MSE, and that of $Peak_{1'}$ moved from –0.42 V to –0.50 V vs MSE. We infer that $Peak_1$ and $Peak_{1'}$ correspond to the following redox reaction, either reductive ($Peak_1$) or oxidative ($Peak_1$'):

$$\boldsymbol{Ag + Br^- \rightleftharpoons AgBr + e^-} \qquad (5.6)$$

The formal potential of the Ag/AgBr/Br^- redox couple (Eqn (5.6)) is reported to be –0.57 V vs MSE [50], noting that the MSE has a potential of 0.64 V vs SHE [54], which is consistent with

the data from the concentration of bromide being 1.6 mM. The inset of Figure.5.2 shows a plot of peak currents against concentrations of bromide, which indicates a linear correlation (R^2 = 0.9999) between peak currents and bromide concentrations again consistent with the suggested assignment.

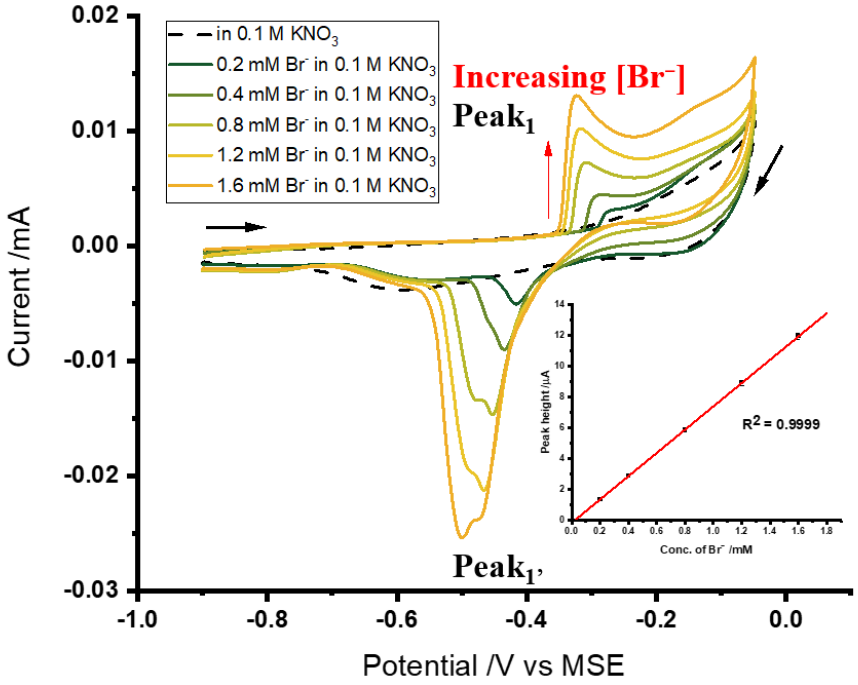

Figure.5.2 Cyclic voltammograms measured at a scan rate of 20 mV s^{-1} using a Ag macro-electrode in degassed 0.1 M KNO_3 with different concentrations of Br^- (insert: calibration plot of the peak current of $Peak_1$ against the concentration of bromide ions). The start potential was −0.90 V vs MSE.

To study the effect of chloride ions, cyclic voltammetry was first conducted using a macro-Ag electrode in a solution of 644 mM KCl. Then, voltammetric measurements were performed in solutions containing 0.84 mM Br^- ions with either 0.1 M KNO_3 or 644 mM KCl and in ASW. Note that the bromide and chloride concentrations are the recommended values for artificial seawater [51], as detailed in the Experimental Section. As indicated in Figure.5.3, the voltammograms started at a potential of −0.90 V vs MSE with a scan reversal at a potential of −0.20 V vs MSE, back to the starting potential. For the experiment in a solution containing KCl

only (red line), $Peak_2$ at −0.34 V and $Peak_{2'}$ at −0.56 V vs MSE were observed. We assign $Peak_2$ and $Peak_{2'}$ to the following redox chemistry:

$$\boldsymbol{Ag + Cl^- \rightleftharpoons AgCl + e^-} \qquad (5.7)$$

which is consistent with the formal potential of the Ag/AgCl/Cl^- couple reported as −0.418 V vs MSE. [50] On adding 0.84 mM KBr (green line), there was no perceptible change in the peak potentials of Peaks 2 and 2'. Voltammetry in ASW (blue line) resulted in a broader redox couple, with an oxidation peak at about −0.32 V and a reduction peak at −0.60 V vs MSE. Accordingly, the redox peaks labelled Peaks 2 and 2' in Figure.5.3 recorded with the addition of 0.84 mM Br^- are again attributed to the Ag/AgCl/Cl^- couple, while the broad peak shape obtained in ASW reflects the deposition from and stripping into the more complex matrix. Note that the crossover detected on the back sweep in the three chloride-containing solutions results from surface nucleation of the new AgCl phase so that increased reductive currents flow after more nuclei are formed. A $peak_1$ at −0.30 V and its back $Peak_{1'}$ at −0.45 V vs MSE were seen in a solution consisting of 0.84 mM Br^- and 0.1 M KNO_3, and are attributed to the Ag/AgBr/Br^- redox couple as above (black line in Figure.5.3). However, for the case with presence of 644mM chloride ions and the ASW (green line and blue line), the strong current when the potential applied was higher than about −0.38 V, from the formation of AgCl ($Peak_2$), fully masked the Ag/AgBr/Br^- oxidation signals ($Peak_1$). The same situation was observed during reductive scans. Thus, whilst silver electrodes can be used to detect bromide in the presence of similar concentrations of chloride, when an excess of the latter is present, $Peak_1$ and $Peak_{1'}$ cannot be used analytically. It is thus not possible to use a silver electrode for bromide detection in seawater. As an alternative, the use of a Pt macro-disc electrode was explored as reported in the following sections.

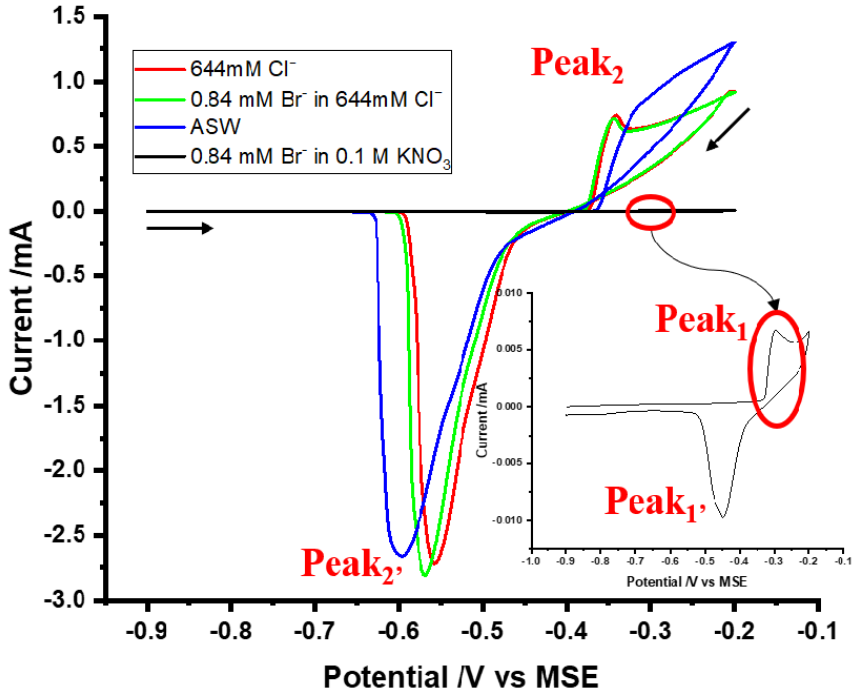

Figure.5.3 Cyclic voltammograms at a scan rate of 20 mV s^{-1} using a Ag macro-electrode in degassed 644 mM Cl^- (red line), 0.84 mM Br^- with 644 mM KCl (green line), ASW containing 0.84 mM Br^- and 644 mM Cl^- (blue line) and 0.84 mM Br^- with 0.1 M KNO_3 (black line). The start potential was −0.90 V vs MSE.

5.3.2 Electrochemical Study of Br^- with a Pt Macro-electrode

In this section, a Pt macro-disc electrode is applied to study its electrochemical behaviour towards bromide ions, especially in the presence of Cl^- at hundred millimolar levels in ASW. The study was first carried out in a degassed solution of 0.84 mM Br^- ions with 0.1 M KNO_3 to fingerprint the bromide peak. Cyclic voltammograms with different scan rates of 20, 50, 100, 200 and 400 mVs^{-1}, of which the potential started at 0 V vs SCE, swept towards 1.7 V before returning to 0 V, were recorded as shown in Figure.5.4 (a). One oxidation peak at 0.98 V vs SCE and one reduction peak at 0.85 V vs SCE were observed at different scan rates. Referring to the observations of Yu *et al.* [55], we infer that Peak 1 (oxidation) and Peak 1' (reduction) correspond to the redox reaction of bromide with hypobromous acid ($HOBr/OBr^-$) being the possible product. The speciation of the product formed at the electrode interface and sequentially during diffusion towards the bulk solution may differ depending on the pH and

other ions present in the solution. The inset to Figure.5.4 (a) shows that the peak current scales with the square root of the voltage scan rate. The linearity confirms a diffusion-controlled electrode process. The diffusion coefficient of the bromide ion in 0.1 M KNO_3 was measured based on the Randles–Ševčík equation for a simple irreversible one-electron transfer oxidation giving a value of 2.1×10^{-5} cm^2/s which compares well with the literature value of 2.08×10^{-5} cm^2/s [56] (see Appendices, Section A5.1-2).

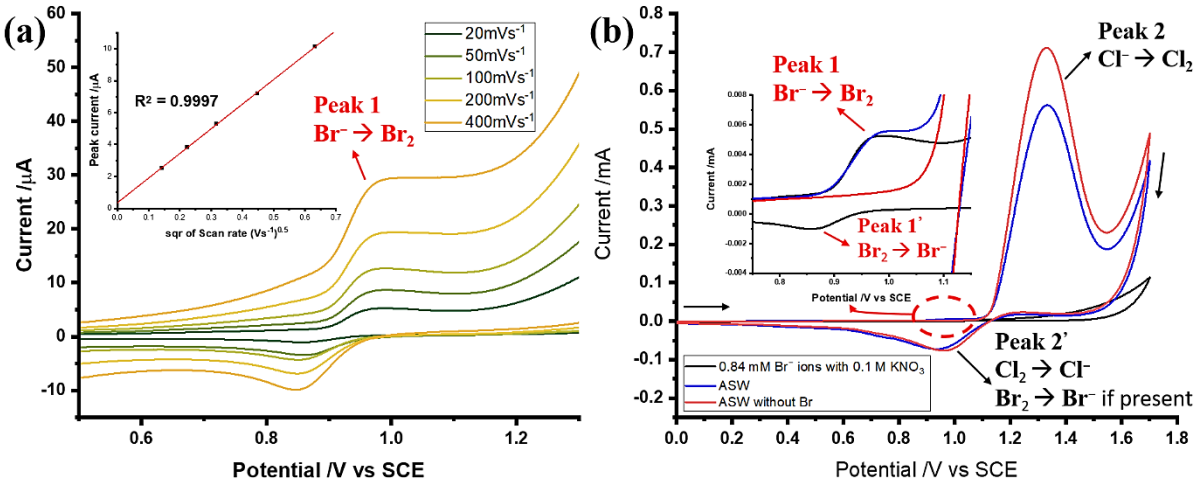

Figure.5.4 (a) Cyclic voltammograms in degassed 0.84 mM Br^- with 0.1 M KNO_3 at variable scan rates of 20, 50, 100, 200 and 400 mV s^{-1}. The inset shows the plot of peak currents of bromide peak as a function of the square root of scan rate. See text for details of the scan range and the start potential. (b) Cyclic voltammograms for Br^- detection using a Pt macro-electrode at a scan rate of 20 mV s^{-1} in degassed 0.84 mM Br^- in 0.1 M KNO_3 (black line), ASW (blue line) and ASW without Br (red line). The inset shows the enlarged CV focusing on bromide redox peaks. See text for details of the scan range and the start potential.

To study the response of Pt electrodes towards bromide in ASW, cyclic voltammetric experiments starting at 0 V vs SCE, swept towards 1.7 V and back to 0 V were again employed in degassed ASW and ASW containing no Br^- at a scan rate of 20 mVs^{-1} (blue line and red line in Figure.5.4 (b)). The ASW voltammogram is dominated by the oxidation of chloride (Peak 2) and the corresponding reduction peak on the reverse scan. The oxidation peak is seen at 1.33 V vs SCE (Peak 2) with a corresponding reduction peak at around 0.96 vs SCE (Peak 2'). One of

the possible products could be hypochlorous acid ($HOCl/OCl^-$) referring to the Pourbaix diagram reported by Radepont *et al.* [57]. As shown in the insert of Figure.5.4 (b), Peak 1 attributed to the oxidation Br^- was still clearly resolved in ASW (blue line), while it was not seen in the absence of bromide (red line). Meanwhile, Peak 2 related to the oxidation Cl^- obtained in ASW (blue line) has a peak height lower than that in ASW without presence of bromide (red line). This is likely explained by that due to the finite surface area of the Pt working electrode, the blockage of its surface by Br^- and/or the oxidised product results to less area available for the chloride oxidation.

To conclude, importantly, the signal of oxidation of Cl^- does not mask the oxidation peak of bromide when voltammetry is conducted in ASW when studied with a platinum electrode. Thus, a Pt macro-disc electrode was evidenced to be suitable for further sensitivity analysis of bromide ions in ASW and natural seawater, as discussed in the following section.

5.3.3 Sensitivity Analysis by Standard Additions Using SWV

In this section, the electroanalytical responses of bromide ions in the presence of high levels of chloride, namely in ASW, were explored on a Pt macro-disc electrode. Standard additions were used since it is recognised as especially appropriate when the sample composition is unknown and/or complex and affects the analytical signal. [39] To obtain the best-defined square wave voltammograms for sensitivity analysis, the optimisation of SWV parameters, including frequency, step potential and amplitude, was implemented in a degassed ASW (Appendices, Section A5.3). The optimised SWV with a frequency of 50 Hz, amplitude of 10 mV and step potential of 1 mV was then applied in two ASW solutions with different concentrations of bromide corresponding to the usual extreme limits of 0.75 and 0.88 mM encountered in natural seawater [6, 58] to explore the sensitivity of detection. As shown in Figure.5.5 (a) and (b), voltammograms were performed starting at a potential of 0 V vs SCE, and stopping at 1.7 V vs SCE for an oxidative scan. The insets show enlarged SWVs with a potential window from 0.75

to 1.10 V, focusing on the bromide peak. Additions of 0.1-0.5 mM KBr to two ASW solutions were conducted. The measurements in the mixture with each addition were repeated three times. There are two oxidation peaks, namely of bromide (0.94 V vs SCE) and of chloride (1.26 V vs SCE), observed at similar potentials as in the CVs (Figure.5.4 (b)). To analyse the data, the oxidation peak currents of the bromide were recorded. The plots of peak current against the concentration of bromide added to original ASW samples with 0.75 mM and 0.88 mM Br^- are shown in Figure.5.5 (c) and (d) respectively. Both showed good linearity. The intercept on the x-axis corresponds to the unknown initial concentration of the analyte. [39] Thus, the intercepts of –0.72 ± 0.03 mM obtained from Figure.5.5 (c) and –0.93 ± 0.05 mM from Figure.5.5 (d) provide a good agreement with the original bromide concentrations in the ASW samples.

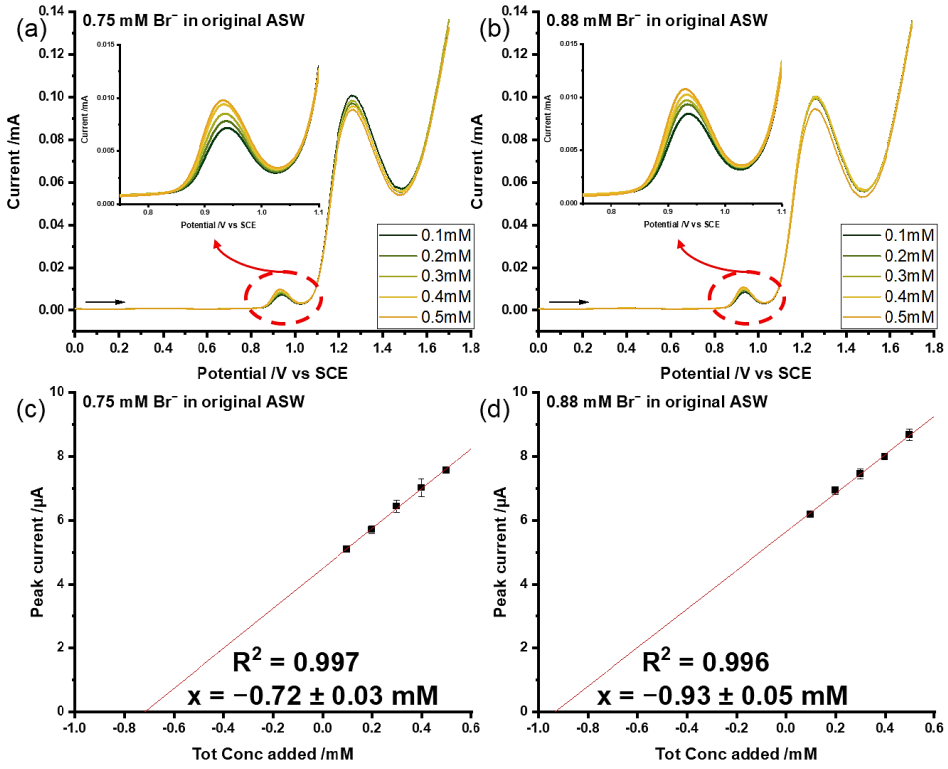

Figure.5.5 Square wave voltammograms (frequency 50 Hz, step potential 1 mV, and amplitude 10 mV) recorded at a macro-Pt electrode in degassed ASW with original bromide concentrations of (a) 0.75 mM and (b) 0.88 mM (the inset shows enlarged SWVs with a potential window from 0.75 to 1.10 V, focusing on the bromide peak); see text for details of the scan range and the start potential. Graphical analysis of standard additions to ASW with an original bromide concentration of (c) 0.75 mM and (d) 0.88 mM.

5.3.4 Real Sample Analysis in Natural Waters

As discussed in the last section, SWV combined with the standard addition method is appropriate for determining the bromide concentration in ASW. To assess the reliability and feasibility of SWV for the electrochemical analysis of real samples, the analysis of three different real samples was performed. The preparation procedure is as described in Experimental section. Ion chromatography measurements were made to independently study the composition of the three samples, the results of which are summarised in Section A5.4. The concentrations of bromide obtained by IC are compared below with the values measured electrochemically.

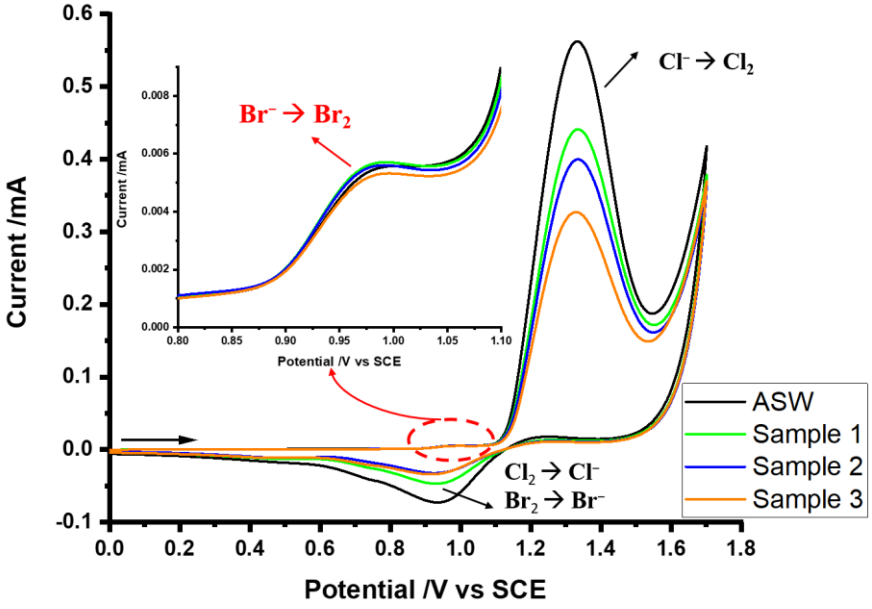

Figure.5.6 Cyclic voltammograms for Br^- detection using a Pt macro-electrode at a scan rate of 20 mV s^{-1}. The start potential was 0 V vs SCE with measurements made in degassed ASW (black line), sample 1 (green line), sample 2 (blue line), and sample 3 (orange line); the inset shows the zoomed CV focusing on bromide oxidation peaks.

Cyclic voltammetry using a Pt macro-disc electrode was used to study the three degassed samples of natural seawater. As shown in Figure.5.6, the scans start at 0 V vs SCE, sweep towards 1.7 V before returning to 0 V. The voltammograms obtained in three natural samples (green, blue and orange lines) have the same voltammetric features as were observed in ASW

(black line). To reiterate, the oxidation peak at ca 0.99 V vs SCE corresponds to bromide oxidation (see insert) and the one at 1.33 V vs SCE corresponds to chloride oxidation, with a reduction peak seen at ca 0.93 V vs SCE.

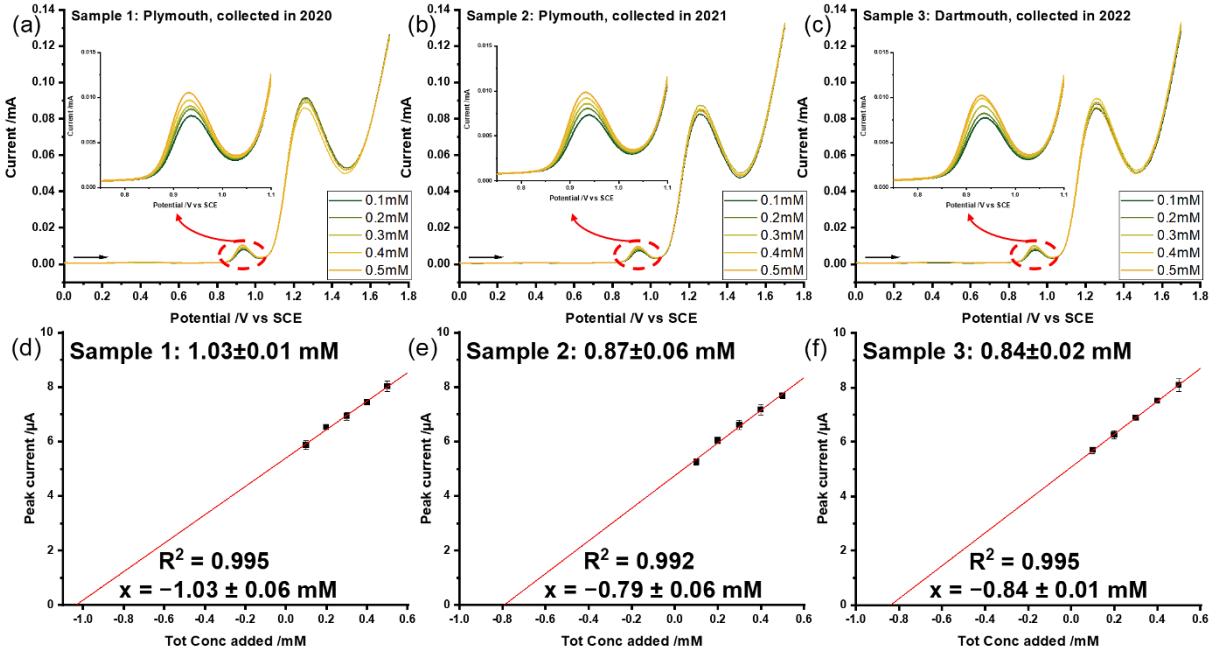

Figure.5.7 Square wave voltammograms (frequency 50 Hz, step potential 1 mV, and amplitude 10 mV) recorded using a macro-Pt electrode in degassed (a) sample 1, (b) sample 2 and (c) sample 3 (the inset shows enlarged SWVs, focusing on bromide peak); see text for details of the scan range and the start potential. Graphical treatment of standard additions to (d) sample 1, (e) sample 2 and (f) sample 3.

Then, three independent analyses were performed for each sample using SWV and the method of standard additions as described in the last section. SWV with the previously optimised parameters of a frequency of 50 Hz, amplitude of 10 mV and step potential of 1 mV was applied and additions of 0.1-0.5 mM KBr to each of them were conducted. As shown in Figure.5.7 (a), (b) and (c), voltammograms were conducted starting at a potential of 0 V vs SCE, and stopping at 1.7 V vs SCE for an oxidative scan. There are two oxidation peaks, namely of bromide (ca 0.93 V vs SCE) and of chloride (ca 1.26 V vs SCE), observed at similar potentials as in ASW (Figure.5.5 (a) and (b)). To analyse the data, the oxidation peak currents of the bromide were recorded as a function of additions of bromide. The plots of peak current against

the total concentration of bromide added to original natural seawater samples are shown in Figure.5.7 (e), (f) and (g) respectively and display good linearity. Table 5.3 summarises the intercepts on the x axis, corresponding to the unknown initial concentrations of bromide in the three samples, and are compared with that measured by IC. Clearly, the developed electrochemical analysis results in a good agreement with IC, even for sample 1 containing bromide ions with a concentration higher than the expected value in natural seawater.

Table 5.3 Comparison of the measured bromide concentrations in three seawater samples

	Measured [Br^-] using SWV /mM	**Measured [Br^-] using IC /mM**
Sample 1	1.03 ± 0.06	1.03 ± 0.01
Sample 2	0.79 ± 0.06	0.87 ± 0.06
Sample 3	0.84 ± 0.01	0.84 ± 0.02

5.4 Conclusions

Though literature shows that silver electrodes can be used for bromide detection in the presence of similar concentrations of chloride [46, 49, 53], the bromide signal obtained in seawater is masked by the much larger chloride signal as reported above. Thus, the use of a Pt macro-disc electrode as an alternative was explored in artificial seawater first, followed by analysis of real seawater samples. By employing SWV to improve the sensitivity and using the standard addition method, a selective quantification of bromide ions can not only be achieved in ASW, but also in natural seawater, despite the high concentration of chloride and the highly complex matrix that is seawater. The obtained concentration of bromide in each sample shows a good match with that measured by ion chromatography, which indicates that electrochemistry may offer a better option with the benefits of low cost, simplicity and rapidity with comparable selectivity for bromide detection in seawater.

Appendices

Section A5.1: Calculation of Transfer Coefficients from Tafel Analysis

This section reports the use of Tafel analysis for obtaining the transfer coefficient β for the bromide oxidation reaction (BOR) at a Pt macro-disc electrode. As shown in Figure.A5.1 (a), cyclic voltammograms were recorded in degassed 0.84 mM Br^- with 0.1 M KNO_3 at variable scan rates of 20, 50, 100, 200 and 400 mV s^{-1}. The potential started at 0 V vs SCE, swept towards 1.7 V before returning to 0 V. An oxidation peak is seen at 0.98 V vs SCE and one reduction peak at 0.85 V vs SCE were observed at different scan rates. The transfer coefficient β was calculated from Eqn. (5.8). [59]

$$\beta = \frac{RT}{F}\frac{\partial ln|I_{ox}|}{\partial E} \qquad (5.8)$$

where I_{ox} is the oxidative current.

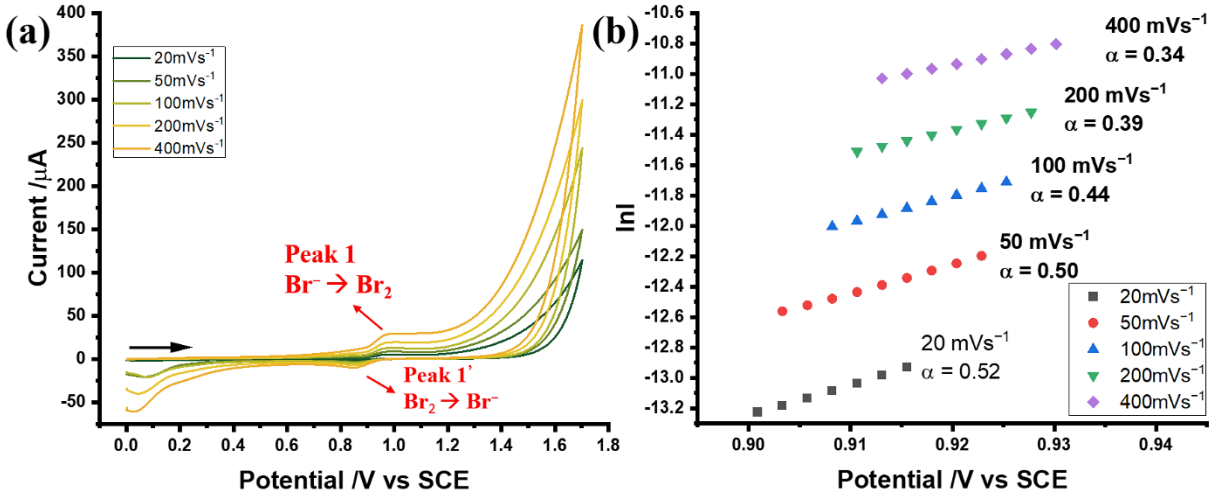

Figure.A5.1 (a) Cyclic voltammograms in degassed 0.84 mM Br^- with 0.1 M KNO_3 at variable scan rates of 20, 50, 100, 200 and 400 mV s^{-1}. The potential started at 0 V vs SCE, swept towards 1.7 V before returning to 0 V. (b) The Tafel plots for the BOR at Pt macro-disc electrode in of 0.84 mM Br^- ions supported by 0.1 M KNO_3 recorded with different scan rates (20, 50, 100, 200 and 400 mVs^{-1}). 10% - 30% of the current range of the forward wave was used.

For the BOR at Pt macro-disc electrode in of 0.84 mM Br^- ions supported by 0.1 M KNO_3 recorded with different scan rates (20, 50, 100, 200 and 400 mVs^{-1}), Tafel plots of $ln|I_{ox}|$ vs potential (V vs SCE) are shown in Figure.A5.1 (b). An average β value was calculated to be 0.44 ± 0.07 for BOR indicating that in the media studied the reaction is electrochemically irreversible.

Section A5.2: Calculation of the Bromide Diffusion Coefficient

This section explains the calculation of the diffusion coefficients, D, for Br^- from the voltammograms obtained as a function of scan rate for BOR. The Randles–Ševčík equation for an irreversible one-electron transfer reaction, $A - e^- \rightleftharpoons B$, was used to estimate the D for Br^- [59]:

$$I_p = 2.99 \times 10^5 \sqrt{\beta}[A]_{bulk} D^{0.5} A v^{0.5} \qquad (5.9)$$

where I_p is the oxidative peak current, β is the transfer coefficient calculated from the Tafel analyses discussed in previous section, A is the area of the Pt macro-disc electrode (0.02 cm^2). $[A]_{bulk}$ is the bulk concentration of the bromide ions (0.84 mM). Figure.A5.2 shows that the peak current scales with the square root of the voltage scan rate as predicted. The linearity confirms a diffusion-controlled electrode process. The diffusion coefficient of the bromide ion in 0.1 M KNO_3 was measured with a value of 2.1×10^{-5} cm^2/s which compares well with the literature value of 2.08×10^{-5} cm^2/s [56] and 2.1×10^{-5} cm^2/s [60].

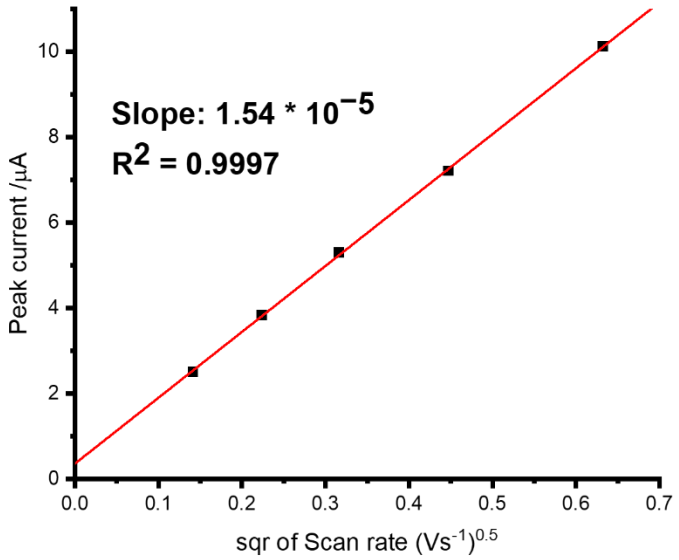

Figure.A5.2 The calibration plot of the peak current of I_p against the concentration of bromide ions measured with a scan rate of 20 mVs^{-1}.

Section A5.3: The Optimisation of SWV Parameters

This section reports the effect of three parameters (frequency, step potential and amplitude) on the SWV signal as tested for the oxidation of bromide ions. Voltammograms were measured in a degassed ASW from a potential of 0 V vs SCE, and stop at 1.7 V vs SCE for an oxidative scan. The optimisation of step potential and amplitude was first performed with a fixed frequency of 50 Hz whilst varying the step potential and amplitude. Figure.A5.3 shows recorded SWVs with a potential range from 0.7 to 1.1 V focusing on the bromide peak (0.94 V vs SCE). Comparison of all the SWVs showed that an amplitude of 10 mV, and a step potential of 1 mV gave a well-defined peak with the best resolution (Figure.A5.3 (a)).

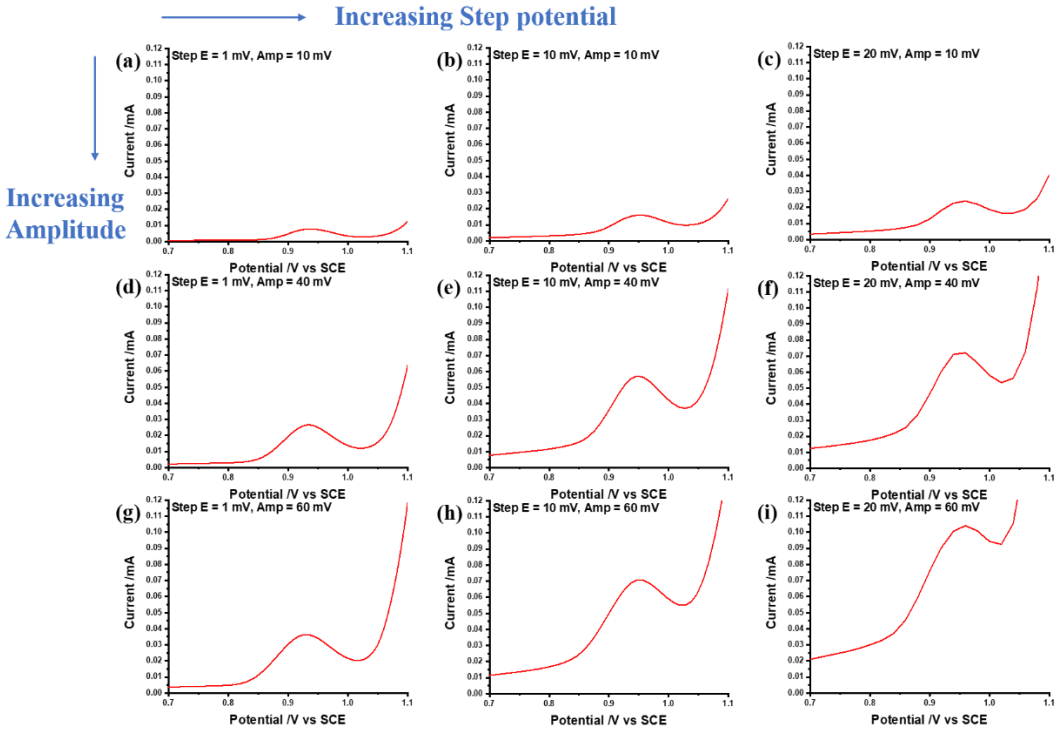

Figure.A5.3 Effect of increasing step potential (from left to right) and increasing amplitude (downward) on the SWV (focusing on bromide oxidation peak) with a fixed frequency of 50 Hz in a degassed ASW. (a) Step E = 1 mV, Amp = 10 mV, (b) Step E = 10 mV, Amp = 10 mV, (c) Step E =20 mV, Amp = 10 mV, (d) Step E = 1 mV, Amp = 40 mV, (e) Step E = 10 mV, Amp = 40 mV, (f) Step E = 20 mV, Amp = 40 mV, (g) Step E = 1 mV, Amp = 60 mV, (h) Step E = 10 mV, Amp = 60 mV, (i) Step E = 20 mV, Amp = 60 mV.

Then, adopting an amplitude of 10 mV and the step potential of 1 mV, the optimisation of the frequency was conducted (Figure.A5.4). Figure.A5.4 (f) indicates overlaid SWVs to demonstrate the effect of varying frequency on the peaks. There are again two oxidation peaks observed, namely of bromide (ca. 0.94 V vs SCE) and of chloride (ca. 1.26 V vs SCE), the peak currents of which increase with the frequency. An acceptable peak shape of bromide oxidation relative to the background at a frequency of 50 Hz was obtained as shown by Figure.A5.4 (c). Thus, the optimised SWV with a frequency of 50 Hz, amplitude of 10 mV and step potential of 1 mV was applied to record the electroanalytical responses of bromide ions in the presence of high levels of chloride.

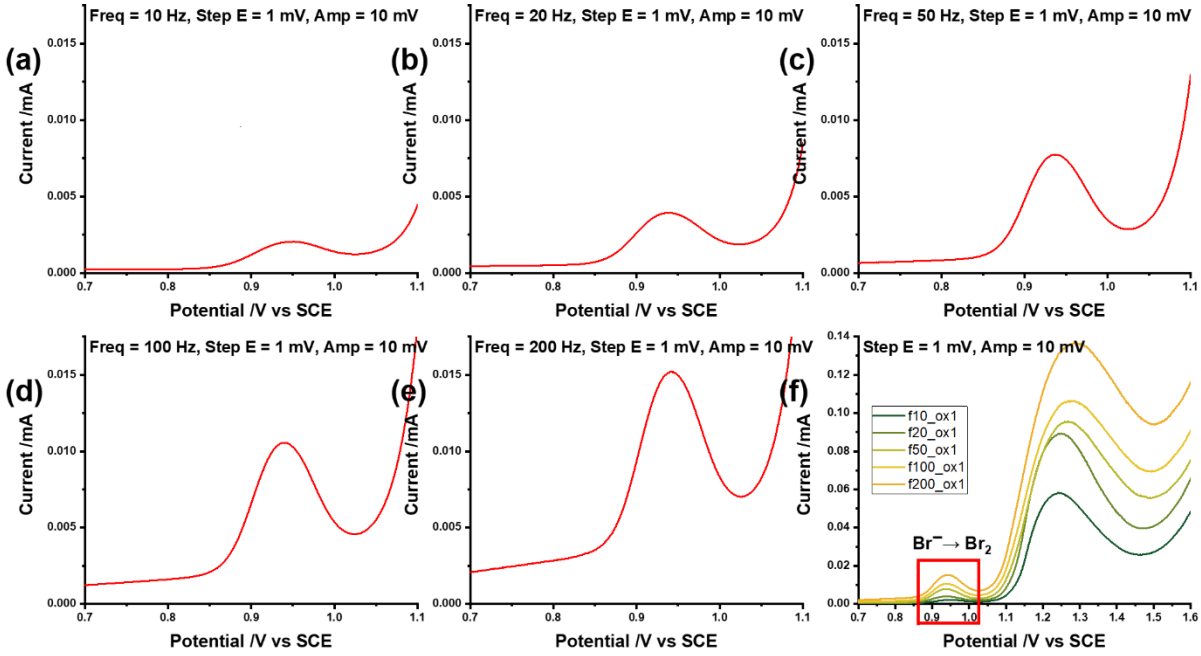

Figure.A5.4 Effect of frequency on the SWV (focusing on bromide oxidation peak) with fixed step potential (1 mV) and amplitude (10 mV) in a degassed ASW. (a) Freq = 10 Hz, (b) Freq = 20 Hz, (c) Freq = 50 Hz, (d) Freq = 100 Hz, (e) Freq = 200 Hz, (f) Overlaid SWV with various frequencies, Step E = 1 mV and Amp = 10 mV.

Section A5.4: The Composition of Natural Seawater Obtained by Ion Chromatography Measurements

Ion chromatography measurements were made using a Dionex (Thermo Scientific, Sunnyvale, CA, USA) ICS-5000+ SP instrument. Separations were carried out using a Dionex IonPac AS23-4um analytical column. The three samples of seawater were each diluted 200-fold with deionized water prior to the analysis. For each sample, two measurements were conducted. The composition of three samples was summarised in Table A5.1.

Table A5.1 Composition of natural seawater

	Fluoride / ppm	Chloride / ppm	Nitrite/ ppm	Bromide / ppm	Nitrate / ppm	Phosphate / ppm	Sulfate / ppm
Sample 1-Measurement 1	0.0076	126.63	n.a.	0.41	n.a.	n.a.	12.08
Sample 1-Measurement 2	0.0077	123.90	n.a.	0.41	n.a.	n.a.	11.75
Sample 2-Measurement 1	0.0070	102.62	n.a.	0.33	n.a.	n.a.	9.44
Sample 2-Measurement 2	0.0063	102.96	n.a.	0.37	n.a.	n.a.	8.89
Sample 3-Measurement 1	0.0066	102.17	n.a.	0.33	n.a.	n.a.	14.31
Sample 3-Measurement 2	0.0067	103.19	n.a.	0.34	n.a.	n.a.	14.49

References

1. Y. Chen and R. G. Compton, *Talanta*, 2023, **253**, 124019.
2. F. R. Spellman, *The Handbook of Nature*, Bernan Press, 2019, Lanham, USA.
3. F. Chai, K. S. Johnson, H. Claustre, X. Xing, Y. Wang, E. Boss, S. Riser, K. Fennel, O. Schofield and A. Sutton, *Nature Reviews Earth & Environment*, 2020, **1**, 315-326.
4. H. K. Lotze, D. P. Tittensor, A. Bryndum-Buchholz, T. D. Eddy, W. W. L. Cheung, E. D. Galbraith, M. Barange, N. Barrier, D. Bianchi, J. L. Blanchard, L. Bopp, M. Büchner, C. M. Bulman, D. A. Carozza, V. Christensen, M. Coll, J. P. Dunne, E. A. Fulton, S. Jennings, M. C. Jones, S. Mackinson, O. Maury, S. Niiranen, R. Oliveros-Ramos, T. Roy, J. A. Fernandes, J. Schewe, Y.-J. Shin, T. A. M. Silva, J. Steenbeek, C. A. Stock, P. Verley, J. Volkholz, N. D. Walker and B. Worm, *Proceedings of the National Academy of Sciences of the USA*, 2019, **116**, 12907-12912.
5. U.S. Environmental Protection Agency, https://www.epa.gov/ocean-acidification/understanding-science-ocean-and-coastal-acidification, (accessed on 6 December 2021, 2021).
6. K. Uraisin, T. Takayanagi, M. Oshima, D. Nacapricha and S. Motomizu, *Talanta*, 2006, **68**, 951-956.
7. S.-M. Fan and D. J. Jacob, *Nature*, 1992, **359**, 522-524.
8. A. C. Leri and S. C. Myneni, *Geochimica et Cosmochimica Acta*, 2012, **77**, 1-10.
9. X. Wei, M. Yang, Q. Zhu, E. D. Wagner and M. J. Plewa, *Environmental Science & Technology*, 2020, **54**, 8909-8918.
10. J. M. Allen, M. J. Plewa, E. D. Wagner, X. Wei, K. Bokenkamp, K. Hur, A. Jia, H. K. Liberatore, C.-F. T. Lee, R. Shirkhani, S. W. Krasner and S. D. Richardson, *Environmental Science & Technology*, 2022, **56**, 392-402.
11. P. S. Heckerling and K. A. Ammar, *American Journal of Nephrology*, 1996, **16**, 537-539.
12. S. Suzuki, K. Kawakami, F. Nakamura, S. Nishimura, K. Yagi and M. Seino, *Epilepsy Research*, 1994, **19**, 89-97.
13. M. E. Pilson, *An Introduction to the Chemistry of the Sea*, Cambridge University Press, 2012, Cambridge, UK.
14. E. L. Lewis, *Marine Geodesy*, 1982, **5**, 350-357.
15. G. S. Lagerloef, C. T. Swift and D. M. Le Vine, *Oceanography*, 1995, **8**, 44-50.
16. J. J. Morgan and W. Stumm, *Aquatic Chemistry: An Introduction Emphasizing Chemical Equilibria in Natural Waters*, New York, NY, John Wiley & Sons, 1981.
17. E. Salameh, A. Tarawneh and M. Al-Raggad, *Arabian Journal of Geosciences*, 2016, **9**, 1-20.
18. D. R. Jones, *Talanta*, 1993, **40**, 43-51.
19. P. I. Anagnostopoulou and M. A. Koupparis, *Analytical Chemistry*, 1986, **58**, 322-326.
20. W. J. M. Emaus and H. J. Henning, *Analytica Chimica Acta*, 1993, **272**, 245-250.
21. K. Uraisin, D. Nacapricha, S. Lapanantnoppakhun, K. Grudpan and S. Motomizu, *Talanta*, 2005, **68**, 274-280.
22. N. Yonehara, S.-i. Chaen, T. Tomiyasu and H. Sakamoto, *Analytical Sciences*, 1999, **15**, 277-281.
23. S. M.R. and J. R. Elah, *International Journal of Industrial Chemistry*, 2011, **2**, 27-32.
24. A. Sheibani, M. R. Shishehbore and Z. T. Ardakani, *Chinese Chemical Letters*, 2011, **22**, 595-598.
25. H. Akaiwa, H. Kawamoto and M. Osumi, *Talanta*, 1982, **29**, 689-690.
26. S. Seefeld and U. Baltensperger, *Analytica Chimica Acta*, 1993, **283**, 246-250.
27. H. Fabre, M. D. Blanchin and N. Bosc, *Analytica Chimica Acta*, 1999, **381**, 29-37.

28. O. Stålberg, K. Sander and C. Sänger-van de Griend, *Journal of Chromatography A*, 2002, **977**, 265-275.
29. J. P. Pascali, M. Trettene, F. Bortolotti, G. d. Paoli, R. Gottardo and F. Tagliaro, *Journal of Chromatography B*, 2006, **839**, 2-5.
30. K. Fukushi, K. Watanabe, S. Takeda, S.-I. Wakida, M. Yamane, K. Higashi and K. Hiiro, *Journal of Chromatography A*, 1998, **802**, 211-217.
31. N. Kocatürk, N. Öztekin and F. Bedia Erim, *Analytical and Bioanalytical Chemistry*, 2003, **377**, 1207-1211.
32. G. Rechnitz and M. Kresx, *Analytical Chemistry*, 1966, **38**, 1786-1788.
33. E. M. Zahran, Y. Hua, Y. Li, A. H. Flood and L. G. Bachas, *Analytical Chemistry*, 2010, **82**, 368-375.
34. Ö. Isildak, O. Özbek and K. Yigit, *Bulgarian Chemical Communications*, 2020, **52**, 448-452.
35. D. Vlascici, N. Plesu, G. Fagadar-Cosma, A. Lascu, M. Petric, M. Crisan, A. Belean and E. Fagadar-Cosma, *Sensors*, 2018, **18**, 2297.
36. L. Pittwell, *Microchimica Acta*, 1975, **64**, 425-429.
37. J. H. Butler, J. E. Pequegnat, L. I. Gordon and R. D. Jones, *Estuarine, Coastal and Shelf Science*, 1988, **27**, 181-203.
38. K. C. Thompson and P. Quevauviller, *Analytical Methods for Drinking Water: Advances in Sampling and Analysis*, John Wiley & Sons, 2005.
39. D. C. Harris, *Quantitative Chemical Analysis*, Macmillan, 2010, London, UK.
40. G. G. Mohamed, T. A. Ali, M. F. El-Shahat, A. M. Al-Sabagh and M. A. Migahed, *Electroanalysis*, 2010, **22**, 2587-2599.
41. G. A. Rechnitz and M. R. Kresx, *Analytical Chemistry*, 1966, **38**, 1786-1788.
42. NT Sensors, Bromide Ion Selective Electrode (ISE), https://www.ntsensors.com/parameters/bromide-ion-selective-electrode/#tab-id-2, (accessed June 24th, 2022).
43. einstein™ Sensors, Bromide Sensor, http://einsteinworld.com/product/bromide-sensor/, (accessed June 24th, 2022).
44. Electro-Chemical Devices, Bromide Sensor, https://ecdi.com/portfolio-item/bromide-sensors, (accessed June 24th, 2022).
45. J. Milikić, I. Stoševski, J. Krstić, Z. Kačarević-Popović, Š. Miljanić and B. Šljukić, *Journal of Analytical Methods in Chemistry*, 2017, **2017**, 2028417.
46. X. Qin, H. Wang, Z. Miao, X. Wang, Y. Fang, Q. Chen and X. Shao, *Talanta*, 2011, **84**, 673-678.
47. Y. Guo and R. G. Compton, *Talanta*, 2021, **232**, 122502.
48. X. Qin, Z. Miao, X. Du and Q. Chen, *Electroanalysis*, 2016, **28**, 555-561.
49. K. Arai, F. Kusu, N. Noguchi, K. Takamura and H. Osawa, *Analytical Biochemistry*, 1996, **240**, 109-113.
50. A. J. Bard, R. Parsons and J. Jordan, *Standard Potentials in Aqueous Solution*, Routledge, 2017.
51. F. M. M. Morel, J. G. Rueter, D. M. Anderson and R. R. L. Guillard, *Journal of Phycology*, 1979, **15**, 135-141.
52. T. J. Smyth, J. R. Fishwick, L. AL-Moosawi, D. G. Cummings, C. Harris, V. Kitidis, A. Rees, V. Martinez-Vicente and E. M. S. Woodward, *Journal of Plankton Research*, 2009, **32**, 585-601.
53. J. Bujes-Garrido, D. Izquierdo-Bote, A. Heras, A. Colina and M. J. Arcos-Martínez, *Analytica Chimica Acta*, 2018, **1012**, 42-48.
54. K. Tsuji and P. J. Elving, *Analytical Chemistry*, 1969, **41**, 216-&.

55. J. Yu, M. Yang, C. Batchelor-McAuley, S. Barton, R. E. M. Rickaby, H. A. Bouman and R. G. Compton, *ACS Measurement Science Au*, 2022, **2**, 342-350.
56. R. E. White and S. E. Lorimer, *Journal of the Electrochemical Society*, 1983, **130**, 1096-1103.
57. M. Radepont, Y. Coquinot, K. Janssens, J.-J. Ezrati, W. de Nolf and M. Cotte, *Journal of Analytical Atomic Spectrometry*, 2015, **30**, 599-612.
58. K. K. Turekian, *Geochimica et Cosmochimica Acta*, 1977, **41**, 1139-1144.
59. R. G. Compton and C. E. Banks, *Understanding Voltammetry*, World Scientific, 3rd edition, 2018.
60. H. Chen, A. Kaliyaraj Selva Kumar, H. Le and R. G. Compton, *Journal of Electroanalytical Chemistry*, 2020, **876**, 114730.

Chapter 6

Direct Electrochemical Analysis in Seawater: Chloride and Bromide Detection

Chloride and bromide are two of the most abundant anions found in seawater, and knowledge of their concentrations is essential for environmental monitoring. However, the analysis of chloride and bromide in seawater is challenging due to the complex nature of the seawater matrix. Inspired by the bromide detection using a Pt electrode as discussed in the precious chapter, in **Chapter 6**, we investigate the suitability of three types of electrodes (Au, glassy carbon, and Pt) for the analysis of Cl^- and/or Br^- in seawater. With the understanding of their electrochemical behaviours in artificial seawater (ASW), optimal voltammetric procedures for their detection are developed. The results show that the Au electrode is unsuitable for use as a Cl^- and/or Br^- sensor due to its dissolution and passivation in ASW. The use of glassy carbon results in poorly defined chloride and bromide signals. Finally, platinum was found to be a good candidate for chloride detection in artificial seawater using square wave voltammetry, and the results obtained in natural seawater by electrochemical measurement were in good agreement with those obtained by ion chromatography. From **Chapters 5-6**, we recommend platinum electrodes for both bromide and chloride analysis.

The work of **Chapter 6** has been published in the journal *Chemosensors* [1]. This article is part of the Special Issue Bionic Recognition and Biosensors: A Theme Issue in Honor of Professor Hong-Yuan Chen.

6.1 Introduction

Water scarcity is a worldwide concern, while climate change exacerbates the water shortage problem [2]. As seawater consists of 96.5% of all known water on the earth and covers

71% of Earth's surface [3], desalinated seawater is a promising solution to the shortage of freshwater, and has been implemented in the Near and Middle East, North Africa, North America and in Mediterranean countries [4]. Meanwhile, noting that the main chemicals in the resultant concentrated seawater, such as salt (sodium chloride), magnesium, potassium and bromine, are basic raw materials for the chemical industry, extracting these highly concentrated and stable chemicals from concentrated seawater reduces energy consumption and makes comprehensive use of natural resources [5, 6]. In this context, to maximise efficiency and utility, an important step is measuring the concentration of targeted ions in seawater before desalination. More generally, it is also meaningful to analyse the compounds in seawater, which reveals the local environment, geology and potential impact on humans. Chloride and bromide are the two anions addressed in this chapter.

As shown in Table 5.1 (Chapter 5), chloride is the most concentrated anion in seawater. The concentration of chloride has been defined as 'chlorinity' [7, 8], and it is so dominant that it was originally used to estimate salinity (the total salts dissolved in seawater) [9]. Salinity is an indicator of the ocean ecosystem, as the relative salt concentration within the body of a creature living in the sea versus the water is what determines the direction of osmotic pressure and the ease of water absorbed into or removed from the body [10]. Meanwhile, measuring the specific chloride level in natural seawater systems is also necessary for both environmental studies and corrosion science. First, toxic substances such as Hg (0) and silver nanoparticles (AgNPs) are more prone to oxidation in the presence of a high concentration of chloride, leading to soluble compounds [11-14]. Secondly, marine chloride can directly lead to metal corrosion [15, 16], which is a major ongoing challenge in shipbuilding and maritime transport.

Bromine is an essential chemical with wide applications, such as in insecticides, flame retardants, refrigerants, photosensitive materials and oilfield mining [17]. About 99% of bromine on earth exists in the form of Br^- in seawater [18], and bromide is one of the most concentrated

anions in seawater (Table 5.1, Chapter 5) [19]. With seawater containing an estimated 89 trillion tonnes of bromine [20], it is one of the main sources of bromine, the extraction of which needs to be informed by measurements of the local concentrations of bromide in seawater. Meanwhile, a key step in seawater desalination is to remove bromide and check its concentration in the resultant water, because it is toxic and carcinogenic [21]. In addition, as the local concentrations of chloride and bromide depend on location and season [22, 23], the ratio between them in normal seawater is used to monitor pollution from agricultural and industrial sources [24, 25]. However, the levels of chloride are hundreds of times higher than those of bromide by weight in natural seawater [26, 27], which can lead to challenges in the determination of Br^- [28, 29]. Thus, it is necessary to develop methods that can measure Cl^- and/or Br^- sensitively and selectively in authentic seawater.

As reported by Guo *et al.* [11], there are several well-established methods to measure the chloride level in seawater. Traditionally, the argentometric method (Mohr's method) [30, 31] and colorimetry using potassium chromate to indicate the endpoint of adding silver nitrate [32] are applied for neutral solutions. Meanwhile, potentiometric titration using silver nitrate [33-35] is considered to be easier and more precise than the colorimetric method, but both involve large sample volumes and toxic chemicals. Thus, instrumental rather than wet methods are currently commonly used for the measurement of chlorinity (*Cl*, g kg^{-1}). Notably, a salinometer based on the electrical conductivity of seawater, together with temperature, provides salinity (*S*) readings. To be more specific, *S* is calculated from the ratio of the conductivity of seawater to that of a KCl solution (32.4356 g/kg), with both measurements made at 15 °C and under one-atmosphere pressure [8, 36-38]. It can then be converted to chlorinity using the Knudsen equation [7]:

$$\boldsymbol{S\ (g\ Kg^{-1}) = 1.80665\ Cl\ (g\ Kg^{-1})} \qquad (6.1)$$

However, there is necessarily a lack of accuracy, as it is an estimated value depending on salinity that primarily indicates the overall ion concentration rather than the chemical

composition [8, 36]. For bromide quantification, there are several techniques available, e.g., kinetic spectrophotometry [39-46], chromatography [47, 48], capillary electrophoresis [49-53] and electrochemistry [54-57], but they have drawbacks from different perspectives [58], which were discussed in the previous chapter.

Electrochemistry provides the benefits of robust, low-cost and simple instrumentation with competitive selectivity and sensitivity, which makes it a potentially good analytical method for bromide and chloride quantification. Although potentiometry has been widely applied as an electrochemical technique [54-57, 59, 60], the complexity of electrode fabrication [55] and the logarithmic relationship between potential and the analyte make it challenging to deliver a precise and sensitive detection. Meanwhile, for existing potentiometric measurements, selectivity, especially for bromide detection with the presence of chloride at hundreds of times the level in seawater, remains a challenge [54, 55]. Indication of the misfunction of potentiometric electrodes is another essential requirement that cannot be easily met. Thus, amperometry is a technique that can avoid the drawbacks of potentiometry [61-65], but traditionally has required analytes with a low concentration so that seawater cannot be directly used. Nevertheless, these problems have recently been solved by Guo *et al*. [11] and Chen et al. [58] (**Chapter 5**), with the first two bespoke regent-free amperometric sensors being proposed for chloride and bromide sensing, respectively, in authentic seawater.

In this Chapter, we assess, compare and contrast different electrode materials for the direct analysis of Cl^- and/or Br^- in seawater. Three electrodes, made of gold, glassy carbon and platinum, are investigated, and the full voltammetric responses seen in undiluted seawater are described and analysed to understand their fundamental (electro-)chemistry using both artificial seawater (ASW) and natural seawater (NSW). The implications for the electrochemical detection of bromide and chloride are assessed, and through optimal voltammetric procedures, we quantify the two anions of interest.

6.2 Experimental

Chemicals and Reagents

Deionised water with a resistivity of 18.2 MΩ cm at 298 K (Millipore, Millipak Express 20, Watford, U.K.) was utilised to prepare all synthetic solutions. All the chemicals used in the experiments were of analytical grade. The "blank" solution with the same ionic strength as seawater [66] was prepared using sodium nitrate ($NaNO_3$, ≥99.5%). Artificial seawater (ASW) was prepared using the composition shown in Table 5.2 of the previous chapter. Details of the chemicals and reagents were listed in Section 2.1.

Electrochemical Apparatus

Electrochemical measurements were conducted using a μAutolab II potentiostat made by Metrohm-Autolab BV in Utrecht, Netherlands. The experiments were performed using a standard three-electrode set-up at a constant temperature of 25.0 ± 0.2 °C in a Faraday cage. The reference and counter electrodes were a mercury–mercurous sulphate electrode (MSE +0.64 V vs SHE, BASi, USA) and a graphite rod in all experiments reported in this chapter. Three different working electrodes were used, namely, a gold macro-electrode (diameter of 1.60 ± 0.01 mm, geometric area of 0.02 cm^2, BASi, USA), a glassy carbon macro-electrode (GCE, diameter of 3.00 ± 0.01 mm, geometric area of 0.07 cm^2, BASi, USA) and a platinum macro-electrode (diameter of 1.66 ± 0.01 mm, geometric area of 0.02 cm^2, BASi, USA). Before each use, the working electrode was polished sequentially with 1.0, 0.3 and 0.05 μm alumina lapping compounds from Bucher, Germany. To remove oxygen from the solutions before electrochemical measurements, high-purity N_2 flow from BOC Gases plc, UK was used as needed. Cyclic voltammetry (CV) was conducted to investigate the electrochemical behaviour of the three working electrodes in ASW. Then, for the quantification of either bromide or chloride in ASW and/or natural seawater, square wave voltammetry (SWV) was applied.

Sample Collection and Ion Chromatography Analysis

There were two authentic seawaters used in this study. Their collection and ion chromatography analysis were described in the previous chapter.

6.3 Results and Discussion

In the following sections, the electrochemical behaviour of a gold electrode in ASW is first reported and interpreted using observations from pure chloride and bromide solutions reported in the literature. Further confirmed by the experiments in ASW, the inferred dissolution of gold in halide solutions is concluded to make Au a less-than-optimal electrode material. Thus, glassy carbon electrodes (GCEs) and Pt electrodes are subsequently considered as alternatives for Cl^- and/or Br^- detection in ASW. In addition to using cyclic voltammetry to assess the merits of the two electrodes as sensors, square wave voltammetry is also attempted/implemented to enhance their sensitivity. In particular, a GCE was used to analyse for Br^- and a Pt electrode for Cl^-, leading to recommendations for the optimal electrode to adopt for each of the two ions. Finally, a bespoke method using a Pt electrode for chloride sensing is applied for quantitative analysis in two samples of natural seawater, while ion chromatography is conducted for the successful validation of the measurements.

6.3.1 Cyclic Voltammetric Study of a Gold Electrode in Artificial Seawater

The electrochemical behaviour of a gold electrode in simple halide solutions has been widely studied since the last century [67-69]. Not least since gold is a noble metal, and methods of extracting, refining, electroplating, electro-etching and electropolishing it have been developed and optimised. As summarised by Nicol [68], chloride and bromide are two ligands that, when present at the millimolar level, coordinate with gold cations and decrease the potential for gold electro-solubilisation in acidic conditions [67, 68]. To be specific, during anodic voltammetric scanning in solutions containing 0.1 M $HClO_4^-$ with either 10 mM Cl^- or Br^-, the oxidation of

Au occurs at similar potentials, ca. 1.0 V vs SCE, with the voltammetric peaks attributed to the conversion of Au into Au (I) or Au (III) [67]. The general mechanism of the electrochemical dissolution of gold in halide solutions is shown below [67, 70]:

$$\boldsymbol{Au + X^- \rightleftharpoons (AuX^-)_{ad}} \quad (6.2)$$

$$\boldsymbol{(AuX^-)_{ad} + X^- \rightleftharpoons (AuX_2^-)_{ad} + e^-} \quad (6.3)$$

$$\boldsymbol{(AuX_2^-)_{ad} \rightleftharpoons AuX_2^-(dissolution)} \quad (6.4)$$

$$\boldsymbol{(AuX_2^-)_{ad} + 2X^- \rightleftharpoons (AuX_4^-)_{ad} + 2e^-} \quad (6.5)$$

$$\boldsymbol{(AuX_4^-)_{ad} \rightleftharpoons AuX_4^-(dissolution)} \quad (6.6)$$

where X represents Cl or Br. It is worth mentioning that the voltammetric peak in perchloric acid corresponding to the oxidation of gold to $AuCl_2^-$ or $AuBr_2^-$ significantly overlaps the peak for $AuCl_4^-$ or $AuBr_4^-$, respectively, and the relative amounts of Au(I) and Au(III) formed during oxidation was reported to be hard to determine [67, 68, 70-72]. Meanwhile, passivation due to the formation of an oxide film was also observed in both halide solutions, at sufficiently positive potentials which were dependent on the pH of the solutions [67, 69, 71, 73, 74]. From the perspective of sensing, the similarity between chloride and bromide presents a significant challenge in terms of selectivity using a gold electrode. Secondly, the unclear mechanism and corresponding species at different stages, namely the dissolution and passivation of gold, make it hard to develop a reliable understanding of the development of a sensor. Moreover, detection in seawater, which presents a much more complex matrix, may be expected to involve further difficulty and uncertainty. Nevertheless, in the following, we report the electrochemical behaviour of gold electrodes in seawater, ultimately leading to confirmation of the conclusion that Au is a poor choice as a Cl^- and/or Br^- sensor.

In following, we turn to experiments on the voltammetry at a gold electrode in seawater where chloride is present at the hundred milli-molar level and the bromide concentration is typically less than 1 mM. Cyclic voltammetric experiments were conducted using an Au

electrode in three degassed artificial seawater (ASW) samples (Figure.6.1). ASW1 contained 0.571 M chloride and 0.84 mM bromide (black line); ASW2 contained 0.484 M chloride and 0.84 mM bromide (blue line); and ASW3 contained 0.571 M chloride and 1.84 mM bromide (green line). Note that for synthetic seawater, the recommended chloride level is in the range of 0.484 M–0.593M [11, 75, 76] and the recommended bromide level is 0.84 mM [75]. The potential sweep started at −0.45 V vs MSE, and swept towards 0.94 V before returning to −0.45 V at a scan rate of 20 mVs^{-1}.

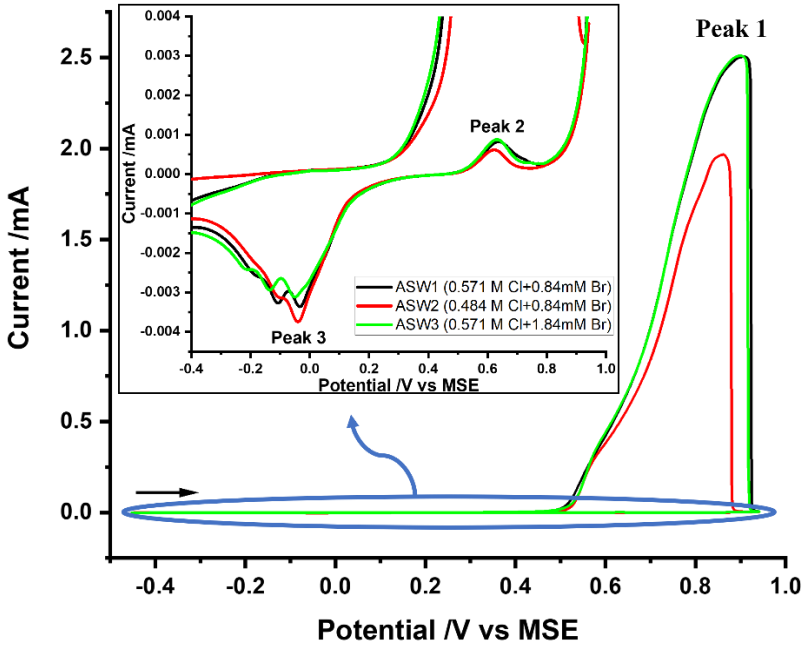

Figure.6.1 Cyclic voltammograms measured at a scan rate of 20 mV s^{-1} using the Au macro-electrode in degassed ASW1(black line), ASW2 (red line) and ASW3 (green line) which contain different concentrations of chloride and bromide as shown in the legend and main text. The start potential is −0.45 V vs MSE, and the stopping potential is 0.94 V vs MSE. Insert: an enlarged CV focusing on the reactivation and reduction peaks.

For ASW1, the voltammetry in Figure.6.1 shows a large anodic peak with a peak potential of 0.90 V vs MSE, followed by abrupt passivation on the forward voltammetric scan. The peak is seen to have a shoulder at ca 0.59 V vs MSE. The abrupt decrease in signal is attributed to the formation of gold oxide on the electrode surface, inhibiting further electron transfer. The main peak and the shoulder are tentatively assigned to the oxidation of Au to $AuCl_4^-$ and $AuBr_4^-$,

and also possibly to the hidden oxidation to $AuCl_2^-$ and $AuBr_2^-$, described by Eqns. (6.2)-(6.6) [67, 70]. The dissolved gold was observed to be partly plated onto the surface of the counter-electrode (Figure.A6.1 (a), Section A6.1) and led to colouration of the solution (Figure.A6.1 (b), Section A6.1) after 20 repeats of the scan, confirming the dissolution of the gold electrode, which would be a serious demerit in terms of its use as a sensor. On changing the scan direction from anodic to cathodic, a small anodic Peak 2 was observed at 0.62 V vs MSE due to partial de-passivation following a loss of material via dissolution during the reverse scan. On continuing to scan reductively, a broad peak (Peak 3) with splitting appears at ca. −0.1 V vs MSE, and is thought to be related to the solubilisation of the gold electrode. The other two solutions show qualitatively analogous responses, as seen in Figure.6.1. Comparison of the voltammograms measured using the three different solutions suggests that the large peak is chloride-related, with the size of the signal qualitatively (but not quantitatively) increasing with the chloride levels. Note that because of the potential and concentration competition between chloride-driven electro-dissolution of the gold and the formation of gold oxide, no simple linear relationship is expected, nor observed, between Peak 1 and the chloride concentration in the seawater. This further discourages the use of gold electrodes for the quantification of chloride in seawater. No clear feature for the oxidation of bromide is visible in any of the voltammograms recorded despite the difference in bromide concentrations. This likely reflects the tiny bromide concentration in comparison with the chloride levels so that any bromide signal is masked by the chloride response. The shoulder noted on Peak 1 is ascribed in the literature to the onset of partial passivation [67, 68, 71, 73], not to bromide oxidation, but in either case, is too ill-defined to be analytically useful.

To summarize, the dissolution and passivation of a Au electrode in artificial seawater were inferred from observations in pure chloride and bromide solutions. It is concluded that a gold electrode is unsuitable for use as a Cl^- and/or Br^- sensor.

6.3.2 Cyclic Voltammetry at Glassy Carbon and Platinum Electrodes in ASW

Next, cyclic voltammetry of ASW using a glassy carbon electrode (GCE) and a Pt electrode was investigated, building on the previous chapter [58]. Cyclic voltammograms were first recorded with a scan rate of 100 mVs^{-1} using either the Pt electrode or the GCE in degassed ASW (Figure.6.2 (a)). For the Pt electrode, the potential sweep started at −0.45 V vs MSE, and swept towards 1.2 V before returning to −0.45 V (red line). For the GCE, the voltammogram started at the same potential of −0.45 V vs MSE, followed by an anodic sweep up to 2.0 V followed by a cathodic scan to −1.3 V before a further anodic sweep back to −0.45 V (blue line). The potential ranges were chosen to obtain both forward and reverse peaks of the redox reactions assigned to the analytes, chloride and bromide, without exceeding the anodic potential of solvent oxidation as discussed as below. The dominant oxidation peak (Peak 2) was observed at 0.94 V vs MSE using the Pt electrode; the corresponding feature appears as a shoulder on the solvent decomposition at ca 1.66 V vs MSE using the GCE. As the insert shows, a first oxidation peak (Peak 1) was recorded at 0.59 V vs MSE using the Pt electrode and 0.86 V vs MSE using the GCE. Referring to the study in the previous chapter [58], Peak 2 is attributed to the oxidation of chloride with the possible formation of hypochlorite/hypochlorous acid ($HOCl/OCl^-$), and Peak 1 is attributed to bromide oxidation with hypobromous acid ($HOBr/OBr^-$). The Peak 2′ corresponds to the reduction of the products from the chloride and bromide oxidation. GC offers a wider anodic potential range compared to platinum.

Inspection of the wave-shapes of the dominant peaks in Figure.6.2 (a) shows that the redox reaction of chloride is relatively much more electrochemically reversible on Pt than on GC, as evidenced by the reduced peak-to-peak separation between the anodic and cathodic peaks, and also the steepness of the current–voltage curves. The Tafel slopes were calculated as described in Section A6.2 [77-80], with the β value for chloride oxidation being 0.64 at the Pt electrode and 0.22 at the GCE. To confirm this relative assessment of reversibility, cyclic voltammetry, with

the same potential range for each electrode, was conducted at a slower scan rate of 20 mVs^{-1} (Figure.6.2 (b)). For the Pt electrode (red line), the oxidation of bromide (Peak 1) occurred at 0.59 V vs MSE and chloride oxidation appeared at 0.94 V vs MSE (Peak 2), followed by a reduction peak at 0.60 V vs MSE (Peak 2′). In contrast to the voltammogram of the Pt electrode that only showed insignificant peak shifts when the slower scan rate was applied, that obtained at the GCE showed more noticeable changes (blue line), with the peak-to-peak separation decreasing with scan rate, as particularly seen in the peak potential of Peak 2′. Again, the chloride oxidation of Peak 2 is heavily merged with the solvent decomposition and is not resolved from it. These observations suggest that chloride oxidation is electrochemically irreversible in GC but less irreversible on Pt.

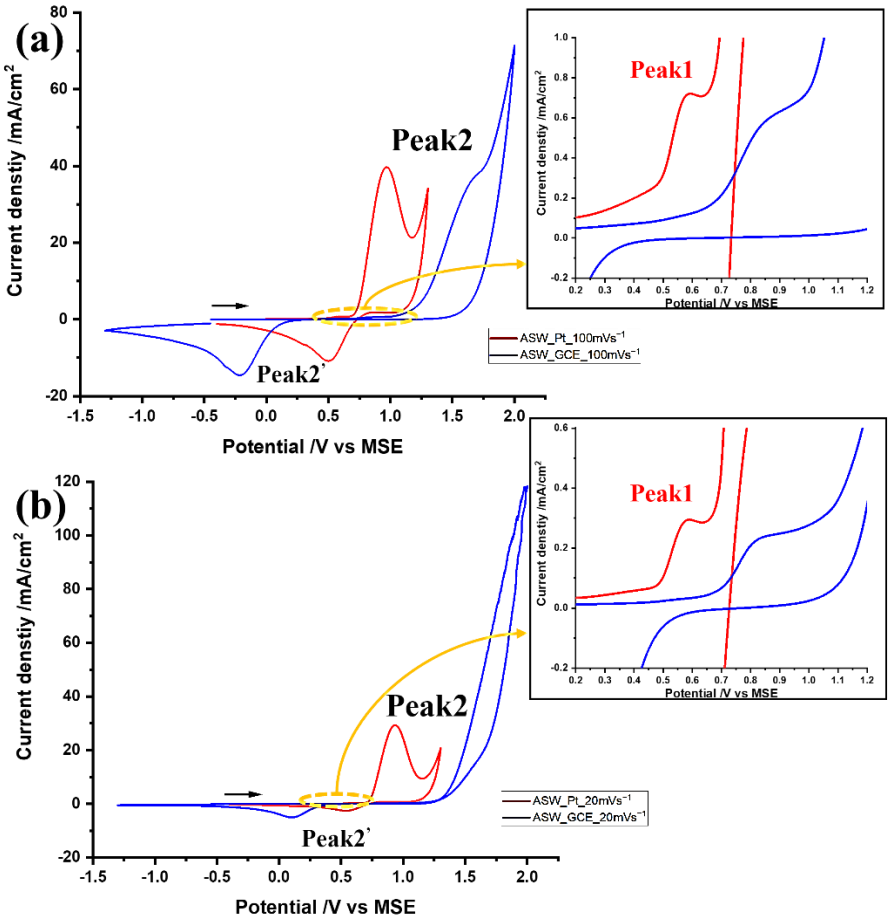

Figure.6.2 Cyclic voltammograms measured using a Pt electrode (red line) and GCE (blue line) in degassed ASW with different scan rates of (a) 100 mVs^{-1} and (b) 20 mVs^{-1}. Insert: expanded bromide oxidation peaks. The start potential was −0.45 V vs MSE.

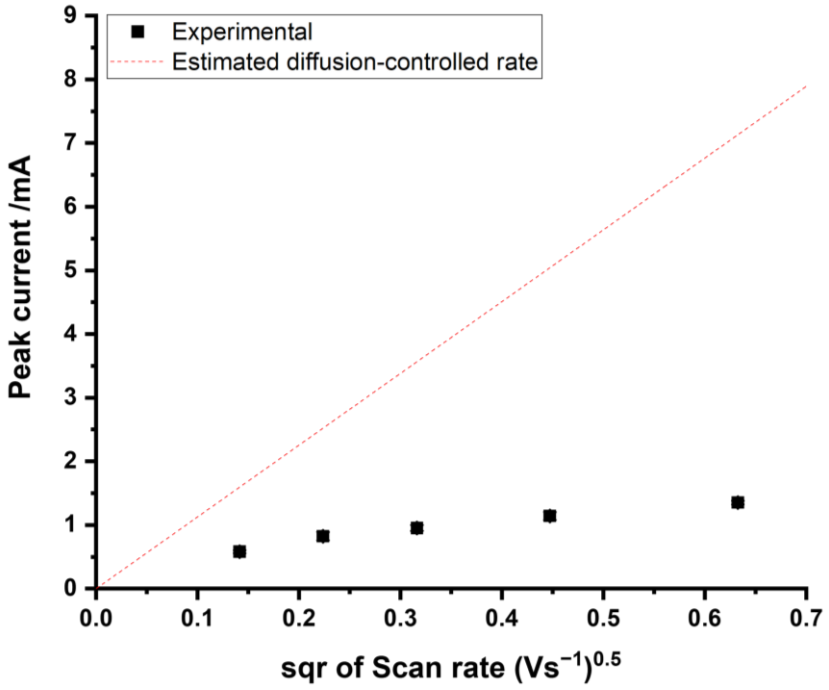

Figure.6.3 The plot of the peak current against the square root of the scan rate. Experimental data: black squares. Estimated diffusion-controlled rate: red dotted line.

From the above, it can be seen that Pt and GC electrodes show signals of similar magnitude (current density) for chloride oxidation, but the proximity of the voltammetric feature to solvent decomposition prevented the identification of a clear peak at the GC electrode, especially at lower scan rates. For the Pt electrode, a plot of the peak current of chloride oxidation obtained experimentally vs the square root of the scan rate is shown in Figure.6.3, where it is compared with the diffusion-controlled response calculated using the Randles–Ševčík equation (Eqn. (6.7)) for an irreversible one-electron reaction at 298K:

$$\boldsymbol{I_p = 2.99 \times 10^5 \sqrt{\beta}(D_{Cl-})^{1/2} C_{Cl-} A v^{1/2}} \qquad (6.7)$$

where the concentration of chloride in ASW is $C_{Cl-} = 0.56 \times 10^{-3}$ mol cm^{-3} [75], the diffusion coefficient of chloride (D_{Cl-}) in seawater is 1.8×10^{-5} cm^2/s [81] and the area (A) of the electrode is 0.02 cm^2. The transfer coefficient reported above ($\beta = 0.64$) was used. Figure.6.3 shows a gradual increase in signal with scan rate, but less than expected for a fully diffusional signal. This likely reflects the extremely high concentration of chloride, resulting in currents in the

order of milliamperes, where the oxidation rate may be largely limited by the availability of adsorption sites for the likely chlorine atom intermediate, together with a contribution to the current from migration effects, since electrolysis is essentially electrically 'unsupported'.

In the case of bromide, signals are seen at less positive potentials than that of chloride for both electrode materials, but these are much smaller in size relative to the chloride peak reflecting the relative concentrations of the two species. Importantly, as the GCE leads to the bromide oxidation peak being more separated from the onset of chloride oxidation compared to the Pt electrode, this gives a superior resolution for Br^- detection. Meanwhile, a Pt electrode is preferable for chloride detection, with a well-defined chloride oxidation peak and a greater degree of electrochemical reversibility. Thus, the use of a GCE for the analysis of bromide ions in ASW was explored further, whilst the merits of using a Pt electrode for the quantitative analysis of chloride were also investigated. In the following sections, the behaviour of the GCE will be discussed first, followed by that of the Pt electrode.

6.3.3 Analysis of Bromide at a Glassy Carbon Electrode

In this section, a GCE is briefly assessed for the oxidation of bromide ions in ASW from an analytical perspective. The study was carried out via cyclic voltammetry with different scan rates of 20, 50, 100, 200 and 400 mVs^{-1}, where the sweep of potential started at −0.45 V vs MSE, and then, swept towards 1.1 V before returning to −0.45 V. The voltammograms are shown in Figure.6.4, where the two features identified above were again observed, namely, bromide oxidation and the corresponding reduction. Although these increased with increasing scan rate, the oxidation of bromide becomes increasingly more difficult to distinguish from the oxidation peak of chloride, which is also found to interfere with the oxygen evolution reaction (OER). In addition to the proximity to chloride oxidation and the OER, the presence of a pre-wave (see below) also prevented quantitative Tafel analysis and the application of the Randles-Ševčík equation. Attempts were made to increase its resolution using square wave voltammetry

but, as reported Section A6.3, these were unsuccessful. Our attention therefore returned to the cyclic voltammetric data and a standard addition [82] approach was adopted.

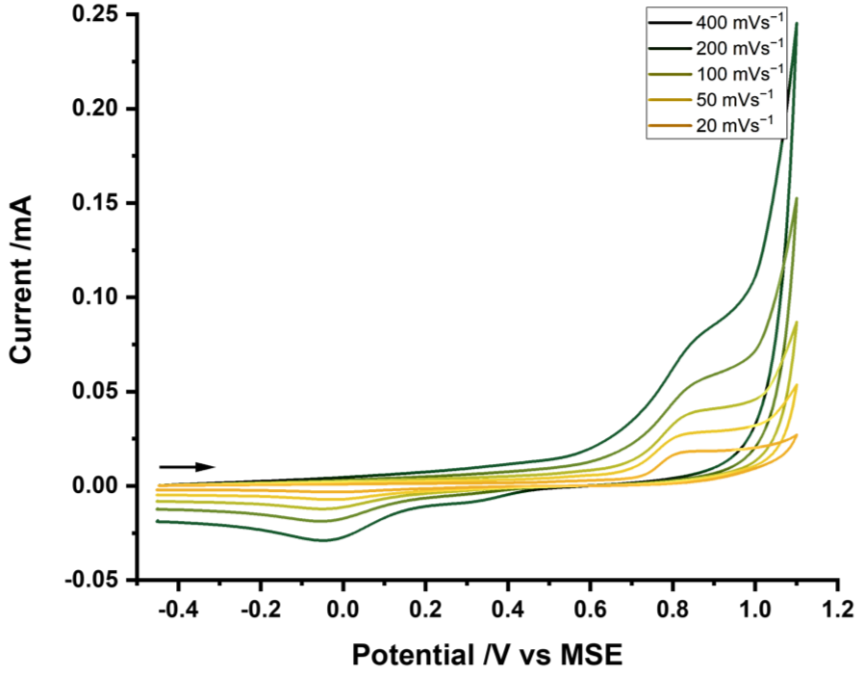

Figure.6.4 Cyclic voltammograms recorded at a GCE in degassed ASW at variable scan rates of 20, 50, 100, 200 and 400 mV s^{-1}.

As shown in Figure.6.5 (a), voltammograms were recorded with a scan rate of 100 mVs^{-1} representing a compromise between a larger Faradaic signal and excessive capacitive charging. The potential scan of the voltammograms started at a potential of −0.45 V vs MSE, with a return potential of 1.1 V, before scanning back to −0.45 V. Figure.6.5 shows that, as expected, Peak 1 increases with the addition of bromide, whilst there is a clear pre-wave to Peak 1 at potentials of around 0.54 V vs MSE. Additions of 0.2-1.0 mM KBr to the ASW solutions were conducted. The measurements taken with each addition were repeated three times. To analyse the data, the oxidation peak currents of Peak 1 were recorded. Because of the pre-wave to Peak 1, a baseline correction was required for each measurement, examples of which are shown in Figure.A6.4, Section A6.4. Figure.6.5 (b) shows a plot of peak current against the concentration of bromide added to the original ASW, indicating good linearity (R^2 = 0.996). As the intercept on the x-

axis corresponds with the unknown initial concentration of the analyte [82], the intercept of –0.84 ± 0.06 mM shows excellent agreement with the known bromide concentration (0.84 mM [75]) in the ASW samples.

Although this suggests the possibility of using a GCE as a bromide sensor, the proximity of bromide oxidation to that of chloride and of the OER to Peak 2, and the challenges of implementing a suitable and unambiguous baseline correction, make this method less attractive than the determination of bromide using a platinum electrode [58], where these problems are mitigated as discussed in the previous chapter.

We next consider the analysis of chloride in seawater using a platinum electrode.

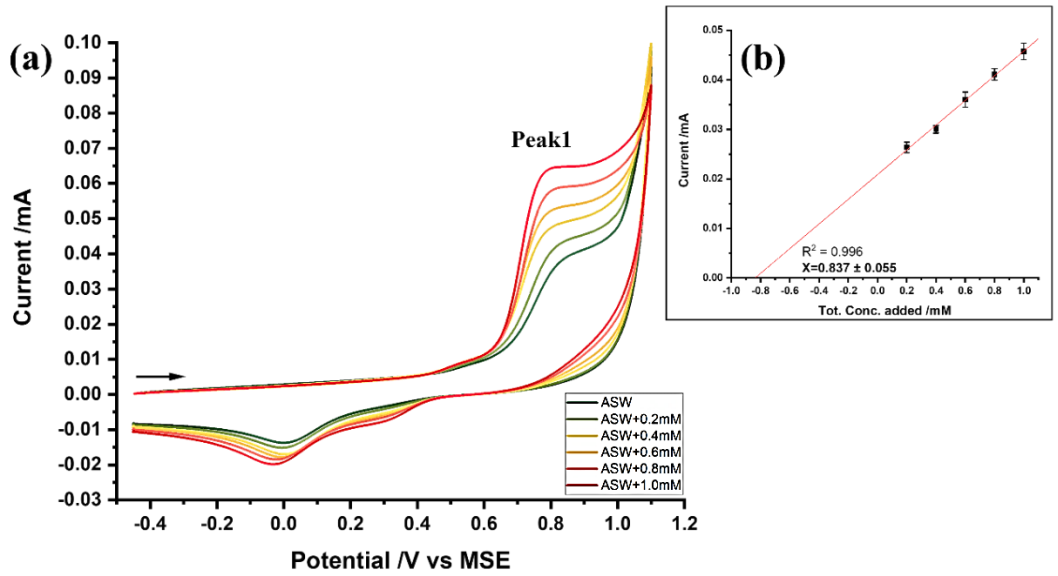

Figure.6.5 (a) ***Cyclic voltammograms recorded at the GCE in degassed ASW and with different standard additions at a scan rate of 100 mV s^{-1}. (b) Graphical analysis of standard addition experiments.***

6.3.4 Analysis of Chloride at the Platinum Electrode

As discussed above, for chloride detection, Pt is a more suitable electrode material compared to GC due to the distinct peak for chloride oxidation and the higher level of electrochemical reversibility. Therefore, the quantitative analysis of chloride in ASW using a Pt electrode was investigated next. This study was conducted in ASW with six different levels

of chloride concentration from 0.484 M to 0.593 M, while the other components followed the standard recipe for ASW (Table 5.2 in the previous chapter [75, 76]). Note that the detection range was expanded slightly beyond the recommended range (from 32 g kg^{-1} to 37 g kg^{-1}) to a range of 31 g kg^{-1} to 38 g kg^{-1} to obtain a potentially wider concentration range of the analyte [11]. To achieve a best-resolved chloride signal, square wave voltammetry was implemented, with the corresponding parameters optimised as shown in Appendices, Section A6.5. A step potential of 1 mV, a frequency of 5 Hz and an amplitude of 50 mV were then employed. To obtain electroanalytical responses, the potential sweep started from −0.45 V and stopped at 1.25 V vs MSE for oxidative scanning in six ASW solutions of variable chloride content in the range specified above (Figure.6.6).

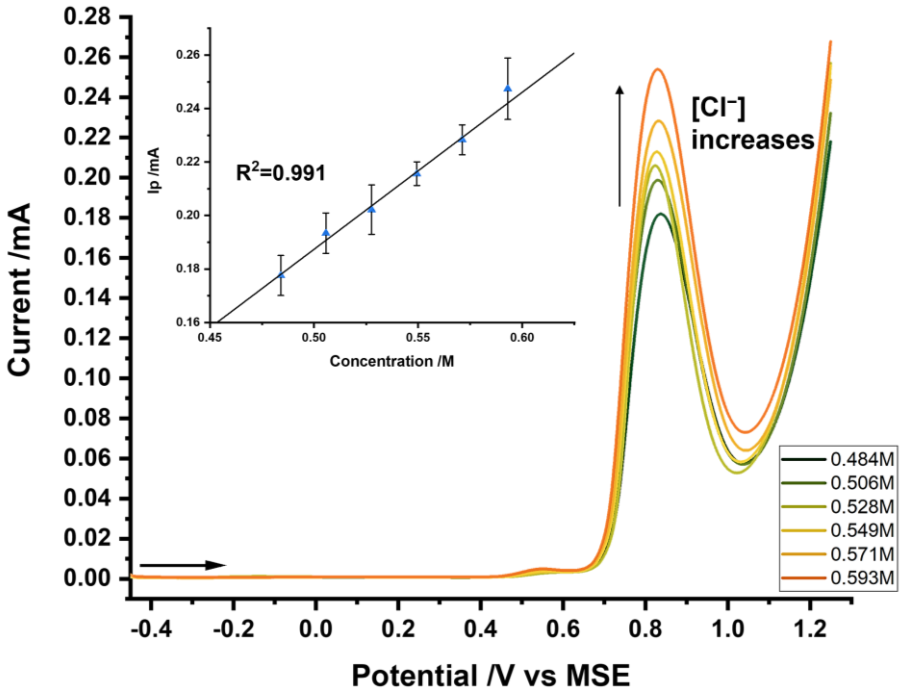

Figure.6.6 Square wave voltammograms (step potential: 1 mV, frequency: 5 Hz, and amplitude: 50 mV) recorded at a Pt electrode in degassed ASW with various chloride concentrations ranging from 0.484M to 0.593M. See text for details of the scan range and the start potential. The inset shows the calibration curve of the chloride oxidation peak height against chloride concentrations, with a regression coefficient R^2 of 0.991. Each data point consists of 3 repeats.

The dominant chloride oxidation peak was recorded at 0.83 V vs MSE. To analyse the data, the oxidation peak currents of the chloride were measured. A plot of the peak current against the chloride concentration in the ASW samples is shown in the insert of Figure.6.6. The peak height increased linearly in the concentration range of chloride studied (from 0.484 M to 0.593 M). The best-fit line (R^2=0.991) was determined as follows:

$$\boldsymbol{I_p = 0.587[Cl^-] - 0.106} \qquad (6.8)$$

where I_p is the peak current (mA) of chloride oxidation and [Cl^-] is the concentration (M) of chloride in ASW.

6.3.5 Real Sample Analysis

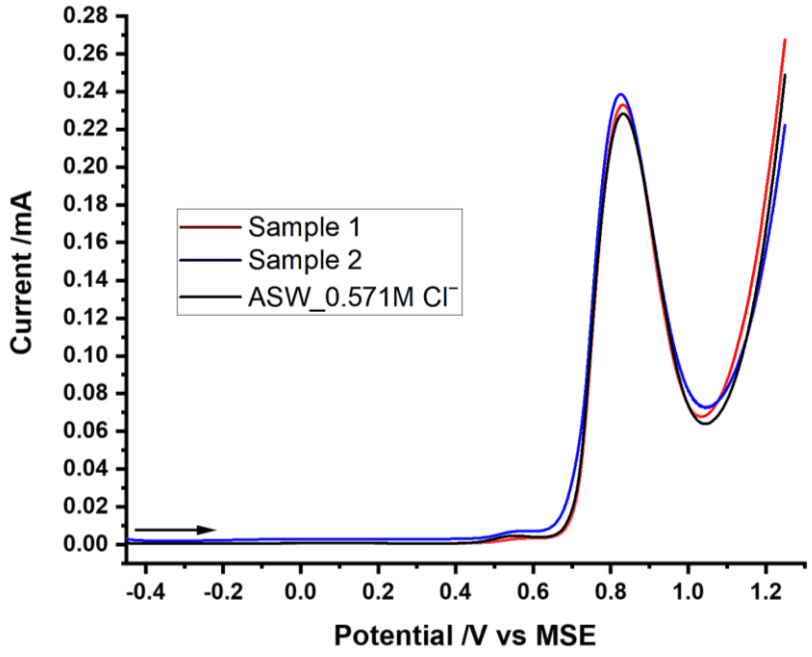

Figure.6.7 Square wave voltammograms (step potential: 1 mV, frequency: 5 Hz and amplitude: 50 mV) recorded at the Pt electrode in degassed sample 1 (red line), sample 2 (blue line) and ASW with a chloride concentration of 0.571 M (black line). See text for details of the scan range and the start potential.

To investigate the method in authentic seawater, an analysis of two different samples was performed. Ion chromatography (IC) measurements were first made for the chloride concentration of the two samples, with a result of 0.579 ± 0.004 M for sample 1 and 0.580 ±

0.001 M for sample 2. The concentrations of chloride obtained via IC were then compared as follows, with the values measured electrochemically, and as performed in ASW via SWV with optimal parameters: a step potential of 1 mV, a frequency of 5 Hz and an amplitude of 50 mV. As shown in Figure.6.7, voltammograms were conducted, starting at a potential of −0.45 V and stopping at 1.25 V vs MSE, to record the chloride oxidation signal. The oxidation peaks of chloride in the three solutions all appear at 0.83 V vs MSE, with no additional features being observed in the real samples. With the three measurements, the average oxidation peak currents of the chloride obtained in sample 1 and sample 2 were recorded and analysed using the calibration made above in ASW (Eqn. (6.8)). The electrochemically measured chloride concentrations in sample 1 and sample 2 are 0.579 ± 0.003 and 0.581 ± 0.005, respectively. The developed electrochemical analysis resulted in good agreement with IC.

6.4 Conclusions

In conclusion, three electrodes, made respectively of gold, glassy carbon and platinum, were investigated for the analysis of Cl^- and/or Br^- in seawater. First, the dissolution and passivation of a Au electrode in ASW, which has a high chloride concentration, indicated that gold was an unsuitable electrode material. This agrees with independent studies on pure chloride and bromide solutions. For GC, while the proximity of the voltammetric feature to solvent decomposition (OER) prevented the identification of a clear chloride oxidation peak, the poorly resolved bromide signal from the chloride oxidation and the OER, and the challenges of making an appropriate baseline correction, also make the material less attractive than using platinum for bromide detection using SWV as described in the previous chapter [58]. In terms of using Pt for chloride quantification, the results measured electrochemically in two real samples show a good match with those measured independently via ion chromatography. Therefore, platinum electrodes are recommended for both bromide and chloride detection for seawater.

Appendices

Section A6.1: The Electro-dissolution of a Au Electrode in ASW

Cyclic voltammetry was conducted using a Au electrode in ASW1 containing 0.571 M chloride and 0.84 M bromide. The potential sweep started at −0.45 V vs MSE, and swept towards 0.94 V before returning to −0.45 V at a scan rate of 20 mVs^{-1}, 20 such potential cycles were made in succession. The dissolved gold can be seen plated onto the surface of the counter electrode in Figure.A6.1 (a) and led to the coloration of the solution (Figure.A6.1 (b)).

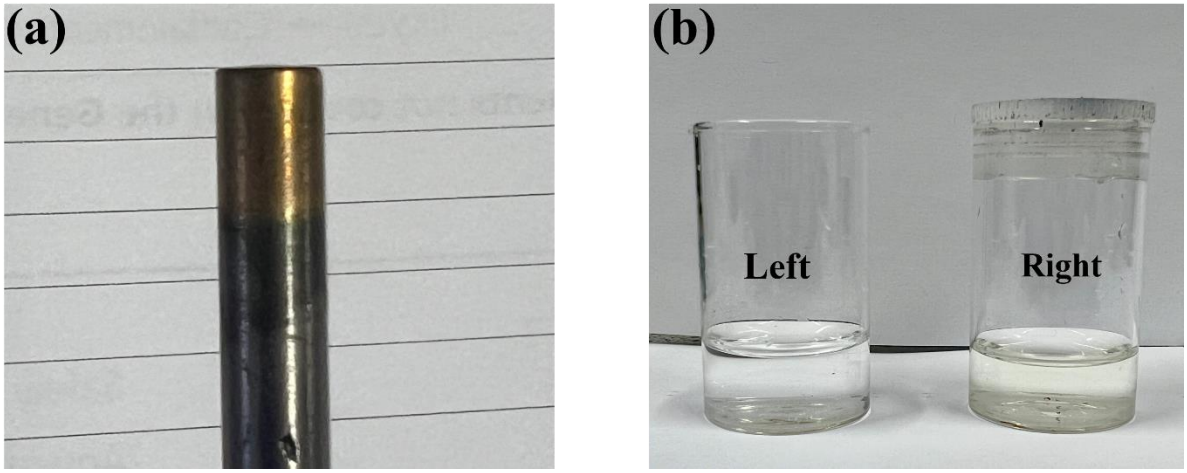

Figure.A6.1 (a) A picture of the counter electrode after 20 scans of CV. The start potential was −0.45 V vs MSE and swept towards 0.94 V before returning to −0.45 V. The golden layer was attributed to replating of dissolved gold from the working electrode on the counter electrode. (b) A picture comparing ASW before and after multiple scan cyclic voltammetry being conducted. The start potential was −0.45 V vs MSE and swept towards 0.94 V before returning to −0.45 V. Left: original ASW; Right: ASW after 20 scans of CV.

Section A6.2: Calculation of Transfer Coefficients for Chloride Oxidation from Tafel Analysis

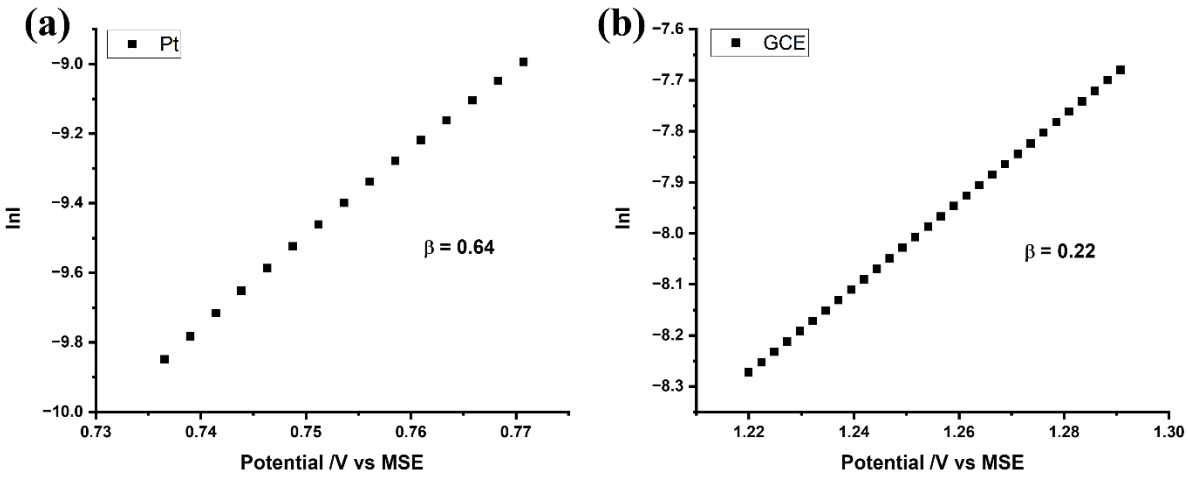

Figure.A6.2 The Tafel plots for the chloride oxidation in degassed ASW recorded at a scan rate of 100 mVs^{-1} (a) at a Pt electrode (b) at a GCE. 10% - 30% of the current range of the forward wave was used.

This section reports Tafel analysis for obtaining the transfer coefficient β for the chloride oxidation reaction at a Pt electrode and a GCE. Figure.6.2 (a) illustrates cyclic voltammograms obtained using either a Pt electrode or a GCE in degassed ASW, with a scan rate of 100 mVs^{-1}. For a Pt electrode, the potential sweep started at −0.45 V vs MSE, and swept towards 1.2 V before returning to −0.45 V. For a GCE, the voltammogram started at the same potential of −0.45 V vs MSE, followed by an anodic sweep up to 2.0 V and then lower to −1.3 V before the sweep back to −0.45 V. These ranges were selected to ensure that both forward and reverse peaks of the redox reactions associated with the analytes, chloride and bromide, were clearly recorded. The dominant oxidation Peak 2 was observed at 0.94 V vs MSE using a Pt electrode and 1.66 V vs MSE using a GCE, with a related cathodic Peak 2'seen at 0.53 V vs MSE and −0.21 V vs MSE respectively. The insert shows a first oxidation peak (Peak 1) recorded at 0.59 V vs MSE using a Pt electrode and 0.86 V vs MSE using a GCE. According to the previous study in **Chapter 5** [58], Peak 2 is attributed to the oxidation of chloride and Peak 1 is assigned

to be the bromide oxidation. The Peak 2' corresponds to the reduction of the products from the chloride and bromide oxidation.

The Tafel analysis of Peak 2 was performed on the voltammograms starting from 10% to 30% of the peak height [77]. The transfer coefficient β was calculated from the following expression 1. [78-80]

$$\boldsymbol{\beta = \frac{RT}{F}\frac{\partial ln|I_{ox}|}{\partial E}} \qquad (6.9)$$

where I_{ox} is the oxidative current.

For the chloride oxidation in ASW recorded at a scan rate of 100 mVs^{-1} at a Pt electrode and a GCE, Tafel plots of $ln|I_{ox}|$ vs potential (V vs MSE) are shown as Figure.A6.2 (a) and (b) respectively. The corresponding β value was calculated to be 0.64 ± 0.03 for a Pt electrode and 0.22 ± 0.03 for a GCE.

Section A6.3: Square Wave Voltammetry Applied to Bromide Oxidation

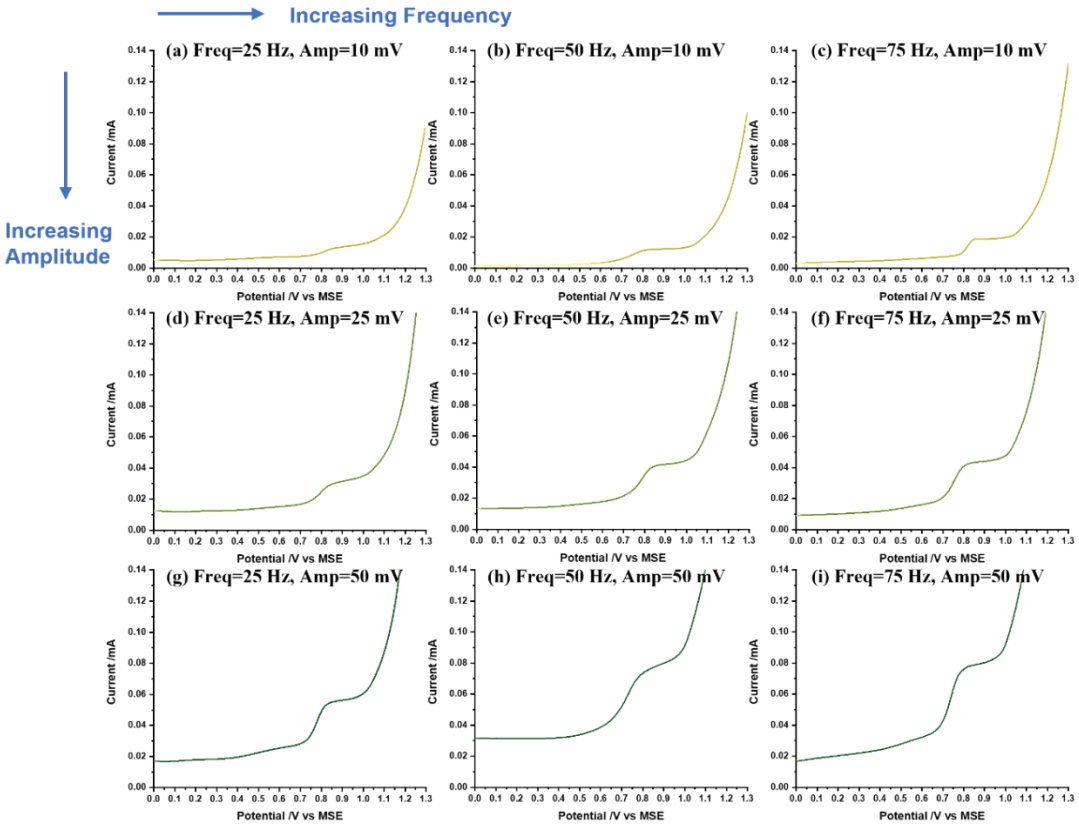

Figure.A6.3 Effect of increasing frequency (from left to right) and increasing amplitude (downward) on the SWV (focusing on bromide oxidation peak) with a step potential of 1 mV in a degassed ASW. (a) Freq = 25 mV, Amp = 10 mV, (b) Freq = 50 mV, Amp = 10 mV, (c) Freq = 75 mV, Amp = 10 mV, (d) Freq = 25 mV, Amp = 25 mV, (e) Freq = 50 mV, Amp = 25 mV, (f) Freq = 75 mV, Amp = 25 mV, (g) Freq = 25 mV, Amp = 50 mV, (h) Freq = 50 mV, Amp = 50 mV, (i) Freq = 75 mV, Amp = 50 mV.

To obtain square wave voltammograms with the best resolution for potential analytical purposes, the optimisation of SWV parameters was conducted in a degassed ASW as shown in Figure.A6.3. Voltammograms were recorded starting at a potential of −0.45 V vs MSE and stopped at 1.3 V with a fixed step potential of 1 mV whilst varying the frequency and amplitude. Figure.A6.3 indicates that as the frequency increases, the signal at ca 0.8 V vs MSE becomes better defined with a higher peak current. A similar trend is observed by increasing the amplitude. Despite the minor improvement, the recorded signal overlaps the response from Peak 2 and also the solvent decomposition. Meanwhile, as with cyclic voltammetry, the

presence of significant currents prior to the analytical signal indicates that a suitable baseline correction would be required for data analysis. Attention therefore returned to the cyclic voltammetric data and standard additions [82] made as described in the main text.

Section A6.4: Method of Baseline Correction Applied to the Bromide Oxidation Voltammetry

To analyse the results of standard additions, voltammograms with the potential range focusing on Peak 1 were recorded as shown in Figure.A6.4 (black curves). Because of the pre-wave to Peak 1, a baseline correction was required for each measurement. This was made by extrapolating the pre-wave as shown by the red lines in Figure.A6.4 and subtracting the baseline from the experimental voltammogram to produce the corrected voltammograms shown in blue. The resultant voltammograms (blue curves) indicate a better-defined bromide oxidation signal and clear peak current of which was then used to plot Figure.6.5 (b) showing the plot of peak current against the concentration of bromide added to the original ASW.

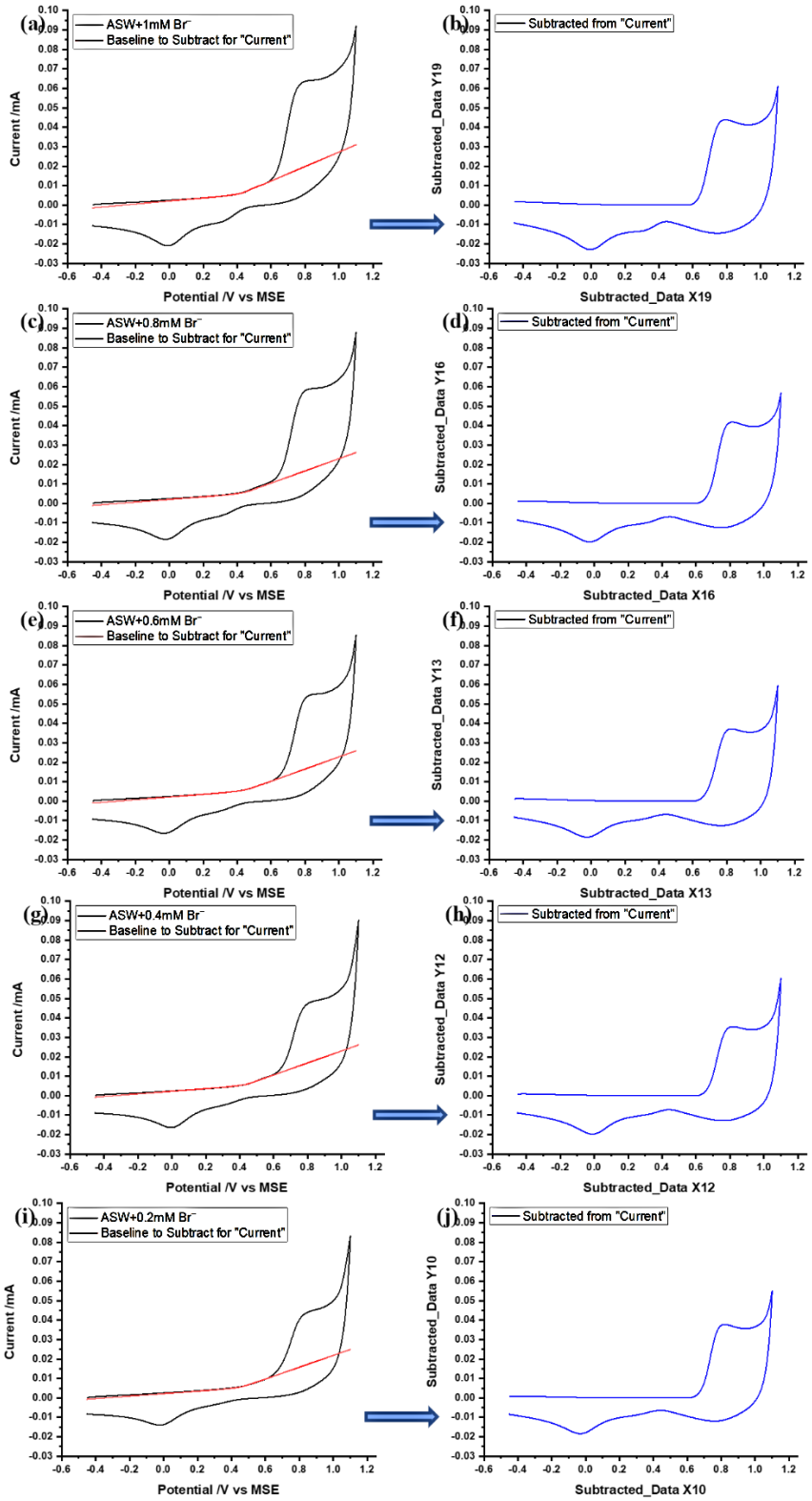

Figure.A6.4 The original voltammograms (black curve) and the modified voltammograms (blue curve) after a baseline correction (red line) obtained in degassed ASW with an addition of bromide concentration of (a-b) 0.2 mM, (c-d) 0.4 mM, (e-f) 0.6 mM, (g-h) 0.8 mM, (i-j) 1.0 mM. The baselines were selected as an extrapolation of the pre-wave.

Section A6.5: The Optimisation of SWV Parameters for Chloride Detection at a Pt Electrode

This section reports the optimisation of SWV parameters for chloride detection in degassed ASW as shown in Figure.A6.5. Voltammograms were recorded from a potential of −0.45 V vs MSE and stopped at 1.25 V with a fixed step potential of 1 mV whilst varying the frequency (5-25 Hz) and amplitude (10-50 mV). For comparison, the SWV with the same parameters was also conducted in 0.7 M $NaNO_3$ (dark lines) with the same ionic strength as seawater [66]. As the frequency increases, there is a higher chloride oxidation peak at ca 0.85 V vs MSE, but one can also notice that the effect of solvent breakdown gets more significant enhancing the current in the vicinity of the diffusion tail. Therefore, the frequency of 5 Hz was subsequently implemented in analytical measurements.

In contrast to the frequency, there is no obvious difference in peak resolution by increasing the amplitude despite the higher peak current as shown in Figure.A6.5. To find the optimal amplitude for chloride oxidation detection, the three amplitudes (10 mV, 25 mV and 50 mV) were assessed by further study in ASW containing various concentrations of chloride (0.484 M-0.593 M) with the criteria being achieving the highest sensitivity and the best linearity. Figure.A6.6 (a-c) display the voltammograms obtained with the three different amplitudes respectively, from which it can be seen that the peak height of the chloride oxidation at 0.85 V vs MSE increases with the concentration of chloride. To analyse the data, the chloride oxidation peak currents were recorded. The plots of peak current against the chloride concentration in ASW samples are shown in Figure.A6.6 (d). We note that an amplitude of 50 mV (blue dots) resulted in the highest sensitivity with the best linearity (R^2 = 0.991). Therefore, the optimised SWV with a frequency of 5 Hz, an amplitude of 50 mV and a step potential of 1 mV was applied to record the electroanalytical responses of chloride ions in ASW and real sample analysis.

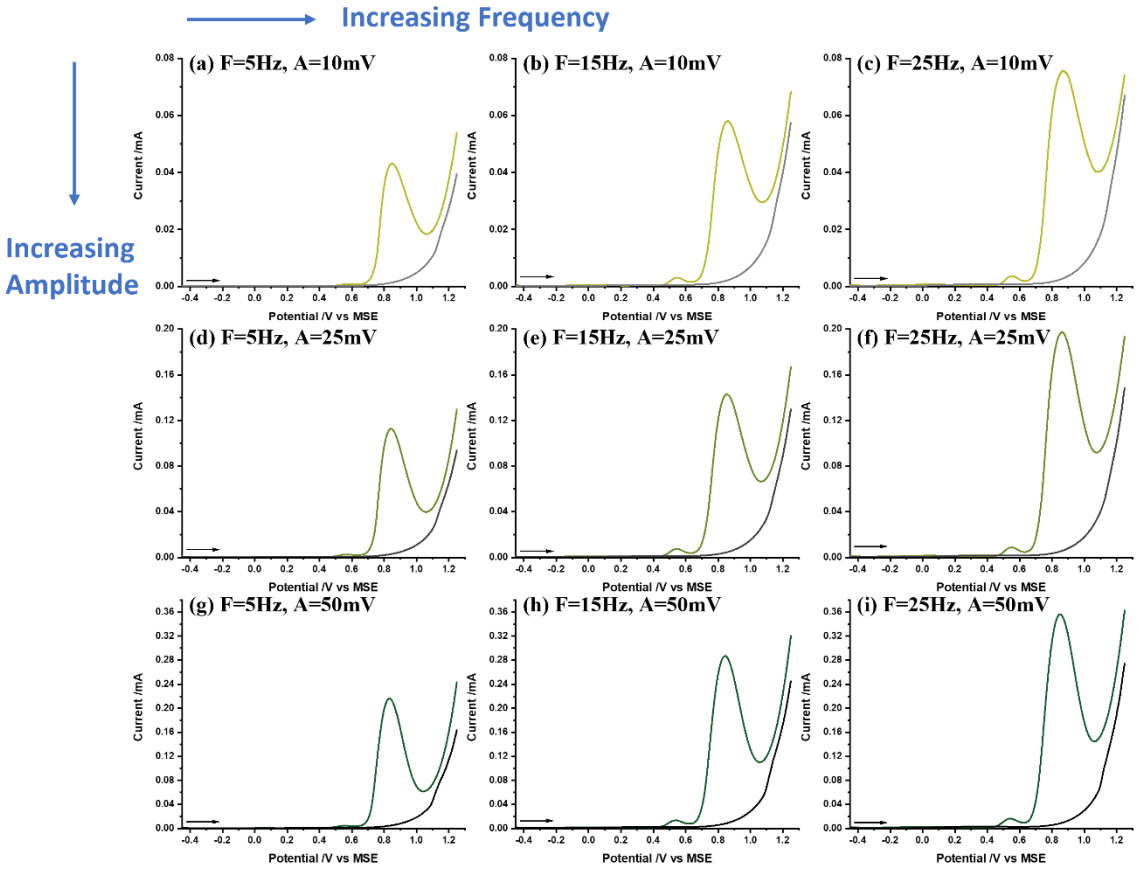

Figure.A6.5 Effect of increasing frequency (from left to right) and increasing amplitude (downward) on the SWV, focusing on chloride oxidation peak, with a step potential of 1 mV in degassed ASW. (a) Freq = 5 mV, Amp = 10 mV, (b) Freq = 15 mV, Amp = 10 mV, (c) Freq = 25 mV, Amp = 10 mV, (d) Freq = 5 mV, Amp = 25 mV, (e) Freq = 15 mV, Amp = 25 mV, (f) Freq = 25 mV, Amp = 25 mV, (g) Freq = 5 mV, Amp = 50 mV, (h) Freq = 15 mV, Amp = 50 mV, (i) Freq = 25 mV, Amp = 50 mV. All voltammograms are compared with data (dark lines) obtained in 0.7 M $NaNO_3$ with the same ionic strength as seawater [66].

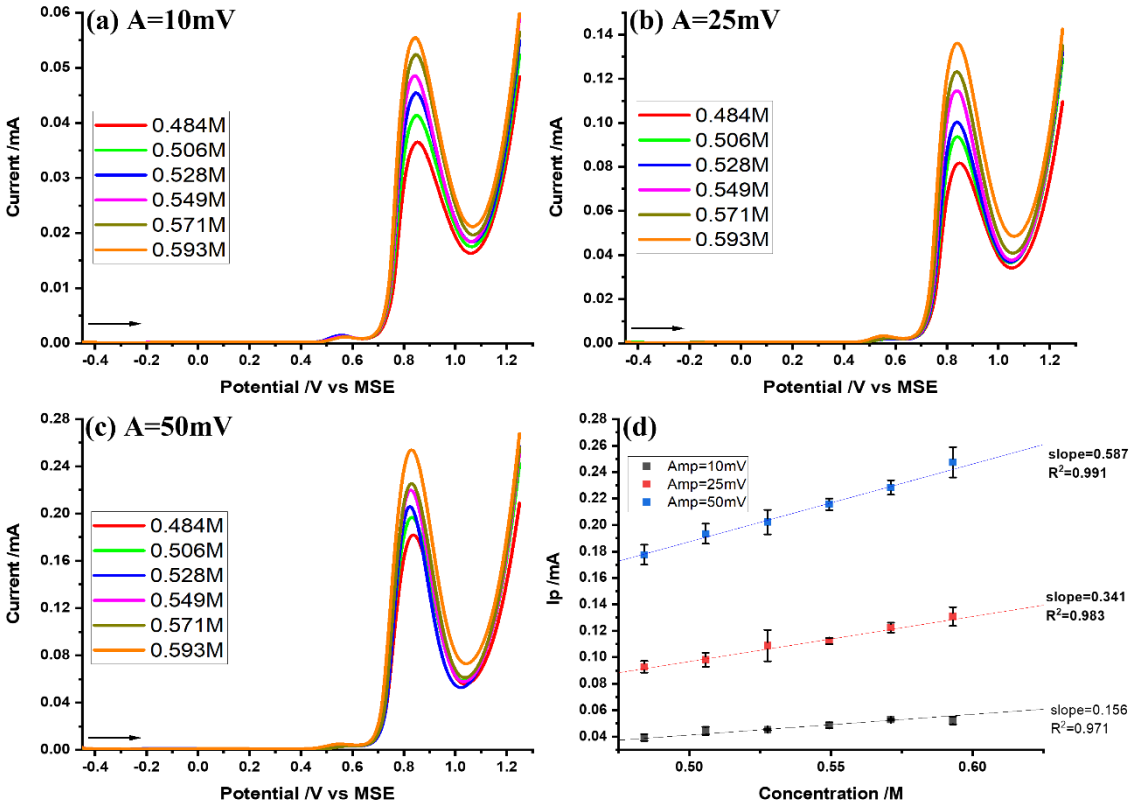

Figure.A6.6 Square wave voltammograms (step potential 1 mV, frequency 5 Hz) recorded at a Pt electrode in degassed ASW with various chloride concentrations of (0.484M-0.593M) with an amplitude of (a) 10 mV, (b) 25 mV and (c) 50 mV. See text for details of the scan range and the start potential. (d) The calibration curves of the resultant chloride oxidation peak heights against chloride concentrations. Amplitude = 10 mV (black dots); Amplitude = 25 mV (red dots); Amplitude = 50 mV (blue dots). Each data point consists of 3 repeats.

References

1. Y. Chen and R. G. Compton, *Chemosensors*, 2023, **11**, 297.
2. Water Scarcity, https://www.unwater.org/water-facts/water-scarcity, (accessed 14 March, 2023, 2023).
3. F. R. Spellman, *The Handbook of Nature*, Bernan Press, 2019, Lanham, USA.
4. H. E. S. Bint El Hassan, D. Guerrier, A. Closas, C. Demilecamps, Y. kassim, C. Lacirignola, N. Lamaddalena, J. Mateo-Sagasta, N. Rivera, *Water Around the Mediterranean*, The Center for Mediterranean Integration (CMI), Marseille, France, 2018.
5. A. Pérez-González, A. M. Urtiaga, R. Ibáñez and I. Ortiz, *Water Research*, 2012, **46**, 267-283.
6. D. H. Kim, *Desalination*, 2011, **270**, 1-8.
7. W. J. Wallace, *The Development of the Chlorinity/Salinity Concept in Oceanography*, Elsevier Science Ltd (1 Jan. 1974), New York, 1974.
8. F. J. Millero, R. Feistel, D. G. Wright and T. J. McDougall, *Deep Sea Research*, 2008, **55**, 50-72.
9. R. H. Stewart, *Introduction to Physical Oceanography*, Department of Oceanography, Texas A&M University, College Station, TX, USA, 2008.
10. S. E. Shumway, *Marine Biology*, 1977, **41**, 153-177.
11. Y. Guo and R. G. Compton, *Talanta*, 2021, **232**, 122502.
12. M. Yamamoto, *Chemosphere*, 1996, **32**, 1217-1224.
13. C. Levard, S. Mitra, T. Yang, A. D. Jew, A. R. Badireddy, G. V. Lowry and G. E. Brown, Jr., *Environmental Science & Technology*, 2013, **47**, 5738-5745.
14. C. Batchelor-McAuley, K. Tschulik, C. C. M. Neumann, E. Laborda and R. G. Compton, *International Journal of Electrochemical Science*, 2014, **9**, 1132 - 1138.
15. M. R. Gilberg and N. J. Seeley, *Studies in Conservation*, 1981, **26**, 50-56.
16. M. Otieno, H. Beushausen and M. Alexander, *Cement and Concrete Research*, 2016, **79**, 373-385.
17. A. J. Downs and C. J. Adams, *The Chemistry of Chlorine, Bromine, Iodine and Astatine: Pergamon Texts in Inorganic Chemistry, Volume 7*, Elsevier, 2017.
18. A. C. Leri, J. A. Hakala, M. A. Marcus, A. Lanzirotti, C. M. Reddy and S. C. B. Myneni, *Global Biogeochemical Cycles*, 2010, **24**, 1-15.
19. M. E. Pilson, *An Introduction to the Chemistry of the Sea*, Cambridge University Press, 2012, Cambridge, UK.
20. G. W. Gribble, *American Scientist*, 2004, **92**, 342-349.
21. P. Dorji, D. I. Kim, S. Hong, S. Phuntsho and H. K. Shon, *Desalination*, 2020, **479**, 114309.
22. E. L. Lewis, *Marine Geodesy*, 1982, **5**, 350-357.
23. G. S. Lagerloef, C. T. Swift and D. M. Le Vine, *Oceanography*, 1995, **8**, 44-50.
24. T. Anfält and S. Twengström, *Analytica Chimica Acta*, 1986, **179**, 453-457.
25. A. Vengosh and I. Pankratov, *Ground Water*, 1998, **36**, 815-824.
26. J. J. Morgan and W. Stumm, *Aquatic Chemistry: An Introduction Emphasizing Chemical Equilibria in Natural Waters*, New York, NY, John Wiley & Sons, 1981.
27. E. Salameh, A. Tarawneh and M. Al-Raggad, *Arabian Journal of Geosciences*, 2016, **9**, 1-20.
28. A. Jain, A. Chaurasia, B. Sahasrabuddhey and K. K. Verma, *Journal of Chromatography A*, 1996, **746**, 31-41.
29. E. P. Borges, A. F. Lavorante and B. F. d. Reis, *Analytica Chimica Acta*, 2005, **528**, 115-119.

30. K. Grasshoff and A. Wenck, *ICES Journal of Marine Science*, 1972, **34**, 522-528.
31. T.-K. Hong, M.-H. Kim and M.-Z. Czae, *International Journal of Analytical Chemistry*, 2010, **2010**, 1-7.
32. R. Reitemeier, *Industrial and Engineering Chemistry, Analytical Edition*, 1943, **15**, 393-402.
33. W. S. Reeburgh and J. H. Carpenter, *Limnology and Oceanography*, 1964, **9**, 589-591.
34. L. S. Clesceri, A. E. Greenberg and A. D. Eaton, *Standard Methods for the Examination of Water and Wastewater*, APHA American Public Health Association, Washington, DC, USA, 20th edn., 1998.
35. H. H. Willard, L. L. Merritt, Jr., J. A. Dean and F. A. Settle, Jr., *Instrumental Methods of Analysis*, Wadsworth Publishing Company, Belmont, CA, USA, 7th edn., 1988.
36. E. Lewis, *IEEE Journal of Oceanic Engineering*, 1980, **5**, 3-8.
37. E. Lewis and R. Perkin, *Deep Sea Research*, 1981, **28**, 307-328.
38. Unesco, *Tenth Report of the Joint Panel on Oceanographic Tables and Standards*, Unesco Division of Marine Sciences, Sidney, BC, Canada, 1980.
39. K. Uraisin, T. Takayanagi, M. Oshima, D. Nacapricha and S. Motomizu, *Talanta*, 2006, **68**, 951-956.
40. D. R. Jones, *Talanta*, 1993, **40**, 43-51.
41. P. I. Anagnostopoulou and M. A. Koupparis, *Analytical Chemistry*, 1986, **58**, 322-326.
42. W. J. M. Emaus and H. J. Henning, *Analytica Chimica Acta*, 1993, **272**, 245-250.
43. K. Uraisin, D. Nacapricha, S. Lapanantnoppakhun, K. Grudpan and S. Motomizu, *Talanta*, 2005, **68**, 274-280.
44. N. Yonehara, S.-i. Chaen, T. Tomiyasu and H. Sakamoto, *Analytical Sciences*, 1999, **15**, 277-281.
45. S. M.R. and J. R. Elah, *International Journal of Industrial Chemistry*, 2011, **2**, 27-32.
46. A. Sheibani, M. R. Shishehbore and Z. T. Ardakani, *Chinese Chemical Letters*, 2011, **22**, 595-598.
47. H. Akaiwa, H. Kawamoto and M. Osumi, *Talanta*, 1982, **29**, 689-690.
48. S. Seefeld and U. Baltensperger, *Analytica Chimica Acta*, 1993, **283**, 246-250.
49. H. Fabre, M. D. Blanchin and N. Bosc, *Analytica Chimica Acta*, 1999, **381**, 29-37.
50. O. Stålberg, K. Sander and C. Sänger-van de Griend, *Journal of Chromatography A*, 2002, **977**, 265-275.
51. J. P. Pascali, M. Trettene, F. Bortolotti, G. d. Paoli, R. Gottardo and F. Tagliaro, *Journal of Chromatography B*, 2006, **839**, 2-5.
52. K. Fukushi, K. Watanabe, S. Takeda, S.-I. Wakida, M. Yamane, K. Higashi and K. Hiiro, *Journal of Chromatography A*, 1998, **802**, 211-217.
53. N. Kocatürk, N. Öztekin and F. Bedia Erim, *Analytical and Bioanalytical Chemistry*, 2003, **377**, 1207-1211.
54. G. A. Rechnitz and M. R. Kresx, *Analytical Chemistry*, 1966, **38**, 1786-1788.
55. E. M. Zahran, Y. Hua, Y. Li, A. H. Flood and L. G. Bachas, *Analytical Chemistry*, 2010, **82**, 368-375.
56. Ö. Isildak, O. Özbek and K. Yigit, *Bulgarian Chemical Communications*, 2020, **52**, 448-452.
57. D. Vlascici, N. Plesu, G. Fagadar-Cosma, A. Lascu, M. Petric, M. Crisan, A. Belean and E. Fagadar-Cosma, *Sensors*, 2018, **18**, 2297.
58. Y. Chen and R. G. Compton, *Talanta*, 2023, **253**, 124019.
59. I. Sekerka and J. F. Lechner, *Journal - Association of Official Analytical Chemists*, 2020, **61**, 1493-1495.
60. M. Montemor, J. Alves, A. Simoes, J. Fernandes, Z. Lourenço, A. Costa, A. Appleton and M. Ferreira, *Cement and Concrete Composites*, 2006, **28**, 233-236.

61. K. Arai, F. Kusu, N. Noguchi, K. Takamura and H. Osawa, *Analytical Biochemistry*, 1996, **240**, 109-113.
62. X. Qin, H. Wang, Z. Miao, X. Wang, Y. Fang, Q. Chen and X. Shao, *Talanta*, 2011, **84**, 673-678.
63. J. Bujes-Garrido, D. Izquierdo-Bote, A. Heras, A. Colina and M. J. Arcos-Martínez, *Analytica Chimica Acta*, 2018, **1012**, 42-48.
64. T. K. Malongo, S. Patris, P. Macours, F. Cotton, J. Nsangu and J.-M. Kauffmann, *Talanta*, 2008, **76**, 540-547.
65. H. Cunha-Silva and M. Julia Arcos-Martinez, *Talanta*, 2019, **195**, 771-777.
66. F. J. Millero, *Annual Review of Earth and Planetary Sciences*, 1974, **2**, 101-150.
67. P. H. Qi and J. B. Hiskey, *Hydrometallurgy*, 1993, **32**, 161-179.
68. M. J. Nicol, *Gold Bulletin*, 1980, **13**, 46-55.
69. M. J. Nicol, *Gold Bulletin*, 1980, **13**, 105-111.
70. B. H. Loo, *The Journal of Physical Chemistry*, 1982, **86**, 433-437.
71. J. Gaur and G. Schmid, *Journal of Electroanalytical Chemistry and Interfacial Electrochemistry*, 1970, **24**, 279-286.
72. S. Cadle and S. Bruckenstein, *Journal of Electroanalytical Chemistry and Interfacial Electrochemistry*, 1973, **48**, 325-331.
73. Michael J. Nicol and E. Schalch, Report Reports Nos. 1844 and 1848, National Institute for Metallurgy, Johannesburg, 1976.
74. T. Heumann and H. S. Panesar, *Zeitschrift für Physikalische Chemie*, 1965, **229O**, 84-97.
75. F. M. M. Morel, J. G. Rueter, D. M. Anderson and R. R. L. Guillard, *Journal of Phycology*, 1979, **15**, 135-141.
76. N. M. Price, G. I. Harrison, J. G. Hering, R. J. Hudson, P. M. Nirel, B. Palenik and F. M. Morel, *Biological oceanography*, 1989, **6**, 443-461.
77. D. Li, C. Lin, C. Batchelor-McAuley, L. Chen and R. G. Compton, *Journal of Electroanalytical Chemistry*, 2018, **826**, 117-124.
78. R. G. Compton and C. E. Banks, *Understanding Voltammetry*, World Scientific, 3rd edition, 2018.
79. R. Guidelli, R. G. Compton, J. M. Feliu, E. Gileadi, J. Lipkowski, W. Schmickler and S. Trasatti, *Pure and Applied Chemistry*, 2014, **86**, 245-258.
80. R. Guidelli, R. G. Compton, J. M. Feliu, E. Gileadi, J. Lipkowski, W. Schmickler and S. Trasatti, *Pure and Applied Chemistry*, 2014, **86**, 259-262.
81. A. Poisson and A. Papaud, *Marine Chemistry*, 1983, **13**, 265-280.
82. D. C. Harris, *Quantitative Chemical Analysis*, Macmillan, 2010, London, UK.

Chapter 7

Reversible Cyclic Voltammetry and Non-unity Stoichiometry: The Ag/AgBr/Br^- Redox Couple

In previous chapters, we focussed on developing working electrodes designed for different applications, notably pH sensing in either freshwater or seawater, and bromide and/or chloride detection for seawater. Noting that the silver/silver bromide redox couple can serve as the basis of a reference electrode [1, 2] like silver-silver chloride or calomel electrodes, and building on the experiments reported in the previous chapter using silver electrodes in solution of bromide ions it is insightful to study the associated fundamental electrochemistry. The voltammetry of Ag/AgBr/Br^-, is investigated experimentally and computationally. The voltammetric waveshape is characterised and shown to give rise to apparent transfer coefficients very considerably in excess of unity, leading to the benefit of using the couple as the basis of a reference electrode.

The work of **Chapter 7** has been published in the journal *Analytical Chemistry* [3]. The simulation part was carried out fully by Dr. Haotian Chen, but is presented in the thesis for consistency and completeness.

7.1 Introduction

Cyclic voltammetry at macroelectrodes is the starting point for almost all fundamental and applied studies in dynamic electrochemistry, [4] not least since the rigorous quantitative analysis of the resulting voltammograms is well- and long-established via the Randles- Ševčík equations. In particular for the simple reaction,

$$\boldsymbol{A(aq) + ne^- \rightleftharpoons B(aq)} \qquad (7.1)$$

the Randles–Ševčík equation for a fully reversible process is at temperature T:

$$I_{peak} = -0.446nFAc\sqrt{\frac{nF\nu D}{RT}} \quad (7.2)$$

where D and c are the diffusion coefficient and bulk concentration of species A respectively. ν is the scan rate and A is the geometrical area of the electrode. Similarly, for an electrochemically irreversible reduction process,

$$I_{peak} = -0.496n\sqrt{n' + \alpha_{RDS}}FAc\sqrt{\frac{F\nu D}{RT}} \quad (7.3)$$

where α_{RDS} is the transfer coefficient of the rate determining step usually having a value close to 0.5 , [4] and n' is the number of electrons transferred before the rate determining step. In both cases the scaling of the peak current with the square root of the voltage scan rate fingerprints the diffusional character of the voltammetry. The distinction between reversible and irreversible electrode kinetics is, as described in Chapter 1, best made via Tafel analysis [5] of the parts of the voltammetric curve corresponding to ca 10-30% of the peak current to avoid distortion via mass transport effects, [6] noting that the IUPAC definition [7, 8] of the reductive transfer coefficient is

$$\alpha = -\frac{RT}{F}\frac{d\ln(I)}{dE} \quad (7.4)$$

where for Butler-Volmer (BV) kinetics a plot of $\ln(I)$ versus E is predicted to be linear, [9, 10] although the linearity is only approximate in the case of Hush-Marcus-Chidsey kinetics. [11] This allows the ready inference of the value of α, where for BV kinetics

$$\alpha = n' + \alpha_{RDS} \quad (7.5)$$

In the "reversible" limit for fast electrode kinetics, plots of $\ln I$ against E, often known as a Tafel plot, yield an 'apparent' transfer coefficient which for a simple one electron process takes the value of unity. Note however that whilst simple electron processes give rise to linear or nearly linear Tafel plots, it is recognised that in the case of reversible or quasi-reversible electrode kinetics coupled to homogeneous chemical kinetics marked deviations occur from the expected value of unity with the apparent transfer coefficient becoming potential dependent. Specifically, the presence of a chemical reaction preceding the electron transfer, as in a CE

process, gives a reduction in the *apparent* transfer coefficient and may thus promote an illusion of electrochemical irreversibility, whilst a following chemical reaction, as in EC and EC_2 processes, can give rise to apparent transfer coefficients in excess of unity and hence to 'super-Nernstian' responses[12, 13] of higher than the ca 60 mV per decade expected for a simple one electron process. These changes are understood to arise from the decrease in the concentrations of species A (CE) or of species B (EC, EC_2) local to the electrode as a result of the homogeneous chemistry impacting the Nernstian behaviour of the redox couple at the electrode-solution interface. Most generally the value of the transfer coefficient reflects the sensitivity of the current response to the electrical potential, and is extensively used and most notably in evaluating candidate redox couples for batteries where the identification of authentic reversibility, rather than the apparent reversibility, is essential. [14] It is notable that Burstein highlighted the pivotal role of the Tafel plot in establishing the extent of reversibility by suggesting the volt-per-decade-of-current unit might be named after Tafel, i.e. that is 1 Tafel = 1 V per decade of current, with the symbol Ta. Thus 1 Ta = 2.3026 V. [15]

In the present chapter, and with the aim of identifying the essential conditions for observing particularly large super-Nernstian responses, we consider the voltammetry expected for the case where a simple electrode reaction leads to the formation of an insoluble product form a soluble reactant, as for example and in particular, in the case of the oxidation of silver in the presence of bromide ion at a silver electrode:

$$\boldsymbol{Ag(s) + Br^{-}(aq) \rightleftarrows AgBr(s) + e^{-}} \qquad (7.6)$$

where the bromide reactant is the only solution phase species, the product being insoluble silver bromide. The redox couple has found use as a (reversible) reference electrode. [1, 2] This then hypothetically represents the extreme case of an EC reaction with ultrafast kinetics in the sense that no soluble products are formed, and so, as will be shown below, both theoretically and experimentally, might be expected to lead to extreme Tafel slopes and anomalously high apparent transfer coefficients. Further we note the link with the highly important and insightful

work of Gomez-Gil, Laborda and Molina [16] in showing that for non-unity stoichiometry reactions of the general form

$$\boldsymbol{aA(aq) + ne^{-} \rightleftarrows bR(aq)} \qquad (7.7)$$

where a ≠ b. The reversible Randles–Ševčík (Eqn. (7.2)) needs modification to reflect the changed stoichiometry although in all cases the scaling of the peak current with $n^{3/2}$ and $\nu^{1/2}$ remains. In particular Gomez-Gil et al considered 2:1, 1:2, 3:1 and 1:3 processes as specific examples of (a:b) non-unity stoichiometry focussing exclusively on couples based on solution phase species. In the following we also establish the appropriate Randles–Ševčík equation, as a consequence of exploring the extreme super-Nernstian response of a 0:1 process, where 0 and 1 are the stoichiometric coefficient of the oxidant and reductant. The value of 0 indicates that the redox species is not in the aqueous phase, but for example, in the solid phase such as AgBr as shown in Eqn. (7.6).

7.2 Experimental

The chemicals and electrochemical apparatus used in this chapter is the same in **Chapter 5**, with the details listed in Section 5.2.

7.3 Theory (work of Dr. Haotian Chen)

7.3.1 Simulation of Voltammetry

We consider the electrochemically reversible, one-electron oxidation of the surface of a solid Ag macro-electrode in the presence of Br^{-} in an aqueous phase as shown in Eqn. (7.6).

The mass transport is assumed to be dominated by linear and semi-infinite diffusion, with migration suppressed by the presence of excess supporting electrolyte, and convection eliminated by making voltammetric measurements at short timescales. Since only Br^{-} is present in the aqueous phase, the Nernst equation describing the electrochemical reaction is:

$$E = E_f^0(Ag/AgBr) - \frac{RT}{F}\ln\left(\frac{c_{Br^-}}{[\ ]^0}\right) \tag{7.8}$$

where $[\ ]^0$ is the reference concentration of 1 molar and the activity of both silver and silver bromide considered as pure solids is unity. E_f^0 is the formal potential of Ag/AgBr/Br^- redox couple. The diffusion equation for the solution phase species Br^- is:

$$\frac{\partial c_{Br^-}}{\partial t} = D_{Br^-}\frac{\partial^2 c_{Br^-}}{\partial x^2} \tag{7.9}$$

For the case of cyclic voltammetry, the spatial boundary conditions at the surface of electrode and the outer boundary of simulation are:

$$\mathbf{x = 0,}\begin{cases} \mathbf{E \le E_{eq}, I = 0;} \quad \mathbf{c_{Br^-} = c^*_{Br^-}} \\ \mathbf{E > E_{eq},} \qquad [\mathbf{Br^-}] = \boldsymbol{exp}\left(-\dfrac{\mathbf{F}}{\mathbf{RT}}\left(\mathbf{E - E_f^0}\right)\right) \times [\ ]^{\mathbf{0}} \\ \mathbf{x \to \infty, c_{Br^-} = c^*_{Br^-}} \end{cases} \tag{7.10}$$

where E_{eq} is the equilibrium potential defined as $E_{eq} = E_f^0(Ag/AgBr) - \frac{RT}{F}ln\left(\frac{c^*_{Br^-}}{[\ ]^0}\right)$ and $C^*_{Br^-}$ is the bulk concentration of bromide.

Linear sweep or cyclic voltammetry increases or decreases the applied potential linearly as a function of time:

$$\begin{cases} E = E_i + \nu t \\ E = E_v - \nu(t - t_{switch}) \end{cases} \tag{7.11}$$

where E_i is the initial potential and the scan rate, ν, is positive for an oxidative potential scan. At time $t = t_{switch}$, the potential reaches E_v, then the direction of the potential sweep reverses. Eqn. (7.11) form the temporal boundary conditions for Eqn. (7.9) together with the condition that at t = 0 the concentration is $c_{Br^-} = c^*_{Br^-}$ for all x.

Note that the origin of the first boundary condition (7.10) above lies in the fact that at the start of the experiment the electrode surface is assumed to be exclusively silver and for potentials below the equilibrium potential no current flows nor is any silver bromide present as its formation is not thermodynamically possible. Once the potential sweep reaches the equilibrium potential the reaction switches on and silver bromide is formed. At this point the

equilibrium in Eqn. (7.8) is established and the surface concentration of bromide is controlled by the second spatial boundary condition; this situation applies as long as silver bromide is present on the electrode surface to maintain the equilibrium. Thus, on the reverse and reductive scan the model predicts the current until all the AgBr is removed at which point the current will fall again to zero.

Table 7.1 Dimensionless parameters for simulation of $Ag/AgBr$ electrode. ϵ is the radius of macro electrode and J is the dimensionless flux defined as $J = -\frac{\partial C}{\partial X}$. D_{Br^-} and $c^*_{Br^-}$ are the diffusion coefficients and bulk concentration of bromide, respectively.

Parameter	Normalization
Concentration	$C = \frac{c_{Br^-}}{c^*_{Br^-}}$
Spatial coordinate	$X = \frac{x}{\epsilon}$
Time	$T = \frac{D_{Br^-} t}{\epsilon^2}$
Potential	$\theta = \left(\frac{F}{RT}\right)\left(E - E_{eq}\right)$
Scan rate	$\sigma = \left(\frac{\epsilon^2}{D_{Br^-}}\right)\left(\frac{F}{RT}\right)\nu$
Current	$I = \left(\frac{FAc^*_{Br^-} D_{Br^-}}{\epsilon}\right)J$

The reaction was simulated using the finite difference method in dimensionless form to increase the generality of simulations. Table 2.1 shows the dimensionless parameters used. Note that the definition of the dimensionless potential, θ, is relative to the equilibrium potential, not the formal potential. The dimensionless form of the diffusion equation and the boundary conditions are:

$$\frac{\partial C_{Br^-}}{\partial T} = \frac{\partial^2 C_{Br^-}}{\partial X^2} \tag{7.12}$$

$$\mathbf{X = 0}, \begin{cases} \boldsymbol{\theta \leq 0, J = 0;} \quad \mathbf{C_{Br^-} = 1} \\ \boldsymbol{\theta > 0,} \quad \mathbf{C_{Br^-} = \exp(-\theta)} \\ \boldsymbol{X \to \infty, C_{Br^-} = 1} \end{cases} \tag{7.13}$$

Below under Results and Discussion we explore the voltammetry experimentally. To do that requires inference of the surface concentration from experimental voltammetry as described in the next section.

7.3.2 Extraction of Electrode Surface Concentrations from Experimental Voltammetric Data

The electrode surface concentration of electroactive species can be extracted from experimental voltammograms using the Backward Implicit method. [17] First, the dimensional voltammogram is converted to dimensionless form to facilitate the calculations: the dimensional potential is converted to the dimensionless potential, θ' where $\theta' = (E - E_i)F/RT$ and the current, I, is converted to dimensionless flux, J (Table 2.1) where E_i is the initial potential of the voltammetric scan. Detailed implementation and explanation can be found in Section A4.1**,** Appendices. Figure.A7.1 illustrates and validates the procedure; it shows electrode surface concentrations extracted from one electron reduction of $[\mathrm{Ru(NH_3)_6}]^{3+}$ as proof of concept since the extracted values coincide with those predicted by the Nernst equation.

7.4 Simulation Methods (work of Dr. Haotian Chen)

Simulations were written in Python and the diffusion equation was solved using the implicit finite difference method [18] with an expanding spatial grid to economize on computational resources. [19] The multi-diagonal sparse matrix was solved using the Newton-Raphson method. [20] Convergence tests showing the sensitivity of the results to the space step, the time step and the expanding grid factor are shown in the Testing and Verification of Simulations section in

the Appendices. Convergence data at $\sigma = 100$ and 1600 is shown in Figure.A7.2 and Figure.A7.3.

7.5 Simulation Results (work of Dr. Haotian Chen)

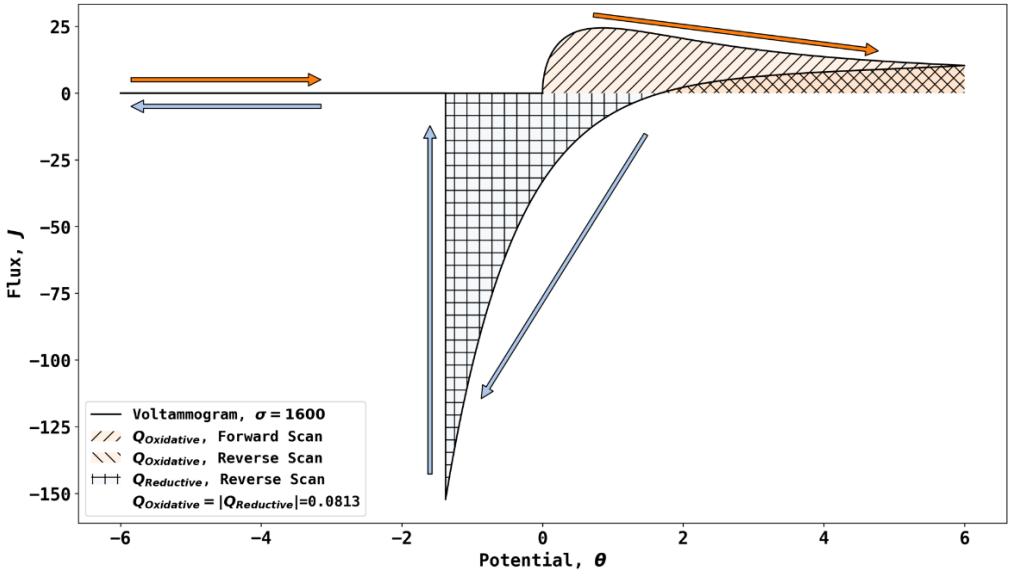

Figure.7.1 A simulated voltammogram for $\sigma = 1600$. The scan starts negative of $\theta = 0$, reverses at $\theta = 6$, and the reductive current on the reverse scan stops when the reductive charges equal the net oxidative charge on the oxidative scan and that part of the reductive scan between the reversal potential and the potential of zero current at a dimensionless potential of 1.683.

First, voltammetry at a dimensionless scan rate of $\sigma = 1600$ was simulated as illustrated in Figure.7.1. Note that, as expected, zero current flows on the initial scan until the potential reaches the equilibrium potential, where $E = E_{eq}$, so that $\theta = 0$. As the formation of solid silver bromide at the silver electrode then becomes thermodynamically possible the onset of rapidly increasing currents is observed. The current increases until it passes through a maximum as the available bromide ion in solution is depleted, and the flux drops as the extent of depletion increases. In Figure.7.1, the oxidative scan is (arbitrarily) reversed at $\theta = 6$. On the reverse scan oxidative currents continue to flow until the reduction of the deposited AgBr film becomes thermodynamically possible at potentials cathodic of the equilibrium potential where the latter

reflects the concentration of bromide local to the electrode surface and this value is depleted below the bulk concentration as a result of the oxidative currents passed consuming bromide ions. As the potential of the reverse scan becomes increasingly negative the current increases more and more until the silver bromide later is exhausted at which point the current returns abruptly to zero and the electrode is again pure silver. Figure.7.1 illustrates that sum of the oxidative charge in the anodic scan and that in the reverse scan from the reversal potential to the equilibrium potential matches exactly the total reductive charge passed on the reverse scan at potentials between the equilibrium potential and the potential at which the reductive current drops sharply to zero.

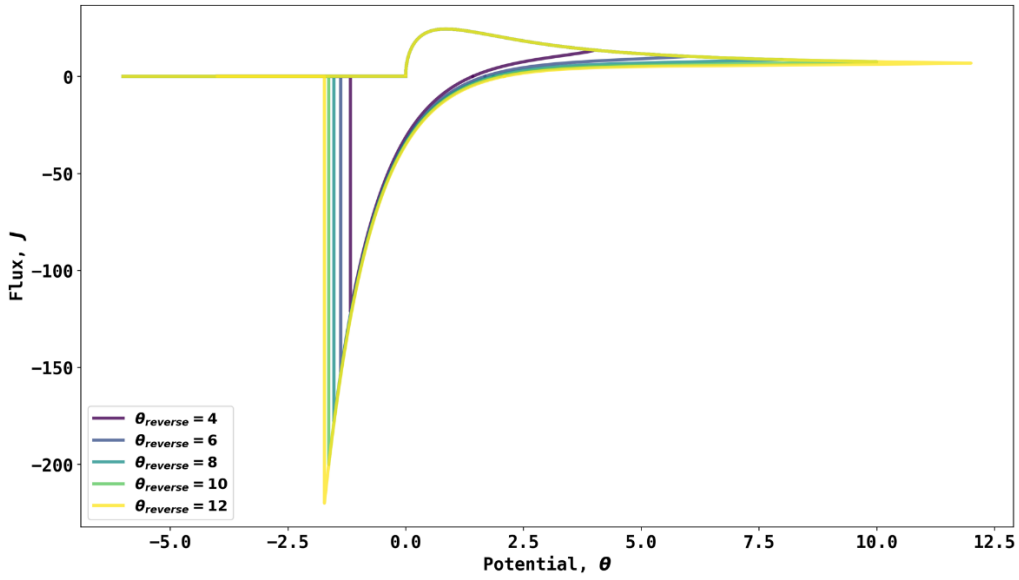

Figure.7.2 Simulation of voltammetry at $\sigma = 1600$ with increasing reversal potentials from 4 to 12.

Figure.7.2 shows the effect of reversing the potential scan at different potentials in the range 4 to 12 whilst maintaining the scan rate at $\sigma = 1600$. Voltammetry was simulated with increasing reverse potentials from 4 to 12. As is evident in the figure reversal at increasingly positive potential leads to the greater deposition of AgBr and hence the potential at which the current corresponding to the removal of AgBr on the reductive scan becomes increasingly

negative. Similarly, the potential on the reverse scan at which reductive currents start to flow becomes increasingly positive consistent with the greater depletion of bromide ions and the corresponding shift of the local equilibrium potential at the electrode surface.

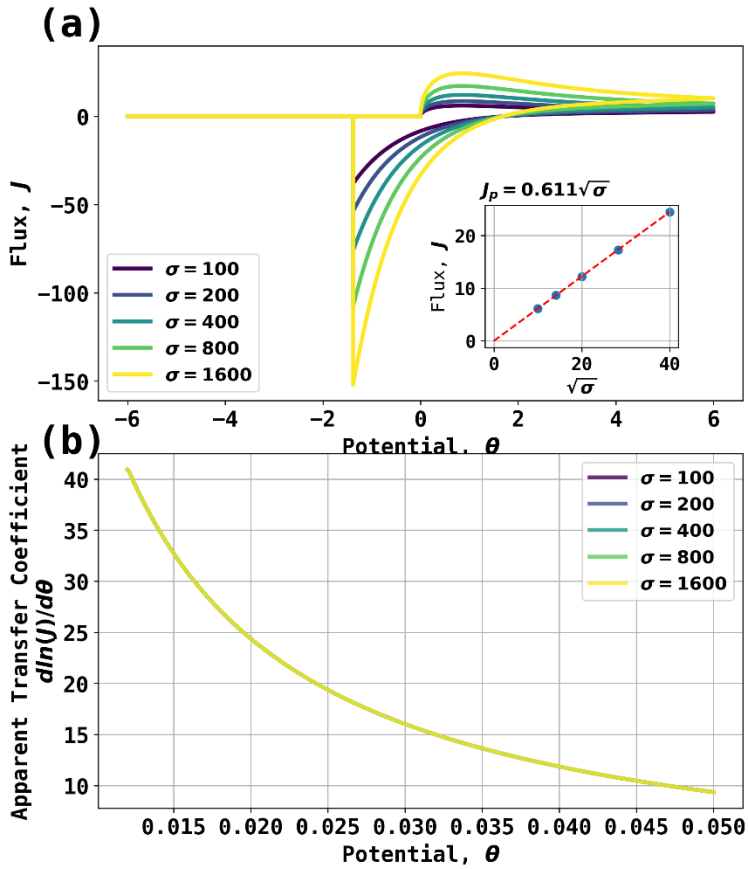

Figure.7.3 (a) Simulated voltammogram from $\sigma = 100$ to $\sigma = 1600$. The inlay shows the regression of peak current vs $\sqrt{\sigma}$; (b) The apparent transfer coefficient from 20% to 40% of voltammogram before peak current.

Next, simulations were conducted for a range of dimensionless scan rates between 100 and 1600. The results are shown in Figure.7.3 (a). The forward (oxidative) voltammetric scan shows a rapidly rising current starting immediately the voltage scan reaches the equilibrium potential, as before, the current reaches a maximum and then decays as the bromide ion concentration is depleted. After reversal of the potential sweep at a dimensionless potential of 8, a reductive wave is observed as the silver bromide formed on the electrode surface in the forward scan is removed. The sudden drop in current corresponds to the completion of the removal process.

Note that the potential at which the current on the reverse scan switches from cathodic to anodic is independent of the scan rate.

As can be seen in Figure.7.3 (a), the peak current occurs at a potential of $\theta_p = 0.854$ independent of scan rate whilst the peak flux increases with the latter. The forward scan peak fluxes, J_p, were regressed with square root of dimensionless scan rates, $\sqrt{\sigma}$ as shown in the inlay, which establishes that for the Ag/AgBr/ Br^- reaction (0:1 stoichiometry),

$$\boldsymbol{J_p = 0.611\sqrt{\sigma}} \tag{7.14}$$

In dimensional form this corresponds to:

$$\boldsymbol{I_{peak} = 0.611FAc\left(\frac{F\nu D}{RT}\right)^{\frac{1}{2}}} \tag{7.15}$$

This contrasts with the corresponding equation for a one electron process with 1:1 stoichiometry [16] where

$$\boldsymbol{J_p = 0.446\ \sqrt{\sigma}} \tag{7.16}$$

Note that the greater sensitivity to scan rate for the 0:1 reaction compared to the 1:1 is related to the more sudden onset of the voltammetric wave in the case of the 0:1 case which only becomes possible at potentials positive of the equilibrium potential. In contrast for a 1:1 process, the voltammetric onset is more gradual reflecting the presence of *both* species, A and B in equation 1, in solution as opposed to the phase change in the system of interest.

The difference between Eqns. (7.15) and (7.16) hints that the electrochemical reaction with 0:1 stoichiometry also exhibits super-Nernstian apparent transfer coefficient slopes. Figure.7.3 (b) shows the transfer coefficient analysis of voltammograms shown in Figure.7.3 (a) taken from 20% to 40% of the peak flux by plotting $\frac{d\ln(J)}{d\theta}$ vs θ. Note the extremely large apparent transfer coefficients observed and their potential dependence whereby the apparent transfer coefficient decreases from ~40 at 20% of the peak flux to ~10 at 40% of the peak flux, showcasing a super-Nernstian behaviour as the apparent transfer coefficient significantly exceeds unity.

7.6 Results and Discussion

Voltammograms were measured using a silver electrode in an aqueous solution of 1.6 mM $Br^-$and 0.1M KNO_3 at a scan rate from 0.02 Vs^{-1} to 0.4 Vs^{-1} starting at a potential of –0.55 V vs the mercury sulfate electrode (MSE) with an oxidative first sweep with reversal of the potential at –0.15 V vs MSE as shown in Figure.7.4 (a). The voltammogram shows an oxidative peak corresponding to the formation of AgBr on the forward scan and a reductive peak on the reverse scan related to the reduction of the AgBr to Ag. The equilibrium potential located between the two peaks is estimated as ca –0.332 ± 0.005 V. Note that the solubility of silver bromide in the medium used is tiny (the solubility product is thought to be ca 5.0×10^{-13} at 298 K) and the experimental conditions are such that the formation of soluble silver complexes of the type $AgBr_n^{(n-1)-}$ where n is greater than or equal to one, are not expected to be formed [21] and as discussed in Section A7.3, Appendices. Specifically, the tabulated and visualized speciation data is shown in Table A7.1 and Figure.A7.4. Variable scan rate experiments were carried out as shown in Figure.7.4 (a) where an increase in the peak currents with square root of scan rate is evident. The voltammetry in Figure.7.4 (a) is qualitatively consistent with that reported by Hassan et al [22] albeit that the latter was measured under self-supported condition, and is qualitatively that expected for a quasi-reversible process in that both oxidative and reductive peaks are clear but unlike a fully reversible process negligible currents flow immediately anodically or cathodically of the equilibrium potential. Comparison of the anodic and cathodic charges passed in the voltammetry suggests that less than 100% of the deposited AgBr is stripped and that the fraction stripped decreases with a decrease in scan rate (more significant at a higher concentration, e.g. 1.6 mM) as shown in the Section A7.4, Appendices and Table A7.2. This is attributed to mechanical loss of deposited AgBr or, more likely, the formation of AgBr particles which are electrically isolated from the electrode and therefore not stripped in the reverse scan.

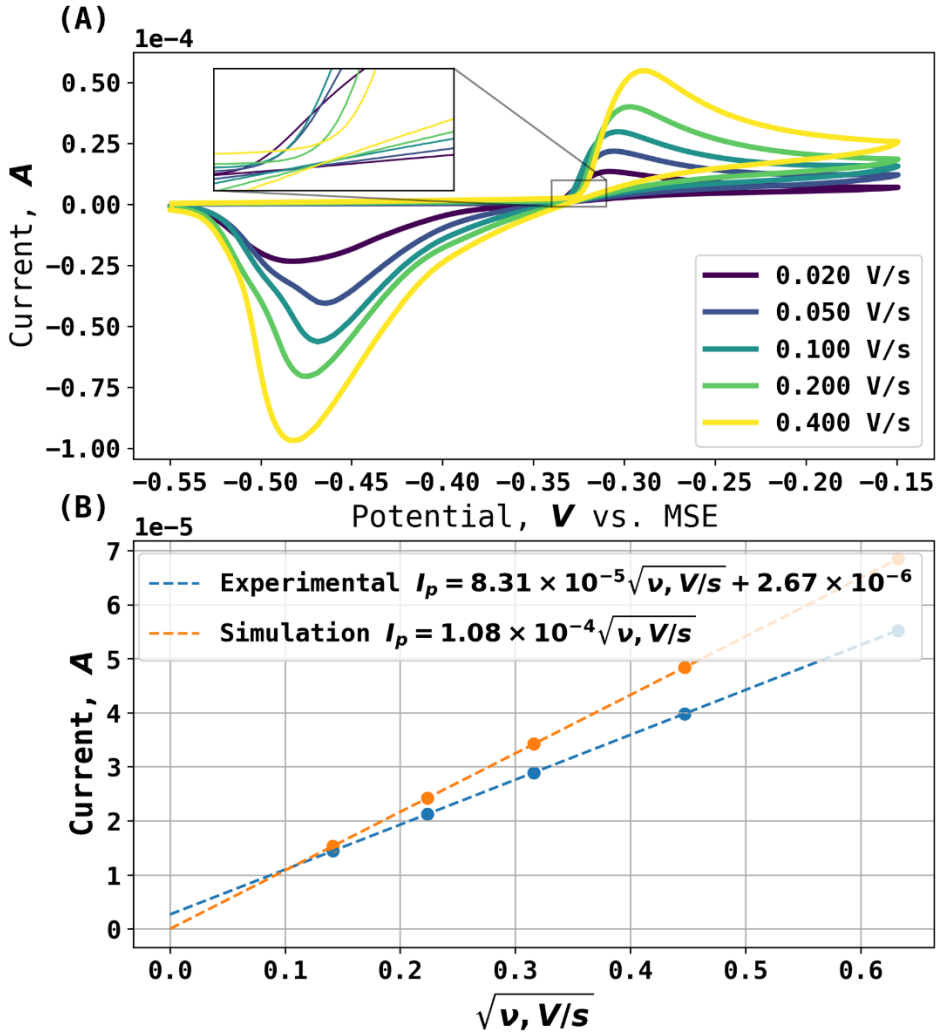

Figure.7.4 (a) Cyclic voltammograms of 1.6 mM Br^- in 0.1 M KNO_3 at Ag macroelectrode as a function of scan rate from 0.02 Vs^{-1} to 0.4 Vs^{-1}. The inset shows the oxidative and reductive current near equilibrium potential. (b) Regressing the forward scan peak currents from experiment (blue trace) and simulation (orange trace) against square root of scan rate.

Figure.7.4 (b) shows a plot of the peak currents measured in Figure.7.4 (a) against the square root of the voltage scan rate (blue dash line). The linear, direct dependence is consistent with a diffusional process. Also shown in Figure.7.4 (b) are the simulated results using a value of $2.1 \times 10^{-9}\ m^2 s^{-1}$ for the diffusion coefficient of the bromide ion as reported by Kumar et al [23] measured using microelectrode voltammetry at 298 K (orange dash line). It is evident that the process is diffusional but that the agreement with simulated results is semi-quantitative with the experimental values seen to be below those predicted theoretically. This can be attributed

to the growing silver bromide film on the electrode inhibiting diffusion to the site of electrochemical reaction at triple interface formed by the three phases of silver, silver bromide and aqueous bromide solution. That said, the quasi-reversible character of the voltammetry is evident. This is further confirmed using the procedure described previously for the inference of surface bromide concentrations from the measured currents as a function of potential as discussed below.

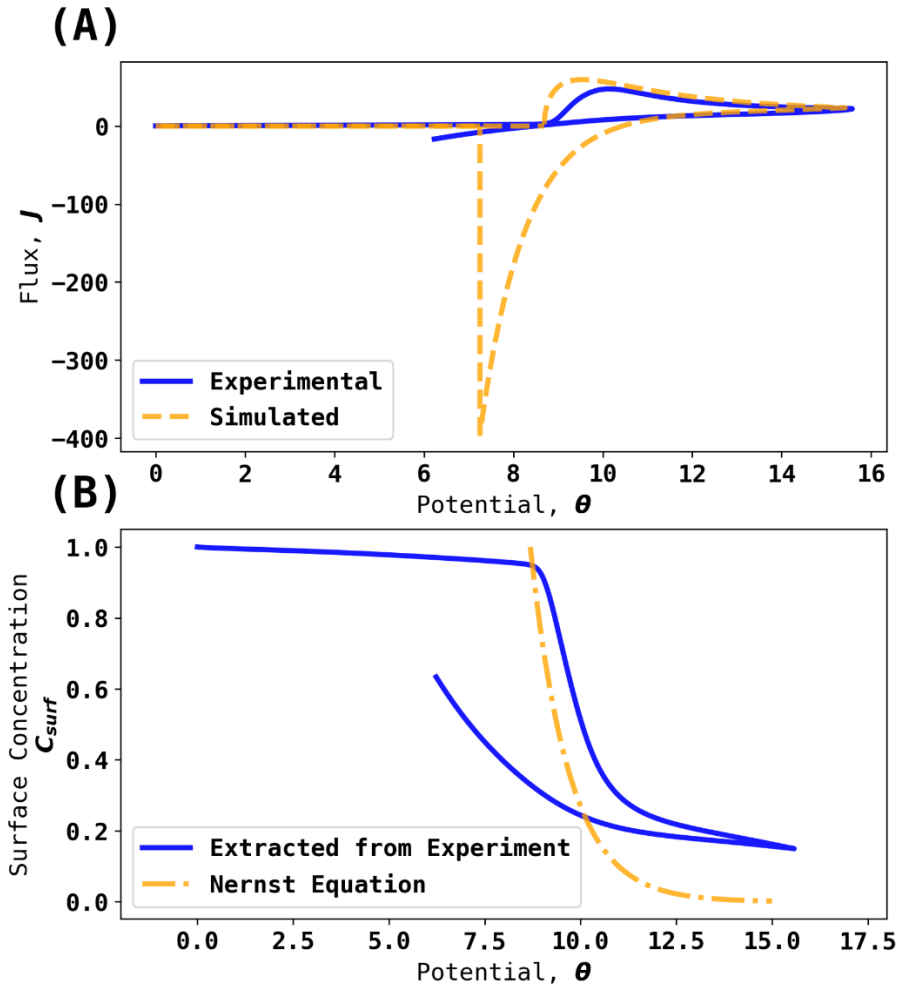

Figure.7.5 (a) Experimental (blue trace) and simulated (orange trace) voltammogram at 0.4 Vs^{-1} and $c^{*}_{Br^-} = 1.6$ mM. (b) Surface bromide concentration extracted from experiment using backward implicit method (blue trace) and predicted via the Nernst Equation with (0:1) stoichiometry (orange trace). Work of Dr. Haotian Chen.

Figure.7.5 (a) shows an experimental voltammogram measured in 1.6 mM Br^- at a scan rate of 0.4 Vs^{-1} alongside the simulated voltammogram, which confirms the inferences of quasi-

reversibility and restricted diffusion made from the Randles–Ševčík equation plot. Figure.7.5 (b) shows the corresponding inferred electrode surface concentrations alongside the expectations of the Nernst equation made using an equilibrium potential of –0.323 V. Figure.7.6 (a) and (b) show analogous data but for the slower scan rate of 0.1 Vs^{-1}. Both Figure.7.5 and Figure.7.6 confirm the quasi-reversibility of the voltammetric wave; the fit with the Nernst equation is approximate and the absolute concentrations observed deviate from those expected for full electrochemical reversibility.

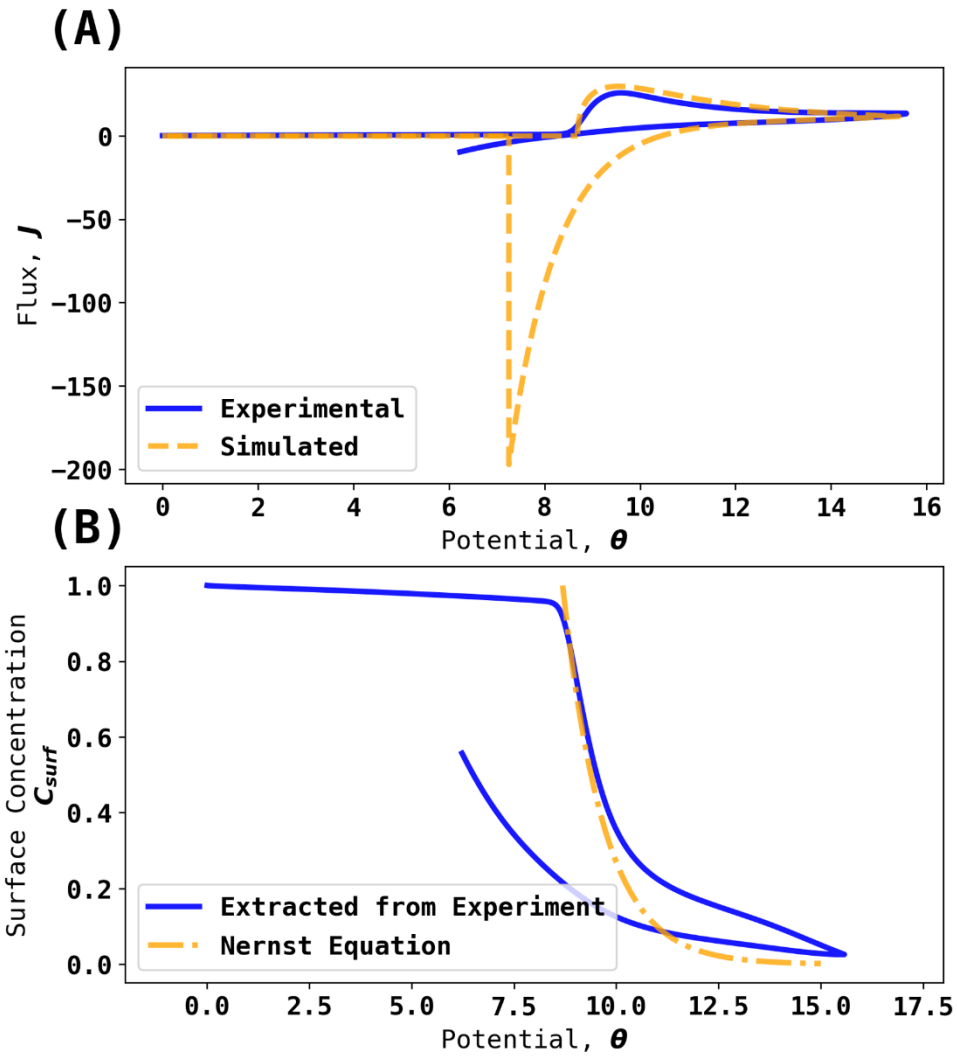

Figure.7.6 (a) Experimental (blue trace) and simulated (orange trace) voltammogram at 0.1 Vs^{-1} and $c^*_{Br^-}$ = 1.6 mM. (b) Surface bromide concentration extracted from experiment using backward implicit method (blue trace) and predicted via the Nernst Equation with (0:1) stoichiometry (orange trace). Work of Dr. Haotian Chen.

To summarise, Figure.7.5 and Figure.7.6 highlight the value of the novel simulations in respect of defining the full reversibility or otherwise by comparison with experiment. The quasi-reversible behaviour is clearly established and this is important if the redox couple is used as a reference electrode. To be more specific for a quasi-reversible redox couple, the potential will markedly deviate from ideal behaviour if significant currents are drawn through the interface, whereas the a reversible one simulated using Nernst equation has a lower potential change with respect to the current change. However, we return to this point further below.

Returning to Figure.7.5 (a), comparison of the simulated reversible behaviour with experimental cathodic stripping peak shows considerable overpotential is required to reduce the deposited silver bromide. Data in Section A4.5 shows that the average thickness of the deposited AgBr film is of the nano-meter scale. Table A7.3 shows the parameters used to calculate the thickness, Figure.A7.5 shows AgBr average thickness progressing with voltammetric scan when $c^*_{Br^-} = 1.6$ mM with a scan rate of 0.4 Vs^{-1}. Table A7.4 tabulates the estimated average AgBr deposit thickness for scans at different concentrations and scan rates. In reality, a non-uniform porous film is likely. Further modelling based, for example, on Butler-Volmer kinetics would need to recognize that the site of nucleation and growth or stripping of the deposit would likely be located at the triple interface formed between solid Ag, solid but poorly conductive AgBr and the bromide in aqueous phase, and of uncertain dimensions. Thus, the simulation of the kinetically controlled quasi-reversible voltammogram is challenging since the use of average AgBr coverages with uniform reactivity such as used for sub-monolayer molecular layers [24] is likely to be unrealistic when a new phase, such as that of AgBr is formed.

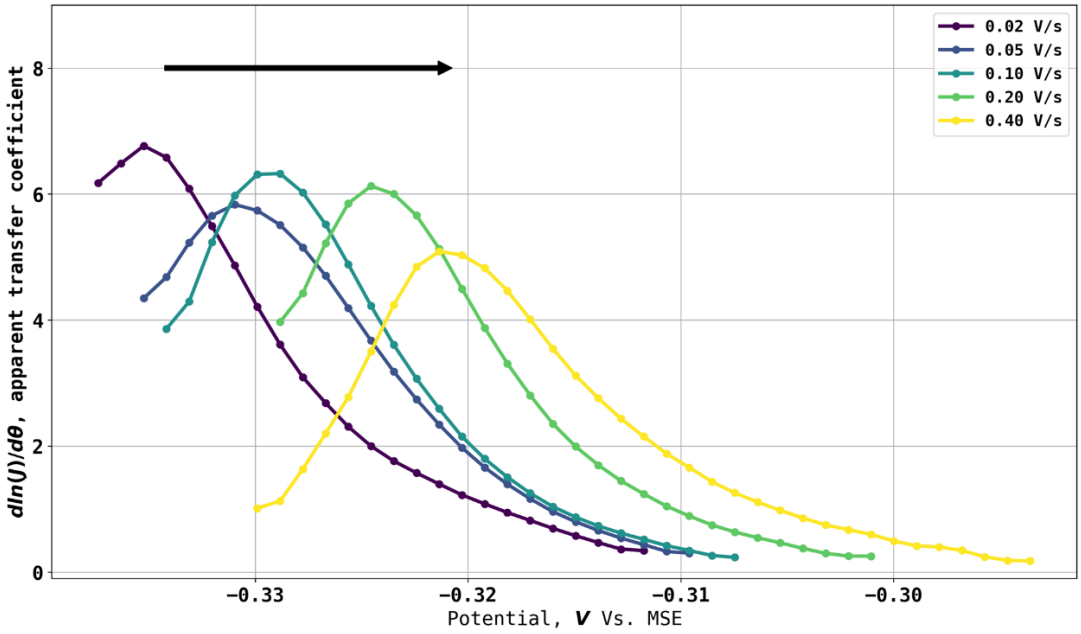

Figure.7.7 Tafel slopes for voltammograms shown in Figure.7.4 (a) at scan rates from 0.02 to 0.4 Vs^{-1}. The Tafel slopes are extracted from part of the voltammogram before the oxidative peak: the starting potential corresponds to 10% of peak current, and the ending potential corresponds to 90% of peak current. The black arrow indicates the direction of scan.

Given that the partial electrochemical reversibility seen experimentally would likely allow the possibility of super-Nernstian responses, attention was next given to transfer coefficient (Tafel-like) analysis of the experimental voltammetry as shown in Figure.7.4 (a) and the results of the transfer coefficient analysis are shown in Figure.7.7. The transfer coefficient analysis was performed by analysing a fraction of the voltammogram before the forward scan peak current and in this case, from 10% to 90% of peak current. The dimensional voltammograms are then converted to dimensionless form, and the apparent transfer coefficients are estimated as $\alpha = \frac{d \ln J}{d\theta}$. It is evident that the latter are both potential dependent and take values very considerably in excess of the value of unity expected for a simple one electron 1:1 process, so validating the hypothesis formulated in the Introduction of this chapter that extreme behaviour in terms of apparent transfer coefficients is expected for 0:1 process with reversible, or in the case studied, even quasi-reversible voltammetry shows super-Nernstian responses. This is an

important new insight. The silver-silver bromide couple has been widely and extensively used as a successful reference electrode for many years [14]. As noted above the couple is voltammetrically quasi-reversible, which at first sight is a disadvantage. However, the intrinsic high sensitivity of the current response to the potential shown above to be characteristic of 0:1 process more than offsets the effects of the quasi-reversibility so that experimentally apparent transfer coefficients in excess of unity are seen. Since a key property of a good reference electrode is holding a near fixed potential even when passing a current, it can be seen that this confers a significant advantage on reference electrodes based on 0:1 processes where a solution phase species is in equilibrium with a solid phase, as for example in silver-silver chloride, calomel and Ag-Ag^+ electrodes in addition to the silver-silver bromide electrode as compared to say the reference electrodes based exclusively on solution phase species.

7.7 Conclusions

The Randles–Ševčík equation for a 0:1 stoichiometry has been established as $J_p = 0.611\sqrt{\sigma}$ in dimensionless form. Simulation of the voltammetry shows that the apparent transfer coefficients significantly exceed unity displaying values as high as 40. The simulated expected super-Nernstian behaviour is observed in the voltammetric experiments of the oxidation of bromide ions at a silver electrode despite the system, displaying quasi-reversible behaviour with apparent transfer coefficients as high as 7. This chapter thus confirms, both computationally and experimentally, super-Nernstian behaviour for redox systems of 0:1 stoichiometry and concludes, generically, that for electrode processes where soluble solution redox species form solids, ultra-high transfer coefficients far exceeding unity can be observed. The latter observation has implications for the design of reference electrodes best able to provide a near constant electrode potential despite the passage of significant current. Electrodes based on redox couples of 0:1 stoichiometry are intrinsically more robust in this respect than couples based entirely on solution phase species.

Appendices

Section A7.1: Extracting Electrode Surface Concentrations (Work of Dr. Haotian Chen)

This section explains the methodology to extract surface concentrations from experimental voltammograms using the method of Henstridge. [17]

First, the voltammogram is converted to dimensionless form using the table shown in the text except for the definition of the dimensionless potential which is noted in the main text. The dimensionless voltammogram then takes the form of dimensionless flux, J, versus dimensionless potential.

In modelling the voltammetry, the flux at time step k, J^k,is approximated by $J^k = \left(\frac{C^k_{X=0} - C^k_{X=\Delta X}}{\Delta X}\right)$, so rearrangement gives $C^k_{X=\Delta X} - C^k_{X=0} = J^k \Delta X$. Note that $C^k_{X=0}$ is the surface concentration of the electroactive species, $C^k_{X=\Delta X}$ is the concentration near electrode surface at $X = \Delta X$, where ΔX is a small spatial step. Using the Newton-Raphson method, $C^k_{X=0}$ can be estimated from a knowledge of J^k.

The backward implicit method solves the diffusion equation in finite difference form:

$$\frac{\boldsymbol{C_i^k - C_i^{k-1}}}{\boldsymbol{\Delta T}} = \frac{\boldsymbol{C_{i-1}^k - 2C_i^k + C_{i+1}^k}}{\boldsymbol{(\Delta X)^2}} \qquad (7.17)$$

where i and k represents the current spatial and time steps. The equation can be rearranged as:

$$\boldsymbol{C_i^{k-1} = -\lambda C_{i-1}^k + (1 + 2\lambda) C_i^k - \lambda C_{i+1}^k} \qquad (7.18)$$

where $\lambda = \frac{\Delta T}{(\Delta X)^2}$. From the boundary condition it can further be inferred that $C^k_{X=\Delta X} - C^k_{X=0} = J^k \Delta X$.

Using the Backward Implicit method, a tridiagonal sparse matrix is constructed to solve for the concentration profile at time step k:

$$\begin{bmatrix} -\mathbf{1} & \mathbf{1} & \mathbf{0} & \mathbf{0} & \mathbf{0} & \mathbf{0} & \mathbf{0} & \mathbf{0} \\ \boldsymbol{\alpha} & \boldsymbol{\beta} & \boldsymbol{\gamma} & \mathbf{0} & \mathbf{0} & \mathbf{0} & \mathbf{0} & \mathbf{0} \\ \mathbf{0} & \boldsymbol{\alpha} & \boldsymbol{\beta} & \boldsymbol{\gamma} & \mathbf{0} & \mathbf{0} & \mathbf{0} & \mathbf{0} \\ \mathbf{0} & \mathbf{0} & \boldsymbol{\alpha} & \boldsymbol{\beta} & \boldsymbol{\gamma} & \mathbf{0} & \mathbf{0} & \mathbf{0} \\ \mathbf{0} & \mathbf{0} & \mathbf{0} & \dots & \dots & \dots & \mathbf{0} & \mathbf{0} \\ \mathbf{0} & \mathbf{0} & \mathbf{0} & \mathbf{0} & \dots & \dots & \dots & \mathbf{0} \\ \mathbf{0} & \mathbf{0} & \mathbf{0} & \mathbf{0} & \mathbf{0} & \boldsymbol{\alpha} & \boldsymbol{\beta} & \boldsymbol{\gamma} \\ \mathbf{0} & \mathbf{0} & \mathbf{0} & \mathbf{0} & \mathbf{0} & \mathbf{0} & \mathbf{0} & \mathbf{1} \end{bmatrix} \times \begin{bmatrix} \boldsymbol{C_0^k} \\ \boldsymbol{C_1^k} \\ \boldsymbol{C_2^k} \\ \boldsymbol{C_3^k} \\ \dots \\ \dots \\ \boldsymbol{C_{n-2}^k} \\ \boldsymbol{C_{n-1}} \end{bmatrix} = \begin{bmatrix} \boldsymbol{J^k \Delta X} \\ \boldsymbol{C_1^{k-1}} \\ \boldsymbol{C_2^{k-1}} \\ \boldsymbol{C_3^{k-1}} \\ \dots \\ \dots \\ \boldsymbol{C_{n-2}^{k-1}} \\ \mathbf{1} \end{bmatrix} \qquad (7.19)$$

where $\alpha = -\lambda$, $\beta = 1 + 2\lambda$, $\gamma = -\lambda$.

By solving the concentration profile sequentially for increasing k, the surface concentration as a function of time or potential can be obtained.

To validate our implementation of the inversible method prior to application to the (0,1) system of interest, the experimental voltammogram for the one electron reduction of $[\mathrm{Ru(NH_3)_6}]^{3+}$ to $[\mathrm{Ru(NH_3)_6}]^{2+}$ was analysed and the resulting electrode surface concentrations compared with Nernst equation. The system is well characterised [25]. The experiment was performed at a scan rate of 0.5 $\mathrm{Vs^{-1}}$ with 1 mM $[\mathrm{Ru(NH_3)_6}]^{3+}$ in 0.1 M KCl electrolyte and with a glassy carbon electrode ($r = 1.5$ mm) as working electrode. From literature, the diffusion coefficient of $[\mathrm{Ru(NH_3)_6}]^{3+}$ in such conditions is $8.43 \times 10^{-10}\, m^2\, s^{-1}$. [25] The extracted surface concentrations shown in Figure.A7.1 (a) agreed quantitatively with the Nernst equation when θ>10, while the small false apparent negative concentration extracted when $\theta < 10$ result from small background currents flowing in the experimental voltammetry. We conclude that the backward implicit model can quantitatively extract the surface concentrations of electro-active species from experimental data.

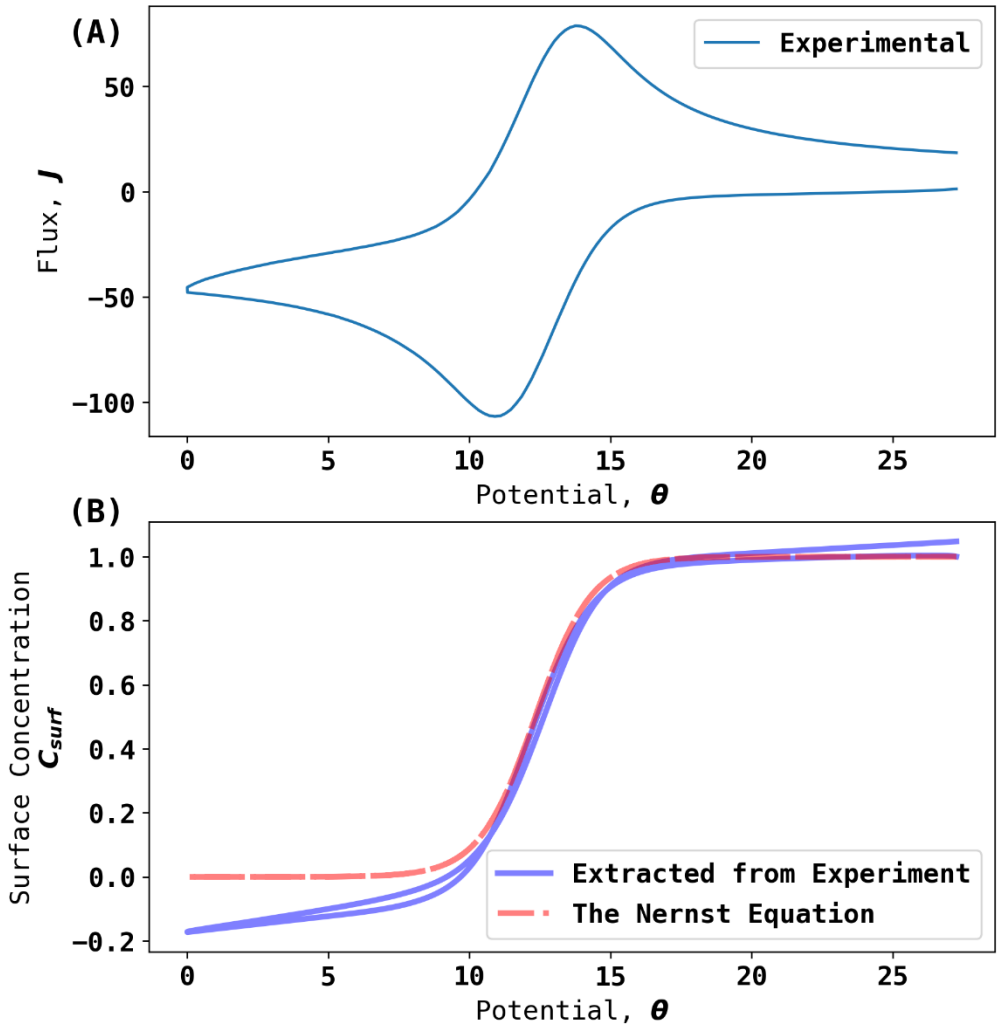

Figure.A7.1 (a) Dimensionless form of a voltammogram of reduction of 1 mM $[Ru(NH_3)_6]^{3+}$ ***in 0.1 M KCl on a glassy carbon electrode. (b) The extracted surface concentration is compared with the Nernst equation with 1:1 stoichiometry.***

Section A7.2: Testing and Verification of Simulations (Work of Dr. Haotian Chen)

Simulation of the electrochemical reaction model utilised expanding space grids [26] to reduce computational time. If the scans start and finish at the same potential, the time for the full scan is $T_{sim} = \frac{2\,|\theta_i - \theta_{switch}|}{\sigma}$, where θ_i and θ_{switch} are the dimensionless starting and switching potentials respectively. σ is the dimensionless scan rate. The maximum spatial distance of the simulation in solution is taken as $X_{sim} = 6\sqrt{T_{sim}}$ [18]. The accuracy of the simulations, were dependent on the spatial step size and time step size. The spatial step size in an expanding grid depends on the initial step size, h_0, and the expanding grid factor, ω, according to the following definition:

$$\boldsymbol{h_i = X_{i+1} - X_i = h\omega^i} \qquad (7.20)$$

where X_i is the dimensionless spatial coordinate at point i. In simulation, h_0 was related to X_{sim} by $h_0 = \lambda X_{sim}$ where λ is a simulation factor determining the initial spatial step. To test convergence of the simulation, λ was varied from 10^{-9} to 10^{-5} and ω varied from 1.01 to 1.2. Since a uniform time grid was used, $d\theta$ was varied from 10^{-5} to 10^{-2} while σ was fixed at 1600 and 100, the highest and lowest scan rates presented in the paper.

The voltammograms generated were validated by comparing the forward scan peak flux, J_p and peak potential, θ_p at different values of $\lambda, d\theta$ and ω as shown in Figure.A7.2 and Figure.A7.3. The simulation parameters at $\lambda = 10^{-7}$, $d\theta = 10^{-4}$ and $\omega = 1.05$ results in converged peak flux at $J_p \approx 24.42$ and peak potential at $\theta_p = 0.85$ when $\sigma = 1600$. At a $\sigma = 100$, using the same set of parameters, $J_p \approx 6.15$ and $\theta_p = 0.85$. The converged peak fluxes and peak potentials using the simulation parameters mentioned above validated the simulations.

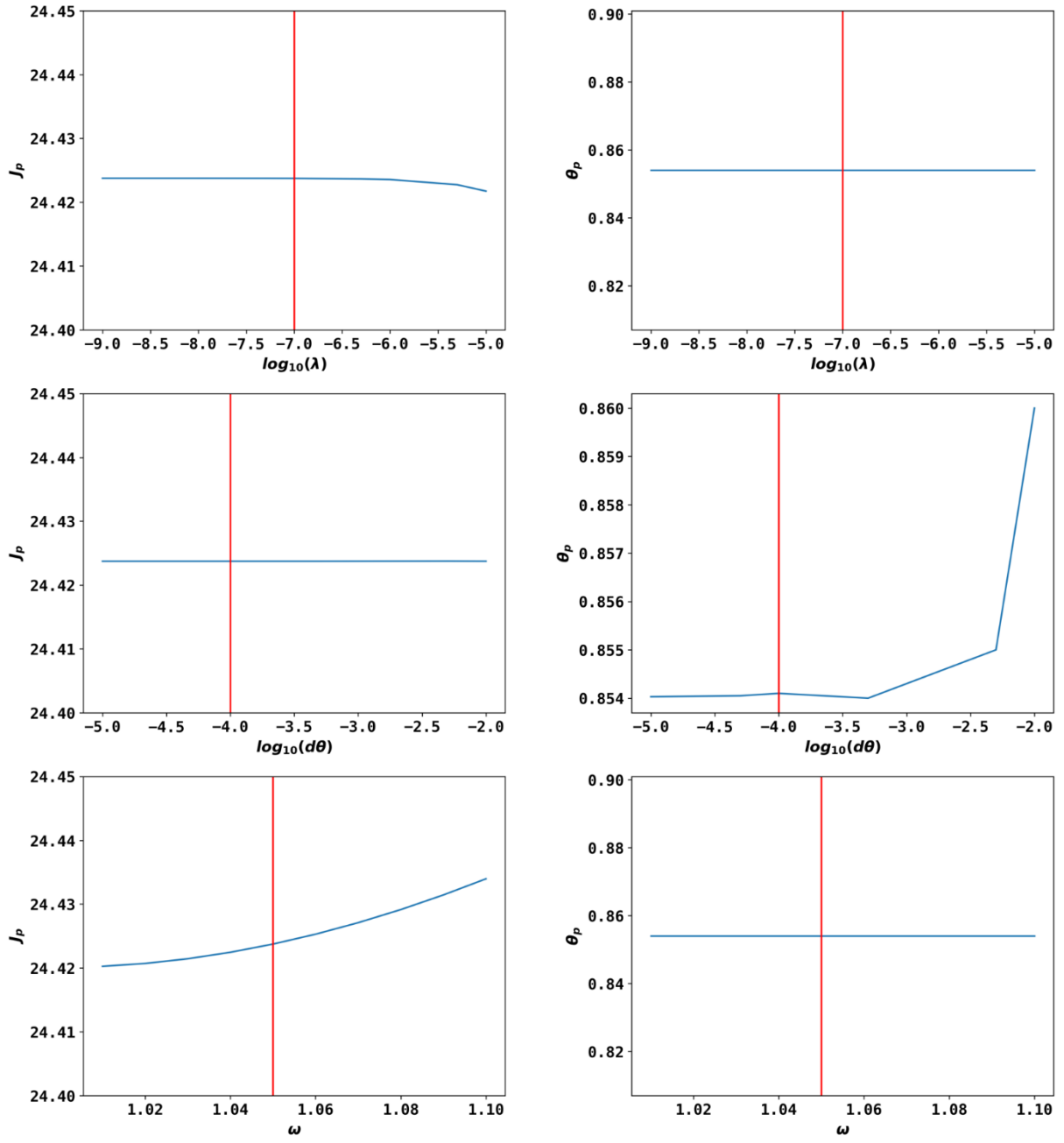

Figure.A7.2 Convergence test as discussed in the text of the Appendices when $\sigma = 1600$, the highest scan rate analysed in text. The left column of three figures shows the responses of the peak flux, J_p, at different values of $\lambda, d\theta$ and ω; the right column shows the corresponding responses of the peak potential, θ_p. The red line shows the values at the three parameters selected for use in the simulations reported in the text.

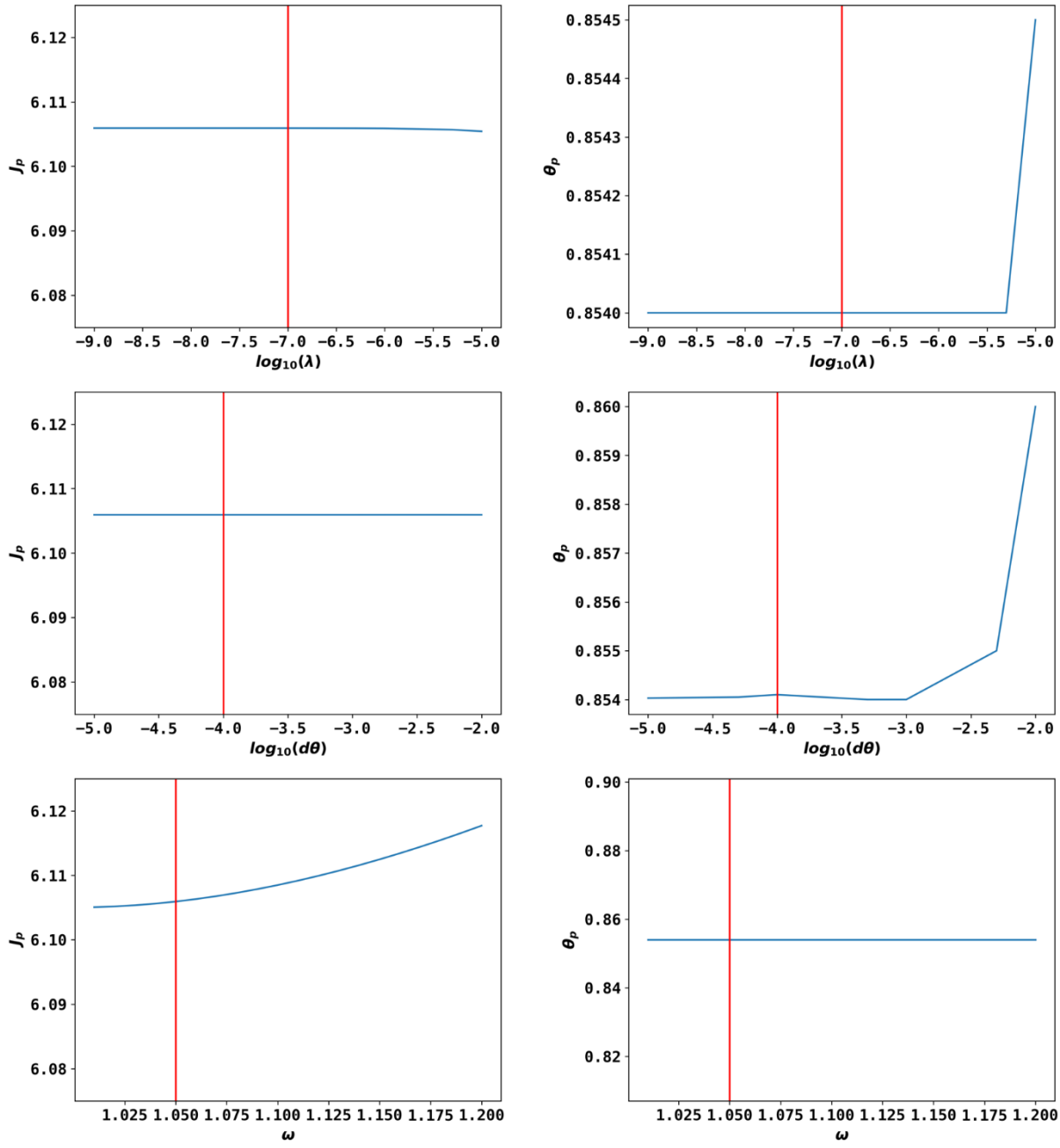

Figure.A7.3 Convergence test as discussed in the text of the Appendices when $\sigma = 100$, the lowest scan rate analysed in text. The left column of three figures shows the responses of the peak flux, J_p, at different values of λ, $d\theta$ and ω; the right column shows the corresponding responses of the peak potential, θ_p. The red line shows the values at the three parameters selected for use in the simulations reported in the text.

Section A7.3: Silver Speciation

To clarify the solution conditions relating to the voltammetry reported in the main text, the speciation of silver (I) in the solutions of interest were calculated using Hydra/Medusa. [27] The chemical equilibria considered were as follows:

$$\boldsymbol{AgBr(s) \rightleftarrows Ag^{+}(aq) + Br^{-}(aq)} \quad (7.21)$$

$$\boldsymbol{AgBr(s) \rightleftarrows AgBr(aq)} \quad (7.22)$$

$$\boldsymbol{AgBr(s) + Br^{-}(aq) \rightleftarrows AgBr_2^{-}(aq)} \quad (7.23)$$

$$\boldsymbol{AgBr(s) + 2Br^{-}(aq) \rightleftarrows AgBr_3^{2-}} \quad (7.24)$$

Figure.A7.4 shows the resulting distribution diagram of the different soluble silver species, $AgBr_n^{(n-1)-}$, as a function of the total bromide concentration. Note that the x-axis scale is logarithmic. The corresponding percentages of different species (Ag^+, AgBr, and $AgBr_2^-$) at different concentrations are summarized by Table A7.1. For voltammetry in a 1.6 mM bromide solution, AgBr(aq) accounts for 76% of the silver (I), while $AgBr_2^-$ and Ag^+ are 11% and 13% respectively. Note that $AgBr_3^{2-}$ is not present in solutions with low concentrations of bromide [21].

Table A7.1 Concentration of Ag^+, $AgBr$ and $AgBr_2^-$ ion as a function of total concentration of Br^-.

$c^*_{Br^-}, mM$	$Ag^+(aq), \%$	$AgBr(aq), \%$	$AgBr_2^-(aq), \%$
0.2	11%	76%	13%
0.4	32%	64%	3.2%
0.8	28%	67%	4.1%
1.2	20%	74%	7.0%
1.6	13%	76%	11%

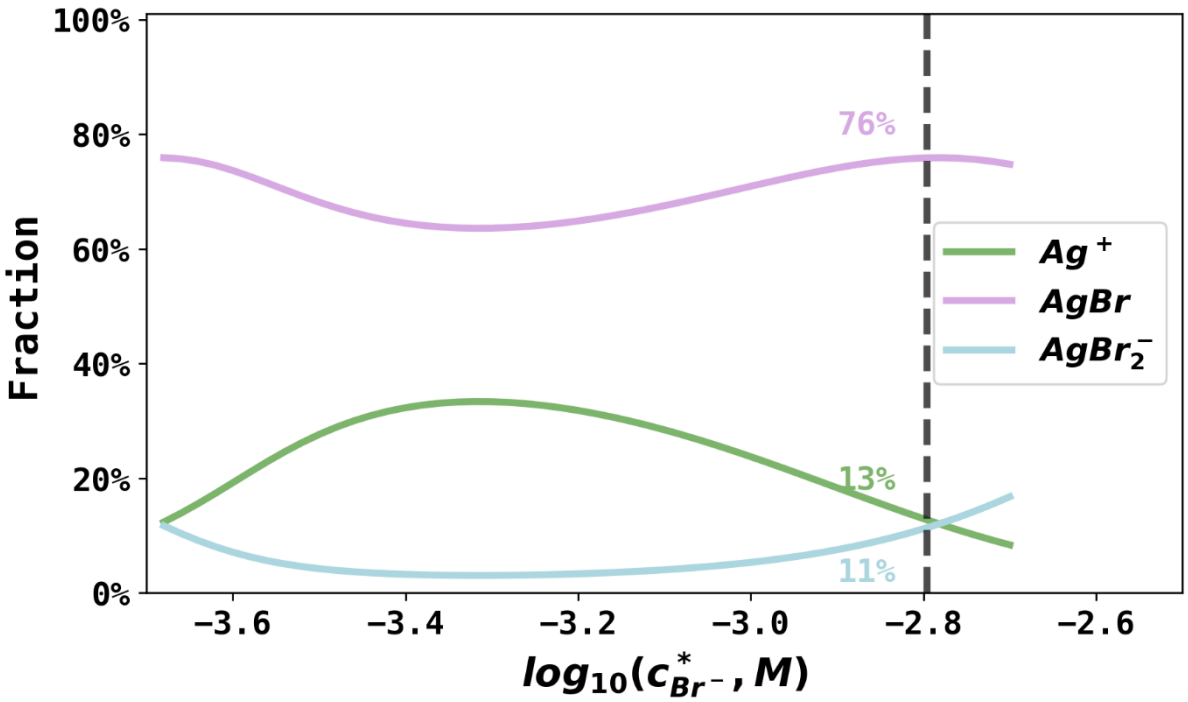

Figure.A7.4 Silver(I) speciation in aqueous solution showing Ag^+, $AgBr$ and $AgBr_2^-$ as a function of $log_{10}\, c^*_{Br^-}$, the logarithm of bulk concentration of bromide ion using Hydra/Medusa. [27] ***The black dashed line and the text near it indicates the fraction of ions when total concentration of bromide is 1.6 mM. Note that the speciation shown is that of the solution phase; solid AgBr is not considered***

Section A7.4: AgBr Stripping Efficiency

By integrating the oxidative and reductive charges the fraction of stripped AgBr was obtained as a function of $c^*_{Br^-}$ and scan rates are shown in Table A7.2. The fraction stripped decreases with a decrease in scan rates and decrease in bulk concentration of bromide. The trends are discussed in the main text.

Table A7.2 The fraction of stripped AgBr by comparing the cathodic relative to anodic charges as a function of, $c^*_{Br^-}$, the bulk concentration of Br^- and scan rates.

	20 mV/s	50 mV/s	100 mV/s	200 mV/s	400 mV/s
0.2 mM	53%	51%	50%	45%	50%
0.4 mM	56%	56%	58%	58%	59%
0.8 mM	77%	75%	80%	79%	78%
1.2 mM	77%	80%	82%	83%	85%
1.6 mM	87%	89%	89%	90%	92%

Section A7.5: AgBr Deposit Thickness

To estimate the AgBr deposit thickness during the experimental voltammetric scans, the current was integrated versus time to obtain the charge transferred, which was then used to estimate the AgBr thickness on the electrode using the following equation:

$$Thickness \approx \frac{charge}{Faraday\ Constant} \times molar\ mass \div density \div area\ of\ electrode$$

The parameters used to calculate AgBr thickness are shown in Table A7.3. Figure.A7.5 gives an example of the estimated AgBr deposit thickness as the voltammetric scan proceeds. The summary of the peak AgBr thickness at different bromide bulk concentrations and scan rates are shown in Table A7.4.

Table A7.3 Parameters used to estimate AgBr thickness during the voltammetric scan.

Parameter	Values
Faraday Constant	96485 C/mol
AgBr molar mass	187.77 g/mol
AgBr density	$6.473 \times 10^6 \frac{g}{m^3}$
Area of electrode	$\pi \times (1.13 \times 10^{-3})^2\ m^2 = 4.01 \times 10^{-6}\ m^2$
Ag density	10.49 g/cm^3
Ag atomic radius	172 pm

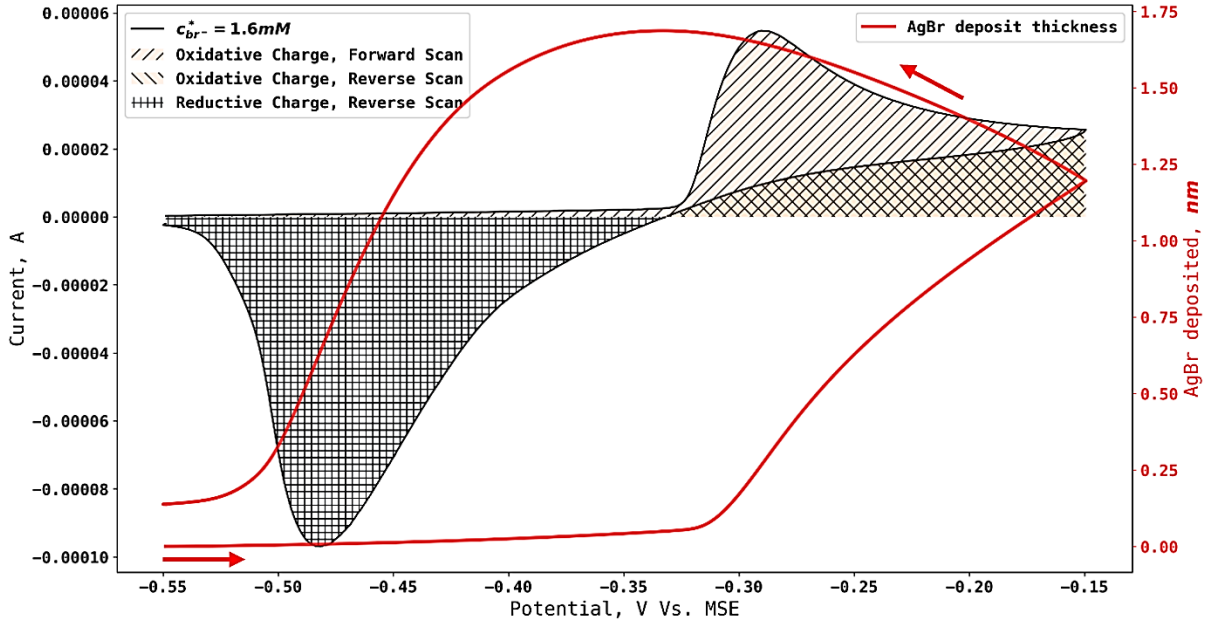

Figure.A7.5 The voltammetric scan when $c^*_{Br^-} = 1.6\ mM$ and $\nu = 400\ mV/s$. The black trace represents the voltammogram, and the red trace represents the AgBr deposit thickness as voltammetric scan proceeds. A maximum of 1.69 nm AgBr is estimated to deposited on electrode surface during scan.

Table A7.4 The maximum AgBr deposit thickness during the voltammetry scan as a function of bulk concentration of bromide, $c^*_{Br^-}$ and scan rate, ν.

AgBr deposited, nm		scan rate, mV/s				
		20	50	100	200	400
$c^*_{Br^-}$, mM	0.2	1.69	1.16	0.79	0.55	0.36
	0.4	4.10	2.24	1.39	0.91	0.61
	0.8	5.02	3.18	2.12	1.46	1.01
	1.2	8.47	4.7	3.08	2.07	1.36
	1.6	**9.31**	**7.79**	**3.90**	**2.54**	**1.69**

References

1. K. Chiba, K. Tsunoda, Y. Umezawa, H. Haraguchi, S. Fujiwara and K. Fuwa, *Analytical Chemistry*, 1980, **52**, 596-598.
2. D. J. G. Ives, G. J. Janz and C. V. King, *Journal of The Electrochemical Society*, 1961, **108**, 246C.
3. H. Chen, Y. Chen and R. G. Compton, *Analytical Chemistry*, 2023, **95**, 1663-1670.
4. R. G. Compton and C. E. Banks, *Understanding voltammetry*, World Scientific, London, 3rd edn., 2018.
5. J. Tafel, *Zeitschrift für Physikalische Chemie*, 1905, **50**, 641-712.
6. D. Li, C. Lin, C. Batchelor-McAuley, L. Chen and R. G. Compton, *Journal of Electroanalytical Chemistry*, 2018, **826**, 117-124.
7. R. Guidelli, R. G. Compton, J. M. Feliu, E. Gileadi, J. Lipkowski, W. Schmickler and S. Trasatti, *Pure and Applied Chemistry*, 2014, **86**, 245-258.
8. R. Guidelli, R. G. Compton, J. M. Feliu, E. Gileadi, J. Lipkowski, W. Schmickler and S. Trasatti, *Pure and Applied Chemistry*, 2014, **86**, 259-262.
9. J. A. V. Butler, *Transactions of the Faraday Society*, 1924, **19**, 729-733.
10. T. Erdey-Grúz and M. Volmer, *Z. Physical Chemistry Chemical Physics*, 1930, **150**, 203-213.
11. M. C. Henstridge, E. Laborda, N. V. Rees and R. G. Compton, *Electrochimica Acta*, 2012, **84**, 12-20.
12. H. Chen, J. R. Elliott, H. Le, M. Yang and R. G. Compton, *Journal of Electroanalytical Chemistry*, 2020, **869**, 114185.
13. H. Chen and R. G. Compton, *Journal of Electroanalytical Chemistry*, 2021, **880**, 114942.
14. S. Hosseini, A. Abbasi, L.-O. Uginet, N. Haustraete, S. Praserthdam, T. Yonezawa and S. Kheawhom, *Scientific reports*, 2019, **9**, 1-12.
15. G. T. Burstein, *Corrosion Science*, 2005, **47**, 2858-2870.
16. J. M. Gomez-Gil, E. Laborda and A. Molina, *Analytical Chemistry*, 2020, **92**, 3728-3734.
17. M. C. Henstridge and R. G. Compton, *Journal of Electroanalytical Chemistry*, 2012, **681**, 109-112.
18. R. G. Compton, E. Laborda, E. Kaetelhoen and K. R. Ward, *Understanding voltammetry: simulation of electrode processes*, World Scientific London, 2nd edn., 2020.
19. M. Rudolph, *Journal of Electroanalytical Chemistry and Interfacial Electrochemistry*, 1991, **314**, 13-22.
20. J. Verbeke and R. Cools, *International Journal of Mathematical Education in Science and Technology*, 1995, **26**, 177-193.
21. C. H. Gammons and Y. Yu, *Chemical Geology*, 1997, **137**, 155-173.
22. H. Ibrahim, S. Mohammed and A. Amin, *International Journal of Electrochemical Science*, 2010, **5**, 278-294.
23. H. Chen, A. K. S. Kumar, H. Le and R. G. Compton, *Journal of Electroanalytical Chemistry*, 2020, **876**, 114730.
24. M. Yang and R. G. Compton, *The Journal of Physical Chemistry C*, 2020, **124**, 18031-18044.
25. Y. Wang, J. G. Limon-Petersen and R. G. Compton, *Journal of Electroanalytical Chemistry*, 2011, **652**, 13-17.
26. D. Gavaghan, *Journal of Electroanalytical Chemistry*, 1998, **456**, 1-12.
27. I. Puigdomenech, *KTH Royal Institute of Technology*, 2004.

Conclusions

Electrochemical sensors are powerful analytical tools that utilise electrochemical principles to detect and quantify target analytes in various samples, namely the protons (pH) in freshwater and seawater, and the bromide and chloride anions in the latter in this thesis. The unique advantages of electrochemical sensors include high sensitivity, rapid response, portability, and ease of use. The design and fabrication of electrochemical sensors involve careful selection of electrode materials, optimisation of sensor geometry, and consideration of factors such as selectivity, sensitivity, and reproducibility. In this thesis, we applied electrochemical methods including cyclic voltammetry, linear sweep voltammetry, square wave voltammetry and chronoamperometry to meet the goals mentioned. Meanwhile, interpreted by the fundamental electrochemistry, the observed electrochemical behaviours provided insightful information such as reaction mechanisms, electron transfer kinetics and so on for a specific analyte at various electrode surfaces. The followings are the conclusions that have been drawn:

1. The optimisation of in-situ electrochemical fabrication allows for the formation of an iridium hydrous oxide film under near-neutral conditions, in contrast to previous reports made on acidic conditions. The formation of a pH-sensitive Ir(III/IV) hydrous oxide film was confirmed by XPS analysis. By employing square wave voltammetry, the electrochemically generated redox signal exhibited a pH dependency of 86.1 ± 1.1 mV per pH unit within the pH range of 2-13. The developed pH sensor was successfully validated using natural water samples. Based on the same fabrication mechanism, a calibration-free Ir sensor for pH measurements in air-saturated seawater was developed. The sensor's calibration-free nature was achieved by measuring the potential difference between Ir(III/IV) and the less sensitive upd H oxidation signal using linear sweep voltammetry, with pH reported on the total hydrogen ion scale. The optimised sensor exhibits a pH dependency of 70.1 ± 1.4 mV per pH unit at 25 °C, demonstrating a super-Nernstian response and high sensitivity.

2. The independent analysis of chloride and bromide in seawater poses challenges due to the complex matrix of seawater and importantly, quantification of sub-millimolar levels of bromide is hindered by the presence of chloride at much higher concentrations. Four types of electrodes (Ag, Au, glassy carbon, and Pt) were evaluated for the analysis of Cl^- and/or Br^- in seawater. While silver electrodes are commonly used for amperometric halide measurements for the ions with similar concentrations, the bromide signal in seawater was masked by the chloride signal due to the presence of chloride ions at high millimolar levels. The use of Au electrodes was found to be unsuitable due to dissolution and passivation in ASW. Glassy carbon electrodes resulted in poorly defined chloride and bromide signals. Lastly, platinum electrodes were identified as suitable for the individual detection of bromide and chloride in artificial seawater using square wave voltammetry. Electrochemical measurements in natural seawater demonstrated good agreement with ion chromatography results.

3. As a reference electrode, the silver–silver bromide couple has been widely and extensively used. The fundamental electrochemistry of the $Ag/AgBr/Br^-$ redox couple was studied by both simulation and experimentation. This is a simple electrode reaction of 0:1 stoichiometry that leads to the formation of an insoluble product from a soluble reactant, namely, the oxidation of silver in the presence of bromide ion at a silver electrode with the formation of solid silver bromide, $Ag(s) + Br^-(aq) \rightleftarrows AgBr(s) + e^-$. Although the couple exhibits quasi-reversibility in voltammetric measurements, which at first sight is a disadvantage, its intrinsic high sensitivity in terms of the current response to potential, as evidenced by the ultrahigh apparent transfer coefficients exceeding unity, compensates for this characteristic. The conclusions drawn for the $Ag/AgBr/Br^-$ redox couple are generic to reverse redox couples with a 0:1 stoichiometry which are seen to be inherently more robust in maintaining a nearly fixed potential even when subjected to significant current flow. This property is crucial for the development of reliable reference electrodes.